RF Project 761420/711626
Interim Technical Report

Project Title:

INVESTIGATION OF INFRARED SPECTRA OF ATMOSPHERIC GASES TO SUPPORT STRATOSPHERIC SPECTROSCOPIC INVESTIGATIONS

John H. Shaw, Principal Investigator
Department of Physics

Ph.D. Dissertation Title:

THE RETRIEVAL OF ATMOSPHERIC CONSTITUENT MIXING-RATIO PROFILES FROM SOLAR ABSORPTION SPECTRA

By
William Allen Shaffer, M.S.

The Ohio State University
1983

NATIONAL AERONAUTICS AND SPACE ADMINISTRATION
Headquarters Contracts and Grants Division
Washington, D.C. 20546

Grant No. NSG-7479

February, 1984

The Ohio State University Research Foundation
1314 Kinnear Road
Columbus, Ohio 43212

THE RETRIEVAL OF ATMOSPHERIC CONSTITUENT MIXING-RATIO PROFILES FROM SOLAR ABSORPTION SPECTRA

William A. Shaffer

Ph.D. Dissertation

The Ohio State University

1983

Page intentionally left blank

Page intentionally left blank

ACKNOWLEDGMENTS

I am indebted to Dr. C. B. Farmer of the Jet Propulsion Laboratory for kindly allowing me to use his ATMOS spectra. Others at the Jet Propulsion Laboratory who instructed me in the use of the ATMOS computer were Dr. L. Brown, Dr. O. Raper, Dr. R. Norton, and Dr. R. Toth. Their patience with my ignorance went a long way towards completing this dissertation.

The slant path calculating program used in this work was provided by Dr. A. Goldman of the University of Denver. His explanations of Treve's theory were invaluable.

As always, a work of this size is not completed without the assistance of many co-workers. Mr. David Castle worked many long hours on the drafting of the figures for this work. Mr. Arthur Levitt translated the ATMOS spectra into readable form. And Dr. M. Hoke and Mrs. Landa Hoke contributed two of the figures used here as well as clarified the ideas contained in this work through many long discussions.

Page intentionally left blank

Page intentionally left blank

TABLE OF CONTENTS

Page intentionally left blank

Page intentionally left blank

LIST OF TABLES

Page intentionally left blank

Page intentionally left blank

LIST OF FIGURES

Chapter I

INTRODUCTION

1.1 SURVEY OF RECENT RESEARCH

In recent years the critical nature of the photochemical interactions involving chlorine, nitrogen, oxygen, and hydrogen compounds occurring in the atmosphere has become apparent. The danger of anthropogenic reduction of the protective ozone layer of the stratosphere (1) and the possible global heating due to increases in CO_2 from deforestation and fossil fuels and methane from agricultural sources (2) are also of concern. The uncertainty surrounding the importance of each of these effects has stirred much interest in understanding the structure of the atmosphere. The study of the atmosphere has recently been recognized as one of the most important fields of scientific inquiry both in its own right and because of its importance to the survival of mankind (3).

In order to understand atmospheric processes it is necessary to know the distribution of the various atmospheric molecules with altitude. The nature and influence of the pollutants in the atmosphere can only be estimated if these distributions are known. Both minor (parts per million) and trace (parts per billion) constituent distributions have been determined by in situ experiments which sample the local

environment and remote-sensing techniques which allow simultaneous concentration measurements over wide altitude, latitude, and longitude ranges of the atmosphere.

A brief summary of some of the methods used to determine various atmospheric gas distributions is given below. Shown in Figure 1 are the experimentally determined mixing-ratio profiles (the mixing-ratio of a gas is the ratio of the number of gas molecules to the number of air molecules) of some atmospheric gases. The range of research being done on the atmosphere makes an exhaustive summary impossible. However, the following treatment illustrates the wide variety of experimental methods employed.

In most in situ experiments stratospheric gas samples are collected at several altitudes by balloon, aircraft, or rocket. These samples are then analyzed by various methods. Mixing-ratio profiles of Cl, ClO, and OH have been determined by laser induced fluorescence of samples obtained by balloon (4-6) and by aircraft (7,8). Others have analyzed gas samples obtained from airplanes (9,10) and balloons (11-15) by gas chromatography in order to determine the molecular abundances of CCl_2F_2, CCl_4, CCl_3F, $CFCl_3$, CF_2Cl_2, $CHClF_2$, CH_3CCl_3, CH_4, CO, $C_2Cl_3F_3$, C_2Cl_4, C_2HCl_3, C_2H_2, C_2H_4, C_2H_6, C_3H_8, C_6H_6, C_7H_8, H_2, and N_2O. Another method used to obtain abundances of CH_4, CO, CO_2, H_2, H_2O, N_2O, and O_3 was mass spectroscopy of samples obtained by a rocket (16) and a balloon (17).

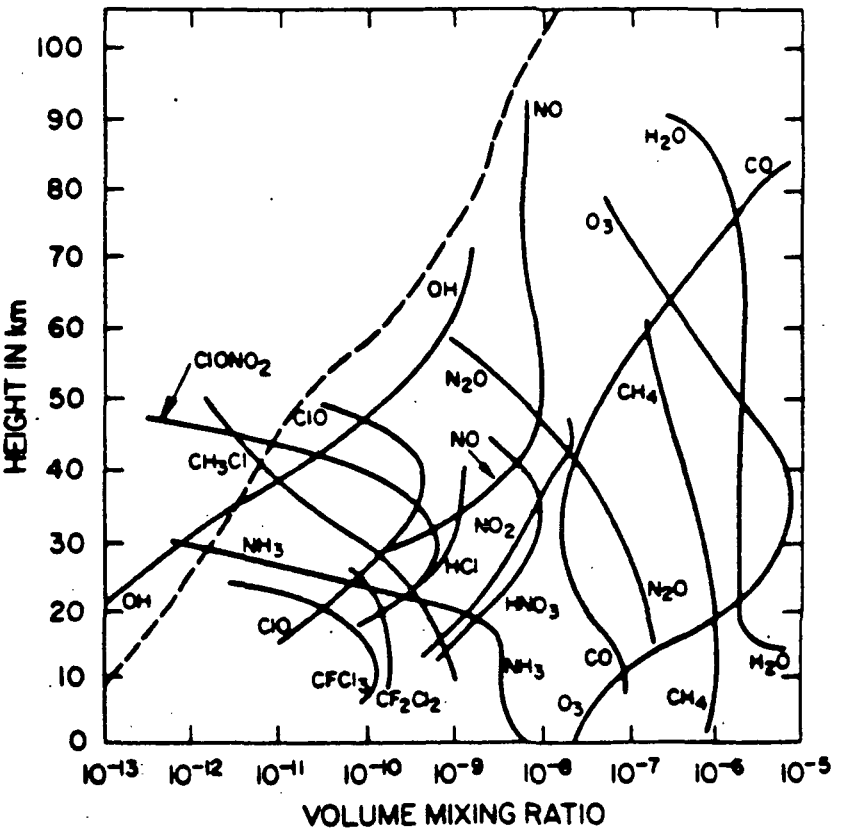

Figure 1: The vertical distribution of several atmospheric gases after Gille (1).

Experiments which depend on the collection of gas samples are subject to the problems of contamination of the sample due to impurities on the container walls, contamination due to leakage of the sample during storage, and the loss of active gases due to chemical reactions. Some investigators have avoided the problems associated with gas sampling by using dyes deposited by balloon or rocket which react chemiluminescently with the atmospheric constituent of interest. The spectral radiance of the sky due to these reactions is a measure of the concentration of the atmospheric constituent. This method has been used to determine the stratospheric profiles of NO (18) and O_3 (19-21).

In situ measurements of atmospheric composition allow only local regions of the atmosphere to be studied. A complete understanding of the atmospheric interactions requires global monitoring of the constituent distributions as well as the temporal variations of these distributions. Rapid observations with large spatial coverage have been made by remote-sensing techniques (22-38).

One remote-sensing technique which has been used is the collection and analysis of atmospheric emission spectra. Atmospheric emission spectra have been obtained from instruments at ground level (22) and in balloons (23). These spectra have been analyzed to obtain mixing-ratio profiles for ClO and OH. The radiation emitted by the atmosphere has also been studied using satellite-borne

instruments and the "onion skin peeling" technique (24,25) to obtain the mixing-ratio profiles of CF_2Cl_2, H_2O, HNO_3, and NO_2. The radiative transfer problem for emission from atmospheric constituents is much more difficult to parameterize than spectral absorptance. This limits the information obtainable from emission spectra analysis. Although adequate for monitoring minor constituents (ppm) and determining atmospheric temperature and pressure profiles, emission spectroscopy is generally not as useful as solar absorption spectroscopy for the study of trace gases (ppb).

Trace gases can be studied by solar absorption spectra, since most gases of interest have strong unobscured absorption bands in the infrared, but accurate analysis of such spectra requires sophisticated analytical techniques and usually many simplifying assumptions. Many techniques have been developed for the interpretation of absorption spectra. Infrared absorption spectra obtained from the ground (26-28), balloons (29-32), and airplanes (33,34) have been used to determine the mixing-ratio profiles of CH_4, CO, COS, CO_2, HCN, HCl, HF, HNO_3, H_2CO, H_2O, NO, NO_2, N_2O, and O_3. Visible absorption spectra obtained from balloons (35) have been used to determine the profile of NO_2. Ultraviolet spectra from balloons (36,37) and satellites (38) have been used to determine the stratospheric ozone profile.

The global and temporal variations of many trace gases over a large altitude range can only be monitored by

absorption spectra obtained from satellites. However, few infrared absorption spectra have so far been obtained from satellite-borne instruments. The Atmospheric Trace Molecules Spectroscopy (ATMOS) experiment represents an attempt to fill this gap. ATMOS will allow the monitoring of many gases (some of which are listed in Table 1) up to 100 km above the earth's surface, nearly doubling the altitude range covered by balloon-borne instruments. The analysis described in this work has been done in support of the ATMOS project (however, the results obtained in this work can be used to aid the interpretation of many types of solar spectra). A description of the ATMOS instrument and experiment are given below.

We have attempted to determine the limits to the information retrievable from analysis of the spectral data which is expected to be obtained from this experiment as well as other experiments. Comparisons have also been made of the results expected from satellites to those obtainable from balloons and ground-based observers.

1.2 THE ATMOS EXPERIMENT

The ATMOS instrument, shown in Figure 2, contains a dual moving cat's-eye interferometer. The interferometer has been designed to make the instrument insensitive to angular and lateral motion of the moving components. This was accomplished by replacing the plane mirrors of a

Table 1: A compilation of some atmospheric gases expected to be detectable by the ATMOS experiment (as of 1980).

Category 1	Category 2	Category 3	
CO	HCl	N_2O_5	SO_2
CO_2	HF	CH_3Cl	H_2O_2
H_2O	NO	NH_3	HO_2
N_2O	NO_2	CH_3F	HO_2NO_2
CH_4	ClO	CH_3Br	CFClO
HDO	HNO_3	F_{11}	CF_2O
O_3	OH	F_{12}	HOCl
		$ClONO_2$	NO_3

Category 1: Minor constituents

Category 2: Trace constituents which have been observed.

Category 3: Trace constituents of specific interest to ATMOS objectives which have not been quantitatively measured by remote sensing.

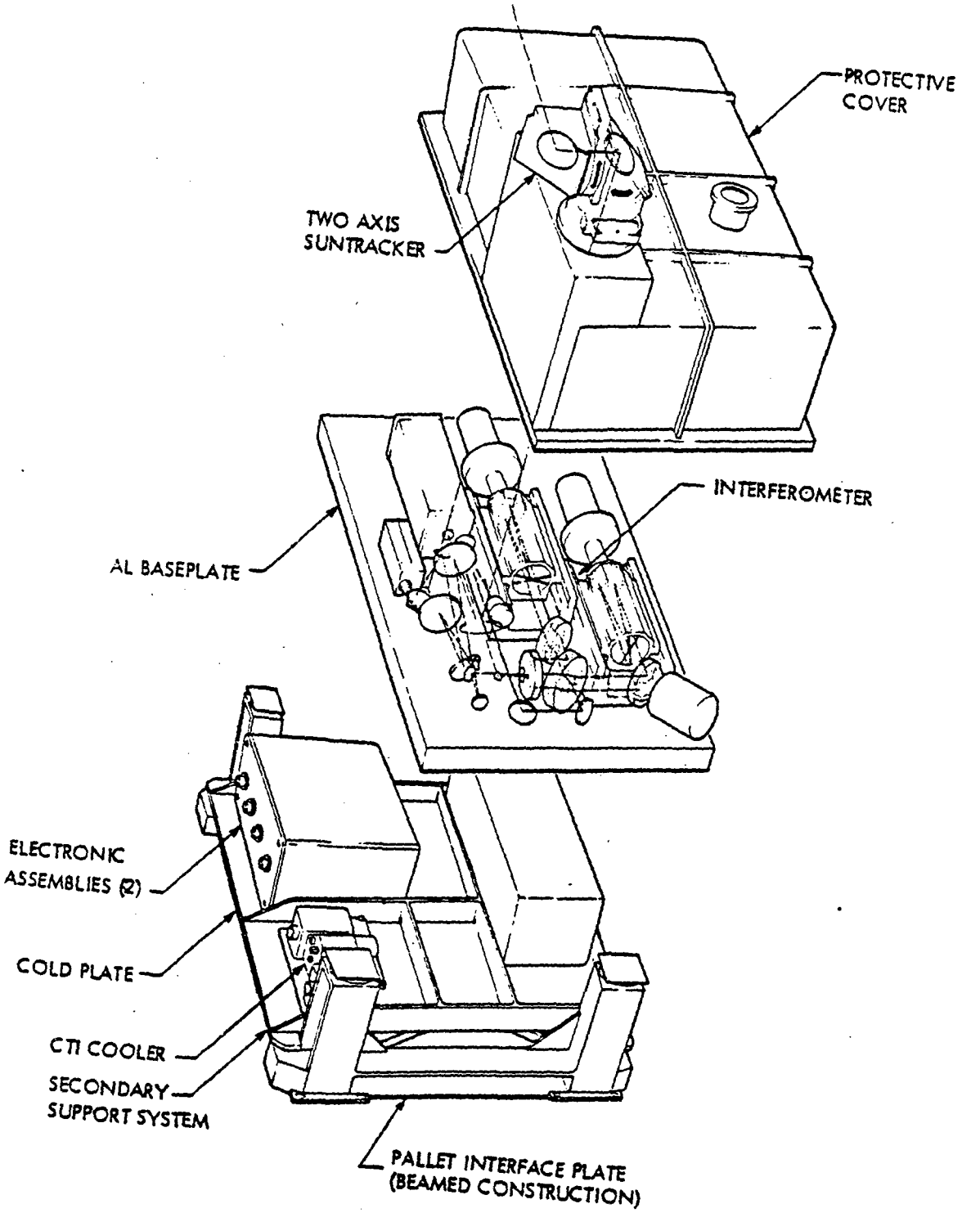

Figure 2: The ATMOS (Atmospheric Trace Molecules Spectroscopy) instrument.

conventional Michelson interferometer with cat's-eye retroreflectors. In addition the radiation is double passed through the arms of the interferometer before being sent to the detector in order to eliminate distortions due to the lateral motion of the instrument. The HgCdTe detector is cooled by liquid nitrogen.

The supporting equipment consists of a suntracker, a telescope, and a camera. The suntracker consists of two single-axis, motor-driven mirrors and a silicon diode assembly for sensing and controlling the position of the mirrors with respect to the sun. An f/2 telescope is used to focus the radiation received by the instrument into a beam suitable for the interferometer. A 16 mm camera records the image of the sun on the entrance aperture to the instrument in order to determine the portion of the disc viewed, to insure, if necessary, that data obtained for a field of view containing a sunspot may be identified and excluded from the data analysis.

The ATMOS instrument is scheduled to fly on Spacelab 3 in 1984. The experiment to be conducted involves viewing the sun with the ATMOS instrument at periods when portions of the earth's atmosphere occult the sun. Measurements will be made of the incident solar radiation as a function of the optical path difference of the beams in the instrument. Fourier transforms of these collected interferograms will give solar absorption spectra covering the region from about

2 μm to 16 μm. Measurements obtained for various radiation paths through the atmosphere will allow the determination of the mixing-ratio profiles of atmospheric constituents. Because of the orbital geometry of the space shuttle and the rate at which the interferograms are measured by the ATMOS instrument as well as the broad wavelength coverage, simultaneous mixing-ratio profiles with good vertical resolution of many constituents will be obtained together with the global variations of these profiles. This will give a three-dimensional view of the constituent abundances, a view which is crucial to an understanding of atmospheric processes. Some of the molecules expected to be detectable by ATMOS are listed in Table 1. Little is known about the global distribution of many of these gases, many of which are important in the reduction or maintenance of the ozone layer.

1.3 SUMMARY OF THIS WORK

In this work an attempt is made to determine the amount of information about the distribution of absorbing gases in the atmosphere obtainable from analysis of the data to be obtained from the ATMOS experiment. The results obtainable for satellite remote-sensing have also been compared to the more common remote-sensing balloon-borne and ground-based experiments.

One method which has been used by others to analyze spectra obtained by satellite-borne instruments is the "onion skin peeling" technique (24,25). In this technique the radiative transfer problem is modeled in the many atmospheric layers traversed by the radiation one at a time. Thus errors introduced by the analysis method into the solution in previous layers will be compensated for in successive layers, propagating the errors throughout the obtained mixing-ratio profile. In this work we have developed a technique which analyzes all portions of the radiation paths of several solar rays simultaneously assuming no a priori knowledge of the shape of the profile to be retrieved. Thus any error in the retrieved mixing-ratio profiles is due only to the experimental noise and uncertainties in the experimental conditions and not to inadequacies in the analysis technique. The results in this work represent the optimum obtainable for the specified experimental conditions.

In Chapter 2 the uncertainty and the vertical resolution as a function of altitude obtained in the retrieval of a vertically-constant, mixing-ratio profile are estimated by analyzing synthetic, equivalent-width data using a linear least-squares technique. Estimates of the uncertainty and vertical resolution are obtained for observing instruments at satellite and balloon altitudes as well as for ground-level observations.

In the third chapter the effects of systematic errors in the parameters describing the instruments orientation with respect to the earth as well as those describing the thermal structure of the atmosphere on the retrieval of mixing-ratio profiles are investigated using a linear least-squares technique. A method is described by which many of these systematic errors can be eliminated in the analysis.

In the fourth chapter the information contained in the shape of spectral lines is estimated. Spectral data obtained from a recent ground-level test of the ATMOS instrument are analyzed using a non-linear least-squares technique to retrieve information about the mixing-ratio of N_2O.

In this work we have not attempted to model the smearing effects on spectral data due to the motion of the observing instrument (39) or the finite field of view of the instrument (40). These effects (and others) need to be considered in order to accurately determine the information content of such data. Although the modeling of such smearing effects will modify the results obtained in this work, we have presented a method of analysis which allows the determination of this information content as well as the structure of retrieved mixing-ratio profiles.

REFERENCES

1) The Stratosphere 1981 Theory and Measurement, WMO Global Ozone Research and Monitoring Project, Report no. 11, 1982.

2) R. A. Kerr, Science, 220, 1364 (1983).

3) Industrial Research and Development, 25, 56 (1983).

4) J. G. Anderson, J. J. Margitan, and D. H. Stedman, Science, 198, 501 (1977).

5) J. G. Anderson, H. J. Grassl, R. E. Shetter, and J. J. Margitan, J. Geophys. Res., 85, 2869 (1980).

6) W. S. Heaps, Appl. Opt., 19, 243 (1980).

7) D. D. Davis, W. Heaps, and T. McGee, Geophys. Res. Lett., 3, 331 (1976).

8) C. C. Wang, L. I. Davis, Jr., P. M. Selzer, and R. Munoz, J. Geophys. Res., 86, 1181 (1981).

9) R. Leifer, L. Toonkel, R. Larsen, and R. Lagomarsino, J. Geophys. Res., 85, 1069 (1980).

10) R. A. Rasmussen, M.A.K.Khahil, and R. J. Fox, Geophys. Res. Lett., 10, 144 (1983).

11) D. J. Hofmann, J. M. Rosen, A. L. Fuller, D. W. Martell, G. L. Olsen, A. L. Schmeltekopf, and P. D. Goldan, Antartic Journal Annual Review, 185 (1978).

12) B. J. Tyson, J. F. Vedder, J. C. Aruesen, and R. B. Brewer, Geophys. Res. Lett., 5, 369 (1978).

13) P. Fabian, R. Borchers, G. Flentje, W. A. Matthews, W. Seiler, H. Giehl, K. Bunse, F. Müller, U. Schmidt, A. Volz, A. Khedin, and F. J. Johnen, J. Geophys. Res., 86, 5179 (1981).

14) P. D. Goldan, W. C. Kuster, A. L. Schmeltekopf, F. C. Fehsenfeld, and D. L. Albritton, J. Geophys. Res., 86, 5385 (1981).

15) R. A. Rasmussen, M.A.K.Khalil, and A. J. Crawford, Geophys. Res. Lett., 9, 704 (1982).

16) D. H. Ehhalt, L. E. Heidt, R. H. Lueb, and E. A. Martell, J. Atm. Sci., 32, 163 (1975).

17) K. Mauersberger, R. Finstad, S. Anderson, and D. Robbins, Geophys. Res. Lett., 8, 361 (1981).

18) J. W. Drummond, J. M. Rosen, and D. J. Hofmann, Nature, 265, 319 (1977).

19) P. Aimedieu, P. Rigaud, and J. Barat, Geophys. Res. Lett., 8, 787 (1981).

20) E. Hilsenrath and P. T. Kirschner, Rev. Sci. Instr., 51, 1381 (1980).

21) I. Konkov, V. A. Kononkov, and S. P. Perov, "A chemiluminescent method of rocket measurement of ozone vertical distribution," (Abstract) International Association of Meterorology and Atmospheric Physics, Third Scientific Assembly, Hamburg, Federal Republic of Germany, 17-28 August 1981.

22) A. Parrish, R. L. de Zafra, P. M. Solomon, J. W. Barnett, and E. R. Carlson, Science, 211, 1158 (1981).

23) J. W. Waters, J. C. Hardy, R. F. Jarnot, and H. M. Pickett, Science, 214, 61 (1981).

24) J. M. Russell III and L. L. Gordley, J. Atm. Sci., 36, 2259 (1979).

25) J. C. Gille, P. L. Bailey, and J. M. Russell III, Phil. Trans. Roy. Soc. Lond. A, 296, 205 (1980).

26) C. P. Rinsland, M. A. H. Smith, P. L. Rinsland, A. Goldman, J. W. Brault, and G. M. Stoke, J. Geophys. Res., 87, 11,119 (1982).

27) A. Goldman, F. G. Fernald, F. J. Murcray, F. H. Murcray, and D. G. Murcray, J. Quant. Spec. Rad. Trans., 29, 189 (1982).

28) P. Marché and C. Meunier, Planet. Space. Sci., (to be published).

29) E. Niple, W. G. Mankin, A. Goldman, D. G. Murcray, and F. J. Murcray, Geophys. Res. Lett., 7, 489 (1980).

30) R. D. Blatherwick, A. Goldman, D. G. Murcray, F. J. Murcray, G. R. Cook, and J. W. Van Allen, J. Geophys. Res., 7, 471 (1980).

31) H. L. Buijs, G. L. Vail, G. Tremblay, and D. J. W. Kendall, Geophys. Res. Lett., 7, 205 (1980).

32) N. Louisnard, G. Fegent, A. Girard, L. Gramont, O. Lado-Bordowsky, J. Laurent, S. Le Boiteaux, and M. P. Lemaitre, J. Geophys. Res., 88, 5365 (1983).

33) C. B. Farmer, O. F. Raper, B. D. Robbins, R. A. Toth, and C. Muller, J. Geophys. Res., 85, 1621 (1980).

34) M. T. Coffey, W. G. Mankin, and A. Goldman, J. Geophys. Res., 86, 7331 (1981).

35) T. Ogawa, K. Shibusaki, and K. Suzuki, J. Meteorol. Soc. Japan, 59, 410 (1981).

36) J. E. Mentall, J. R. Herman, and B. Zak, "Ozone profile and solar fluxes from a grating spectrometer," The Stratrom VIII Effort, NASA Technical Paper 1640, E. Reed, editor, pp. 117-123, April 1980.

37) P. C. Simon and W. Peetermans, "Ozone trend in the upper stratosphere: Results from solar UV absorption measurements from 1976-1980," (Abstract) International Association of Meteorology and Atmospheric Physics, Third Scientific Assembly, Hamburg, Federal Republic of Germany, 17-28 August 1981.

38) A. C. Aikin, B. Woodgate, and H. J. P. Smith, Appl. Opt., 21, 2421 (1982).

39) J. H. Park, Appl. Opt., 21, 1356 (1982).

40) J. P. Naudet, P. Rigaud, and D. Huguenin, Geophys. Res. Lett., 7, 701 (1980).

Chapter II

THE RESOLUTION OF RETRIEVED MIXING-RATIO PROFILES

2.1 INTRODUCTION

The analysis of solar spectral data to retrieve mixing-ratio profiles of atmospheric constituents requires assumptions to be made about the kind of information retrievable and the quality of this information.

If it is assumed that a continuous mixing-ratio function of known shape can be retrieved and the shape of the assumed function is incorrect or if the data contain insufficient information, then it is possible to obtain a profile with no apparent systematic errors but very large uncertainty. The inclusion of the a priori information (1) forces a solution which may not be correct. If it is assumed that only independent, discrete values of the mixing-ratio profile can be obtained, it is necessary to know how many values are obtainable from the data, their spacing, and their uncertainty in order to determine the appropriate analytical method.

The extraction of geophysical information from gross earth data containing noise has been considered by Backus and Gilbert (2-7). A method was derived in which the vertical resolution of retrieved geophysical profiles was

found in terms of the uncertainty in the retrieved profile. The method of Backus and Gilbert has been used to estimate such varied quantities as the vertical resolution of atmospheric temperature profiles (1,8,9), aerosol size distributions (10), and the conductivity in the earth's mantle (11). No such studies have been done on the vertical resolution of constituent mixing-ratio profiles obtained from absorption spectra.

In this chapter the problem of obtaining a mixing-ratio profile from spectral data containing noise by assuming all the other physical parameters describing the experiment are exactly known is investigated. The data analyzed consisted of absorber amounts, calculated by using Eqs. (A.95)-(A.97) (See Appendix A), for various paths through the atmosphere as shown in Figure 3. These absorber amounts, as shown in section 2, could be obtained from equivalent width analysis of weak lines appearing in the spectra.

In section 3 the method of Backus and Gilbert is applied to the extraction of mixing-ratio profiles from absorber amount data. The analysis shows that only discrete mixing-ratio values are retrievable and the uncertainties in the retrieved values are minimized if the sum of the square residuals (RSS), where the residual is the difference between the measured absorber amount and that obtained using the retrieved profile, is a minimum. It was found that the uncertainty increases and the resolution degrades with altitude.

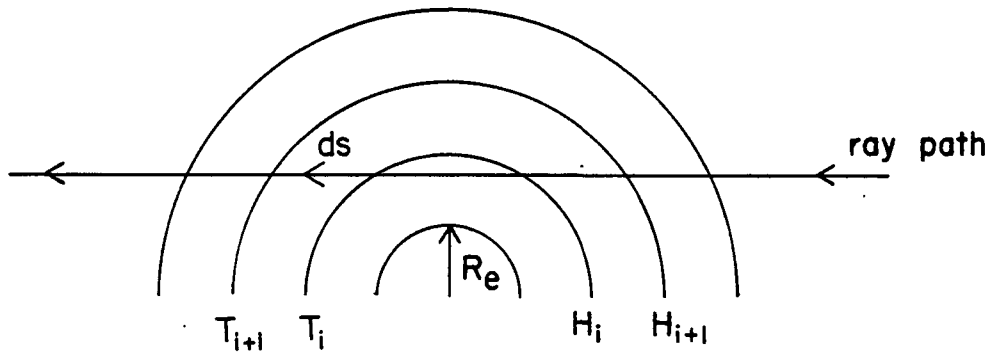

Figure 3: The path of radiation through a layered atmosphere where each layer is characterized by lower geopotential altitude H_i, upper altitude H_{i+1}, and temperature T_i at altitude H_i. The optical airmass encountered by the ray in element of path ds is da.

An analytical method which uses the minimization of the RSS (described in section 4) was developed to retrieve mixing-ratio profiles from absorber amount data. The atmosphere, as shown in Figure 3, was divided into concentric shells at which the temperature, pressure, and density are defined. Absorber amounts were calculated for each ray path by assuming a constant mixing-ratio profile for the absorber. Random noise was added to the absorber amount data sets. The mixing-ratio values were then retrieved from these simulated data sets by using P9R (12), a linear least-squares computer program.

This program retrieved a set of local mixing-ratio values and their standard deviations. The standard deviations were used to estimate the uncertainty in the retrieved profiles. In section 5 a general relation is given for this uncertainty in terms of the altitude and the mixing-ratio value spacing.

The vertical resolution was determined in the sixth section by using the uncertainty function obtained in the previous section. The forms of these expressions agree with those predicted by the Backus and Gilbert method.

The mixing-ratio value spacing needed for a particular analysis is determined by the vertical resolution. This spacing should not be less than half the vertical resolution at any altitude and thus it also determines the number of retrieval values. By reducing this number the amount of

computer time required is reduced, an important factor when the retrieval is accomplished by modeling the spectral line shapes of several overlapping lines. In the seventh section the appropriate retrieval parameter spacing for two values of the SNR is discussed.

Finally it is desirable that the derived relations for the uncertainty and the vertical resolution be extended to mixing-ratio profiles of arbitrary shape. In the final section comparisons were made of retrievals from data obtained from other profiles. The functional forms obtained for the uncertainty and the vertical resolution in the fifth and sixth sections were found to be adequate to describe that obtained for these profiles.

In brief the goal of this chapter is to determine the maximum amount of information about the mixing-ratio profile retrievable from absorber amount data and the quality of the retrieved values with the object of constructing the optimum retrieval scheme for a particular data set.

As an aid to the reader, the symbols used in this work are listed in Appendix B.

2.2 EQUIVALENT WIDTH ANALYSIS OF SPECTRA

In this chapter we investigate the analysis of absorber amount data. A set of solar spectra obtained from solar radiation passing through various portions of the atmosphere contains information about the distribution of absorber along

the path traversed by the radiation. The total absorber amount along the ray can be determined by equivalent width analysis of the spectra.

Let I_ν be the intensity of radiation per unit area from a nearly parallel beam. After passing through a path-length da_m of absorber, the change in intensity dI_ν is

$$dI_\nu = -g_\nu k_\nu I_\nu da_m \tag{1a}$$

where g_ν is some function representing the effect of the instrument on the observed radiation and k_ν the absorption coefficient at frequency ν. The total change in the energy in the beam dI is

$$dI = -\int_{-\infty}^{\infty} g_\nu k_\nu I da_m d\nu \ . \tag{1b}$$

If the instrument function is defined only over some frequency interval $\Delta\nu$ the total change in energy is

$$dI = -\int_{\Delta\nu} g_\nu k_\nu I da_m d\nu \tag{1c}$$

and, if $\Delta\nu$ is small* (i.e., high spectral resolution) then k_ν and I are constant over the integral or

$$dI = -k_\nu I_\nu da_m \int_{\Delta\nu} g_\nu d\nu \ . \tag{1d}$$

Thus the total observed change in energy is scaled by the integral of the instrument function. Normalization of

---

*Nielsen et al. (13) have shown that the equivalent width is independent of the instrument function width.

Eq. (1d) gives

$$dI = -k_\nu I da_m \tag{1e}$$

or upon integration

$$\frac{I(\nu)}{I_o} = \exp[-k_\nu a_m] \ . \tag{1f}$$

If the transmittance T_ν is defined as $I(\nu)/I_o$, then

$$T_\nu = \exp[-k_\nu a_m] \ . \tag{2a}$$

The spectral absorptance at frequency ν is defined by

$$A_\nu = 1 - T_\nu \ . \tag{2b}$$

For a single spectral line the area under the absorption curve shown in Figure 4 is given by

$$W(a_m) = \int_{-\infty}^{\infty} A_\nu d\nu \ . \tag{3}$$

The area W(a) is equal to the area under a rectangle of width W(a) as shown in Figure 5 and W(a) is defined as the equivalent width of the spectral line of Figure 4. Combining Eqs. (2) and (3) gives

$$W(a_m) = \int_{-\infty}^{\infty} (1 - \exp[-k_\nu a_m]) d\nu \ . \tag{4}$$

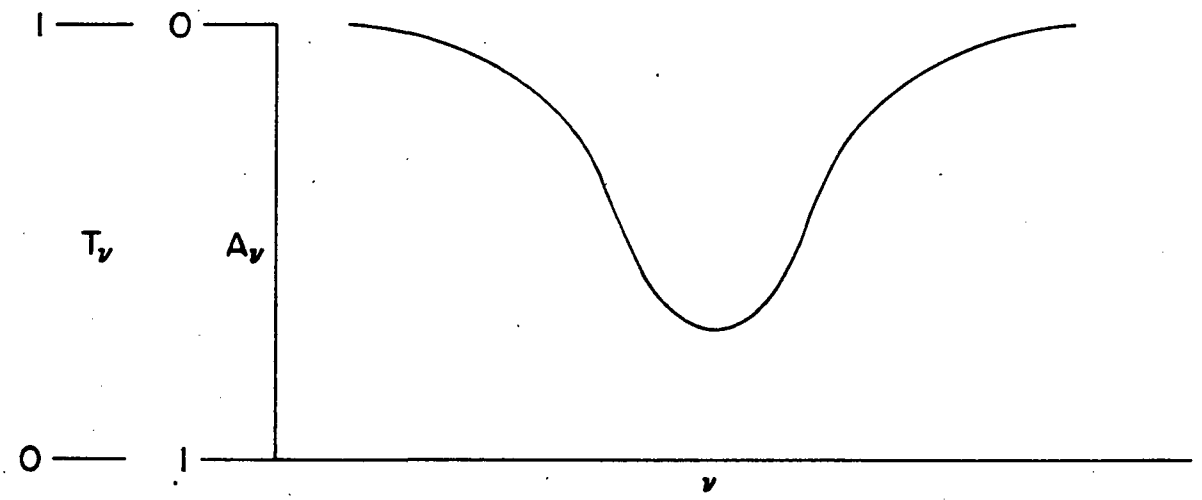

Figure 4: A single absorbtion line.

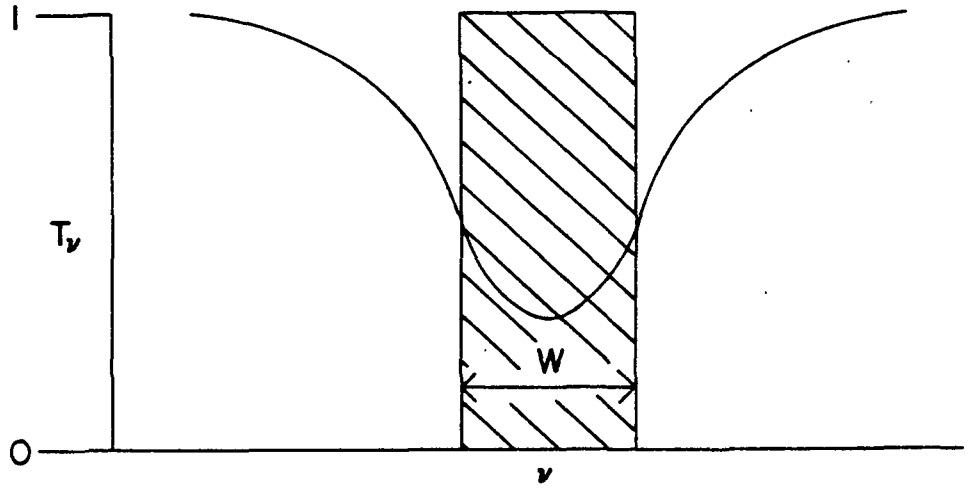

Figure 5: The equivalent width W of a single absorption line. The area of the rectangle is equal to the area between the absorption line and $T_\nu = 1$.

If $k_\nu a_m << 1$ then the exponential in Eq. (4) can be approximated by the first two terms in the series expansion. Thus the equivalent width becomes

$$W(a_m) = \int_{-\infty}^{\infty} k_\nu a_m d\nu \ . \tag{5}$$

Since a_m does not depend on the frequency,

$$W(a_m) = a_m \int_{-\infty}^{\infty} k_\nu d\nu \ . \tag{6}$$

The intensity S of the spectral line is defined as

$$S = \int_{-\infty}^{\infty} k_\nu d\nu \ , \tag{7}$$

so

$$W(a_m) = S a_m \ . \tag{8}$$

For weak lines ($A_\nu << 1$) the equivalent width is proportional to the absorber amount along the path provided S is not dependent on the temperature. If the line intensity is known and the area under the absorptance curve is measured, then the absorber amount if found by

$$a_m = W(a_m)/S \ . \tag{9}$$

This expression was obtained for a homogeneous gas sample. The atmosphere is inhomogeneous, and the temperature and density vary along the path. The absorption coefficient k_ν is temperature and pressure dependent and the intensity S is temperature dependent. The problem of the inhomogeneous path is complicated. However, if the atmosphere is divided into concentric layers the ray path can be divided into a series of atmospheric portions which can be considered to be homogeneous. Provided $A_\nu << 1$, since the equivalent widths of weak lines are additive, the total absorber amount can be estimated for atmospheric paths.

For larger values of A_ν Eq. (9) is no longer true. In this case the expressions for $W(a_m)$ are more complicated (14,15) and it is more difficult to extract information about the absorber amount. We have considered only the case of weak spectral lines in this chapter. This represents not only the simplest set of data to analyze but also, because of the additive nature of the equivalent widths, it yields the maximum information.

The equivalent width method is useful when the true spectral features are narrower than the spectral resolution, since the equivalent widths obtained from actual spectra are essentially independent of the shape of the instrumental response function and its width (15). Equivalent width analysis has been used by many groups including Buijs et al (16) who determined the mixing-ratio profiles of HCl and HF

between 15 and 30 km altitude from spectra obtained by a balloon-borne instrument. Other investigators (17,18) have used equivalent width analysis to obtain mixing-ratio profiles for CH_4 (17) and H_2CO (18) from ground-level observations. In the two ground-level retrievals a priori assumptions were made about the shapes of the mixing-ratio profiles to be obtained. Even so the vertical resolution was very poor. Some of the reasons for this are discussed below.

2.3 THE THEORY OF BACKUS AND GILBERT

2.3.1. General formalism

The total constituent absorber amount a_m encountered by a solar ray traversing the atmosphere is given by

$$a_m = \int m(r)\,da \tag{10}$$

where m(r) is the constituent mixing-ratio by volume of absorber m, da is the number of atmospheric molecules per unit area in path element ds and r is the distance from earth's center (see Figure 3). The retrieval of the mixing-ratio profile from a set of absorber amounts involves the inversion of Eq. (10). The inversion of integral equations of this type is often required in atmospheric problems and these inversions are often difficult. If no a priori assumptions are made about the functional form of m(r), only

discrete, mean values of m(r) can be obtained at values of r corresponding to the peak in da for each absorber amount. Also the noise in the experimental absorber amounts causes uncertainties in the discrete mixing-ratio values retrieved.

Backus and Gilbert (2-7) have considered the inversion of equations of this type and have shown the noise causes an unavoidable trade-off between the vertical resolution and the uncertainties in the derived profiles.

Consider N_o measurements of the absorber amount along N_o different ray paths through the atmosphere. The mixing-ratio profile m(r) is obtained by simultaneous solution of the N_o linear, first-order, integral equations

$$a_{mi}(m) = \int_{r_{Ti}}^{r_{TOP}} m(r) \frac{da_i}{dr} dr \qquad (11)$$

where r_{Ti} is the radius of the sperical shell which contains the closest approach or tangent height of the ray and r_{TOP} is the radius of the spherical boundary of the top of the atmosphere.

It is convenient to introduce the dimensionless parameter

$$y = \frac{r - r_{Ti}}{r_{TOP} - r_{Ti}} . \qquad (12)$$

In terms of this parameter Eq. (11) becomes

$$a_{mi}(m) = \int_o^1 m(y) \frac{da_i}{dy} dy \ . \tag{13}$$

Thus the N_o $a_{mi}(m)$ measurements are given in terms of the $da_i(y)/dy$ weighting functions.

A composite weighting function can be constructed from the N_o weighting functions of Eq. (13) by defining

$$D(y) = \sum_{i=1}^{N_o} b_i \frac{da_i(y)}{dy} \tag{14}$$

where the constants $b_1,\ldots,b_{N_o}$ are chosen such that $D(y)$ is unimodular or

$$\int_o^1 D(y)dy = 1 \ . \tag{15}$$

We would also like to choose $b_1,\ldots,b_{N_o}$ so that $D(y)$ is weighted heavily near a value of y_o where the local average $\langle m_e \rangle_{y_o}$ of $m_e(y)$ is desired. The function $m_e(y)$ is the true mixing-ratio profile to be retrieved. It is desirable to have weighting function $D(y)$ closely approximating the delta function about y_o. Thus the average $\langle m_e \rangle_{y_o}$ which is retrieved is nearly equal to the true value $m_e(y_o)$.

The spread of weighting function $D(y)$ from y was defined by Backus and Gilbert (7) as

$$S(y_o, D) = 12 \int_o^1 (y - y_o)^2 D(y)^2 dy \ . \tag{16}$$

This spread is a measure of the width of the peak in the weighting function D(y). This width approximates the possible vertical resolution in the retrieved profile.

An inner product in the function space of the kernels of the integral equations given from Eq. (13) can be defined

$$\langle m, D \rangle = \int_o^1 m(y)D(y)dy \ . \tag{17}$$

The variation of the retrieved profile from the true mixing-ratio profile $m_e(y)$ is defined as

$$\Delta\langle m_e, D\rangle = \langle m, D\rangle - \langle m_e, D\rangle \ . \tag{18}$$

In terms of the inner product

$$\Delta\langle m_e, D\rangle = \sum_{i=1}^{N_o} b_i \int_o^1 [m(y) - m_e(y)] \frac{da_i(y)}{dy} dy \ . \tag{19}$$

The difference between measurement i of the absorber amount and the absorber amount given by the true mixing-ratio profile $m_e(y)$ is

$$\Delta E_i = \int_o^1 [m(y) - m_e(y)] \frac{da_i(y)}{dy} dy \ . \tag{20}$$

Thus the variation is

$$\Delta\langle m_e, D\rangle = \sum_{i=1}^{N_o} b_i \Delta E_i \ . \tag{21}$$

Since ΔE_i is the noise in measurement i, then $\overline{\Delta E_i} = 0$ if the noise is randomly distributed over the N_o data values. The square of the variation is

$$(\Delta\langle m_e, D\rangle)^2 = \left(\sum_{i=1}^{N_o} b_i \Delta E_i\right)\left(\sum_{j=1}^{N_o} b_j \Delta E_j\right) . \tag{22}$$

The mean square variation is given by

$$\overline{(\Delta\langle m_e, D\rangle)^2} = \sum_{i,j=1}^{N_o} b_i b_j \overline{\Delta E_i \Delta E_j} . \tag{23}$$

In terms of the matrix formulation

$$\overline{(\Delta\langle m_e , D\rangle)^2} = b^T E b , \tag{24}$$

where E is the covariance matrix of the measured values a_{mi}. The ith mean square variation is equal to the standard deviation σ_i of the ith retrieved value (16) so

$$\sigma^2 = b^T E b . \tag{25}$$

The optimum combination of retrieval value uncertainty and vertical resolution is found by minimization of the linear combination

$$Q(y) = qS(y) + (1 - q)\alpha\sigma^2(y) \tag{26}$$

where α is a factor which converts σ^2 into the same units as $S(y)$. The relationship obtained for $S(y)$ in terms of $\sigma(y)$ is called the trade-off curve. The appropriate combination of spread and standard deviation can be found for all values of $0 \leq q \leq 1$.

2.3.2 The theory applied to mixing-ratio retrieval

We wish to determine the best possible uncertainty (standard deviation) and vertical resolution (spread) in the retrieval of mixing-ratio profiles from absorber amount data. The smallest uncertainty corresponds to $q = 0$ and the highest vertical resolution to $q = 1$ in Eq. (26). These represent bounds for σ and S.

The kernel da_i/dy of Eq. (14) is proportional to the air density $\rho_i(y)$ along the ith path through the atmosphere. Since the composite weighting function is required to be unimodular the coefficient of the ith kernel is given by

$$b_i = \frac{1}{\int_o^1 \frac{da_i}{dy}\, dy} \quad . \tag{27}$$

For an isothermal atmosphere

$$\rho(y) = \rho(0)\exp[-y/H_s] \quad , \tag{28}$$

where H_s is the scale height given by

$$H_s = \frac{R^*T}{Mg} \quad . \tag{29}$$

Thus

$$b_i \alpha \exp[y/H_s] \quad . \tag{30}$$

If the N_o measurements of a_m are independent the cross terms of the covariance matrix E are zero, thus

$$E = \sigma_E{}^2 \underline{I} \quad , \tag{31}$$

where σ_E is proportional to the noise in the experimental data. From Eq. (25) σ^2 becomes

$$\sigma^2 = \sigma_E{}^2 b^T b \tag{32}$$

or

$$\sigma = \sigma_E \sqrt{b^T b} \quad . \tag{33}$$

Finally, combining Eqs. (30) and (33) we get

$$\sigma \alpha \frac{e^{\frac{y}{H_s}}}{SNR} \quad , \tag{34}$$

since σ_E is proportional to the experimental noise. Using the definition for y and the relation

$$r = R_e + A \tag{35}$$

where A is the geometric altitude above the earth's surface, Eq. (34) becomes

$$\sigma \alpha \frac{e^{\frac{A}{H_s}}}{SNR} . \tag{36}$$

Thus the minimum uncertainty in the retrieval increases exponentially with altitude.

The other limit that is needed is the minimum vertical resolution (spread). Rewriting Eq. (17) in terms of the composite weighting function gives

$$S \alpha \sum_{i,j=1}^{N_o} b_i b_j \int_o^1 (y - y_o)^2 e^{-\frac{2y}{H_s}} dy . \tag{37}$$

Upon integration Eq. (37) reduces to

$$S \alpha \sum_{i,j=1}^{N_o} b_i b_j \, e^{-\frac{y}{H_s}} \tag{38}$$

or

$$S \alpha \sum_{i,j=1}^{N_o} b_i b_j \frac{e^{-\frac{y}{H_s}}}{\sigma} . \tag{39}$$

Thus the spread reduces to

$$S \alpha \frac{e^{\frac{y}{H_s}}}{\sigma} \tag{40}$$

or, in terms of the altitude,

$$S \alpha \frac{e^{\frac{A}{H_s}}}{\sigma} \quad . \tag{41}$$

Therefore it is expected that the minimum uncertainty will increase and the optimum vertical resolution will degrade exponentially with altitude. The constants of proportionality in Eqs. (36) and (41) cannot be determined by the Backus-Gilbert method alone. They are obtainable from simulated retrievals on synthetic absorber amount data. This theory does allow the method of analysis which will give a minimum uncertainty to be determined. In the following derivation the proper method of analysis is determined.

2.3.3 Criterion for minimum uncertainty

The integral relations in Appendix A, Eqs. (A.95)-(A.97), for the optical airmass encountered by a refracted ray can be approximated by numerical integrations if the atmosphere is divided into concentric layers in which the relations (A.95)-(A.97) can be applied successively. In this formulation the jth absorber amount value is given by

$$a_{mj} = \sum_{i=1}^{N_o} m_i a_{ij} \quad , \tag{42}$$

where m_i is the local mixing-ratio value (assumed constant) in layer i and a_{ij} is the optical airmass encountered by the

jth ray in layer i.

If it is assumed that the atmosphere is uniform in all variables except altitude (i.e., the atmosphere is "horizontally" uniform), then the N_o weighting functions in Eq. (14) are identical and the composite weighting function becomes

$$D(y) = b \frac{da(y)}{dy} . \tag{43}$$

Using Eq. (43) the standard deviation given by Eq. (24) reduces to

$$\sigma^2 = b^2 \sum_{i,j=1}^{N_o} \overline{\Delta E_i \Delta E_j} . \tag{44}$$

Expansion of the j summation gives

$$\sigma^2 = b^2 \sum_{i=1}^{N_o} \overline{\Delta E_i^2} + \overline{\Delta E_1 \Delta E_2} + \ldots + \overline{\Delta E_{N_o} \Delta E_{N_o-1}} . \tag{45}$$

If N_o is large then

$$\Delta E_1 (\Delta E_2 + \Delta E_3 + \ldots + \Delta E_{N_o}) \tilde{\sim} \Delta E_1 \sum_{i=1}^{N_o} \Delta E_i) , \tag{46}$$

so Eq. (45) becomes

$$\sigma^2 = b^2 \left[\sum_{i=1}^{N_o} \overline{(\Delta E_i)^2} + \Delta E_1 \overline{\sum_{i=1}^{N_o} \Delta E_i} + \ldots + \Delta E_N \sum_{i=1}^{N_o} \Delta E_i \right] . \tag{47}$$

But

$$\sum_{i=1}^{N_o} \Delta E_1 \simeq 0 \ , \tag{48}$$

if the noise is randomly distributed over the N_o data values. Thus the mean square deviation is given by

$$\sigma^2 = b^2 \sum_{i=1}^{N_o} (\Delta E_i)^2 \tag{49}$$

or, in terms of the measured absorber amounts, a_m.

$$\sigma^2 = b^2 \sum_{i=1}^{N_o} (a_{mi} - a_{m_e i})^2 \ . \tag{50}$$

The residual sum of squares (RSS) is defined by

$$RSS = \sum_{i=1}^{N_o} (a_{mi} - a_{m_e i})^2 \ . \tag{51}$$

Thus the uncertainty σ is minimized if, and only if, the RSS is minimized. In order to analyze synthetic absorber amount data we chose a computer program (P9R) which performs linear inversion by RSS minimization. This guaranteed that the uncertainties in the retrieved values would be minimized.

The sections which follow describe the method used to calculate the synthetic absorber amounts and the method of retrieval of the mixing-ratio profile. These have been used to find the proportionality constants in Eqs. (36) and (41)

from analysis of synthetic absorber amount data calculated assuming a constant mixing-ratio profile. These constants, in general, will depend on the earth-observer geometry as well as the mixing-ratio profile retrieved. It is useful to determine these constants so that the magnitudes of the uncertainty and the vertical resolution can be estimated. The results of this analysis are given in sections 7 and 8.

2.4 RETRIEVAL METHOD

2.4.1 General comments

We have shown that the total absorber amount along a ray path could be obtained from the equivalent widths of a single spectral line in spectra corresponding to different paths and that the uncertainty in the mixing-ratio profile retrieved from such data is minimized if the RSS is minimized. If the retrieval problem is represented by Eq. (42), the mixing-ratio values can be retrieved by linear inversion.

The path of radiation through the atmosphere can be characterized by the path length segments and the direction of travel through concentric layers or by the optical air-mass encountered by the ray in each layer. The airmass can be obtained from Eqs. (A.95) and (A.97) if the temperature and air density at each layer boundary are known. If the airmass elements a_{ij} of Eq. (42) are calculated for each segment of the N_o ray paths, Eq. (42) can be inverted to give up to N_o local mixing-ratio values.

In the following section the method used to construct an atmospheric model, necessary for the application of Treve's formalism (19,20), is discussed. Next the ray path calculation technique (i.e., the calculation of the a_{ij} values), using Eqs. (A.95)-(A.97) of Appendix A, is given. Finally, the linear least squares method of retrieving local mixing-ratio values from a set of total absorber amount values is presented.

A more detailed presentation of the atmospheric model and the optical airmass calculation is given in Appendix A. It may be helpful for the reader to examine Appendix A before continuing.

2.4.2 Construction of the atmospheric model

The optical airmass encountered by radiation passing through the atmosphere was obtained using the relations derived in Appendix A. The complicated nature of the integrands required that the integrations be performed numerically. In order to do this the atmosphere was divided into concentric spherical layers, as shown in Figure 3, characterized by the heights of the upper and lower boundaries or break points of each layer and the temperature and density at each break point. If the height and temperature of each break point, together with the pressure at the bottom of the lowest layer are given, the value of each of the quantities in Eqs. (A.95)-(A.97) can be determined.

If the latitude of observation is known the geopotential height of each break point can be obtained from Eq. (A.14). The pressure at each break point can be calculated from

$$P_{i+1} = \begin{cases} P_i \left[\dfrac{T_i}{T_i + L_i (H_{i+1} - H_i)} \right]^{\frac{g_o' M}{R^* L_i}} & L_i \neq 0 \\ P_i \exp\left[-\dfrac{g_o' M}{R^* T_i} (H_{i+1} - H_i) \right] & L_i = 0 \end{cases} \quad \text{if} \tag{52}$$

where L_i, the temperature gradient in the ith layer, is given by

$$L_i = \frac{T_{i+1} - T_i}{H_{i+1} - H_i} \, . \tag{53}$$

The mass density at each break point was found using the ideal gas law

$$\rho_{mi} = \frac{M P_i}{R^* T_i} \, . \tag{54}$$

The number density was obtained from

$$\rho_{vi} = \frac{N_A P_i}{R^* T_i} \, . \tag{55}$$

The index of refraction of air for T = 288 K and P = 1 atm was given by Edlen's formula (21)

$$\begin{aligned} (n - 1) \times 10^8 &= 6432.8 + 2949810. (146 - 1/\lambda^2)^{-1} \\ &\quad + 25540. (41 - 1/\lambda^2)^{-1} \, , \end{aligned} \tag{56}$$

where λ(μm) is the wavelength of the observed radiation. The index of refraction at each break point was found from the Lorenz-Lorentz formula (22)

$$\frac{1}{\rho_{vi+1}} \frac{n_{i+1}^2 - 1}{n_{i+1}^2 + 2} = \frac{1}{\rho_{vi}} \frac{n_i^2 - 1}{n_i^2 + 2} . \qquad (57)$$

Thus far we have constructed an atmosphere consisting of layers defined by the various physical parameters at the boundaries. Within each layer the pressure, temperature, and index of refraction varied according to Eqs. (52), (55), and (57) respectively. The temperature gradient L_i was assumed constant throughout a given layer.

We assumed that the atmosphere was "horizontally" uniform. The temperature and density at altitude A were assumed independent of the position defined by the latitude and longitude of the earth. The size of the errors which result from this assumption are considered in the next chapter.

2.4.3 Calculation of the optical airmass

Now that the atmospheric model is defined the airmass encountered by a ray traversing a refracted path through the atmosphere can be computed.

Consider radiation with wavelength λ reaching an instrument at height A_o at an apparent zenith angle Z_o. If we assume that the source of the radiation is an infinite distance away from the earth and that λ, A_o, and Z_o are

known, the path of the radiation and the optical airmass a_{ij} in each layer are obtained from Eqs. (A.95)-(A.97). The optical airmass values were computed using a version of the program described by Snider (23) and Snider and Goldman (24) modified to allow observer heights up to 500 km. The method used for the numerical integration was Gauss quadrature with K = 6 (25). Treve (20) has shown that this approximation is accurate over the lowest 90 km of the atmosphere. Since all the atmosphere of interest in our investigation was below 60 km this was considered adequate for our purposes.

There are two classes of rays through the atmosphere. The first reaches the observer at some apparent zenith angle $Z_o \leq 90^o$. This case is the simpler of the two, since the observer height is the lowest penetration of the ray in the atmosphere. The second case is $Z_o > 90^o$. For these apparent zenith angles the ray passes through a portion of the atmosphere below the observer. However, if the closest approach to the earth of the ray (the tangent height) can be determined, the ray path can be divided about the tangent height into two paths of the first type.

2.4.4 The two possible geometries

If $Z_o \leq 90^o$, is shown in Figure 6, the angle of entry Z_i in layer i is related to the angle of exist Z_{oi} by

$$Z_i = W_i + Z_{oi} - \Omega_i \tag{58}$$

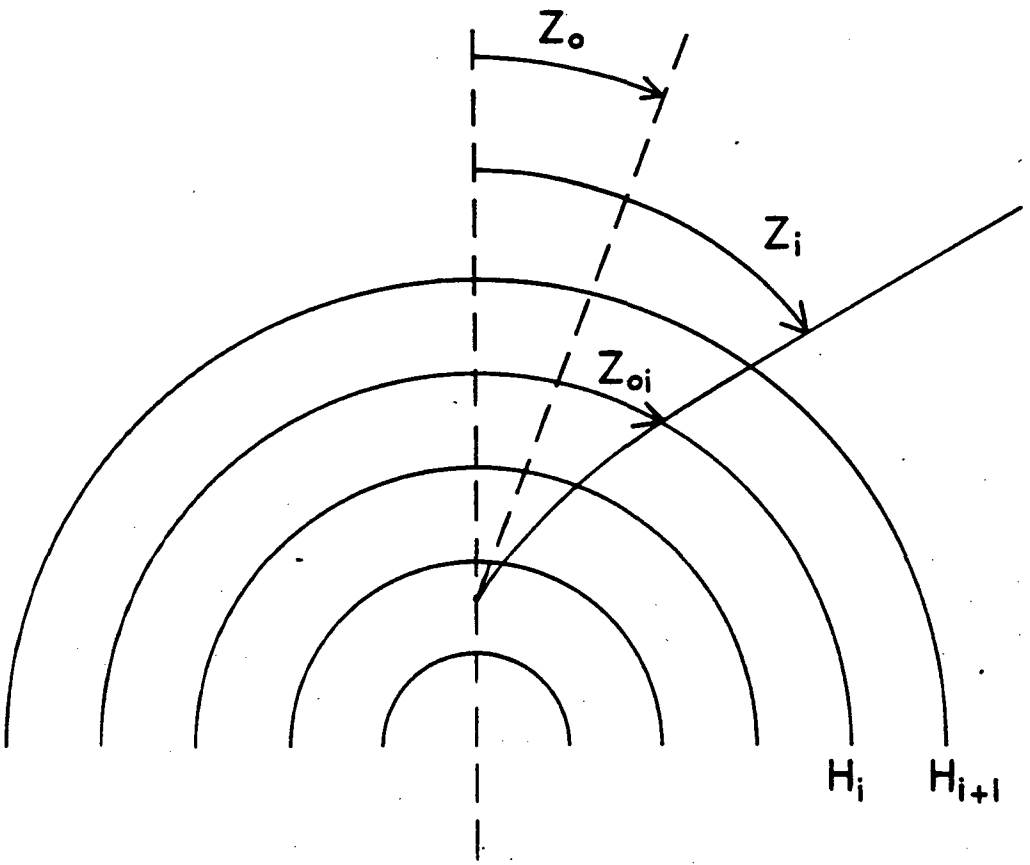

Figure 6: The slant path geometry for a balloon observer and a ray reaching the observer at apparent zenith angle $Z_o \leq 90^o$. The angle of entry into the i^{th} layer is Z_i and the angle of exit Z_{oi}.

(see Figure 77 in Appendix A) where the angle W_i is found from Eq. (A.96) and Ω_i from Eq. (A.95). The angle of entry Z_i is equal to the angle of exit Z_{oi+1} from the layer above. Thus the path of the ray and the total airmass encountered can be obtained by successive used of Eqs. (A.95)-(A.97) from the layer of the observer to the top of the atmosphere (of the source height A_s). The connection between each layer is provided by

$$Z_i = Z_{oi+1} \ . \tag{59}$$

The more difficult case of $Z_o > 90^o$ is shown in Figure 7. In this case the ray traverses a portion of the atmosphere below the observer height A_o. The closest approach of the ray to the earth is called the tangent height A_T. This ray path can be divided into two portions; that from the tangent height to the source and that from the tangent height to the observer. Since the apparent zenith angle at the tangent height is $Z_T = 90^o$ the problem reduces to two problems of the first type discussed.

The tangent height can be determined by use of Fermat's principle (see Eq. (A.45))

$$nr\sin Z = n_o r_o \sin Z_o \ . \tag{60}$$

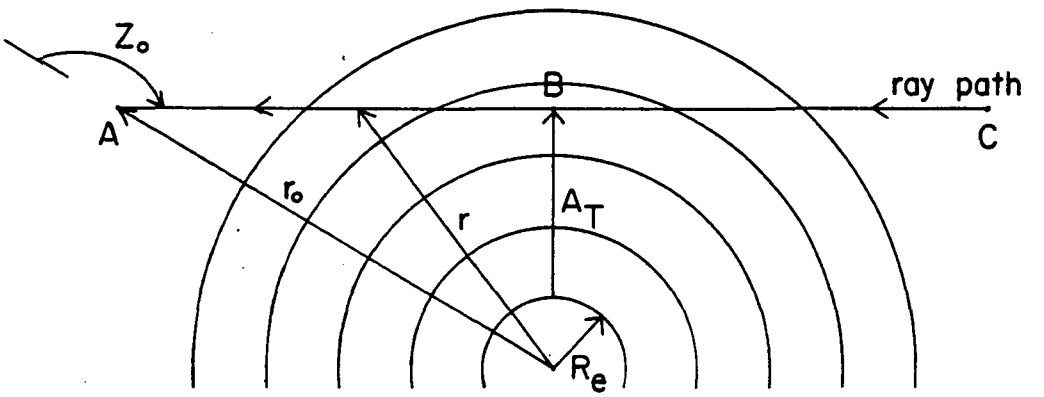

Figure 7: The slant path geometry for a satellite observer and a ray reaching the observer at apparent zenith angle $Z_o > 90^o$. The closest approach of the ray to the earth (the tangent height) is A_T. The ray path is divided into two portions CB and BA about the tangent height.

At the tangent height $\sin(Z_T) = 1$, so Eq. (60) reduces to

$$nr = n_o r_o \sin Z_o \, . \tag{61}$$

The tangent height is found by solving the transcendental equation

$$nr - n_o r_o \sin Z_o = 0 \, , \tag{62}$$

where r is obtained from Eq. (A.14)

$$r = \frac{R_e^2}{R_e - \frac{H_T}{\gamma}} \, , \tag{63}$$

and H_T is the geopotential equivalent of A_T, and γ is the conversion factor from geometric to geopotential meters.

As noted in Appendix A all altitudes used in the airmass computation are in geopotential meters. At the earth's surface the difference between geometric and geopotential altitude is 0 km. At 50 km the difference is about 0.4 km. Thus, if geometric altitudes are used instead of the geopotential altitude the error in tangent height below 50 km can be as large as 0.4 km.

Once the tangent height is determined the ray in Figure 7 can be replaced by the two ray segments BA and BC and the problem reduces to solution of the ray tracing problem from the tangent height to the source and from the

tangent height to the observer. The total airmass is found by successive application of Eqs. (A.95)-(A.97) in each of the layers in the two portions of the ray.

Thus the airmass elements a_{ij} in Eq. (14) can be calculated for any set of ray paths. Synthetic absorber amount data can be obtained from Eq. (14) if a mixing-ratio profile is assumed. Now that the a_{ij} matrix and the $N_o a_m$ values are known Eq. (14) can be inverted to give the local mixing-ratio values. The retrieval method used in this work is described below.

2.4.5 Mixing-ratio profile retrieval method

The synthetic amount of absorber along a ray path is given in terms of the local mixing-ratio values by

$$a_m(Z_{oi}) = \sum_{j=1}^{N} m_j a_{ij} + \varepsilon_i \qquad (64)$$

where Z_{oi} is the apparent zenith angle of the ith ray and ε_i is the noise contained in the ith absorber amount.

The formulation of Eq. (64) has implicitly assumed that there is no "horizontal" variation in the vertical mixing-ratio profile along the ray path. If, as in Figure 8, the mixing-ratio profile in the first half of the path is different from that in the second half then Eq. (64) becomes

$$a_m(Z_{oi}) = \tfrac{1}{2} \sum_{j=1}^{N} m_{1j} a_{ij} + \tfrac{1}{2} \sum_{j=1}^{N} m_{2j} a_{ij} + \varepsilon_i \ , \qquad (65)$$

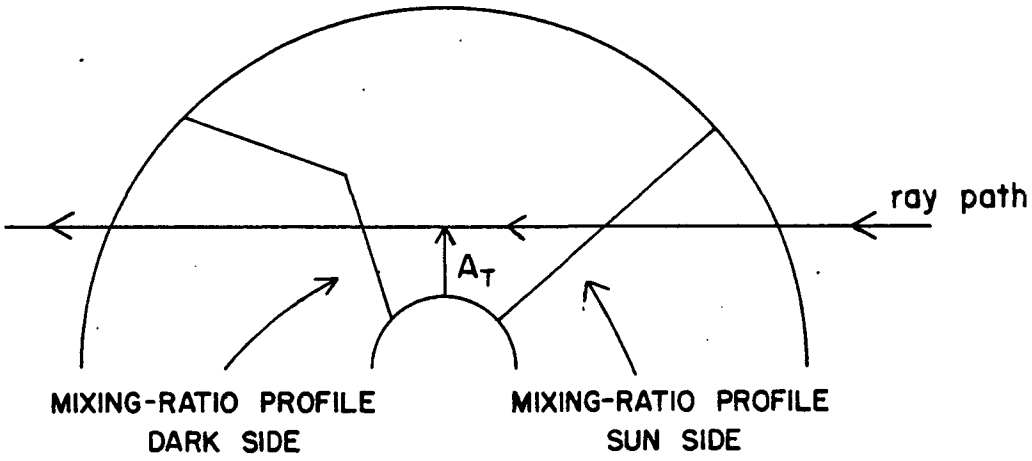

Figure 8: The case of an absorber with a mixing-ratio profile which is different for the two halves of the ray path.

which reduces to

$$a_m(Z_{oi}) = \sum_{j=1}^{N} \tfrac{1}{2}(m_{1j} + m_{2j})a_{ij} + \varepsilon_i \ . \qquad (66)$$

In this case, as shown in Figure 9, the mixing-ratio profile retrieved is the average of the two profiles. Such variations in the mixing-ratio profile may occur for molecules such as NO or ClO (26,27) whose concentrations change rapidly at sunrise or sunset. In these analyses we have only considered the case of a constituent mixing-ratio profile which is "horizontally" constant.

By making the simplifying assumptions discussed above the local mixing-ratio values in Eq. (64) can be retrieved with linear regression methods. The method used in this work (computer program P9R (12)) minimizes the RSS. As shown in section 3 this linear least squares technique retrieves local mixing-ratio values with minimum uncertainty. This program also has the capability to determine the number of values retrievable from a data set containing insufficient information. This feature was particularly useful for data obtained for a ground-level observer.

The data sets analyzed by this method consisted of 125 absorber amounts corresponding to 125 different apparent zenith angles Z_{oi}. If these are known the a_{ij} elements in each layer can be obtained. For the purpose of the airmass computation we divided the atmosphere between 0 and 50 km

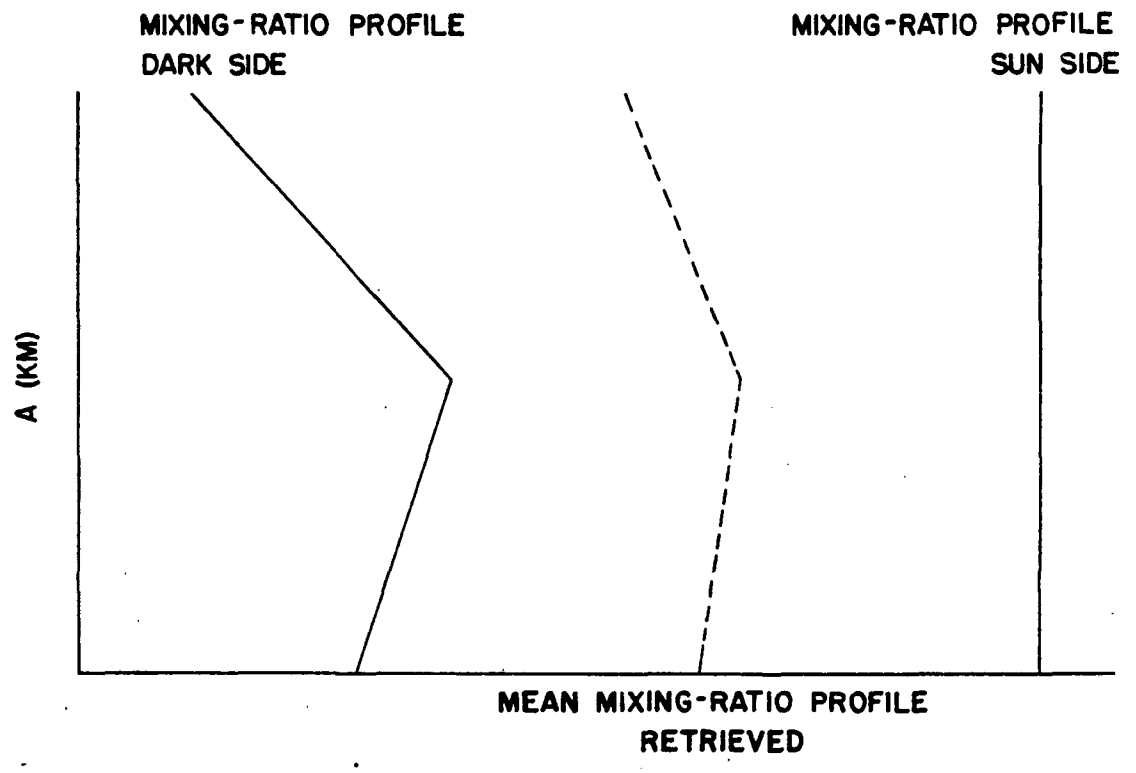

Figure 9: A mean "retrieved" profile for an absorber with a mixing-ratio profile which is different for the two halves of the ray path.

into 200 layers, each 0.25 km-thick. As shown in the next chapter this thickness is sufficiently small to avoid significant systematic errors in the airmass calculation.

If only 125 absorber amount values exist in each data set, at most 125 local mixing-ratio values can be retrieved. The mixing-ratios in the atmosphere between the retrieved values were assumed to vary linearly with height. Thus if the local mixing-ratio value m_k in layer i is to be retrieved (see Figure 10), the local mixing-ratio value in layer i+1 is given by

$$m_{i+1} = m_k + \frac{(m_{k+1} - m_k)}{s} , \tag{67}$$

where s is the number of atmospheric layers between the local mixing-ratio values m_k and m_{k+1} to be retrieved. If the N_R mixing-ratio values to be retrieved are equally spaced with altitude Eq. (64) can be written as

$$a_m(Z_{oi}) = \sum_{k=1}^{N_R} \sum_{\ell=1}^{s} m_k + \frac{(\ell - 1)(m_{k+1} - m_k)}{s} \; a_{i,[(k-1)s + \ell]} + \varepsilon_i . \tag{68}$$

This equation can be rearranged to give a linear combination of the local mixing-ratio values. This linear combination is

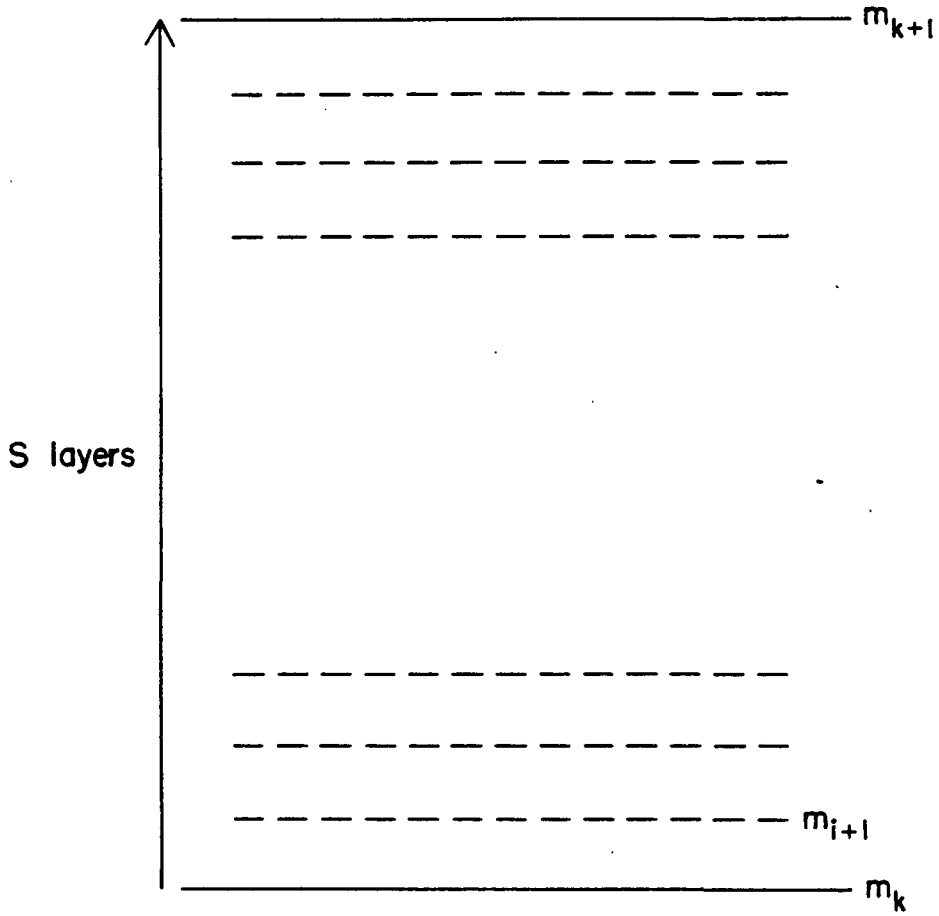

Figure 10: The structure of the retrieval atmosphere. Discrete mixing-ratio profiles were retrieved for layers k and k + 1. The ray path was traced through the S layers between k and k + 1.

$$a_m(Z_{oi}) = m_1 \sum_{\ell=1}^{s} \frac{s+1-\ell}{s} a_{1\ell} + \sum_{k=2}^{N_R} m_k \Big[\sum_{\ell=1}^{s} \frac{\ell}{s} a_{i,[(k-2)s+\ell+1]}$$

$$+ \sum_{\ell=1}^{s-1} \frac{s-\ell}{s} a_{i,[(k-1)s+\ell+1]} \Big] + \varepsilon_i \ . \qquad (69)$$

Equation (69) can be written as

$$a_m(Z_{oi}) = \sum_{k=1}^{N_R} m_k a'_{ik} + \varepsilon_i \ , \qquad (70)$$

where

$$a'_{i1} = \sum_{\ell=1}^{s} \frac{s+1-\ell}{s} a_{i\ell} \ , \qquad (71)$$

and

$$a'_{ik} = \sum_{\ell=1}^{s} \frac{\ell}{s} a_{i,[(k-2)s+\ell+1]}$$

$$+ \sum_{\ell=1}^{s-1} \frac{s-\ell}{s} a_{i,[(k-1)s+\ell+1]}, \text{ for } k \neq 1 \ . \qquad (72)$$

Thus for any number N_R ($<N_O$) of local mixing-ratio values the inversion reduces to that of Eq. (64).

Since the N_R equally-spaced, local, mixing-ratio values were assumed to be independent no a priori assumptions about the shape of the profile to be retrieved were necessary. The retrieval method (P9R) obtained both the local mixing-ratio value m_k and its standard deviation σ_k.

This retrieval method was used to analyze absorber amount data obtained assuming various mixing-ratio profiles and observer altitudes. The results of these investigations are presented in the remaining sections of this chapter.

2.5 THE UNCERTAINTY IN A PROFILE RETRIEVAL

2.5.1 General comments

We have shown in section 3 that the uncertainty in a set of retrieved mixing-ratio values is minimized if the RSS is minimized. In section 4 a retrieval method utlizing RSS minimization was described. In this section this retrieval method is used on synthetic absorber amount data obtained assuming a constant mixing-ratio profile, shown in Figure 11, in order to estimate the minimum uncertainty in the retrieved mixing-ratio values.

We have considered three typical observer geometries which represent the three types of occultation experiments. The first was the satellite geometry shown in Figure 12 A) where the observer height was 500 km. The second typical geometry is the balloon geometry of Figure 12 B) where A was 30 km. The last geometry considered was the ground-level observer of A = 0 km. For the satellite observer all the Z_{oi} values were greater than 90^{o}. For the ground observer all the Z_{o} values were less than 90^{o}. The balloon observer is a combination of the satellite and ground geometries.

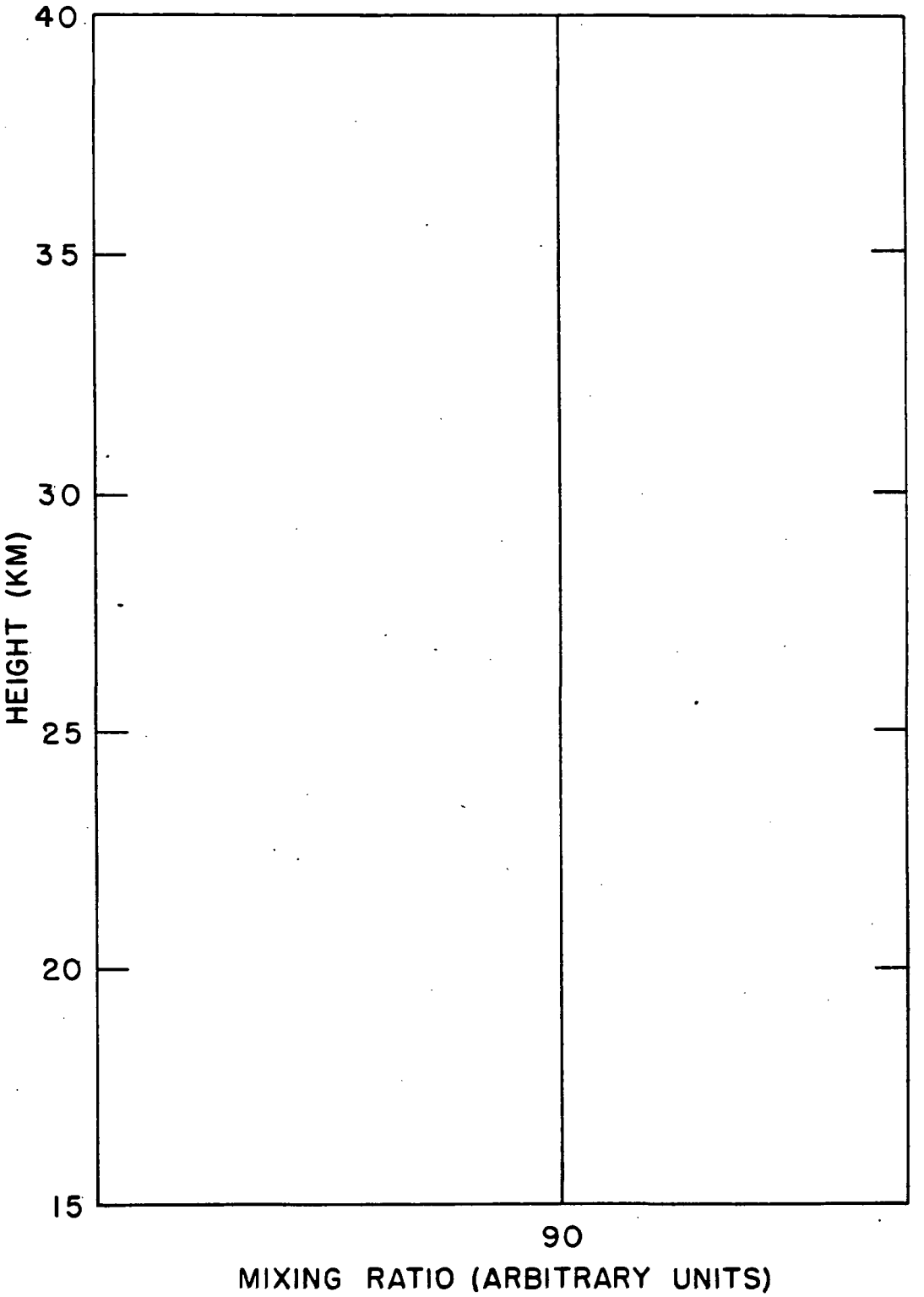

Figure 11: A mixing-ratio profile constant with altitude.

Figure 12: Occultation geometries for experiments performed at satellite A) and balloon B) altitudes. The observer position is given by O.

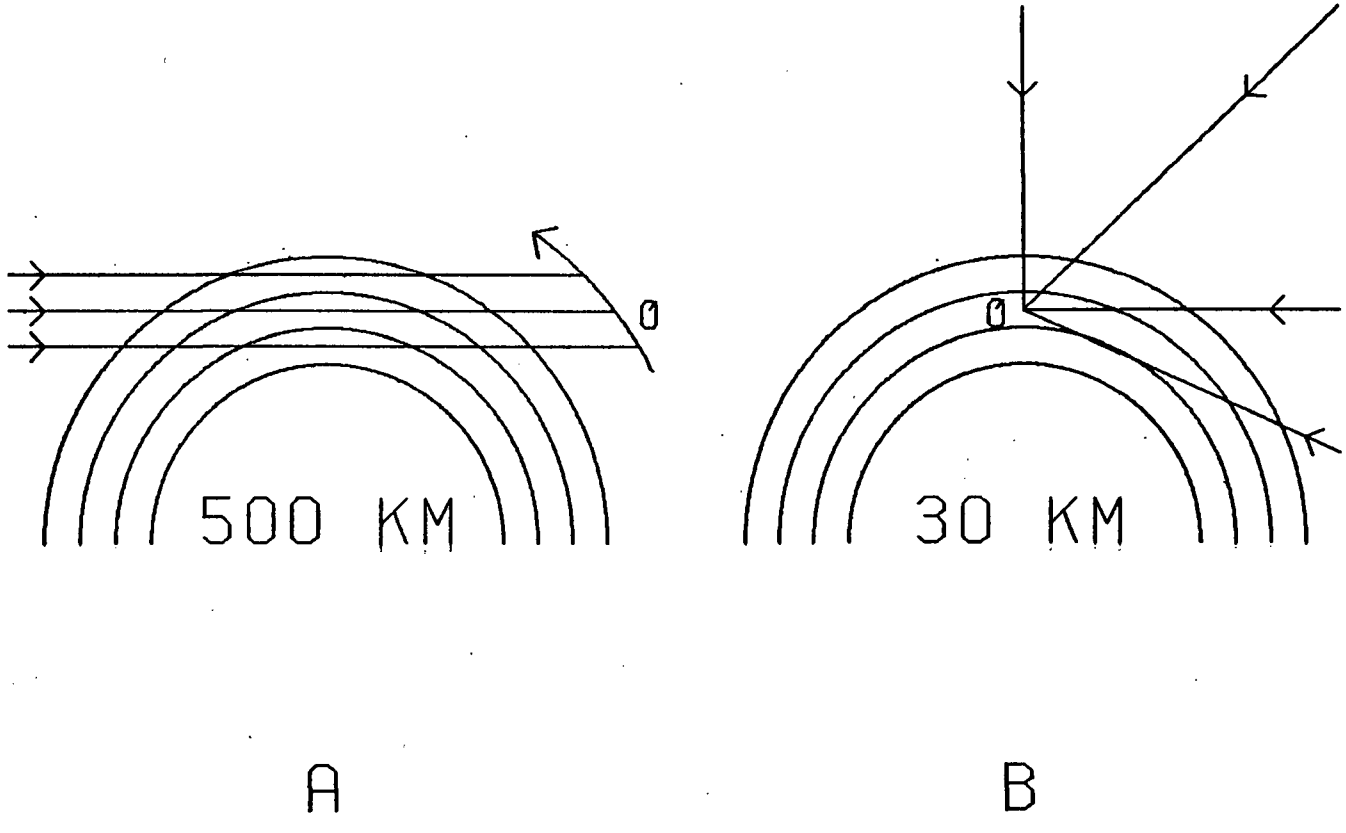

Figure 12

Table 2: The distribution of the apparent zenith angles corresponding to the 125 data values computed for the 0 km observer.

Angular range	Angular spacing of adjacent rays	Number of rays in each range
10° - 60°	2.0°	25
60° - 85°	0.5°	50
85° - 90°	0.1°	50

Table 3: Standard atmospheric values used for the retrieval of mixing-ratio profiles.

Parameter	Assumed value
latitude (which gives R_e and g_o)	45°
observer altitudes	500, 30, and 0 km
temperature profile	U.S. Standard Atmosphere 1976
sea-level pressure	1 atm
wavelength	5 μm

All the data sets analyzed by the method of section 4 contained 125 absorber amount values obtained using Eq. (64) and corresponding to 125 different Z_o values. For $A_o = 500$ km the apparent zenith angles were chosen to have a constant angular spacing of 0.00879^o, corresponding to a tangent height spacing less than 500 m over the entire range (0-50 km). The distribution of the apparent zenith angles given in Table 2 for the 0 km observer data sets were chosen to bias the data sets in favor of large apparent zenith angles to enhance the information content. This choice may affect the proportionality constants obtained for Eqs. (36) and (41). In general, the results obtained in this chapter are expected to be better than those obtained from the analysis of real data with an equivalent SNR.

The Z_o distribution for the 30 km observer contained 60 values greater than 90^o and these values were arranged so that the tangent height spacing was less than 500 m. In order to achieve this spacing the Z_o values were adjusted "by hand." Thus the apparent zenith angle spacing varied over the entire range above 90^o. Below 85^o an apparent zenith angle spacing of 5^o was used. In the range $85^o \leq Z_o \leq 90^o$ the apparent zenith angle spacing was 0.10417^o.

The values assumed for the atmospheric parameters needed to construct the model atmosphere of section 4 are listed in Table 3. These were all assumed to be known exactly.

The effects of noise were simulated by adding normally-distributed random numbers with a mean of zero and a standard deviation σ_o to the calculated absorber amounts. Since negative absorber amounts are unphysical, this sum was set equal to zero when the sum of the absorber amount and the random noise was negative. This preserved the total number N_o of $a_m(Z_{oi})$ values upon which the vertical resolution of the retrieval depends. The SNR of each data set thus constructed was defined as a_{max}/σ_o where a_{max} was the largest absorber amount value in each data set. These synthetic data sets were used as "experimental" data and mixing-ratio values were retrieved by inverting Eq. (70) and constraining the mixing-ratio value above 50 km to zero.

2.5.2 500 km observer

Typical absorber amount data sets with an SNR of 100 obtained from the constant mixing-ratio profile for the 500 km and 0 km observers are shown in Figures 13 and 14 respectively. A retrieval done with the data in Figure 13 is shown in Figure 15.

The percent uncertainty for the kth retrieved mixing-ratio value can be defined as

$$U_k = \frac{100\sigma_k}{m} , \qquad (73)$$

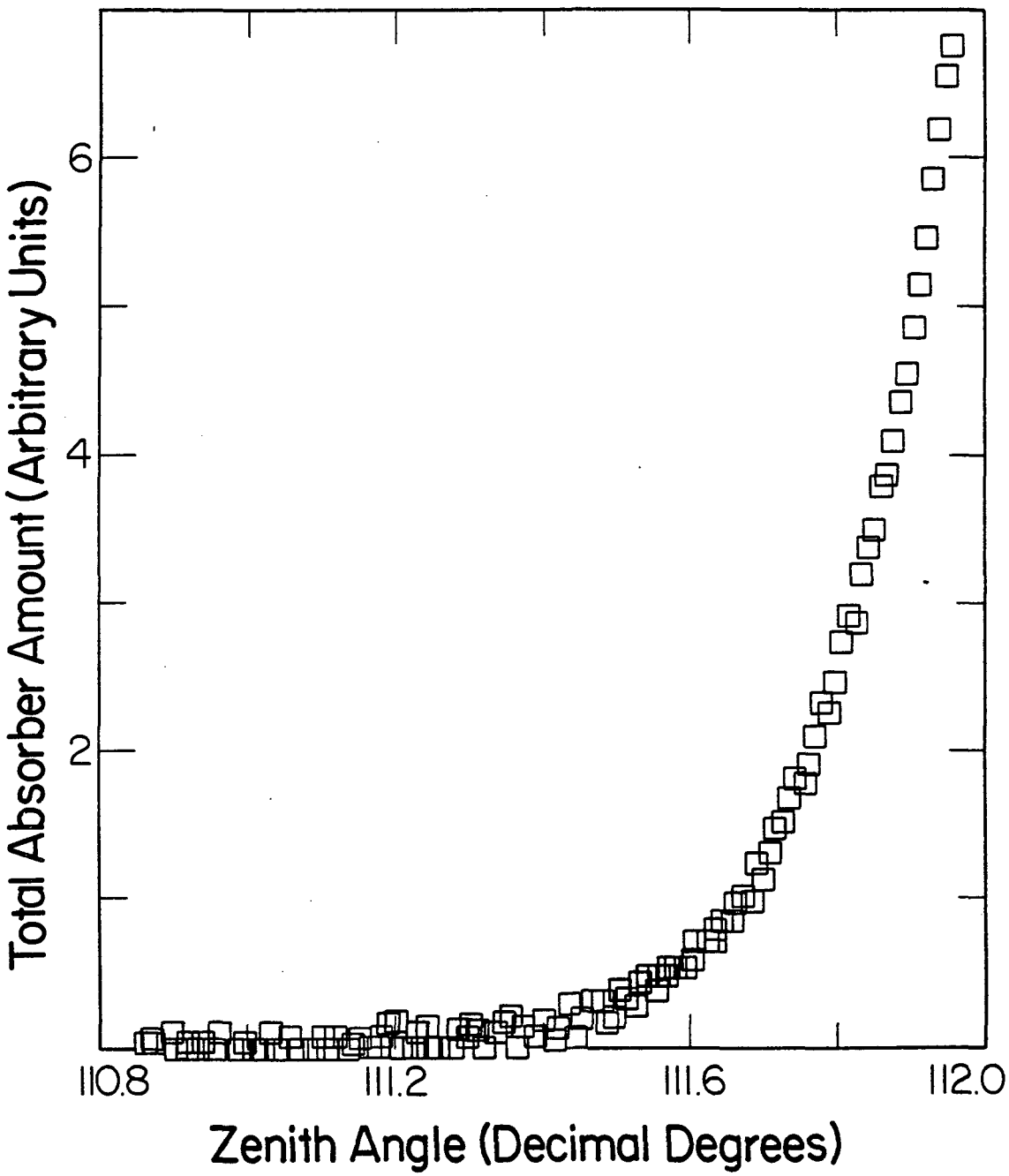

Figure 13: Total absorber amount data with SNR of 100, calculated for the constant mixing-ratio profile for an observer at 500 km, as a function of the apparent zenith angle of arrival of the rays.

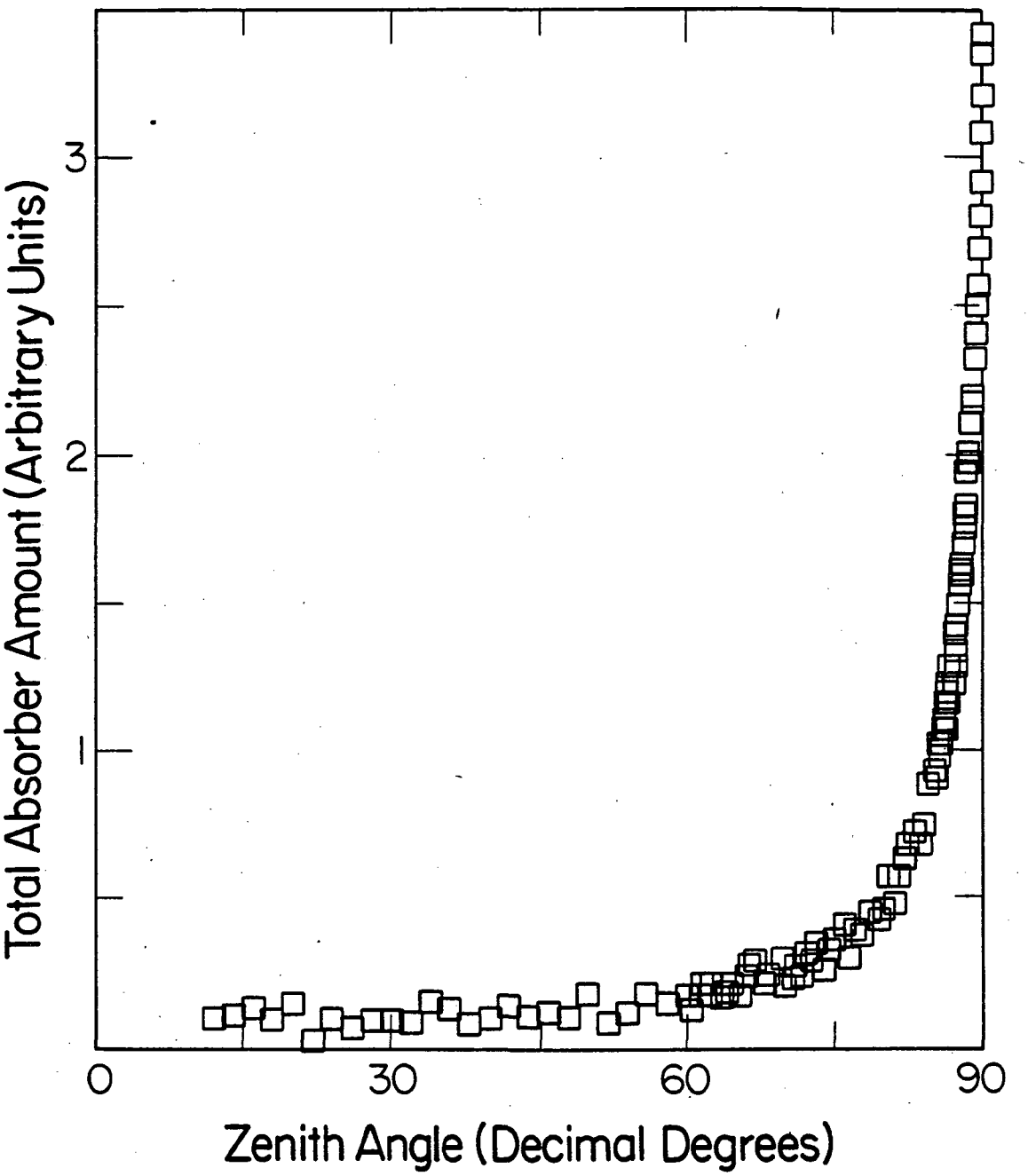

Figure 14: Total absorber amount data with SNR of 100, calculated for the constant mixing-ratio profile for an observer at 0 km, as a function of the apparent zenith angle of arrival of the rays.

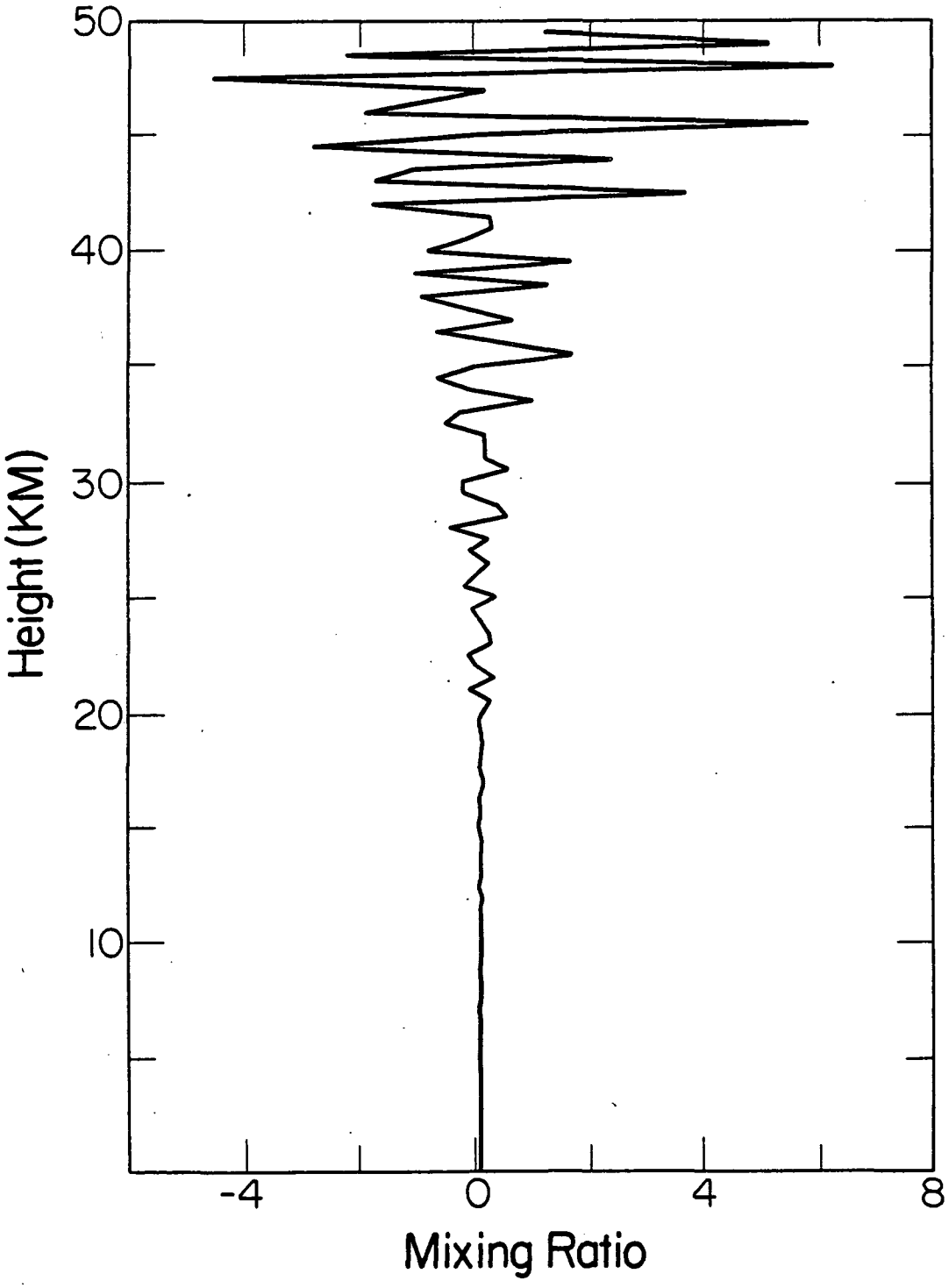

Figure 15: A retrieval of the constant mixing-ratio profile performed on the data shown in Figure 13 for 50 equally-spaced local mixing-ratio values.

where m is the value of the assumed constant mixing-ratio profile used to calculate the synthetic data. It was found that these uncertainty values could be decreased by reducing the number of values N_R to be retrieved or by increasing the SNR or the number of data values N_O.

Retrievals of the constant mixing-ratio profile were performed for an observer at 500 km and different values of N_R, SNR, and N_O. As shown, in Table 4 the percent uncertainty, as defined by Eq. (73), is approximately inversely proportional to the SNR. The data sets used to obtain these results were constructed from identical sets of random numbers scaled to give the SNR listed.

As shown in Table 5, the percent uncertainty is inversely proportional to $N^{\frac{1}{2}}$. The results obtained for a data set of 500 rays in Table 5 were obtained by combining four data sets each containing 125 values with an SNR of 100 but different added random noise. For each tangent height there were four absorber amount data values. Thus the information content of the data set was increased without affecting the vertical resolution of the retrieval.

The dependence of the uncertainty on the number of equally-spaced mixing-ratio values N_R to be retrieved was determined by varying N_R. The uncertainty values retrieved for N_R values of 5, 10, 25, 50, and 100 are shown in Figure 16 as a function of altitude. The physically unrealistically large uncertainty values shown in Figure 16 were given to

Table 4: Some ratios of retrieved mixing-ratio uncertainties for $N_R = 100$, $N_O = 125$, $A_O = 500$ km, and various SNR values.

	SNR			
A (km)	$\frac{500}{500}$	$\frac{100}{500}$	$\frac{50}{500}$	$\frac{10}{500}$
0	1.0	3.8	7.2	34
10	1.0	4.0	7.4	36
20	1.0	3.9	7.5	36
30	1.0	4.0	7.6	36
40	1.0	4.0	7.6	36

Table 5: Some retrieved mixing-ratio uncertainties for $N_R = 100$, $A_O = 500$ km, SNR = 100, and N_O values of 125 and 500.

A (km)	$N_O = 125$	$N_O = 500$	$\frac{U(N_O = 125)}{U(N_O = 500)}$
0	3.8%	1.8%	2.1
10	19	9.2	2.1
20	63	31	2.0
30	400	190	2.1
40	1800	880	2.0

demonstrate the quality of the fit to the straight lines over the entire altitude range. The straight lines in Figure 16 show that the uncertainty at any altitude is proportional to N_R, since doubling N_R doubles the uncertainty (note the logarithmic scale of the uncertainty axis).

In summary these results show that the uncertainty at any altitude obeys

$$U \alpha \frac{N_R}{SNR\, N_O^{\frac{1}{2}}} . \tag{74}$$

The proportionality constant can be determined by examination of Figure 16. Since the uncertainty axis in this plot is logarithmic, the uncertainty increases exponentially with altitude. Noting that the slope of the lines in Figure 16 is approximately 0.15 km^{-1}, Eq. (74) becomes

$$U(A,500) = 50 \frac{N_R \exp(0.15A)}{SNR\, N_O^{\frac{1}{2}}} \tag{75}$$

where 500 designates the observer altitude in kilometers.

The scale height for the U.S. Standard Atmosphere 1976 (28) is shown in Figure 17 as a function of altitude. The reciprocal of the mean value of H_s is 0.14 km^{-1} and the factor 0.15 km^{-1} in Eq. (75) is thus nearly H_s^{-1}. For an isothermal atmosphere with constant molecular weight the atmospheric pressure at altitude A can be approximated by

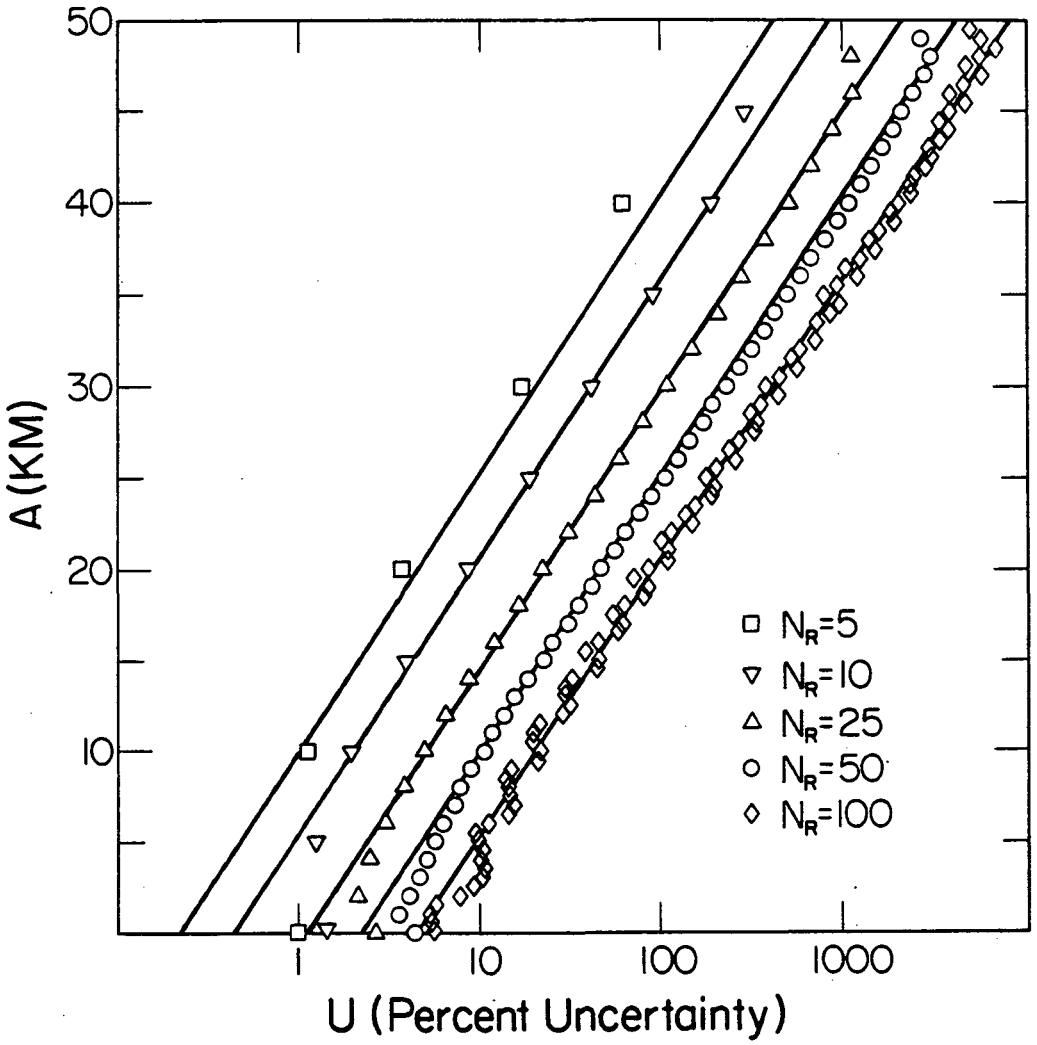

Figure 16: Uncertainty in the retrieved mixing-ratio values for an observer at 500 km obtained from data with SNR = 100, N_O = 125, and N_R = 100, 50, 25, 10, and 5. The straight lines are the corresponding functions from Eq. (2.75).

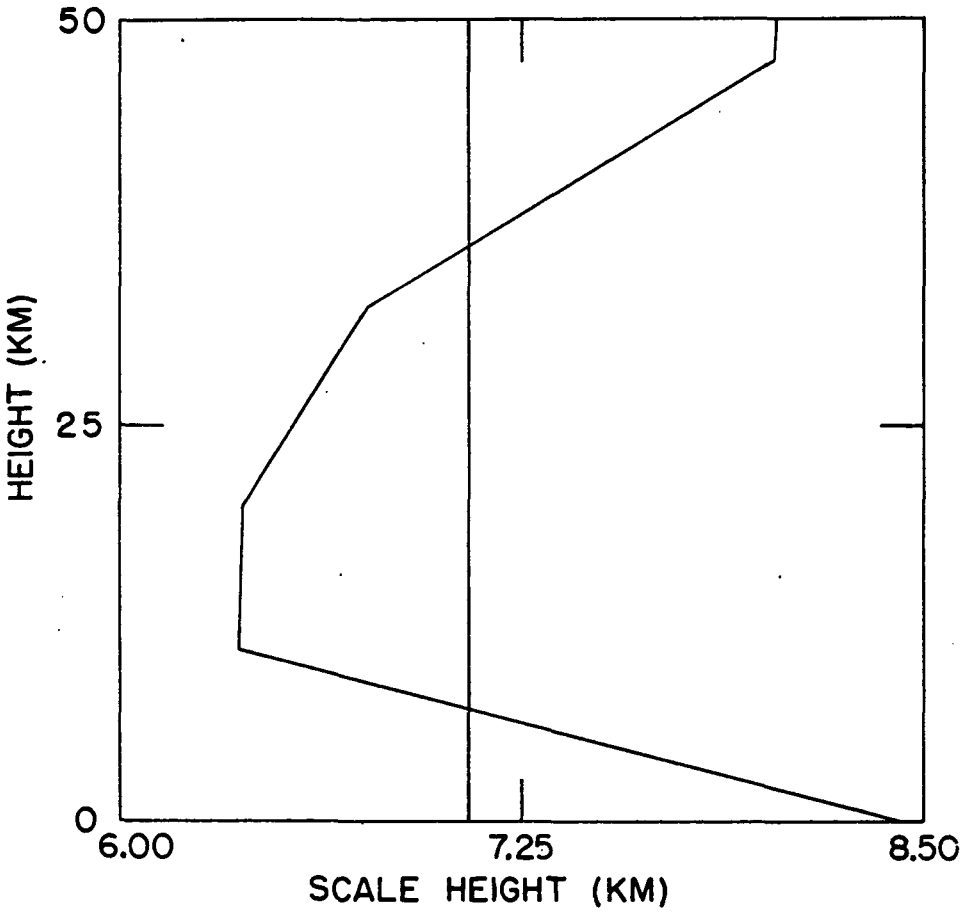

Figure 17: The scale height of the U.S. Standard Atmosphere 1976 (27) as a function of altitude. The vertical line represents the average scale height value of 7.08 km.

$$P(A) = P(o)\exp(-A/H_s) \tag{76}$$

where P(o) is the pressure at sea-level. Thus the uncertainty in the mixing-ratio value at height A in terms of P(A) is approximated by

$$U(A,500) \simeq \frac{[50\ N_R P(o)]}{[SNR\ N_o^{\frac{1}{2}}\ P(A)]} \tag{77}$$

and it is inversely proportional to the pressure. Therefore the uncertainties in retrieved mixing-ratio profiles are primarily due to the rapid decrease in the air density of the hydrostatic atmosphere with altitude. If Eq. (77) is written in terms of the scale height

$$U(A,500) \simeq \frac{50\ N_R\ P(o)\exp(A/H_s)}{SNR\ N_o^{\frac{1}{2}}} . \tag{78}$$

This formulation is in agreement with the result obtained from the Backus-Gilbert theory (Eq. (36)).

2.5.3 0 km observer

For apparent zenith angles less than 90^o the atmosphere is nearly plane-parallel. In this case

$$a_{ij}\tan Z_{oj} \simeq a_{i,j+1}\tan Z_{oj+1} . \tag{79}$$

Thus for the observer within the atmosphere for absorber amounts corresponding to rays with apparent zenith angles less than 90° the a_{ij} elements for the jth ray will be near multiples of the elements of the coefficient vectors of all other rays with zenith angle less than 90°. For these conditions the $\{a_{ij}\}$ matrix is nearly singular and the inversion of the matrix becomes extremely difficult. This near singularity could be reduced by reducing the number N_R of parameters until the $\{a_{ij}\}$ matrix is invertible. The inversion program (P9R), beginning with the least important parameter (determined by a calculated tolerance factor for each parameter), eliminated parameters (starting with the smallest tolerance) until the $\{a_{ij}\}$ matrix is invertible. The retrieved mixing-ratio values obtained by this process are highly correlated due to the scaling in Eq. (79). A more detailed explanation of the tolerance determination can be found in the BMDP manual (12). We have used a tolerance of 0.0001 in this work. For the 0 and 30 km observers the resultant number of retrievalbe parameters was less than N_R except for N_R less than five.

Similar data sets to that shown in Figure 14 were analyzed for an instrument at 0 km. The program P9R found that it was not possible to obtain more than 10 local, mixing-ratio values in the 0 to 50 km region for all values of the SNR used (including the case of no added noise). Although N_{max} is essentially independent of the set of normally distributed

random numbers used to create the synthetic absorber amount data, the altitudes of the retrieved local, mixing-ratio values varied for each data set analyzed. This was interpreted as being due to the poor vertical resolution and the high correlation of the retrieved values. An example is shown in Table 6 for N_O of 125, N_R of 50, and an SNR of 100 for a constant mixing-ratio value of 1.0. The mixing-ratio values were retrieved from identical absorber amount data with different sets of noise. The vertical resolution was so poor above 3 km that the altitude variation of the retrieved values was more than 15 km for different experimental noise but identical SNR.

The retrieved standard deviations were also found to depend on the random numbers used to model experimental noise. The mean value of the standard deviation at some altitude A was found by averaging the retrieved standard deviation values from retrievals using 16 data sets constructed in the same way as those for Table 6. As seen in Table 6, above 3 km the altitudes at which the mixing-ratio values were retrieved depended on the data set analyzed. Thus, for example, only once in sixteen retrievals was a mixing-ratio value retrieved at 40 km, while at 0 km the mixing-ratio value was always retrieved. At 0 km the average standard deviation could be calculated from 16 values but at 40 km the average consisted of just one value. These numbers of values used to obtain the averages are listed in

Table 6: Sample retrievals of constant mixing-ratio profile ($m = 1.0$) for $N_O = 125$, SNR = 100, $N_R = 50$, and an observer altitude of 0 km.

Retrieval 1			Retrieval 2		
k	A_k (km)	m_k	k	A_k (km)	m_k
1	0	1.03	1	0	0.94
2	1	0.82	2	1	0.93
4	3	4.90	4	3	5.36
10	9	4.46	26	25	154
27	26	71.4	50	49	-1890

Table 7. The existence of six retrieved values at 49 km was due to the constraint of the mixing-ratio to zero at 50 km. These values contain little information about the true profile. The spread of the standard deviations at any altitude about the average increases rapidly with altitude. Since the number of values retrieved decreases rapidly with altitude we have restricted our analyses to the region below 30 km (below 15 km for an N_R of 50). The retrieval method used obtained a unique set of mixing-ratio and standard deviation values determined mathematically by linear inversion with no regard to the possible physical meaning of the retrieved values. Thus, as shown in Table 6, physically-meaningless, negative mixing-ratio values were sometimes retrieved.

The average uncertainty was obtained by using Eq. (73) where m is the value of the constant mixing-ratio used to calculate the absorber amount data. The average uncertainties for an N_O of 125, an SNR of 100, and N_R of 5, 10, and 50 are shown in Figure 18. The straight line estimates of the uncertainty values were obtained from

$$U(A,0) = 45\ U(A,500)\ . \tag{80}$$

Shown in Table 8 are some of the average uncertainty values obtained for different values of the SNR. Comparison of the retrieved values in Table 8 shows that the uncertainty is

Table 7: The altitude distribution of the mixing-ratio values retrieved from the 16 absorber amount data sets corresponding to an observer altitude of 0 km.

A (km)	Number of times retrieved in 16 trials
0	16
1	14
3	12
9	3
12	2
13	2
14	1
16	2
17	2
21	1
24-27	4
30	1
49	6

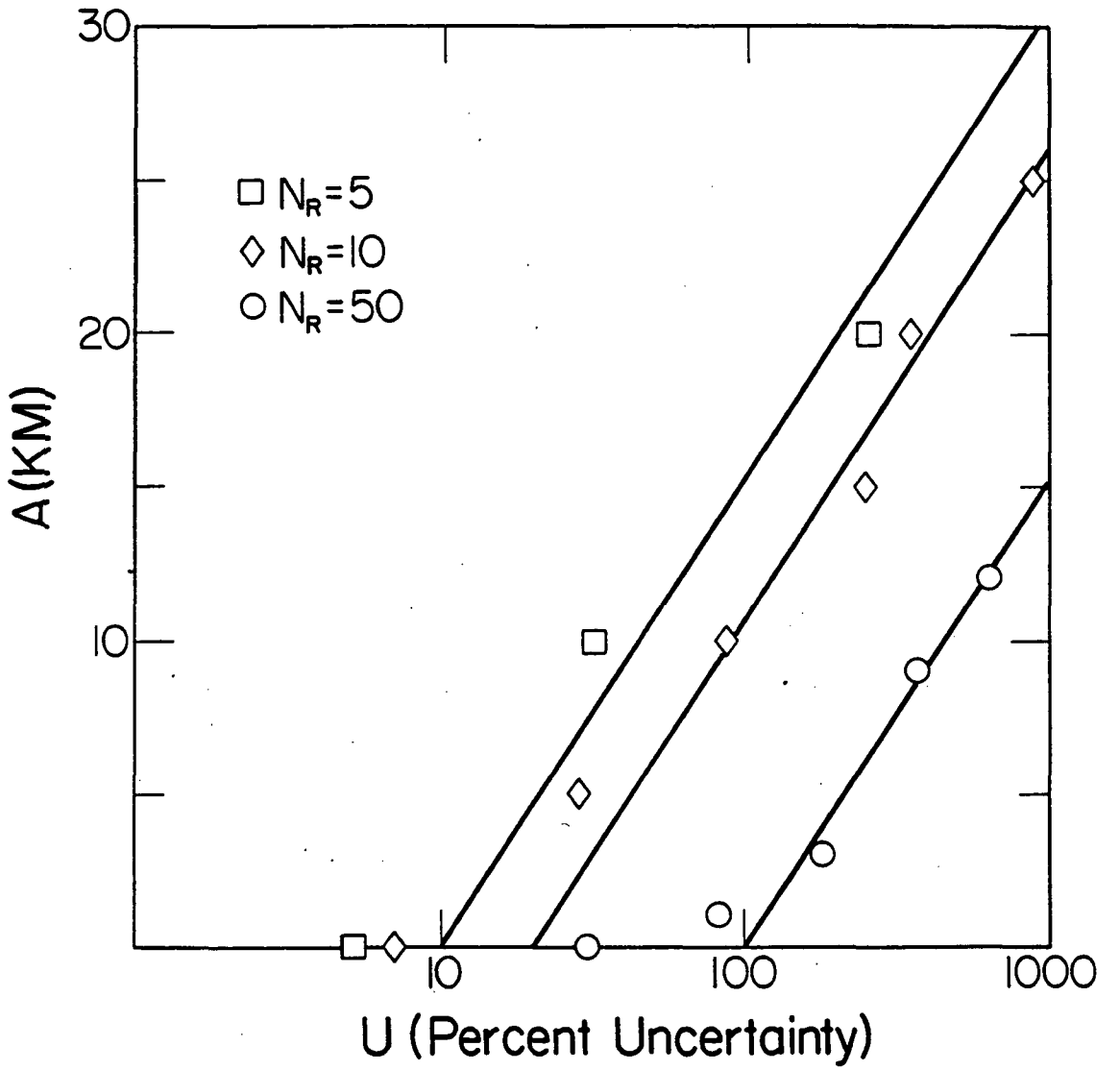

Figure 18: Average uncertainty in the retrieved mixing-ratio values for an observer at 0 km from retrievals from 16 data sets with SNR = 100, N_O = 125, and N_R = 50, 10, and 5. The straight lines are the corresponding functions from Eq. (2.80).

Table 8: Some retrieved mixing-ratio uncertainties for $N_R = 50$, $N_O = 125$, $A_O = 0$ km, and various SNR values.

A (km)	SNR		
	100	1000	5000
0	47%	4.1%	1.2%
1	97	8.0	2.4
3	250	16	4.9
9	590		
18			100
19		400	
26	4200		
28			400
29		1700	

approximately inversely proportional to the SNR. In Table 9 are listed the values obtained for an N_O of 125 and 500, which indicate that the uncertainty is nearly inversely proportional to the square root of N_O. Thus the dependence of Eq. (80) on N_O and the SNR is essentially identical to that obtained for the 500 km observer.

2.5.4 30 km observer

For an instrument at 30 km attempts were made to retrieve a total number N_R equally-spaced mixing-ratio values. It was found that the maximum number of mixing-ratio values retrievable below the observer was approximately equal to the number of rays with $Z_O > 90^O$ in the data set, but that very few values were obtained above the observer.

The average uncertainties in the retrieved mixing-ratio values were calculated from 16 retrievals as described previously. Equation (80) also describes these retrieved uncertainties reasonably well; but at these altitudes there is a large scatter in the retrieved values.

The uncertainties in the retrieved mixing-ratio profile below the 30 km observer show the same dependence of N_R, N_O, and the SNR as for a 500 km observer. The values of U(A,30) for the atmosphere below 30 km are shown in Figure 19 for N_O of 125, an SNR of 100, and N_R values of 5, 10, 25, and 50. The straight lines calculated from Eq. (75), in this figure, show that the same expression can be used to describe the

Table 9: Some retrieved mixing-ratio uncertainties for N_R = 50, SNR = 100, A_o = 0 km, and N_o values of 125 and 500.

A (km)	N_o = 125	N_o = 500
0	47%	20%
1	97	39
3	250	71
9	590	
19		950
26	4200	
49		65000

Figure 19: Average uncertainty in the retrieved mixing-ratio values for an observer at 30 km obtained from retrievals from 16 data sets with SNR = 100, N_O = 125, and N_R = 50, 25, 10, and 5. The straight lines are the corresponding functions from Eq. (2.75).

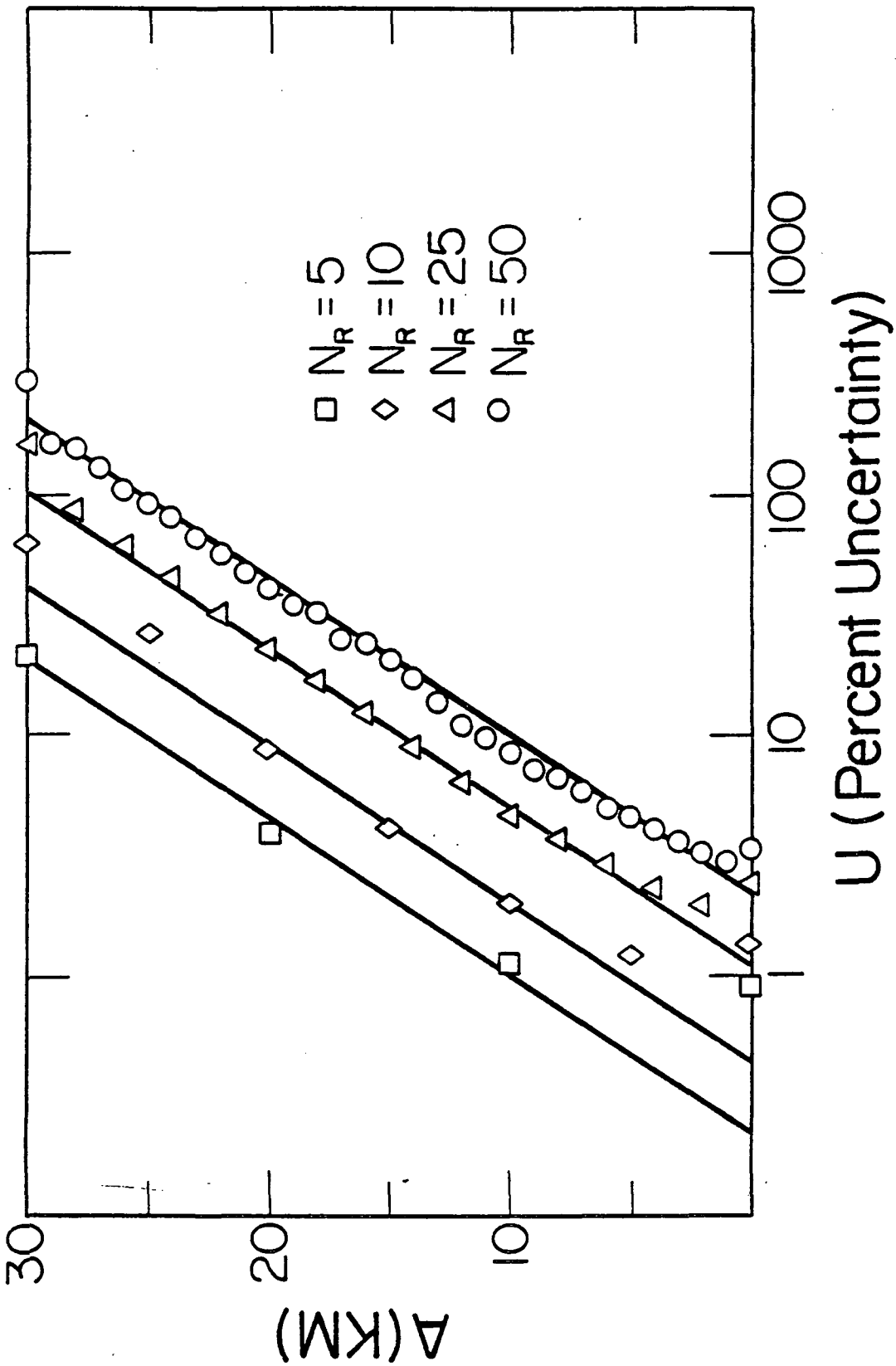
A (KM)
30
20
10
U (Percent Uncertainty)
1
10
100
1000
N_R = 5
N_R = 10
N_R = 25
N_R = 50

Figure 19

uncertainties in the mixing-ratio profiles obtained at both 30 and 500 km. To illustrate this point some retrieved uncertainty values below the observer for various SNR values are listed in Table 10. In Table 11 a comparison is given of the uncertainties obtained for two different N_o values (all other parameters the same). These show the same dependence as given in Eq. (80). Therefore it is concluded that, Eqs. (75) and (80) describe the uncertainties in the mixing-ratio values below and above the instrument for all observing heights, for the case of an absorber with a constant mixing-ratio.

It was found that, for other mixing-ratio profiles, the variations of $a_{mi}(Z_{oi})$ can be substantially different from those shown in Figures 13 and 14. This altered a_{max}, the effective SNR, and the values of the constants in Eqs. (75) and (80). However, the functional form was qualitatively similar (i.e., the uncertainty increased with height and depended on the SNR, N_R, and N_o in the same fashion as for the constant profile). These other profiles are discussed later in this chapter.

2.5.5 Summary

In this long section we have determined the uncertainty in the retrieved mixing-ratio values as a function of altitude for the case of absorber amount data obtained for an absorber with a vertically constant mixing-ratio profile.

Table 10: Some retrieved mixing-ratio uncertainties below the observer for N_R = 100, N_O = 125, A_O = 30 km, and various SNR values.

A (km)	SNR			
	500	100	50	10
0	0.80%	3.9%	7.3%	35%
5	1.6	6.3	12	56
10	2.6	11	20	94
15	8.7	35	66	310
20	13	50	95	450
25	28	110	210	1000

Table 11: Some retrieved mixing-ratio uncertainties below the observer for N_R = 100, SNR = 100, A_o = 30 km, and N_o values of 125 and 500.

A (km)	N_o = 125	N_o = 500
0	3.9%	1.9%
5	6.3	3.1
10	11	5.1
15	35	17
20	50	25
25	110	55

We have found that the uncertainty in these retrieved values increases exponentially with altitude, depends on the SNR of the data, the number of data values analyzed, and the number of mixing-ratio values retrieved, it is much larger above the observer than below, and it is independent of the observer altitude. Above the observer small uncertainties are only possible for small N_R, or large SNR, or large N_O. For the region below the observer the uncertainty in the retrieved mixing-ratio values above 30 km was larger than 10% no matter what retrieval value spacing was used. Thus reasonable uncertainties in the retrieved mixing-ratio values above 30 km also require small N_R, or larger SNR, or large N_O.

These results were obtained for the case of a mixing-ratio profile retrieval from absorber amount data (equivalent width data). These data represent only one piece of information from each spectrum. More information is contained in the shapes of the spectral lines. The uncertainty in retrieved mixing-ratio values obtained from spectral curve-fitting is considered in the fourth chapter.

The uncertainties in the retrieved mixing-ratio values could be reduced if a number of different spectral lines are analyzed. If, for example, one spectral line with intensity S is used to determine the absorber amount for occultations corresponding to tangent heights less than 25 km and a second line with intensity 100xS is used to determine the absorber amount for occultations corresponding to tangent

heights between 25 and 50 km the effective noise contained in the absorber amount data for tangent heights above 25 km will be less than if only the one line with intensity S were used for the entire region. Thus the overall effective SNR of the data will be reduced so that the uncertainty will also be smaller.

2.6 THE VERTICAL RESOLUTION

2.6.1 Resolution determination

If N_R equally-spaced, mixing-ratio values are retrieved over an altitude interval ΔA (=50 km) the corresponding vertical resolution can be defined as

$$Res = \frac{2\Delta A}{N_R} . \tag{81}$$

It has been found that if the SNR is sufficiently high, N_R can be increased to nearly N_O and the ultimate resolution in a mixing-ratio profile retrieval is

$$R_{ULT} = \frac{2\Delta A}{N_O} . \tag{82}$$

Equations (75) and (80) and the straight lines in Figures 16, 18, and 19 show the dependence of the uncertainty of the retrieved mixing-ratio values on altitude for a particular vertical resolution defined by the spacing of the retrieved mixing-ratio values. But in order to determine the optimum

distribution of retrieval values in the analysis of a given set of a data, it is more useful to know the dependence of the vertical resolution on altitude for a fixed retrieval value uncertainty at all altitudes.

By combining Eqs. (75) and (81) the profile resolution $Res_B(A)$ below the observing instrument is

$$Res_B(A) = \frac{100\Delta A \exp(0.15A)}{N_O^{\frac{1}{2}} U \, SNR} . \tag{83}$$

Some examples are shown in Figure 20 for $R_{ULT} = 1.0$ km and constant values of U of 0.1, 1, 5, and 25%. A vertical resolution greater than 25 km is unrealistic for the altitude range of 50 km sampled. Figure 20 shows a vertical resolution up to 100 km in order to describe the dependence of Res_B on altitude. The cut-off at 1 km is due to the limit $R_{ULT} = 1$ km. The form of Eq. (83) is in agreement with Eq. (41) obtained from the Backus-Gilbert theory. The vertical resolution is inversely proportional to the retrieval value uncertainty.

The corresponding relation for the atmosphere above the observer, obtained from Eq. (80) is

$$Res_A(A) = 45 Res_B(A) . \tag{84}$$

Examples of the dependence of the resolution $Res_A(A)$ on height for the case of $R_{ULT} = 1.0$ km and an uncertainty U of 5, 25, and 100% are shown in Figure 21. Even for the

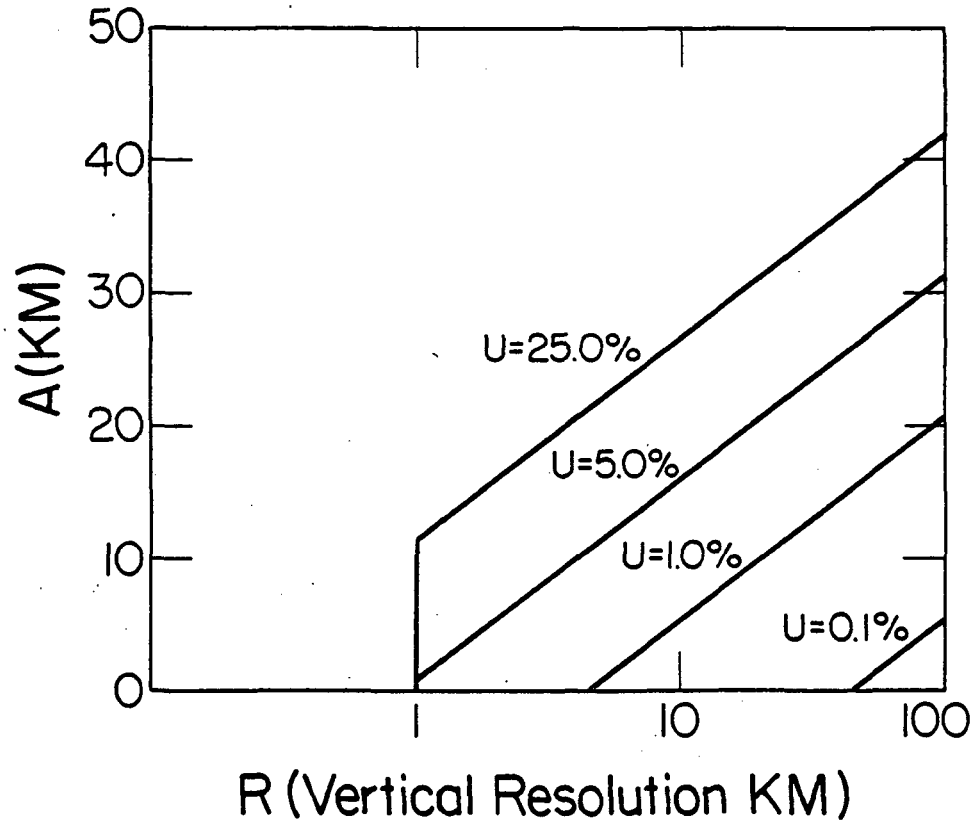

Figure 20: Vertical resolution of the retrieved profiles obtained from Eq. (2.83) for the region below the observer for SNR = 100, R_{ULT} = 1.0 km, and U = 25.0, 5.0, 1.0, and 0.1%.

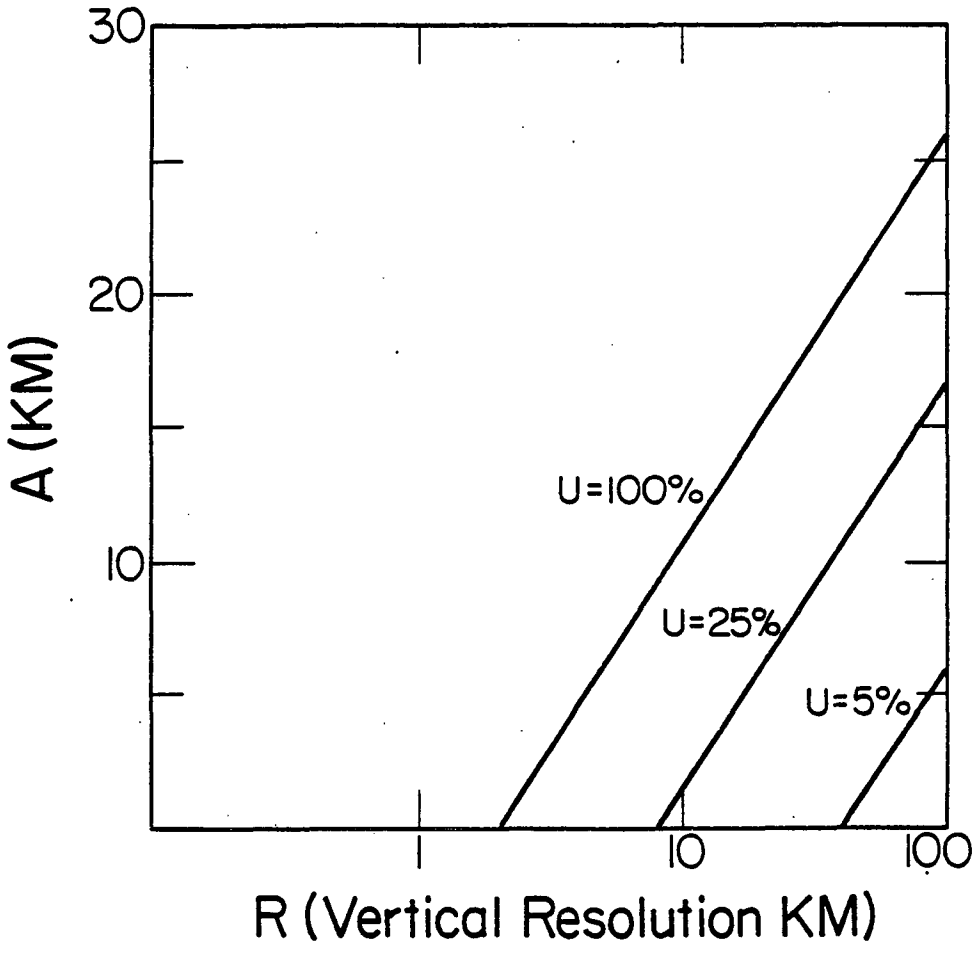

Figure 21: Vertical resolution of the retrieved profiles obtained from Eq. (2.84) for the region above the observer with SNR = 100, R_{ULT} = 1.0 km, and U = 100, 25, and 5%.

optimistically large values of 125 and 100 for N_o and the SNR respectively, it is not possible to obtain significant resolution above the observer if an uncertainty of 5% or better in the retrieved mixing-ratio values is desired. Indeed, to obtain a vertical resolution of 10 km at a height of 20 km above the instrument, together with an uncertainty of 5% in the retrieved mixing-ratio values, an SNR of 10^4 is required for the case of a constant mixing-ratio retrieval.

In summary, if no a priori information about the vertical mixing-ratio profile is assumed, the quality of the retrieved profiles degrades nearly exponentially with altitude, is considerably better for the atmosphere below than above the observer, and is independent of the instrument height.

2.6.2 The spacing of retrieval parameters

The previous results suggest that, by spacing the local, mixing-ratio values to be retrieved according to the expected vertical resolution and desired uncertainty, it is possible to reduce significantly the number of atmospheric layers used in the calculations and the number of local, mixing-ratio values to be retrieved, and hence the amount of computer time required for the analysis.

The vertical resolution defined in Eq. (81) was given as twice the mixing-ratio value spacing in the retrieval. Similarly, the spacing of adjacent parameters at altitude A is given by one half the vertical resolution at altitude A from Eq. (83).

This suggests that if the first mixing-ratio value is to be retrieved at $A_1 = 0$ km, the second mixing-ratio value should be retrieved at approximately $A_2 = R_o/2$ where, from Eq. (83)

$$R_o = \frac{100\Delta A}{\sqrt{N_o}\, U\, SNR}\ , \tag{85}$$

in order to give a constant uncertainty U in the retrieval values. Similarly, the altitude of the third retrieval value is

$$A_3 = A_2 + \frac{R_o}{2}\ \exp(0.15A_2) \tag{86}$$

and the altitude of the kth mixing-ratio retrieval value should be approximately

$$A_k = A_{k-1} + \frac{R_o}{2} \exp(0.15A_{k-1})\ . \tag{87}$$

In principle, Eq. (87) gives the altitude of the kth retrieval parameter in terms of the vertical resolution at R_o. Equation (87) cannot be expressed in a simple closed form, nor it is well-behaved when approximated by the Taylor series.

It can be used iteratively to determine the spacing of retrieval values in order to give a constant uncertainty U. The appropriate retrieval parameter altitudes for $A_o = 500$ km,

$\Delta A = 50$ km, $N_o = 100$, $U = 1\%$, and an SNR of 100 and 500 are shown in Table 12. A retrieval performed on data obtained from a constant mixing-ratio profile for the conditions of Table 12 and an SNR of 100 are given in Table 13. The uncertainties in the retrieved values at higher altitudes are substantially reduced for the variable spacing retrieval and are approximately independent of altitude. A comparison of the uncertainties in this retrieval and those obtained for a constant spacing show that the appropriate distribution of retrieval values allows the retrieval of mixing-ratio values over the entire region of interest with nearly constant uncertainty.

The distribution of mixing-ratio values for a 0 km observer is substantially worse. For $\Delta A = 50$ km, $N_o = 100$, and $U = 1\%$ an SNR of 225 is required to retrieve two mixing-ratio values, and an SNR of 1200 is necessary to retrieve three values. Retrievals performed by Zander et al (29) on absorption spectra with an SNR of 300 obtained at Kitt Peak in order to determine the column abundances of FC-11, FC-12, and FC-22 show that not more than one well-determined mixing-ratio value is obtainable. Thus it is concluded that our results are in general agreement with experiment.

A parameter spacing which varies with altitude has been used by Goldman et al (30) to retrieve mixing-ratio values from spectra taken at ground-level. In this case the uncertainties were reduced by using a scheme similar to the one

Table 12: Sample retrieval profiles which give an uncertainty in the mixing-ratio values of 1% at all altitudes for ΔA = 50 km, N_o = 100, and an SNR of 100 and 500.

SNR = 100		SNR = 500	
Parameter #	Height (km)	Parameter #	Height (km)
1	0	1	0
		2	0.5
		3	1.04
2	2.5	4	1.62
		5	2.26
		6	2.96
		7	3.74
3	6.14	8	4.62
		9	5.62
		10	6.78
4	12.42	11	8.16
		12	9.86
		13	12.05
5	28.53	14	15.10
		15	19.92
		16	29.84

Table 13: A sample mixing-ratio profile retrieval of the constant profile of m = 1.0 using the retrieval profile of Table 12 for SNR = 100, N_o = 100, ΔA = 50 km.

Retrieved uncertainty values			Uncertainty values predicted from Eq. (54) for N_R = 5	
A (km)	m_k	U_k	A (km)	U_k
0	1.03	2.6	0	0.2
2.5	0.99	1.7	10	1.1
6.0	0.99	1.5	20	5.0
12.5	1.02	2.0	30	22
28.5	0.98	6.0	40	101

described here. The results obtained in this work suggest that the representation of mixing-ratio retrievals can be improved by suitable spacing of the mixing-ratio values.

2.7 RETRIEVALS OF OTHER PROFILES

The nature of the trade-off, due to the experimental noise in absorber amount data, between the uncertainty in the retrieved mixing-ratio values and the vertical resolution of other assumed mixing-ratio profiles has been examined by considering a number of profiles. The standard values of Table 3 were used with an observer altitude of 500 km. As was the case for the previous retrievals no a priori assumptions were made about the shape of the profile to be retrieved.

Two of the profiles considered, the quadratic profile of Figure 22 and the quadratic spike shown in Figure 23, were chosen for study since many atmospheric molecules have similar mixing-ratio profiles (31). The quadratic profile is similar to the profile of HNO_3 and the quadratic spike similar to the profile of NO_2.

In addition to these smoothly varying profiles, we have constructed a discontinous profile in order to test the uncertainty-resolution trade-off found previously. This profile, shown in Figure 24, consisted of six 1 km-thick segments with constant mixing-ratio values. In between these segments the mixing-ratio values were zero. Thus all the absorber was concentrated in six discrete regions of

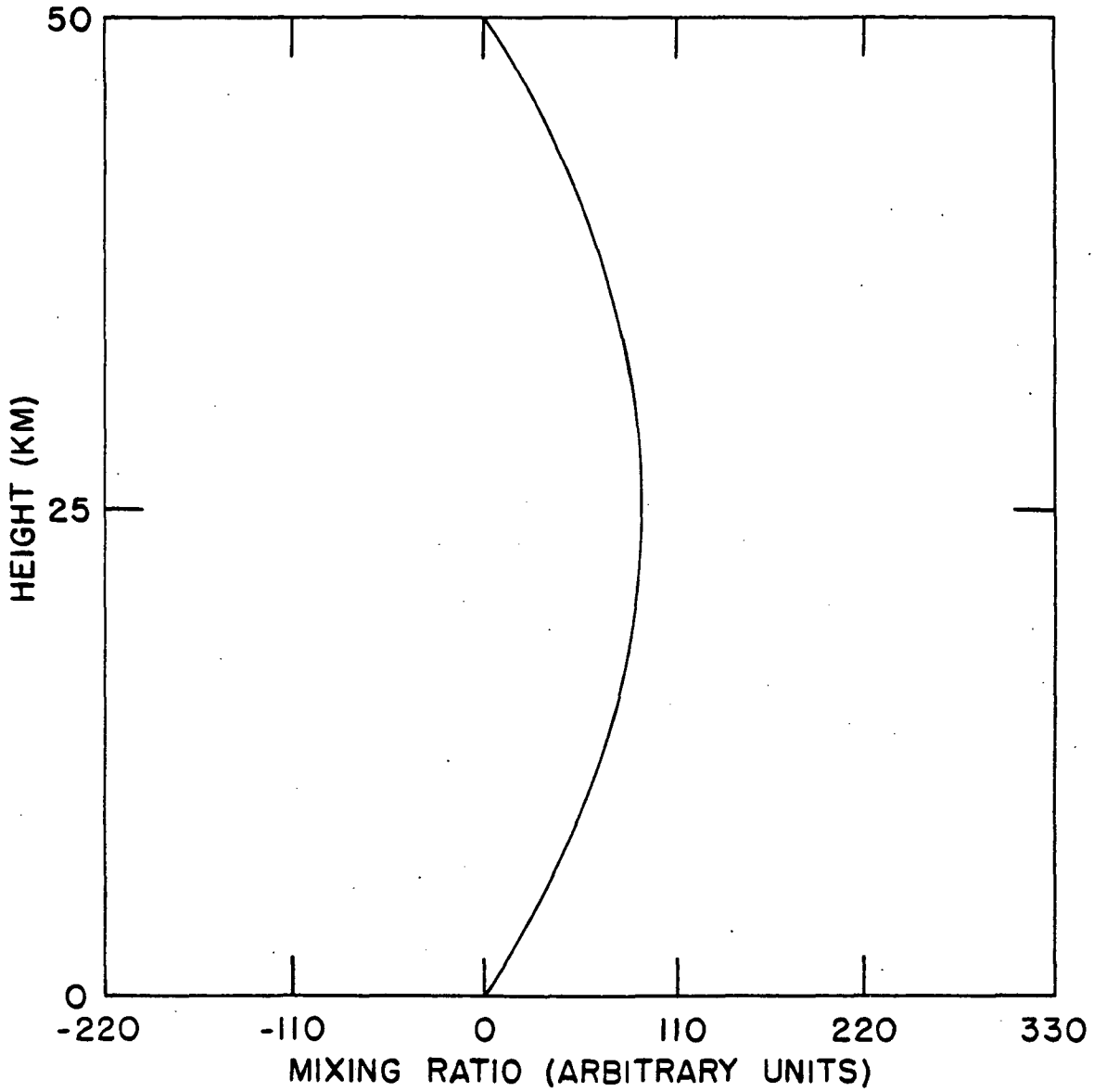

Figure 22: A mixing-ratio profile which varies quadratically with altitude and is a maximum at 25 km.

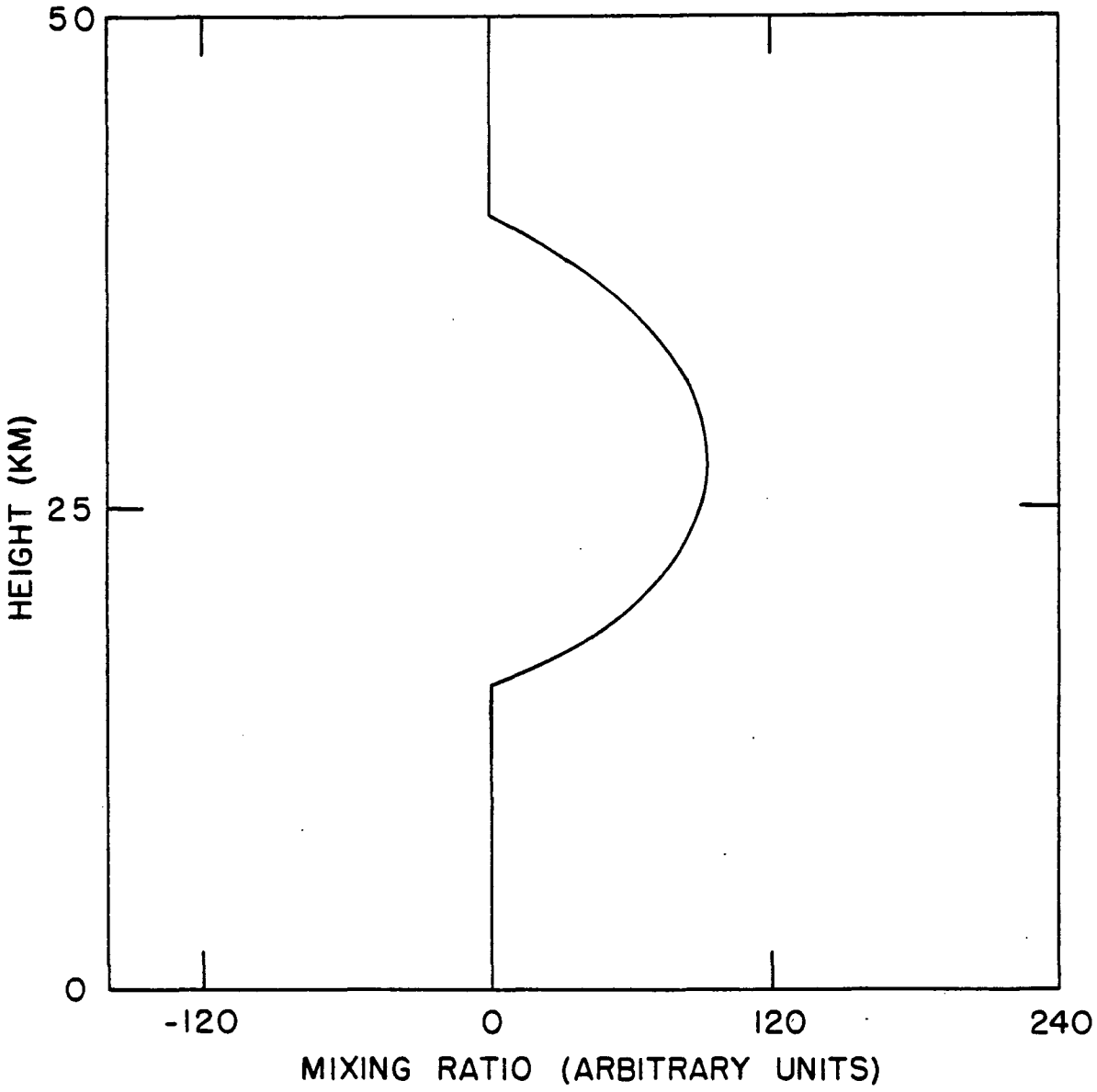

Figure 23: A mixing-ratio profile which varies quadratically with altitude between 15 and 40 km and is a maximum at 37.5 km.

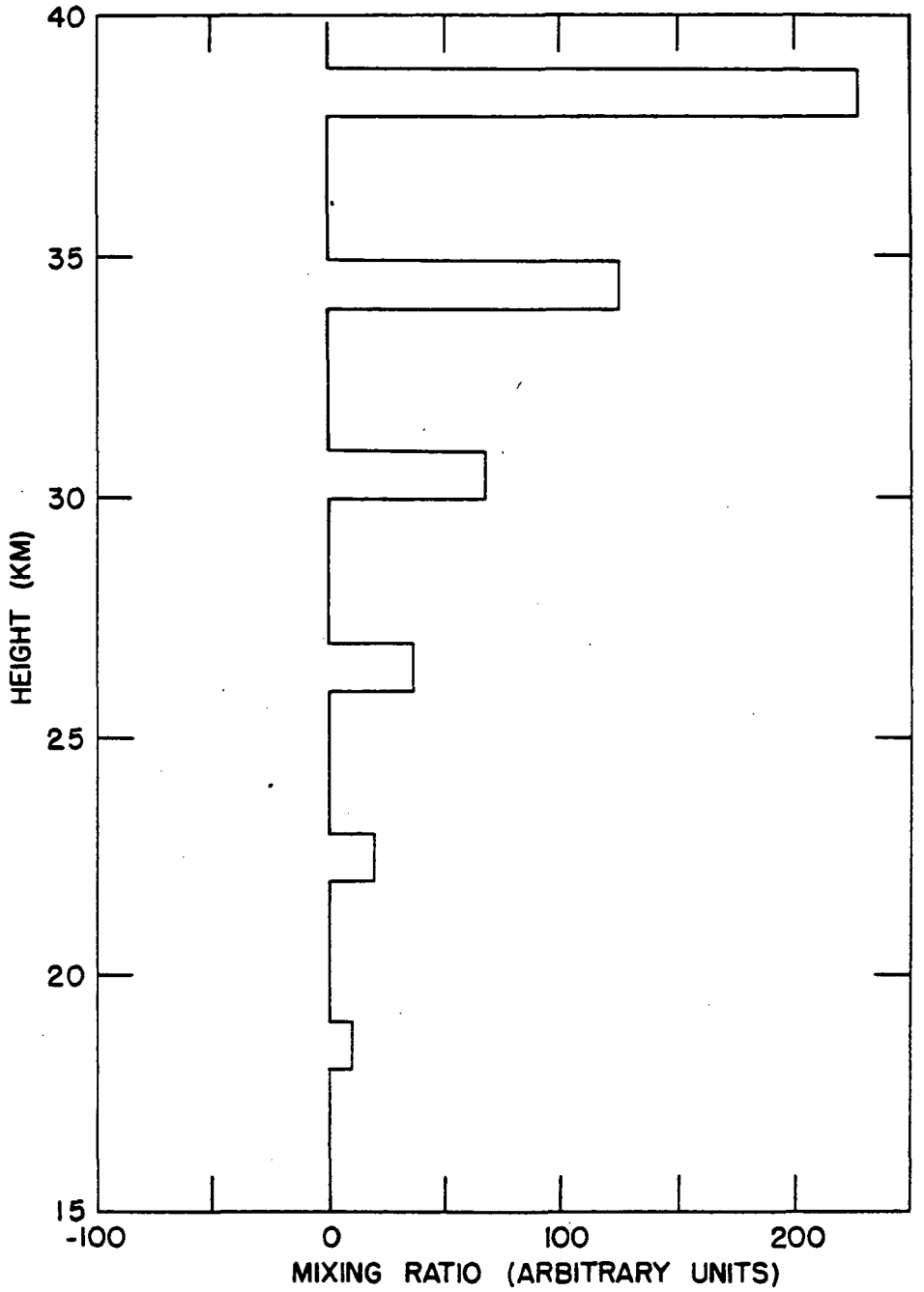

Figure 24: The "comb" mixing-ratio profile. The mixing-ratio values in the six 1 km-thick layers were chosen such that the absorber amount in a vertical column is the same for each layer.

the atmosphere separated by 3 km in altitude (a highly unphysical situation). The mixing-ratio values of each segment were chosen such that a vertical column in each segment contained the same number of absorber molecules.

The data sets constructed from these mixing-ratio profiles contained absorber amount values corresponding to 125 apparent zenith angles of constant spacing with tangent heights between 0 and 50 km (the range of tangent heights for the "comb" profile of Figure 24 was 15 to 40 km). The tangent height spacing was less than 500 m for all tangent heights (for the "comb" profile the spacing was less than 250 m). The observer altitude was 500 km.

The data set calculated using the quadratic profile is shown in Figure 25. Random noise was added to the calculated absorber amounts to give an SNR of 200. The data set obtained from the quadratic spike with an SNR of 100 is shown in Figure 26.

The absorber amount data shown in Figure 27 calculated from the comb profile indicate the existence of the discrete non-zero layers. The peaks allow the separation of the layers if the noise is sufficiently small. The SNR of the data in Figure 27 is 50.

One hundred local, mixing-ratio values with a spacing of 500 m between 0 and 50 km were retrieved from the data shown in Figure 25. The retrieved profile is shown in Figure 28. As expected the uncertainty in the retrieved values

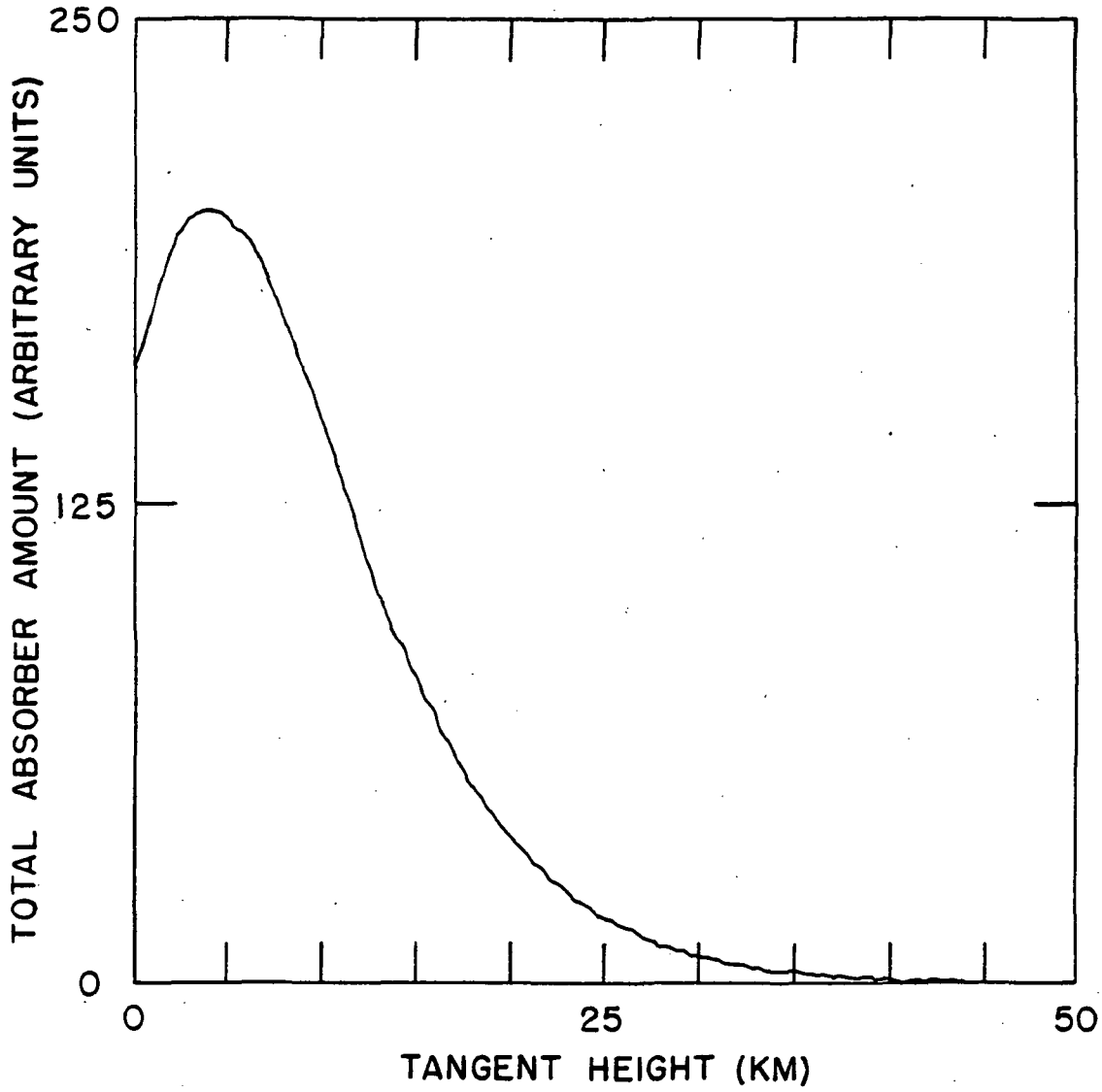

Figure 25: The total absorber amount as a function of the tangent height of the ray with an SNR of 200 obtained from the quadratic mixing-ratio profile and an observer altitude of 500 km.

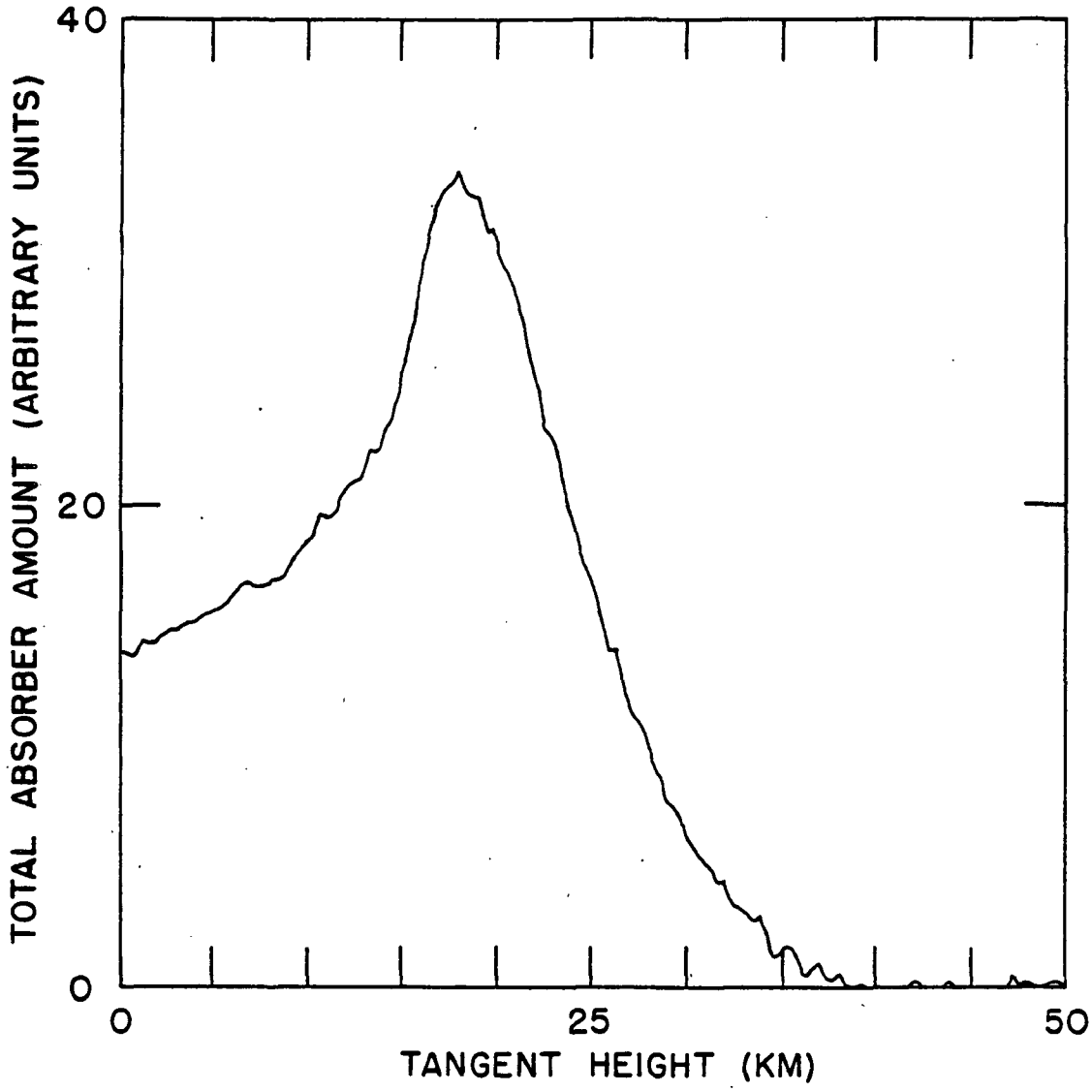

Figure 26: The total absorber amount as a function of the tangent height of the ray with an SNR of 100 obtained from the quadratic spike mixing-ratio profile and an observer altitude of 500 km.

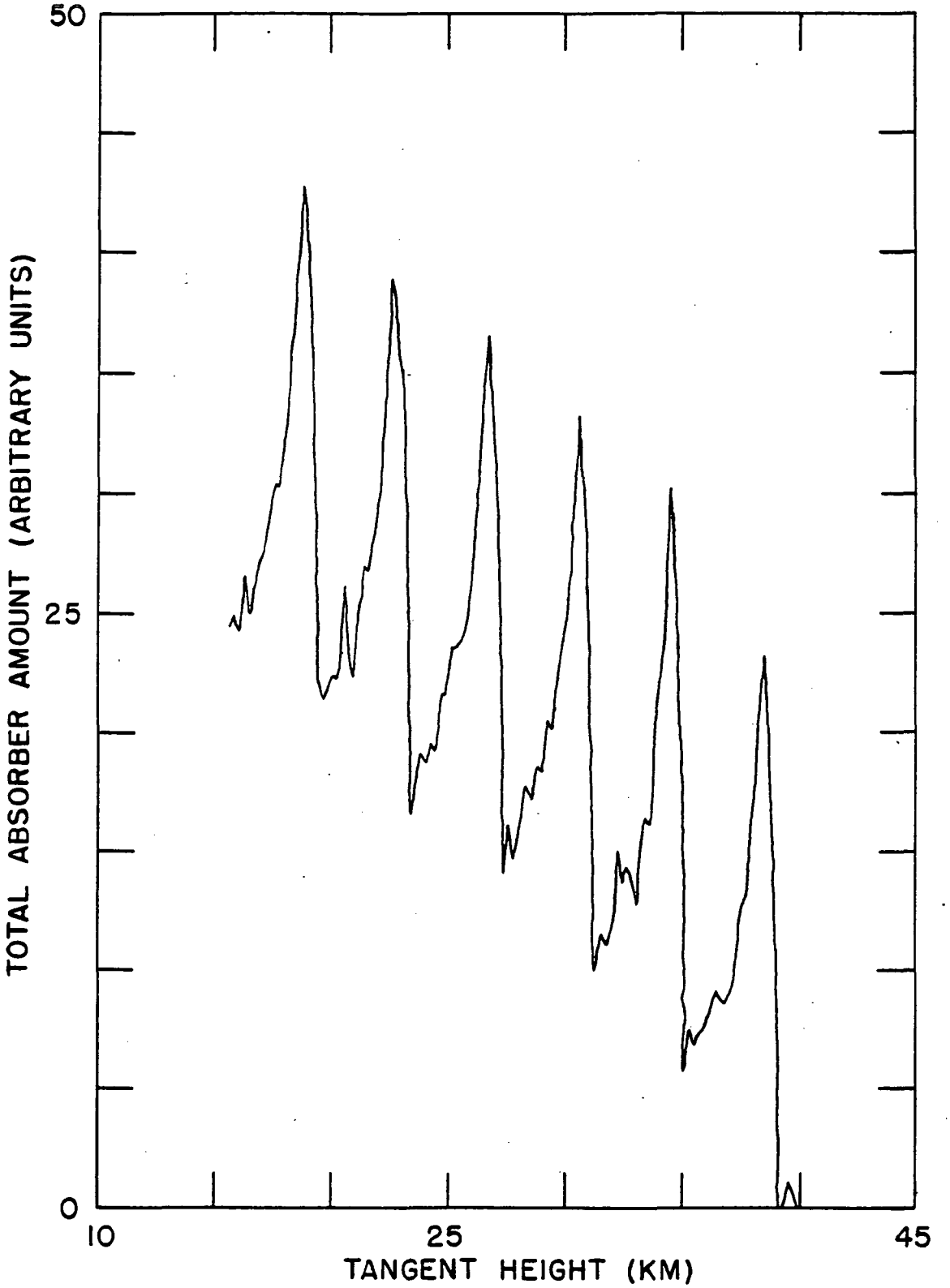

Figure 27: The total absorber amount as a function of the tangent height of the ray with an SNR of 50 obtained from the comb mixing-ratio profile and an observer altitude of 500 km.

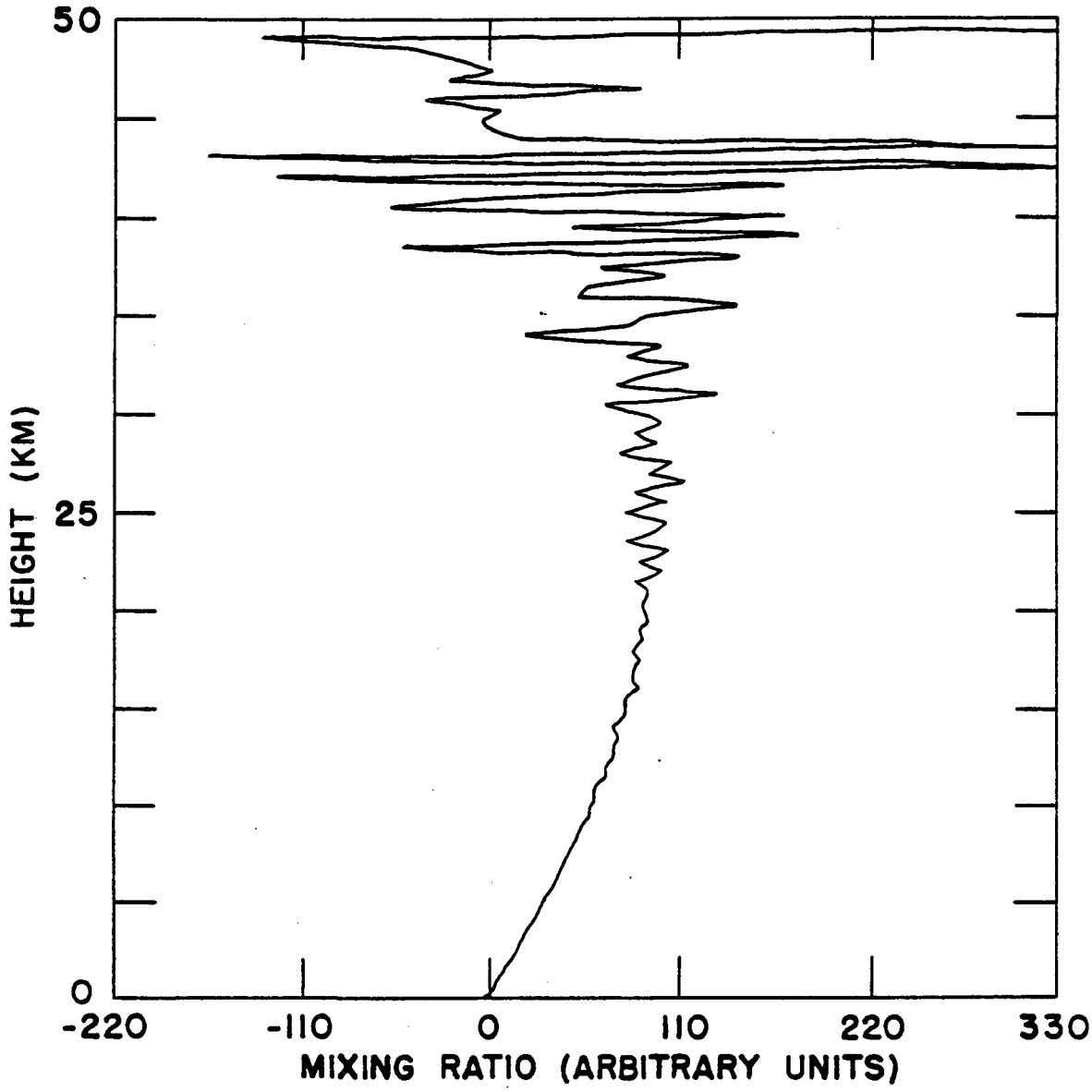

Figure 28: A retrieval obtained from the data of Figure 25 for a mixing-ratio spacing of 0.5 km.

increases rapidly with height. Above 35 km it is so large that no useful values are obtained. A retrieval performed on these data for a mixing-ratio value spacing of 5 km is shown in Figure 29. The uncertainty is greatly reduced and the altitude range of useful values is extended to 45 km. These profiles show that the uncertainty in the mixing-ratio values can be reduced by increasing the spacing between parameters in agreement with the results obtained for the constant profile in Eq. (75). The effect of reducing the number of parameters is to increase the amount of data per parameter retrieved. The retrievals shown in Figures 28 and 29 show no systematic errors in the retrieval. At low altitudes the retrieval fits the true shape extremely well. At higher altitudes departure from the true profile are due only to the noise in the synthetic data. No obvious calculational errors were found in any of the retrievals done for this work.

Similar results were found from analysis of the quadratic spike data shown in Figure 26. The uncertainty increased rapidly with altitude but could be reduced by increasing the parameter spacing. Retrievals obtained for a spacing of 500 m are shown in Figure 30 and those obtained for a 5 km spacing are shown in Figure 31.

Ten data sets similar to those shown in Figure 26, obtained from the comb profile, were constructed by adding different sets of random noise so that in all cases the SNR was 50.

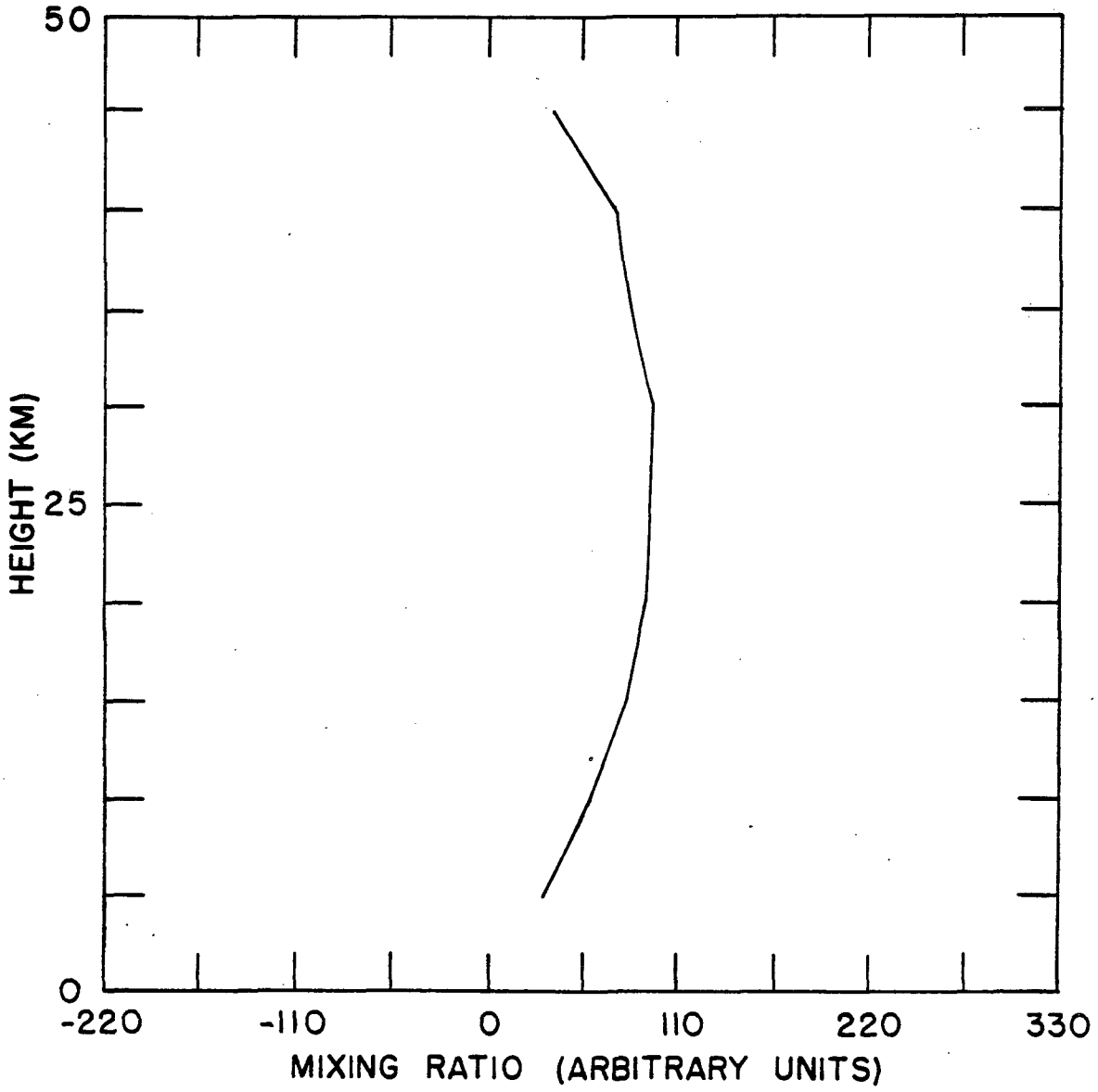

Figure 29: A retrieval obtained from the data of Figure 25 for a mixing-ratio spacing of 5 km.

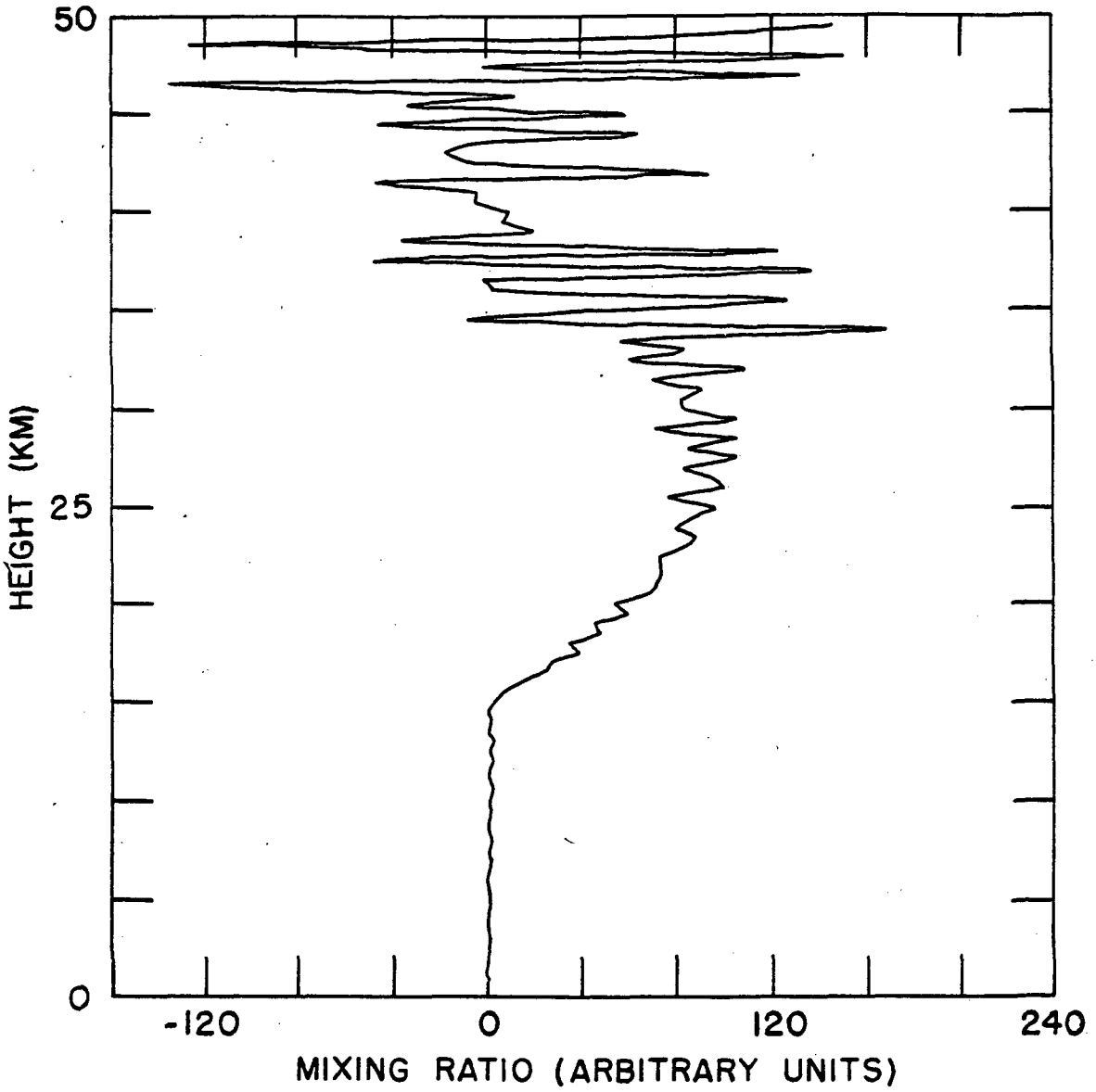

Figure 30: A retrieval obtained from the data of Figure 26 for a mixing-ratio spacing of 0.5 km.

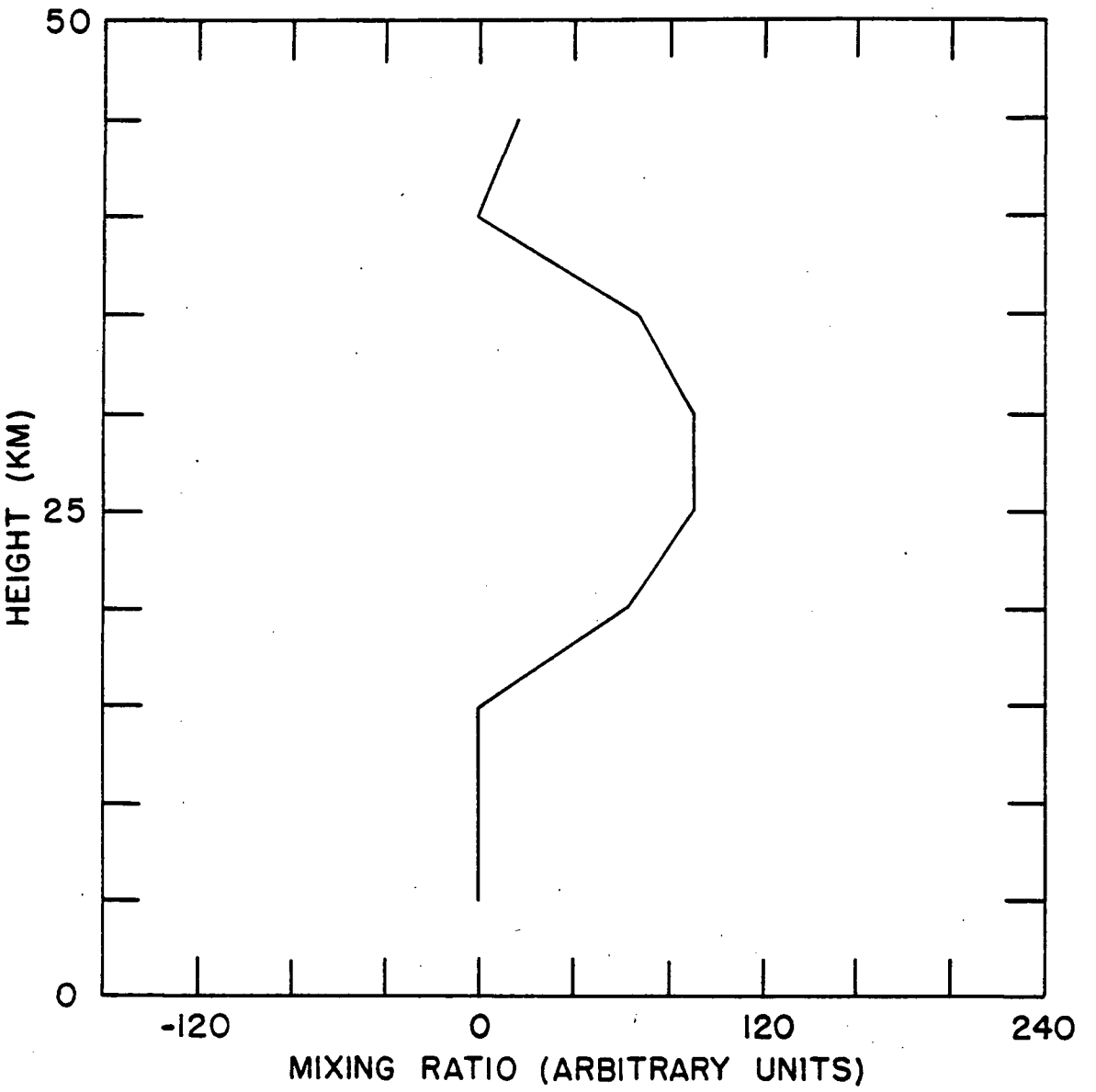

Figure 31: A retrieval obtained from the data of Figure 26 for a mixing-ratio spacing of 5 km.

Retrievals were made by using these ten data sets and a parameter spacing of 250 m. At each altitude the average parameter value together with its standard deviation was calculated from the ten retrievals. The effect of averaging the ten sets of mixing-ratio values with SNR of 50 was identical to one retrieval made on data with SNR of about 160 as expected. The average mixing-ratio values are shown in Figure 32 together with the standard deviations. The retrieved values are seen to be accurate at all altitudes. The standard deviations, shown in Figure 33, increase with altitude (except above 40 km, where the standard deviations are smaller than expected due to the constraint on the mixing-ratio value at 50 km) as was the case for the constant mixing-ratio profile retrievals.

Similar averages were obtained using the same data sets for a parameter spacing of 2.5 km. The calculated averages and standard deviations are shown in Figures 34 and 35. Comparison of Figure 33 and 35 show that although the uncertainty in the retrieved values can be reduced by increasing the parameter spacing, it is accompanied by a degradation in the vertical resolution.

The previous analysis suggests that if no a priori assumptions are made about the shape of the profile, the uncertainty in the retrieved mixing-ratio values is given by Eq. (75) or Eq. (80) and the vertical resolution of the retrieved profile is given by Eq. (83) or Eq. (84) regardless

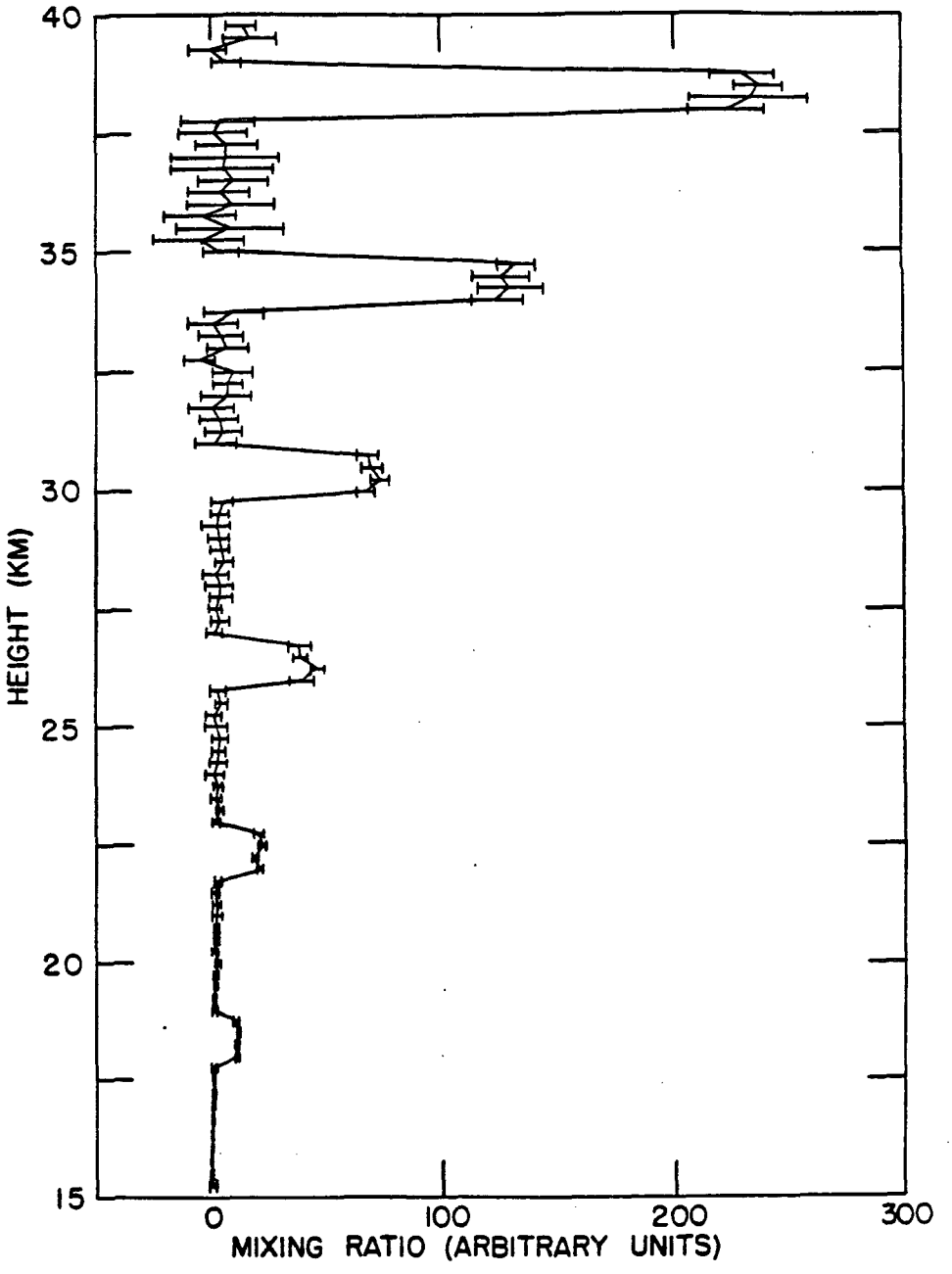

Figure 32: The average of ten retrievals obtained from ten data sets similar to that shown in Figure 27 for a mixing-ratio spacing of 0.5 km.

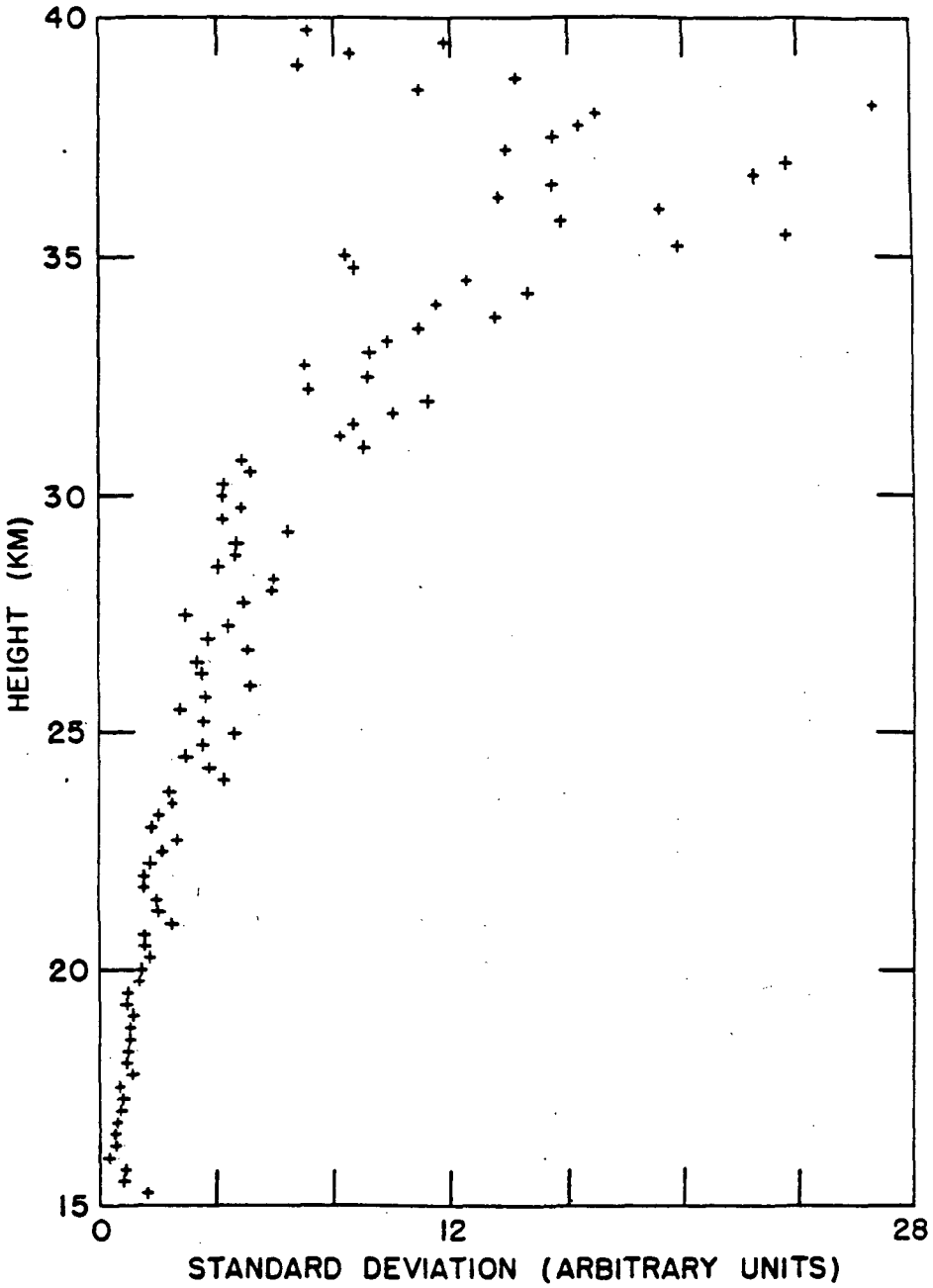

Figure 33: The standard deviations of the mixing-ratio values retrieved from ten data sets similar to that shown in Figure 27 for a mixing-ratio spacing of 0.5 km.

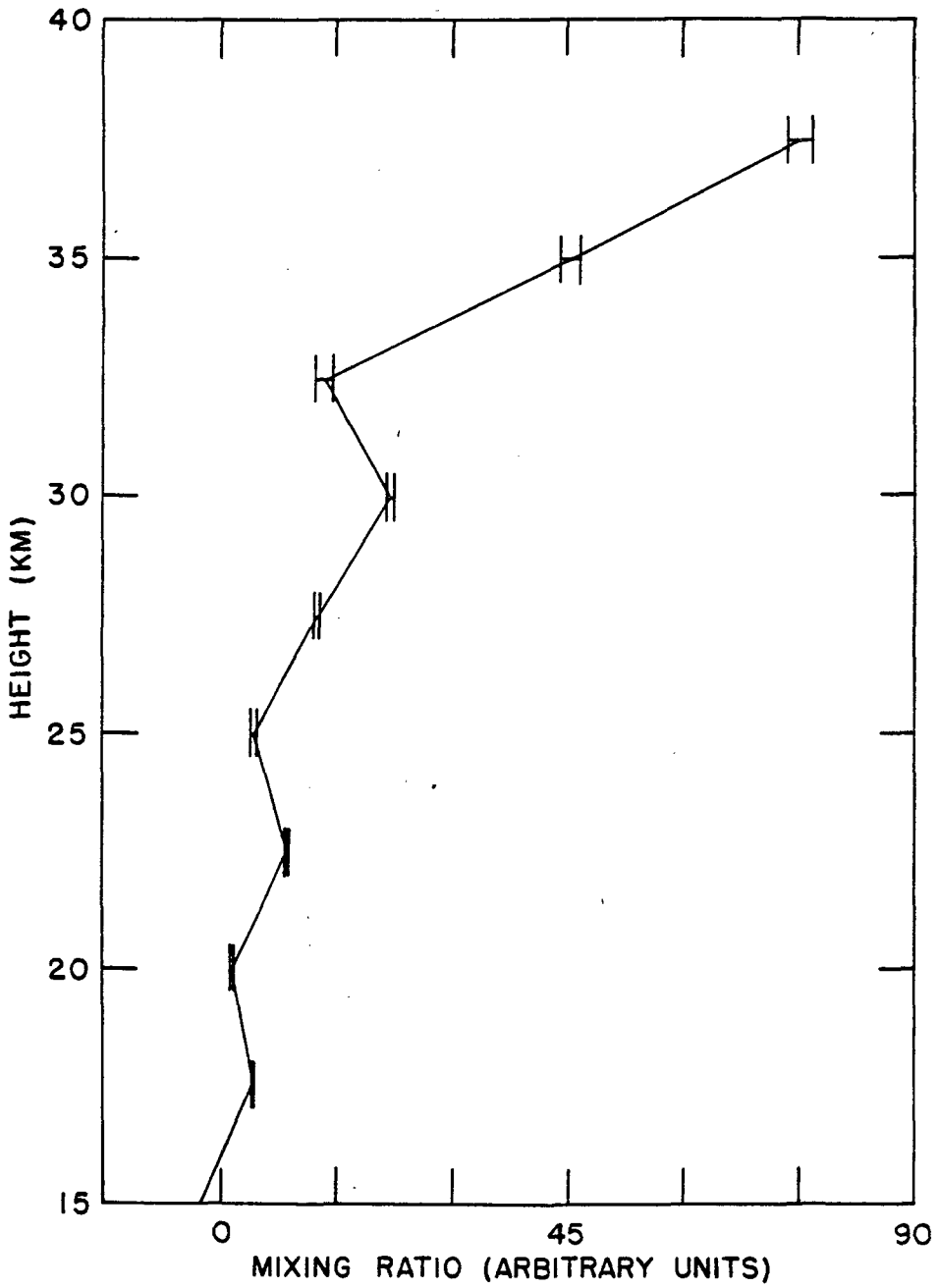

Figure 34: The average of ten retrievals obtained from ten data sets similar to that shown in Figure 27 for a mixing-ratio spacing of 5 km.

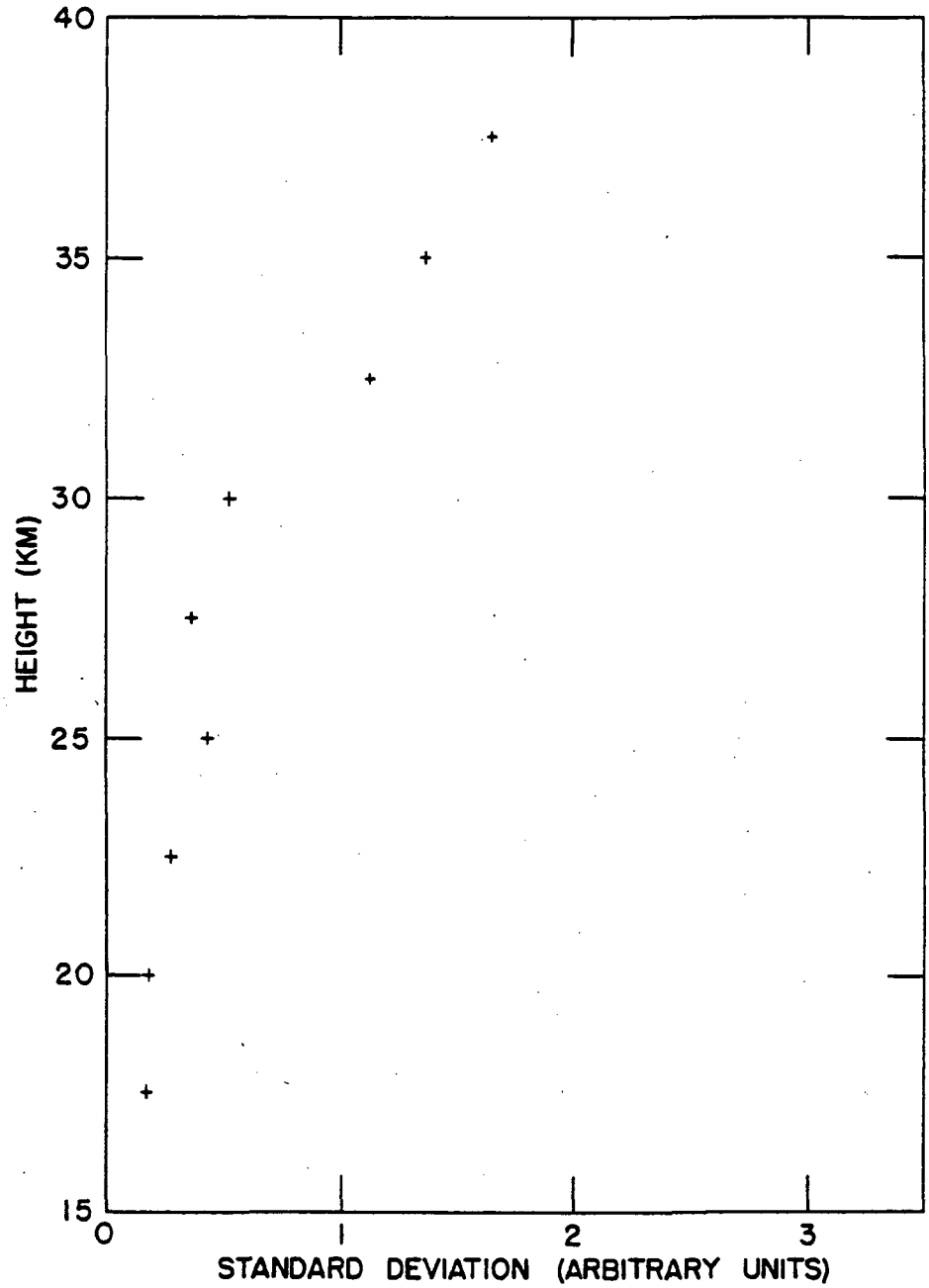

Figure 35: The standard deviations of the mixing-ratio values retrieved from ten data sets similar to that shown in Figure 27 for a mixing-ratio spacing of 5 km.

of the shape of the profile to be retrieved. For a particular profile the constants in these equations will have different values than those defined for Eqs. (75), (80), (83), and (84) but the functional form of these equations remains the same. These constants can be determined for any profile of interest by the methods already described.

Analysis of data sets obtained for various profiles and an observer altitude of 0 km show, as expected from Eq. (84), that there is very little ability to discriminate a mixing-ratio profile above the observer. An example shown in Figure 36 was obtained from data calculated using the quadratic profile (with no added noise) with an N_R of 50 and an N_O of 125. As seen in this figure no useful information is retrieved above 3 km and the vertical resolution is very poor. The number N_R of parameters retrieved was found to be independent of the profile studied and in all cases the uncertainties were large and increased rapidly with altitude and the vertical resolution was very poor.

2.8 SUMMARY

In this chapter we have obtained expressions for the uncertainty in retrieved mixing-ratio profiles, if no assumptions are made about the shape of the profile to be retrieved, both above and below the observer altitude. These uncertainty expressions suggest that many investigators may have underestimated the errors in their reported retrievals

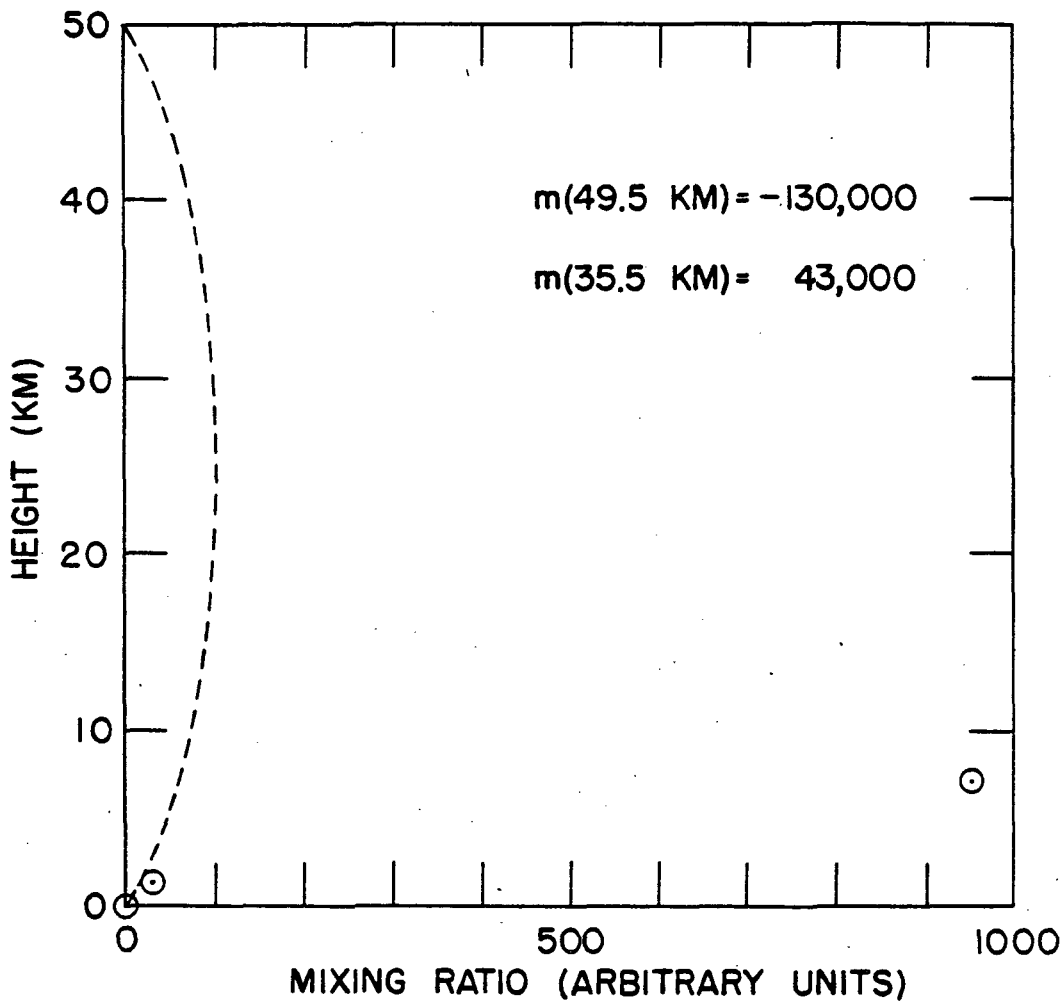

Figure 36: A retrieval obtained from a data set calculated using the quadratic profile and an observer at 0 km with no added noise.

from solar spectra. By the methods outlined in this chapter it is now possible to estimate the uncertainty in a mixing-ratio profile retrieval based entirely on the experimental conditions and not on any a priori assumptions about the errors.

The uncertainty in retrieved mixing-ratio values was found to increase exponentially with altitude, to decrease with increasing SNR, to increase if more values were retrieved, to decrease if more data values were analyzed, it was much larger above the observer than below, and it was independent of the observer altitude. These relations were found to be true for all the mixing-ratio profiles studied. Thus the uncertainty expressions (with slight modification) can be used to express the retrieval of any mixing-ratio profile from equivalent width data.

The vertical resolution of retrieved mixing-ratio profiles degraded exponentially with altitude and was much worse above than below the observer. The vertical resolution expressions can be used to determine the appropriate spacing of the retrieval values in order to obtain an uncertainty in the retrieved values which is constant with altitude.

Thus the effects of experimental noise on the analysis of equivalent width data obtained from a single spectral line can be described by the equations obtained in this chapter. Similar analyses can also be used to describe other experimental situations, such as the analysis of

equivalent width data obtained from several spectral lines in each spectrum or equivalent width data obtained from spectral lines with different intensities (each intensity is used to obtain equivalent widths with corresponding tangent heights in a particular region of the atmosphere). The additional information contained in the spectral line shape is considered in the fourth chapter.

In the next chapter we investigate the effects of systematic errors in the describing physical parameters on the retrieval of mixing-ratio profiles.

REFERENCES

1) C. D. Rodgers, J. Atmos. Sci., 33, 707 (1976).

2) G. E. Backus and J. F. Gilbert, Geophys. J. R. astr. Soc., 13, 247 (1967).

3) G. Backus and F. Gilbert, Geophys. J. R. astr. Soc., 16, 169 (1968).

4) G. Backus, Proc. Nat. Acad. Sci., 65, 1 (1970).

5) G. Backus, Proc. Nat. Acad. Sci., 65, 281 (1970).

6) G. Backus, Proc. Nat. Acad. Sci., 67, 282 (1970).

7) G. Backus and F. Gilbert, Phil. Trans. Roy. Soc., London, 266, 123 (1970).

8) B. J. Conrath, J. Atmos. Sci., 29, 1262 (1972).

9) G. Peckham, Quart. J. R. Met. Soc., 100, 406 (1974).

10) E. R. Westwater and A. Cohen, Appl. Opt., 12, 1340 (1973).

11) R. L. Parker, Geophys. J. R. astr. Soc., 22, 121 (1970).

12) M. Brown, ed., BMOP Statistical Software 1981, Univ. California Press, Berkeley, 1981.

13) J. R. Nielsen, V. Thornton, and E. B. Dale, Rev. Mod. Phys., 16, 307 (1944).

14) R. M. Goody, Atmospheric Radiation I: Theoretical Basis, pp. 122-170, Oxford, 1964.

15) J. T. Houghton and S. D. Smith, The Infra-red Spectra of Molecules, pp. 46-51, Oxford, 1966.

16) A. L. Buijs, G. L. Vail, G. Tremblay, and D. J. W. Kendall, Geophys. Res. Lett., 7, 205 (1980).

17) L. Goldberg, Astrophys. J., 113, 567 (1951).

18) P. Marché, Thèse, Univ. Reims (1981).

19) Y. M. Treve, "New values of the optical air mass and the refraction and comparison with previous Tubles," Technical Report ESD-TDR-64-103, Mitre Corp. (1964).

20) Y. M. Treve, "A New Method for the Calculation of the Atmospheric Refraction and Optical Airmass," (unpublished).

21) B. Edlen, Metrologia, 2, 71 (1966).

22) H. A. Lorentz, collected papers, Vol. 2, The Hague (1936).

23) D. E. Snider, J. Atmos. Sci., 32, 2178 (1975).

24) D. E. Snider and A. Goldman, "Refractive Effects in Remote Sensing of the Atmosphere with Infrared Transmission Spectroscopy," BRL Report no. 1970, Ball. Res. Lab., Aberdeen Proving Grounds, Maryland (1975).

25) W. Squire, Integration for Engineers and Scientists, pp. 135-139, American Elsevier Publishing Company, Inc., New York, 1970.

26) B. A. Ridley, M. McFarland, J. T. Bruin, H. I. Schiff, and J. C. McConnell, Can. J. Phys., 55, 212 (1977).

27) R. Boughner, J. C. Larsen, and M. Natarajan, Geophys. Res. Lett., 7, 231 (1980).

28) U.S. Standard Atmosphere 1976, NOAA-S/T-76-1562, GPO, Washington, D.C. (1976).

29) R. Zander, G. M. Stokes, and J. W. Brault, Geophys. Res. Lett., 10, 521 (1983).

30) A. Goldman, F. G. Fernald, F. J. Murcray, F. H. Murcray, and D. G. Murcray, J. Quant. Spec. Rad. Trans., 29, 189 (1982).

31) The Stratosphere 1981: Theory and Measurement, WMO Global Ozone Research and Monitoring Project, Report no. 11, 1982.

Chapter III

SYSTEMATIC ERRORS

3.1 INTRODUCTION

In the previous chapter we determined functional relationships for the uncertainty and the vertical resolution of mixing-ratio profiles retrieved from analysis of synthetic absorber amount data. In order to do this we assumed that the thermal structure of the atmosphere and the orientation of the observing instrument were exactly known. Systematic errors in the parameters necessary to describe the atmospheric structure and the position of the observer will cause additional uncertainties in the retrieved mixing-ratio values. In this chapter we examine the effects of these systematic errors on the retrieval of mixing-ratio profiles from absorber amount data.

Other investigators have examined the effects of errors in the surface pressure, temperature profile and spectral line intensities, the effects of errors due to neglect of refraction and the Doppler shift, and the smearing of spectral data due to the finite field of view of the sun on the interpretation of satellite radiance measurements in order to determine mixing-ratio profiles of atmospheric constituents (1-3) and the atmospheric temperature and pressure profiles (4,5). The effect of error in the atmospheric temperature

profile has also been examined for the retrieval of the CO mixing-ratio profile from solar absorption spectra obtained from balloons (6). No studies have been performed on the effects of systematic errors on the retrieval of mixing-ratio profiles (with no a priori assumptions about the profile shape) from analysis of equivalent width data.

The types of systematic errors considered in this chapter were

1) those due to incorrect physical modeling of the slant path problem,
2) those due to incorrect assumed values for parameters describing the thermal structure of the atmosphere, and
3) those due to incorrect assumed values for parameters describing the orientation of the observing instrument with respect to the earth's surface and the source of the radiation.

The systematic errors in the retrieved mixing-ratios considered in each category were determined by the slant path calculating program (7,8) used for the optical airmass computation. The slant path program, as described in the previous chapter, required the specification of the temperature at discrete altitudes, the pressure at some base level, the apparent zenith angle of the incoming radiation, the altitude of observation, the latitude of observation, and the wavelength of the observed radiation. Thus the Type 1 errors

consisted of spacings of the layer break points so large that the numerical integrations of Eqs. (A.95)-(A.97) were not accurate, and the effects of neglecting atmospheric refraction (included here were errors in the wavelength of the observed radiation since the index of refractions of air given by Edlen's formula (9) is wavelength dependent). The Type 2 errors considered were in the assumed temperature profile and in the assumed sea-level pressure. Type 3 errors included the apparent zenith angle of observation, the altitude of observation, and the latitude of observation. These errors are summarized in Table 14.

As shown in Figure 37, a mixing-ratio profile can be obtained by comparing the absorber amount data along several ray paths to the corresponding optical airmasses along identical ray paths through the atmosphere. For the case of a constant mixing-ratio profile, as shown in Figure 37 b), the mixing-ratio at any altitude can be found by taking the ratio of the absorber amount to the optical airmass for the ray with tangent height corresponding to the desired altitude.* If there is a systematic error in the defining parameters, the optical airmass values are incorrectly determined (see Figure 38). Thus the ratio of the correct absorber amounts to the incorrect airmasses gives the incorrect retrieved

---

*This is not the retrieval method used here. Rather each path is broken into N_R segments and all the N_O data are analyzed simultaneously.

Table 14: The systematic errors considered in this work.

Type 1
due to incorrect modelling of the physical problem
layer thickness
refraction

Type 2
due to incorrect values for defining atmospheric parameters
P(O)
T(A)

Type 3
due to incorrect values for defining observer geometry parameters
A_o
Z_o
ϕ

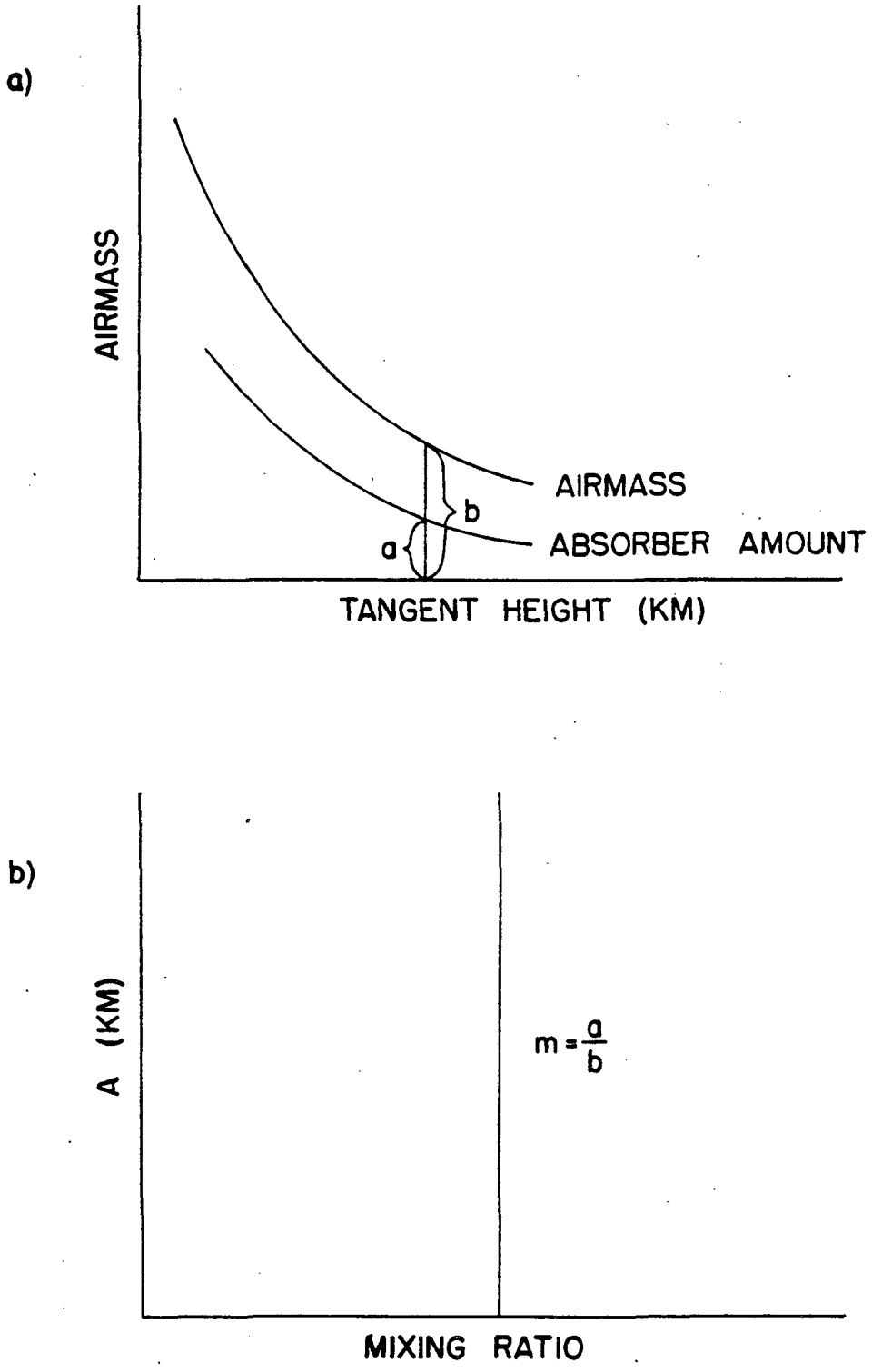

Figure 37: Schematic retrieval of a constant mixing-ratio profile by comparison of the optical airmass to the absorber amount. The mixing-ratio at altitude A in b) is obtained by the ratio of the two curves in a) at tangent height A.

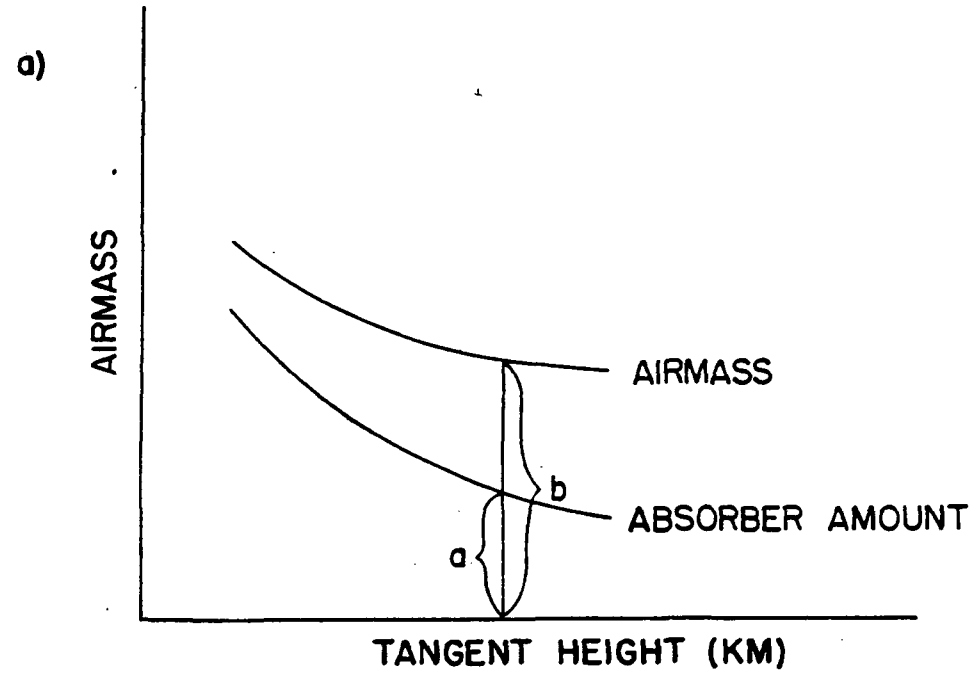

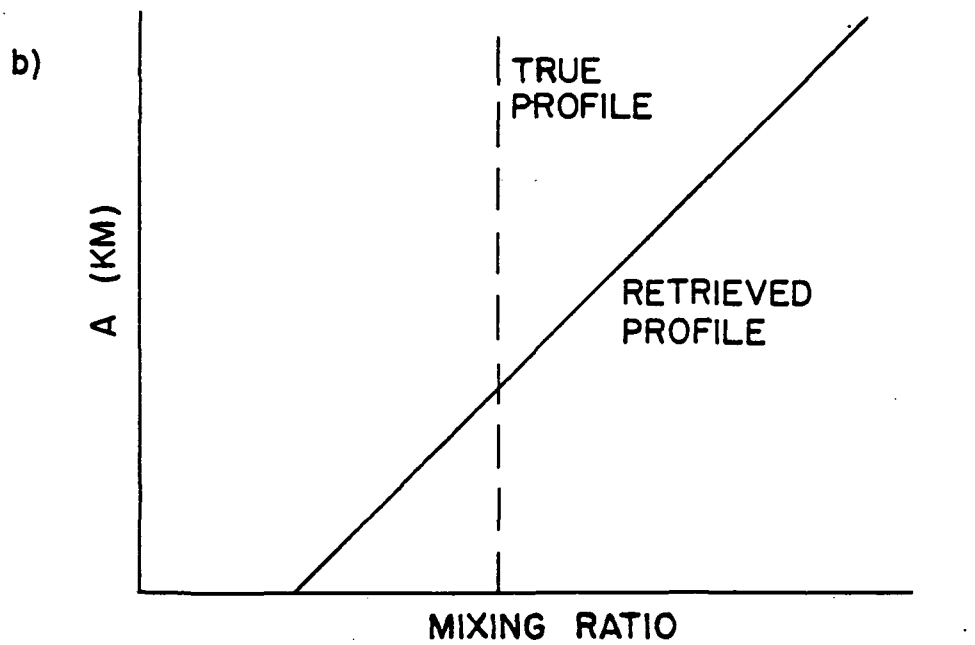

Figure 38: Schematic retrieval of a constant mixing-ratio profile in the presence of a systematic error. The error causes a shift in the optical airmass curve a) which gives an erroneous profile in b).

mixing-ratio profile of Figure 38 b). It is instructive to estimate the error introduced into the retrieved mixing-ratio values by errors in the defining parameters and to estimate the critical altitudes where these errors become smaller than the uncertainty due to experimental noise.

The effects of systematic errors were estimated by analyzing data sets consisting of 125 synthetic absorber amounts, corresponding to rays with 125 different apparent zenith angle values. These absorber amounts were calculated by using the standard values of Table 15 and a mixing-ratio profile which was constant with altitude. No noise was added to these data before the analysis. The a_{ij} values of Eq. (2.70) were calculated assuming an error in each parameter of Table 15 independently. Mixing-ratio values were retrieved by analyzing the synthetic absorber amount data with the linear inversion program (10) described in the previous chapter. The method of analysis used in this work was a direct linear least-squares method which determined all the retrieved mixing-ratio values simultaneously. Unlike other methods, such as the "onion skin peeling" technique (11,12), this precludes the possibility that the effects of the systematic errors are due to errors introduced by the retrieval method. The results obtained agree qualitatively with those predicted by variation of Eq. (2.70) and the use of some simplifying assumptions.

We have considered only the case of a 500 km observer, although the analyses suggest that similar errors can be

Table 15: Standard atmospheric values used for investigation of systematic errors.

Parameter	Assumed value
sea-level pressure	1 atm
temperature profile	U.S. Standard Atmosphere 1976[13]
apparent zenith angles	110° - 112°
observer altitude	500 km
latitude of observer	45°

expected for observers at other altitudes. We have also briefly examined the effects of smearing of the retrieved information due to the motion of the observer (14) or the finite size of the solar disc viewed (15).

In the next section the effects of systematic errors on the calculation of the optical airmass encountered along the ray path are discussed. In the following section we consider the much more interesting problem of the effects of these errors on the retrieved mixing-ratio profiles. In the fourth section estimates are given for the combined error in a mixing-ratio profile and the critical altitude at which the systematic errors are comparable to the uncertainty due to noise. In the final section a method of internally calibrating the data in order to eliminate these errors is described. The relative merits of internal calibration as opposed to using externally determined parameters are discussed.

3.2 THE EFFECTS OF SYSTEMATIC ERRORS ON THE AIRMASS

3.2.1 Type 1 - layer thickness

The calculation time necessary for the analysis can be reduced by decreasing the number of atmospheric layers. This savings may result in a loss of accuracy in the calculation of the optical airmass traversed.

The effects of the layer thickness on the optical airmass calculation were estimated by calculating optical airmasses for the standard values of Table 15 with layer thicknesses

ranging from 25 m to 20 km. Three apparent zenith angles were chosen, corresponding to rays with tangent heights of 48.5 km, 12.0 km and 2.6 km. The percent error in the calculated total optical airmass traversed by the rays was defined as

$$\% \text{ error} = 100\left(\frac{a - a_{25}}{a_{25}}\right) \tag{1}$$

where a_{25} is the optical airmass calculated for a layer thickness of 25 m.

These errors are shown in Figure 39 as a function of the layer thickness. For a tangent height of 2.6 km the error is insignificant for layer thicknesses up to 20 km. However, for a tangent height of 48.5 km a layer thickness larger than 600 m causes errors greater than 1%.

The narrowness of the layers required to maintain accuracy for paths with large tangent heights was unexpected since the atmospheric density above 50 km is three orders of magnitude smaller than that near the earth's surface and the effects of refraction were expected to be negligible. The small layer thickness required for accuracy is believable due to the discontinuities in the assumed temperature profile, shown in Figure 40, near the tangents of 12 and 48.5 km. The assumption that the temperature gradient is constant in the tangent height layer is not true for these tangent heights for layer thicknesses larger than 1 km.

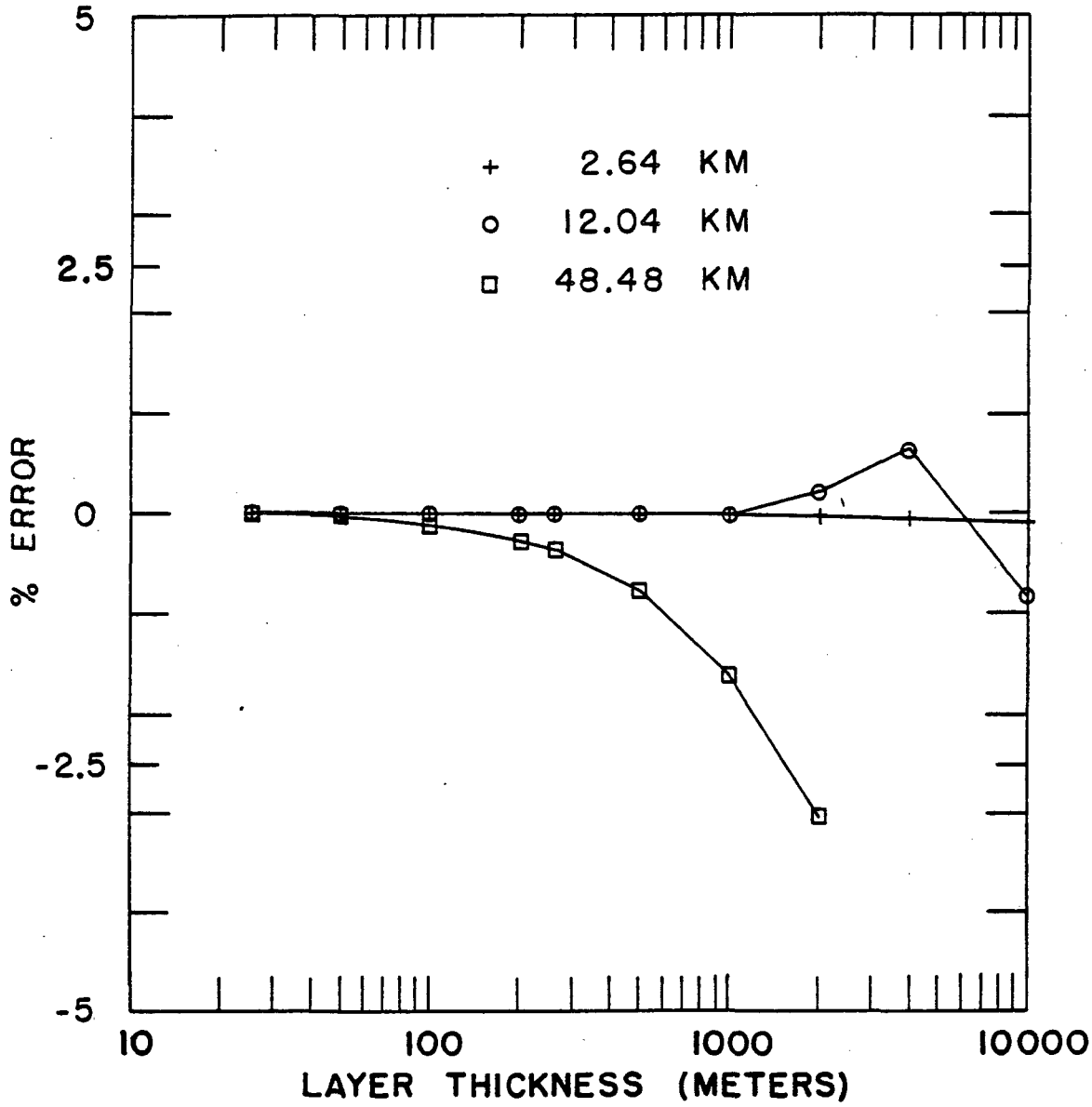

Figure 39: The error in the calculated optical airmass due to improper layer thickness for tangent heights of 2.64, 12.04, and 48.48 km.

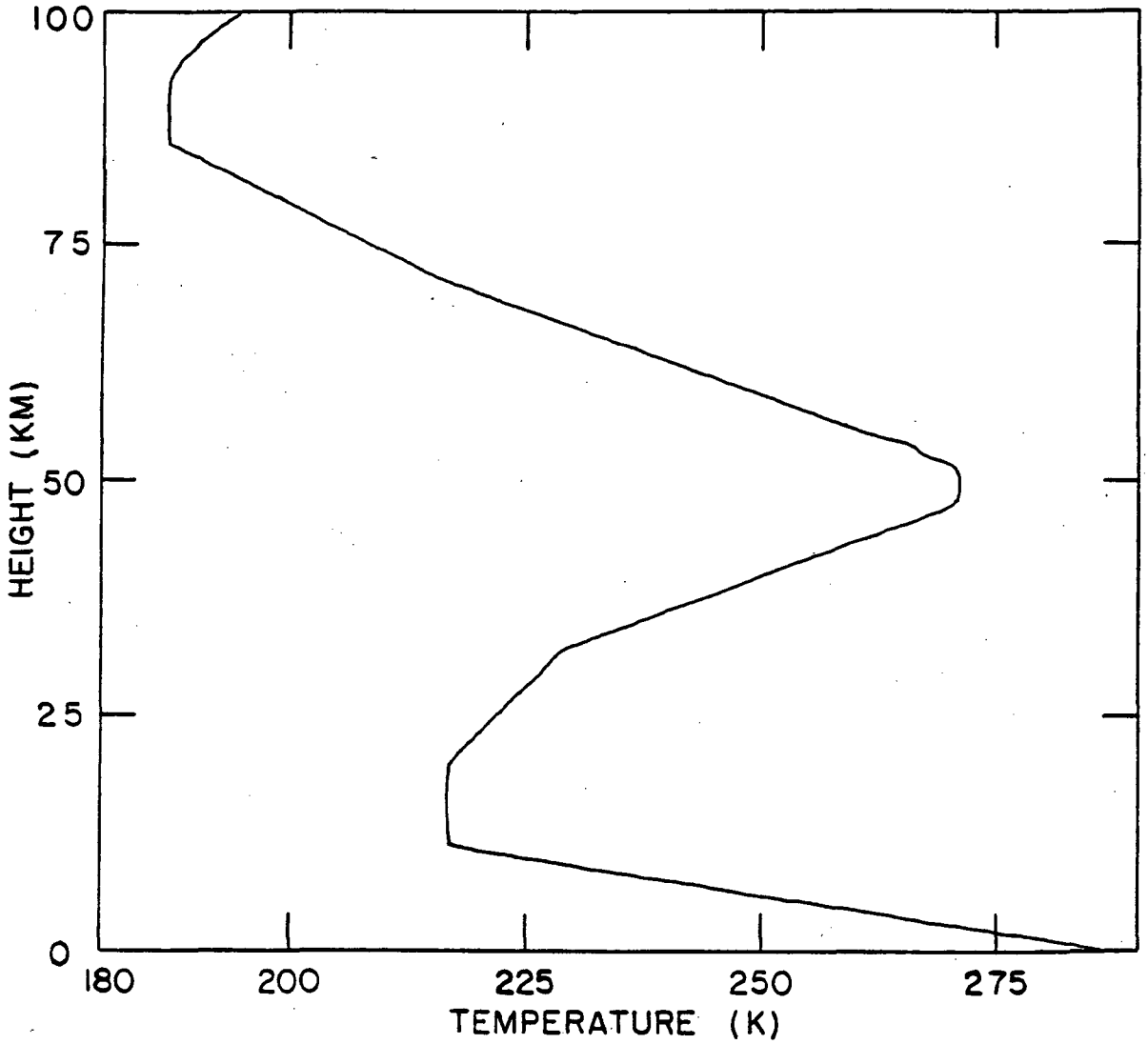

Figure 40: The U.S. Standard Atmosphere 1976.

The consistency of each of the curves in Figure 39 suggests that the round-off errors in the double-precision calculations were small. It also appears that, for a ray with a 2 km tangent height, only 5 layers between 0 and 100 km altitude are required to estimate the total optical airmass accurately although larger relative errors may occur in the airmass along specific segments of the path. For a ray with a 50 km tangent height, a layer spacing of 500 m near the tangent height is required if accuracies of 1% in the total airmass are needed. We have chosen a layer thickness of 250 m for the remainder of the calculations of this section. The problem of a layer thickness which varies with altitude has not been considered.

For the analysis of absorber amount data containing experimental noise the results of the previous chapter suggest that, due to the inherent lack of information contained in the data because of the noise, the layer thickness can often be increased from the values indicated by this analysis. However, the presence of the structural features obtained in the retrievals of a constant mixing-ratio profile (these retrievals are discussed in the next section) imply that even small layer thicknesses can introduce artifacts into the retrieved profile.

3.2.2 Type 1 - refraction index of air

The index of refraction of air is calculated from Edlen's formula and the Lorenz-Lorentz formula (16). For T = 288 K,

P = 1 atm and λ = 5 μm, at sea-level

$$(n_o - 1) = 2.727 \times 10^{-4} \ . \qquad (2)$$

Since $(n - 1) << 1$ at all altitudes, and from the Taylor expansion of the Lorenz-Lorentz formula, $(n - 1)\alpha\rho$, the importance of refraction decreases rapidly with altitude due to the exponential decrease in the air density. Thus it might be expected that refraction has little effect on the path traversed by solar radiation especially at high altitudes.

In order to measure the effects of refraction, the airmass was calculated for the standard values of Table 15 for rays with tangent heights between 0 and 90 km. These values were compared to optical airmasses calculated for the same values of the apparent zenith angle but $(n_o - 1) \equiv 0$. This causes the index of refraction at all altitudes to be identically equal to one. Some of the total airmasses obtained for these conditions are compared in Table 16. The error was calculated for each tangent height by

$$\% \text{ error} = 100 \left(\frac{a_{unref} - a_{ref}}{a_{ref}} \right) , \qquad (3)$$

where a_{unref} was the optical airmass assuming no refraction and a_{ref} was the airmass if refraction was included. The error is shown in Figure 41 as a function of the tangent height of the refracted ray. It is less than 1% for rays with tangent

Table 16: A comparison of slant paths calculated including the effects of refraction to those neglecting refraction.

	Airmass		Tangent Height (km)	
z_o	with refraction	with no refraction	refraction	no refraction
110.0	0.004	0.0004	85.75	85.75
110.2	0.0014	0.0014	77.52	77.52
110.4	0.0048	0.0048	69.20	69.20
110.6	0.015	0.015	60.80	60.80
110.8	0.043	0.043	52.33	52.33
111.0	0.12	0.12	43.77	43.78
111.2	0.42	0.42	35.13	35.15
111.4	1.6	1.6	26.39	26.44
111.6	6.5	6.3	17.46	17.65
111.8	28	24	8.04	8.79

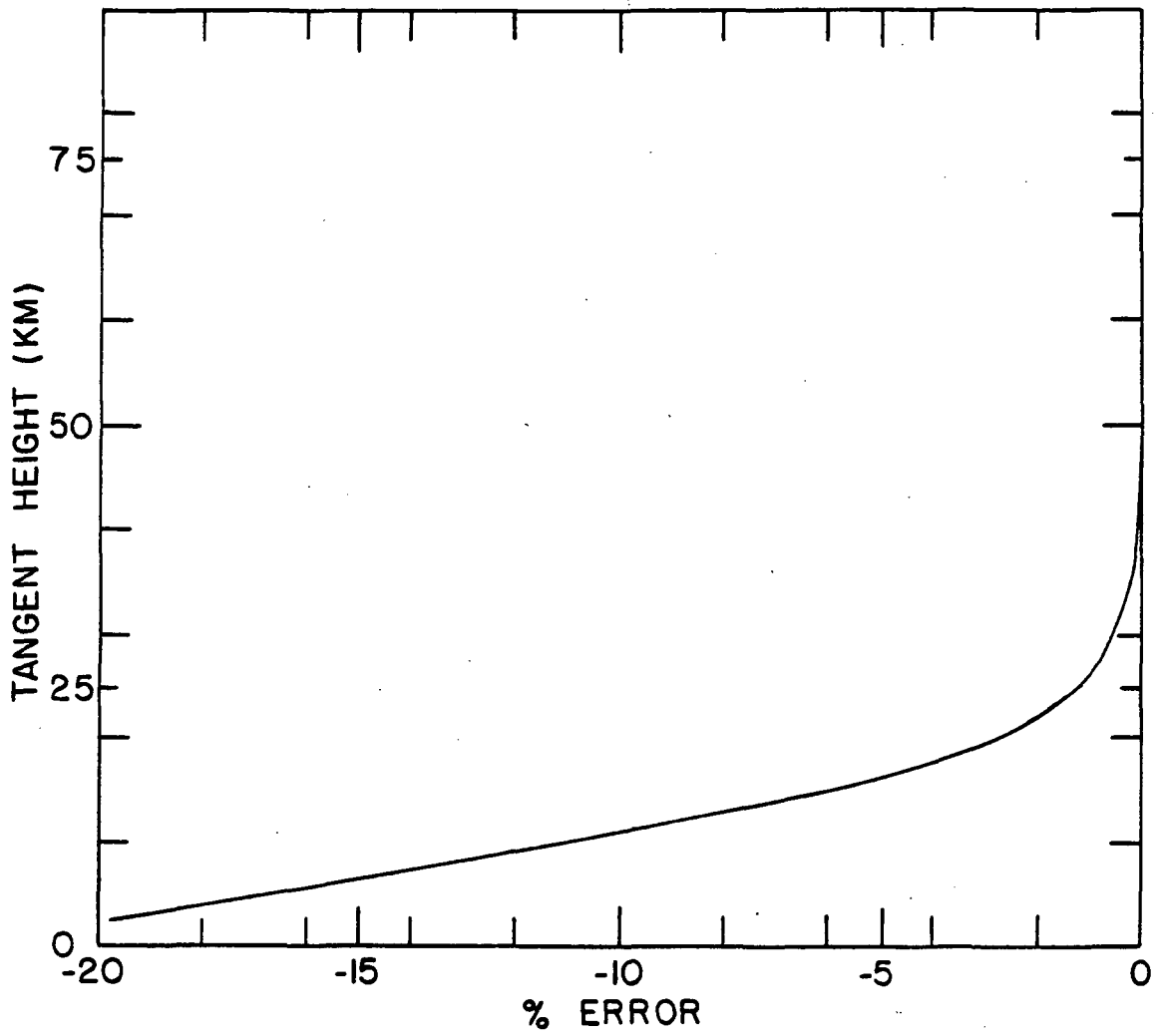

Figure 41: The error in the calculated optical airmass due to neglect of the effects of refraction.

heights above 25 km but it increases rapidly as the tangent height decreases. The small difference in tangent height, between the refracted and unrefracted ray, causes a large change in the optical airmass. Refraction can be ignored above 25 km if accuracies of the order of 1% are sufficient. The results shown in Figure 41 agree qualitatively with those obtained by Snider and Goldman (8) for an observer at 40 km.

Wavelength dependence

Although the wavelength of spectral features can be determined typically to 1 part in 10^6 the path traversed by radiation in the visible spectrum may be substantially different than that traversed by infrared radiation, for rays arriving at the instrument at the same zenith angle, due to the wavelength dependence of the refractive index of air. If the observing instrument is aligned with the sun using the visible image of the sun, the apparent position of the infrared image may be displaced from the visible image.

The effects of changes in the wavelength were estimated by determining the variation of $(n_o - 1)$ between 0.1 μm and 20 μm as shown in Table 17. Over most of the region this variation is less than 1% with respect to the value at 5 μm although it increases rapidly at wavelengths below 0.5 μm.

The systematic errors in total airmass traversed due to changes in the wavelength given by the relation

$$\% \text{ error} = 100\left(\frac{a_\lambda - a_{5\mu m}}{a_{5\mu m}}\right), \qquad (4)$$

Table 17: Some values of $(n_o - 1)$ of Edlen's formula for the reference T_o = 288.16 K, P_o = 1 atm, and various wavelengths.

λ (μm)	$(n_o - 1) \times 10^6$
0.1	701.26
0.2	324.08
0.3	291.56
0.4	282.76
0.5	278.96
0.7	275.79
0.9	274.52
1.0	274.15
2.0	272.98
5.0	272.66
10.0	272.61
20.0	272.60

are shown in Figure 42 as a function of wavelength for three tangent heights (48.5 km, 12 km, and 2.6 km). For rays with tangent heights less than 50 km, the errors were less than 1% for $\lambda > 0.4$ μm. For the infrared region ($\lambda > 0.7$ μm) the error was less than 0.5% for all tangent heights less than 50 km. This implies that if the instrument is aligned with the sun in the visible, then there is little error in the estimated total optical airmass traversed by the infrared radiation by using the apparent zenith angle of visible wavelengths.

3.2.3 Type 2 - sea-level pressure

The optical airmass encountered by a ray passing through the atmosphere is given by

$$a = \sum_{j=1}^{N} \rho_j \delta \ell_j \ , \qquad (5)$$

where ρ_j is the local air density in layer j, $\delta \ell_j$ is the length of the ray path through layer j, and N is the number of layers. If the air density is written as some function f(A) of the altitude

$$\rho_j = \rho(o) f(A_j) \ , \qquad (6)$$

where $f(A_j)$ is a function of temperature and altitude but not of the sea-level density, then Eq. (5) becomes

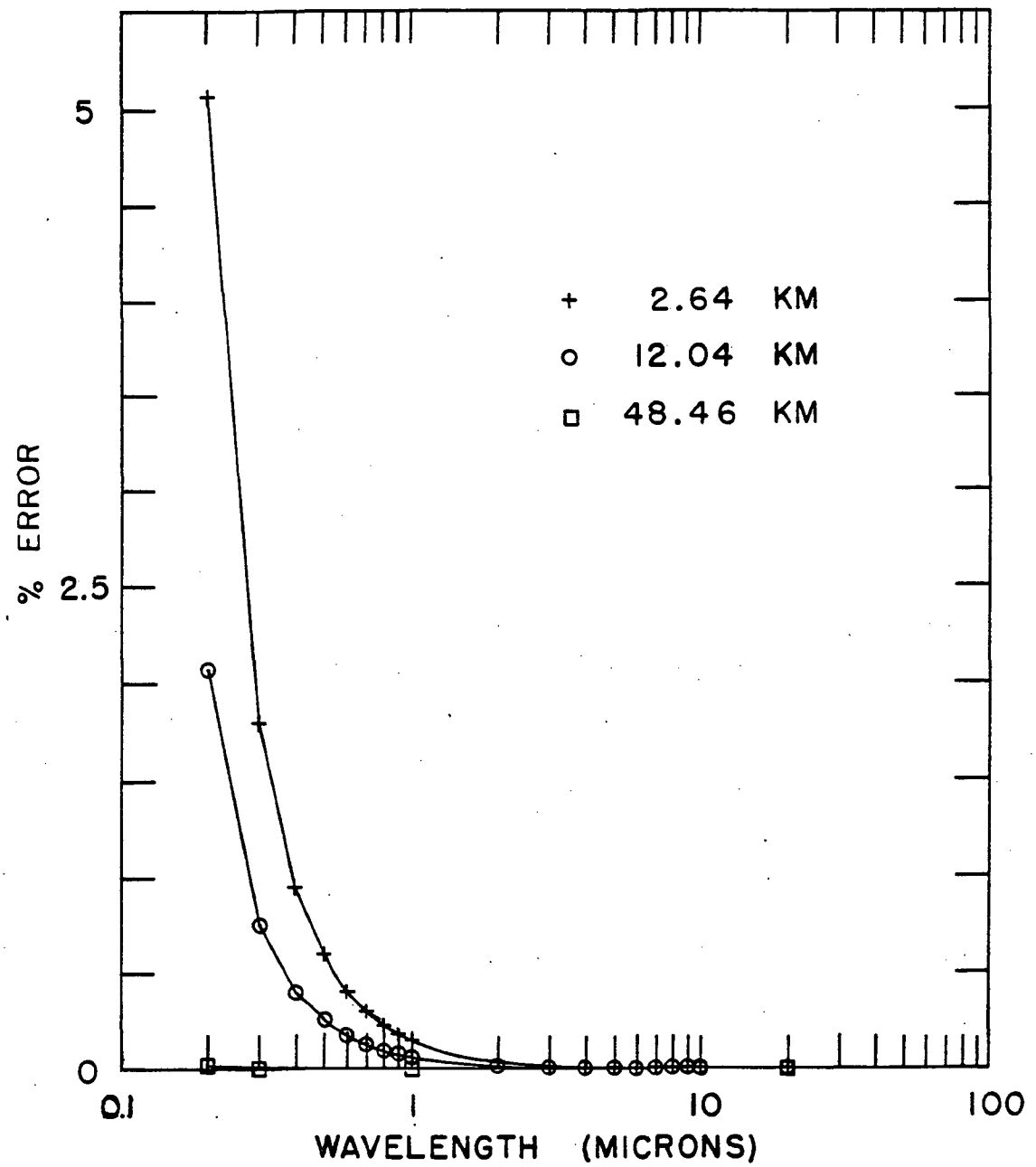

Figure 42: The error in the calculated optical airmass due to error in the radiation wavelength with respect to 5 μm for tangent heights of 2.64, 12.04, and 48.46 km.

$$a = \sum_{j=1}^{N} \rho(o) f(A_j) \delta \ell_j \ . \tag{7}$$

A difference in sea-level density $\Delta\rho(0)$ results in a variation of the optical airmass Δa given by

$$\Delta a = \sum_{j=1}^{N} \Delta\rho(o) f(A_j) \delta \ell_j \ , \tag{8}$$

provided the temperature profile remains constant, or

$$\Delta a = \frac{\Delta\rho(o)}{\rho(o)} \sum_{j=1}^{N} \rho(o) f(A_j) \delta \ell_j \ . \tag{9}$$

Thus the fractional change in the optical airmass is

$$\frac{\Delta a}{a} = \frac{\Delta\rho(o)}{\rho(o)} \ . \tag{10}$$

If we assume that the pressure $P(A)$ at altitude A is given by

$$P(A) = P(o) f(A) \tag{11}$$

then

$$\frac{\Delta\rho(o)}{\rho(o)} = \frac{\Delta P(o)}{P(o)} \tag{12}$$

and

$$\frac{\Delta a}{a} = \frac{\Delta P(o)}{P(o)} \ . \tag{13}$$

Thus if the sea-level pressure is uncertain by x percent the total optical airmass is also in error by x percent. This, of course, does not show the resultant errors in a mixing-ratio profile retrieved using these erroneous airmasses. This problem is dealt with in the next section.

The predictions of Eq. (13) were tested by comparing the optical airmass obtained from the standard values of Table 15 to those obtained for various errors in the base level pressure. The systematic error due to errors in the sea-level pressure was defined by

$$\% \text{ error} = 100\left(\frac{a - a_s}{a_s}\right) \tag{14}$$

where a_s was the total airmass obtained from the standard values, and is shown in Figure 43 for four tangent heights.

As expected, the error in the optical airmass is nearly independent of tangent height for a pressure error of less than 5%. The small increase with decreasing tangent height from the predictions of Eq. (13) are due to the effects of refraction which were not included in Eq. (8). There appears to be little advantage to moving the reference pressure base level up to the tangent height since the error in the calculated optical airmass is essentially independent of the tangent height. In fact, the pressure at the tangent height may be less certain than the corresponding ground-level pressure.

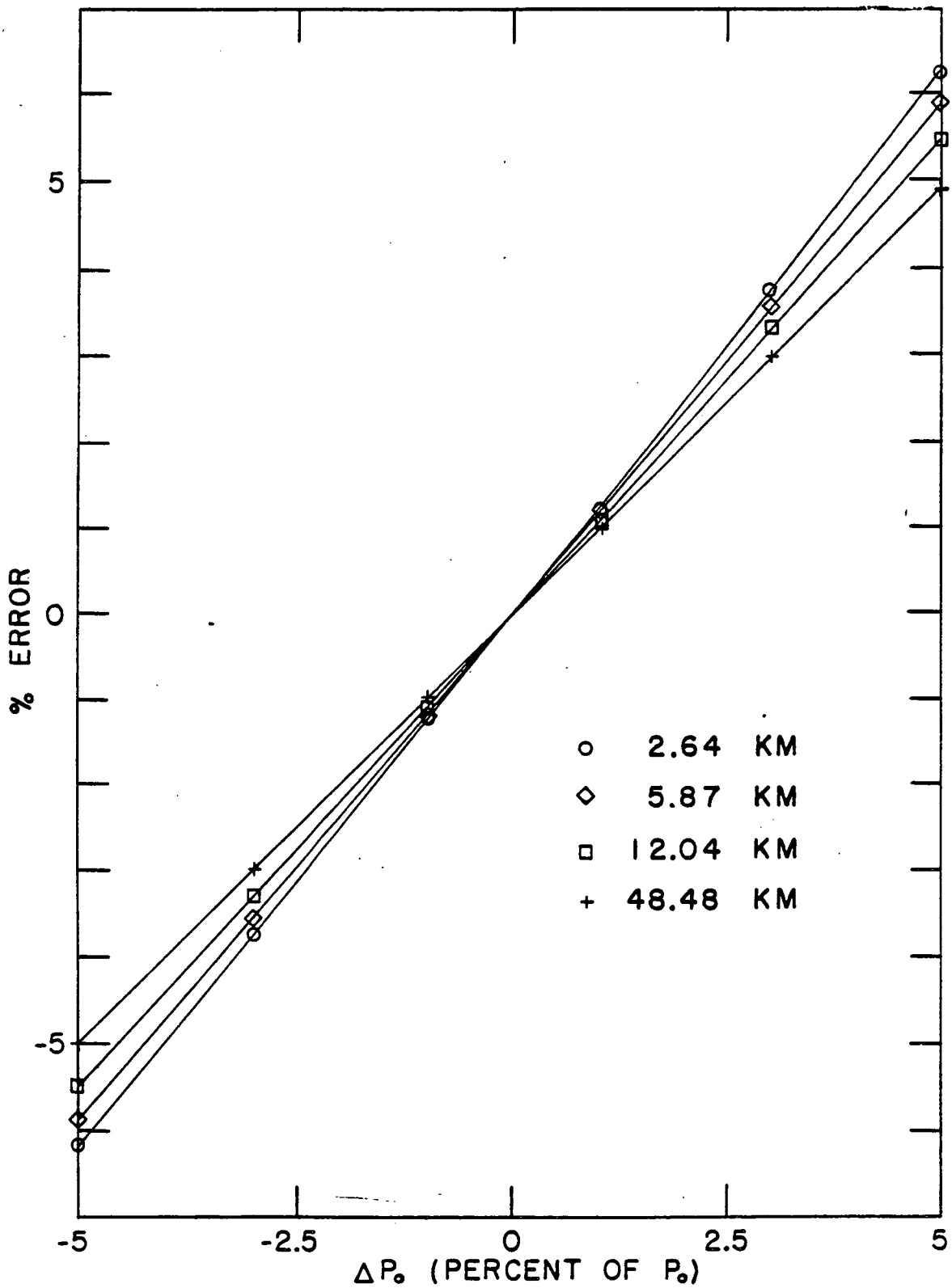

Figure 43: The error in the calculated optical airmass due to error in the sea-level pressure for tangent heights of 2.64, 5.87, 12.04, and 48.48 km.

For the long ray paths through the atmosphere encountered in occultation spectroscopy the sea-level pressure directly below these paths may vary appreciably along the ray path. As shown in Figure 44 the length of the grazing ray path through the lowest 50 km of the atmosphere is approximately 1000 km. As seen in the surface weather map for the United States on April 9, 1980 (17) given in Figure 45, the typical variation of the sea-level pressure over such distances is typically of the order of 5%. Thus from Eq. (13) it is expected that the error in the airmass determination could be as large as 5%.

Because of the rapidly decreasing air density with altitude most of the airmass is encountered in the vicinity of the tangent height. The error in the airmass determination due to base level pressure errors can be reduced by using the base level pressure directly below the tangent height.

3.2.4 Type 2 - temperature profile

Horizontal and seasonal variations

We have assumed that the thermal structure of the atmosphere was correctly represented by the U.S. Standard Atmosphere 1976 and that the structure was "horizontally" uniform along the ray path. As shown in Figure 44, and noted previously, the path length through the lowest 100 km of the atmosphere, for a grazing ray, is approximately 2000 km. This path length corresponds to a maximum latitude change of 10^{o}.

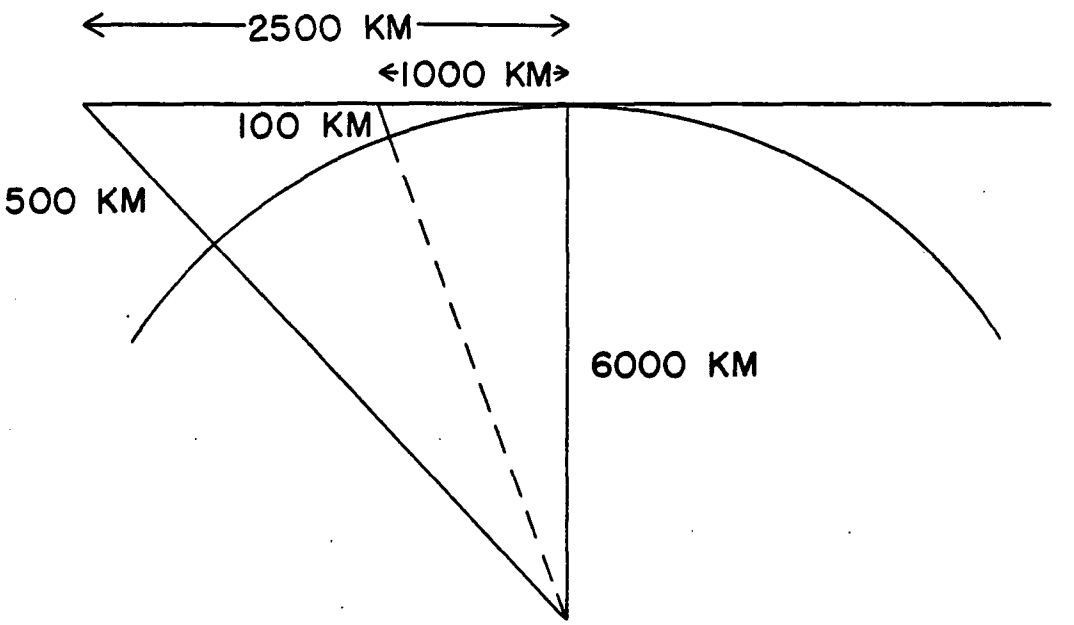

Figure 44: The lengths of grazing ray paths through the atmosphere.

Figure 45: Surface weather map for April 9, 1980 showing the sea-level pressure.

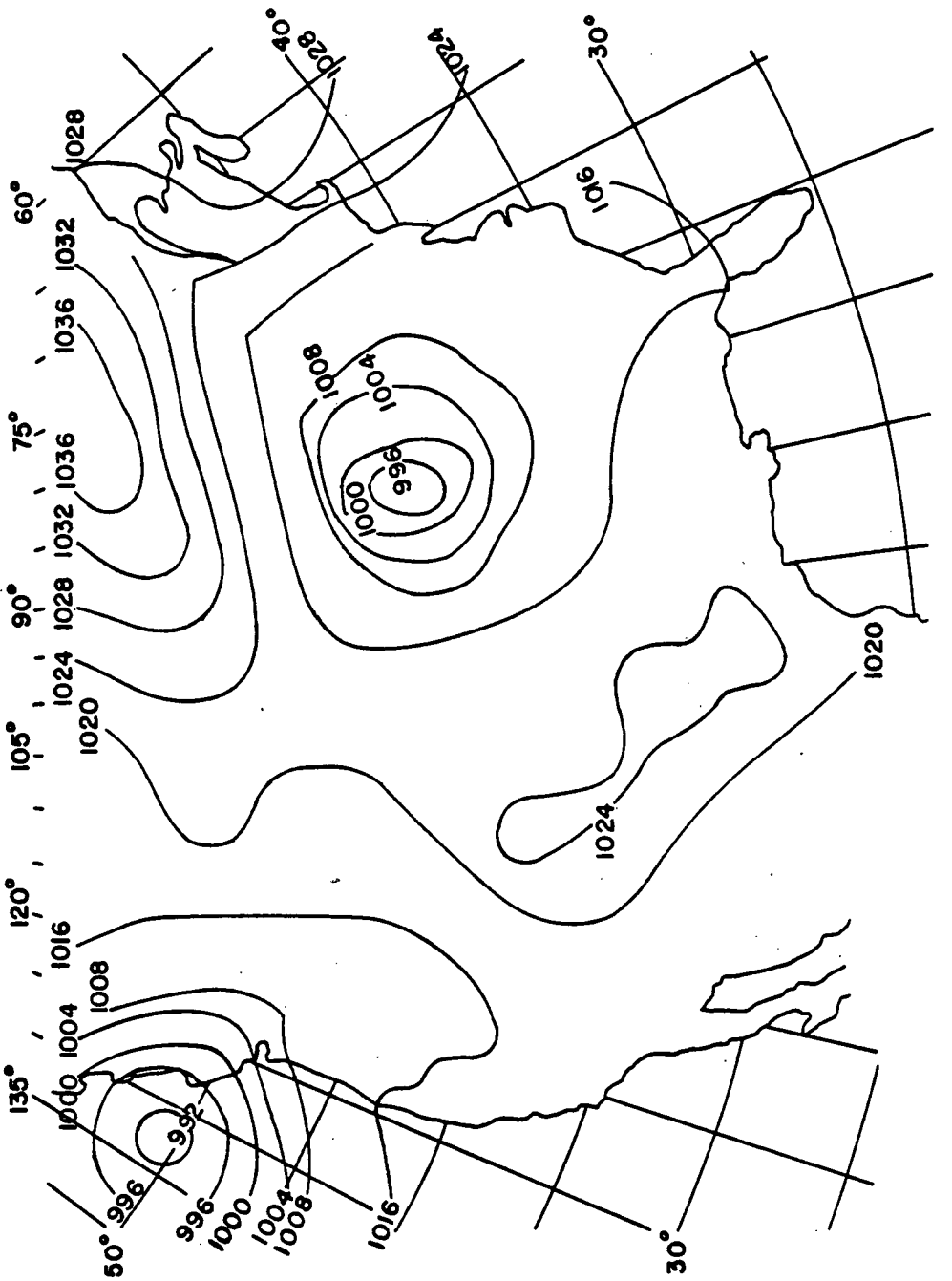
135°
120°
105°
90°
75°
60°
40°
30°
50°
30°
1000
1004
1008
1012
1016
1020
1024
1028
1032
1036
996
992
988

Figure 45

Even in the ideal case, where the atmosphere at some point along the path, preferably the tangent height, is adequately described by the U.S. Standard Atmosphere, departures from this temperature profile can occur along the paths of grazing rays.

Table 18, obtained from Kantor (18), gives the mean monthly latitudinal density gradients for the mid-latitude atmosphere. These density gradients are due both to changes in sea-level pressure and the changing temperature profile. For a 2000 km path length the mean variation of the density at any altitude is about 5% although the instantaneous variation can be much greater.

Errors in the estimated airmass may also arise if an improper atmospheric temperature profile is used. The U.S. Standard Atmosphere, used in this work, represents a yearly mean mid-latitude temperature profile and does not include the seasonal or short-term variations in temperature nor does it describe well the arctic or tropical thermal structure. Listed in Table 19 is a comparison of the U.S. Standard Atmosphere 1976 density profile to the mid-latitude summer and winter, the arctic summer and winter, and the tropical density profiles obtained from the U.S. Standard Atmosphere 1962 (19).

Although these density variations are not entirely attributable to variations in the atmospheric temperature profile, the numbers in Tables 18 and 19 suggest that the error in the estimated optical airmass could be large if the temperature

Table 18: Mean monthly latitudinal density gradients (percent change per 100 nmi) between 30° and 45°N.

Altitude (km)	January Gradient (%)	April Gradient (%)	July Gradient (%)	October Gradient (%)
20	0.66	0.52	0.18	0.47
25	0.03	0.02	0.28	0.14
30	0.14	0.04	0.39	0.08
35	0.44	0.18	0.37	0.27
40	0.81	0.41	0.41	0.44
45	1.04	0.45	0.32	0.77
50	1.13	0.43	0.32	1.05
55	1.14	0.34	0.57	1.14
60	1.28	0.33	0.55	1.01

Table 19: Seasonal and latitudinal variations of the air density at various altitudes.

Height (km)	U.S. Standard 1976	45° Summer 1966	45° Winter 1966	75° Summer 1966	75° Winter 1966	15° Annual 1966
0	1.2250	1.192 -2.7%	1.301 6.2%	1.265 3.3%	1.417 16%	1.167 -4.7%
5	7.3643×10^{-1}	7.211×10^{-1} -2.1%	7.411×10^{-1} 0.6%	7.317×10^{-1} -0.6%	7.518×10^{-1} 2.1%	7.198×10^{-1} -2.3%
10	4.1351×10^{-1}	4.159×10^{-1} 0.6%	4.071×10^{-1} -1.6%	4.036×10^{-1} -2.4%	3.802×10^{-1} -8.1%	4.203×10^{-1} 1.6%
15	1.0476×10^{-1}	2.104×10^{-1} 8.0%	1.890×10^{-1} -3.0%	1.887×10^{-1} -3.1%	1.735×10^{-1} -11.0%	2.260×10^{-1} 16.0%
20	8.8910×10^{-2}	9.453×10^{-2} 6.3%	8.690×10^{-1} -2.3%	9.007×10^{-2} 1.3%	7.797×10^{-2} -12.0%	9.516×10^{-2} 7.0%
30	1.8410×10^{-2}	1.971×10^{-2} 7.1%	1.783×10^{-2} -3.2%	2.023×10^{-2} 9.9%	1.518×10^{-2} -18.0%	1.831×10^{-2} -0.5%
40	3.9957×10^{-3}	4.505×10^{-3} 13.0%	3.625×10^{-3} -9.3%			4.181×10^{-3} 4.6%
50	1.0269×10^{-3}	1.202×10^{-3} 17.0%	8.954×10^{-3} -13.0%			1.101×10^{-3} 7.2%

profile, including the variation along the ray path, is not properly modeled.

Inherent variations of the temperature profile both along the ray path and seasonally make the accurate retrieval of mixing-ratio profiles difficult. One method of avoiding this difficulty is to retrieve a temperature profile from the spectral data to be analyzed. Temperature dependent line intensities and the known mixing-ratio profile of gases such as CO_2 can be used to extract the thermal structure of the atmosphere by analysis of the CO_2 lines in the spectra. It must be noted that the temperature profile thus obtained will be some mean profile over the entire path. Since, as discussed in section 2.4, the retrieved mixing-ratio profile is also a mean over the path, the mean temperature profile obtained from the experimental spectral data is preferable to the use of standard atmospheres.

The previous discussion implies that these errors can be reduced if the temperature profile is determined internally (by using the same spectral data that is used to determine the mixing-ratio profile). The relative advantages of internal calibration over the use of externally determined physical parameters is discussed later in this chapter.

Uncertainty in the temperature profile

The systematic errors due to the inherent error in the temperature profile can be estimated by a simple derivation. Assume that the atmosphere is isothermal and the pressure at

altitude A is given by

$$P(A) = P(o)\exp(-A/H_S) \tag{15}$$

where H_S, the pressure scale height is

$$H_S = \frac{R^*T}{Mg} \ . \tag{16}$$

From Eq. (15) at altitude A a fractional change in pressure ΔP occurs in an altitude change ΔA given by

$$\frac{\Delta P}{P} = -\frac{\Delta A}{H_S} \ . \tag{17}$$

Equation (15) can be written in terms of the temperature by combining it with Eq. (16) yielding

$$P(A) = P(o)\exp(-AMg/R^*T) \ . \tag{18}$$

From Eq. (18) the change in temperature ΔT due to a change in the pressure ΔP is given as

$$\frac{\Delta P}{P} = \frac{AMg\Delta T}{R^*T^2} \ . \tag{19}$$

The ideal gas law gives the density at altitude A as

$$\rho(A) = MP(A)/R^*T \ . \tag{20}$$

A change in density $\Delta\rho(A)$ results in changes in the pressure and temperature given by

$$\Delta\rho(A) = \frac{M\Delta P(A)}{R^*T} - \frac{MP(A)\Delta T}{R^*T^2} , \tag{21}$$

or

$$\frac{\Delta\rho(A)}{\rho(A)} = \frac{\Delta P(A)}{P(A)} - \frac{\Delta T}{T} . \tag{22}$$

Combining Eqs. (17) and (22) yields

$$\frac{\Delta\rho(A)}{\rho(A)} = \frac{A\Delta T}{H_S T} - \frac{\Delta T}{T} , \tag{23}$$

or

$$\frac{\Delta\rho(A)}{\rho(A)} = \frac{(A - H_S)\Delta T}{H_S T} . \tag{24}$$

Since, from Eq. (10), the fractional change in density equals the fractional change in the calculated optical airmass Eq. (24) becomes

$$\frac{\Delta a}{a} = \frac{(A - H_S)\Delta T}{H_S T} . \tag{25}$$

Thus, for an isothermal atmosphere uncertain by amount ΔT, the error in the estimated optical airmass will be zero at an altitude equal to the scale height.

The error due to temperature error in the U.S. Standard Atmosphere was investigated by comparing optical airmasses, corresponding to several tangent heights, calculated using the standard values of Table 15 to those obtained using identical values with the U.S. Standard Atmosphere profile incremented at all altitudes by ±5 K. Some of the results from this comparison are listed in Table 20 together with the errors predicted by Eq. (25).

As expected a change in sign of the error occurs near the scale height. The errors obtained for $\Delta T = \pm 5$ K agree well with those predicted by Eq. (25). The small differences are attributed to the non-isothermal structure of the atmosphere used.

3.2.5 Type 3 - observer altitude

As shown in Figure 46 an error in the altitude ΔA_o of the observing instrument results in an error in altitude along the entire path of approximately $\Delta A_o \sin Z_o$ or

$$\Delta A \simeq \Delta A_o \sin Z_o \ . \qquad (26)$$

Previously it was noted that the fractional decrease in pressure for an increase in altitude is given by Eq. (17). Equivalently an increase in altitude ΔA will result in a decrease in pressure ΔP given by

Table 20: Error in computed optical airmass for systematic temperature error of ±5 K at all altitudes.

Z_o	Tangent Height (km)	Airmass computed for standard values	Fractional error in airmass computed assuming systematic error		Fractional error predicted from Eq. (25)
			$\Delta T = 5$ K	$\Delta T = -5$ K	
110.95	45.9	0.14	0.14	-0.13	0.10
111.08	40.3	0.25	0.12	-0.12	0.093
111.21	34.7	0.50	0.11	-0.10	0.085
111.34	29.0	1.1	0.087	-0.083	0.070
111.46	23.7	2.5	0.065	-0.066	0.052
111.59	17.9	6.1	0.044	-0.046	0.035
111.72	11.9	16.0	0.025	-0.023	0.016
111.84	6.08	37.0	-.0014	-0.0033	-0.003
111.91	2.53	57.0	-0.0083	0.0083	-0.012

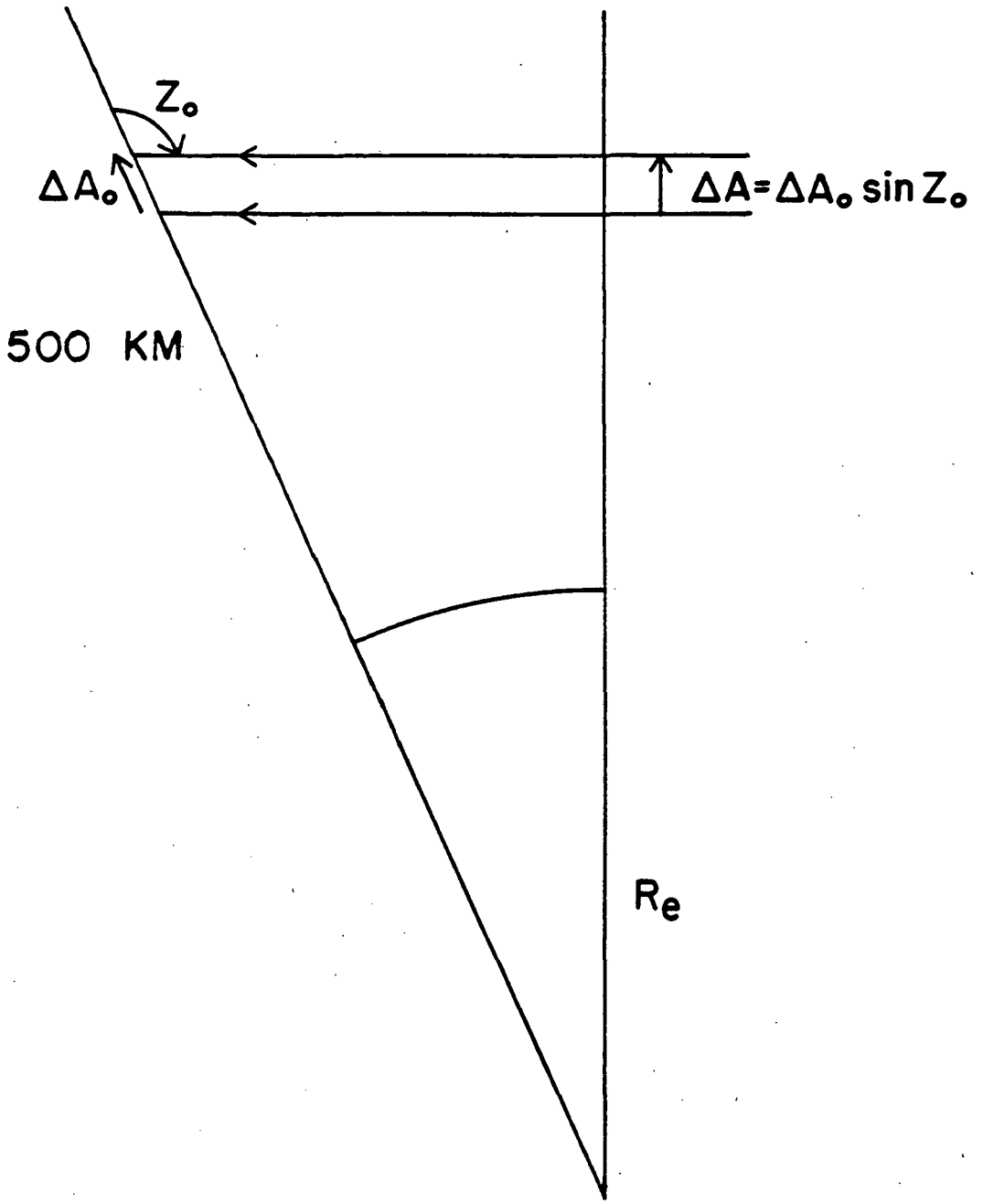

Figure 46: The effect of observer altitude error on the tangent height.

$$\frac{\Delta P}{P} = - \frac{\Delta A_o \sin Z_o}{H_s} \quad . \tag{27}$$

The optical airmass encountered along a ray path increases proportionately if the pressure increases (see Eq. (13)). Therefore

$$\frac{\Delta a}{a} = - \frac{\Delta A_o \sin Z_o}{H_s} \quad . \tag{28}$$

Thus for a particular apparent angle and an isothermal atmosphere the fractional error in the estimated optical airmass traversed by a ray is proportional to the error in the observer altitude.

This relation was examined by comparing the optical airmass calculated from the standard values of Table 15 to airmasses calculated using identical values but with different observer altitudes ranging from 499.5 km to 500.5 km. In these cases the maximum error in the airmass, from Eq. (28), should be 6.6%. Results obtained for three tangent heights are shown in Figure 47. The larger than expected error for the 21.96 km tangent height is probably due to departures of the standard atmosphere temperature profile from isothermal near the tangent height of this ray. The smaller error obtained for $+\Delta A_o$ as compared to $-\Delta A_o$ is believed to be due to refractive effects not considered in the derivation of Eq. (28).

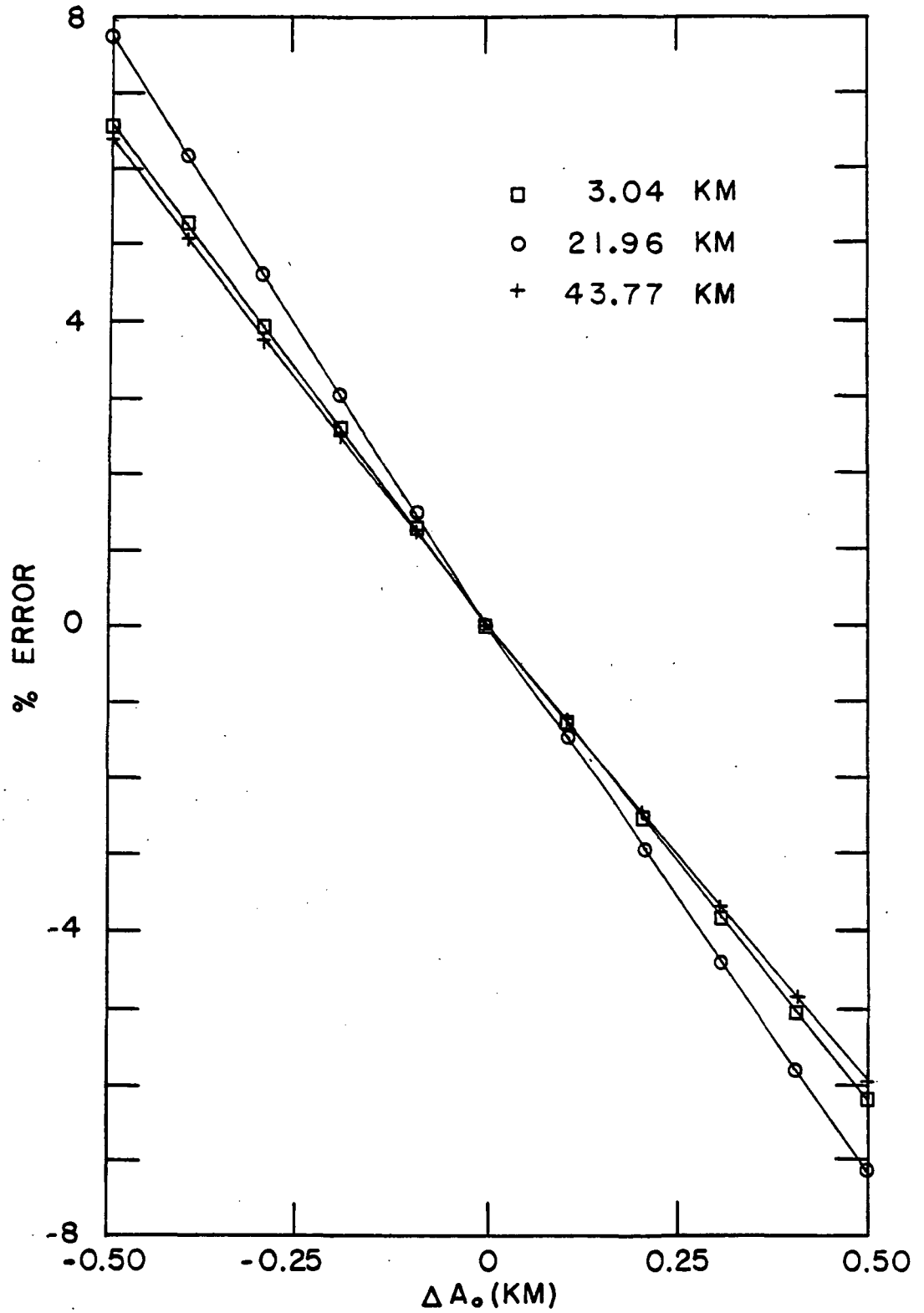

Figure 47: The error in the calculated optical airmass due to error in the observer altitude for tangent heights of 3.04, 21.96, and 43.77 km.

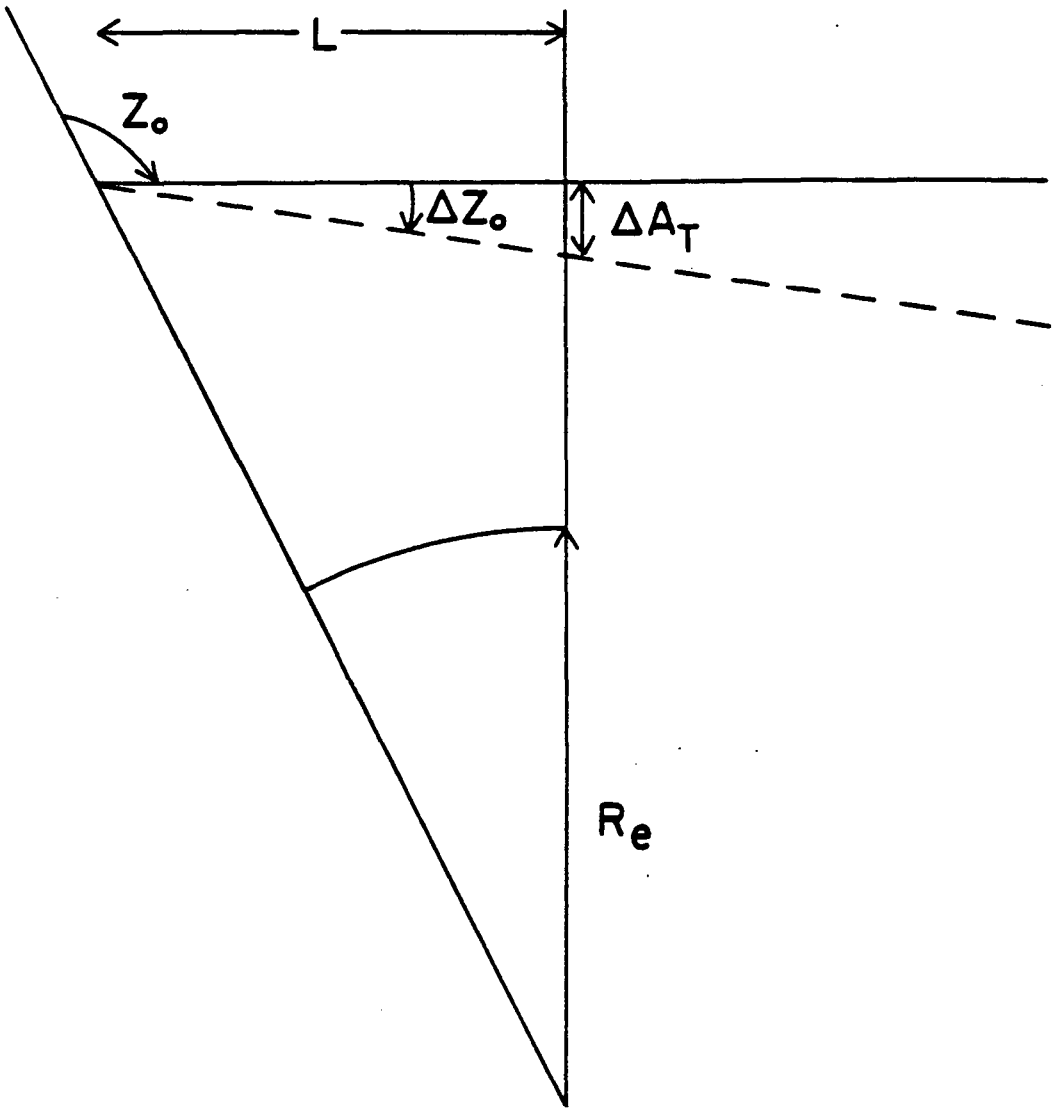

Figure 48: The effect of apparent zenith angle error on the tangent height.

Thus for an observer altitude of 500 km, errors of 0.5 km in the altitude of observation result in errors of 6.6% in the calculated optical airmass. In order to maintain 1% error in the estimated optical airmass this altitude must be known to within 75 m, suggesting that high precision is necessary in determining the satellite height.

3.2.6 Type 3 - apparent zenith angle

In practice the apparent zenith angle used in the slant path calculation is not usually measured directly. This angle can be determined from the geometry of the orbit by recording the time of observation and the portion of the solar disc viewed. If refraction is included the apparent zenith angle can then be calculated. Estimates of the effects of time error on the estimation of the optical airmass can be made from consideration of the errors in the apparent zenith angle.

If there is an error ΔZ_o in the measurement of the apparent zenith angle the true tangent height of the ray is shifted by ΔA_T (see Figure 48). If ΔZ_o is small then

$$\Delta A_T \simeq -L\Delta Z_o \qquad (29)$$

where L, the path length between the tangent height and the observer, is approximately 2500 km for a 500 km observer altitude. Combining Eqs. (13), (17), and (29) gives

$$\frac{\Delta a}{a} = L \frac{\Delta Z_o}{H_s} \quad . \tag{30}$$

Thus due to the long path lengths for an observer altitude of 500 km, an error of about 0.2 milliradians results in an error of about 7% in the airmass calculation. The errors due to the inherent error of the apparent zenith angle are large for any satellite experiment.

The effects of apparent zenith angle errors were examined by comparing the optical airmass calculated for the standard values of Table 15 to those obtained using identical values and an incremented apparent zenith angle. Some results, shown in Figure 49, were obtained for three different tangent heights. The error predicted from Eq. (30) for an apparent zenith angle error of 0.01^{o} is 6.2% for all three tangent heights. The variations seen in Figure 49 between the three tangent heights, which were not predicted by Eq. (30), are probably due to the temperature variation with altitude of the standard atmosphere. The asymmetry, about $\Delta Z_o = 0$, is believed to be due to the effects of refraction not included in this derivation.

Smearing due to observer motion and the field of view

For the case of a satellite-borne instrument, which moves in orbit during the time necessary to complete one occultation, the optical airmass encountered by rays reaching the instrument at the end of the collection period will be substantially different than that encountered by

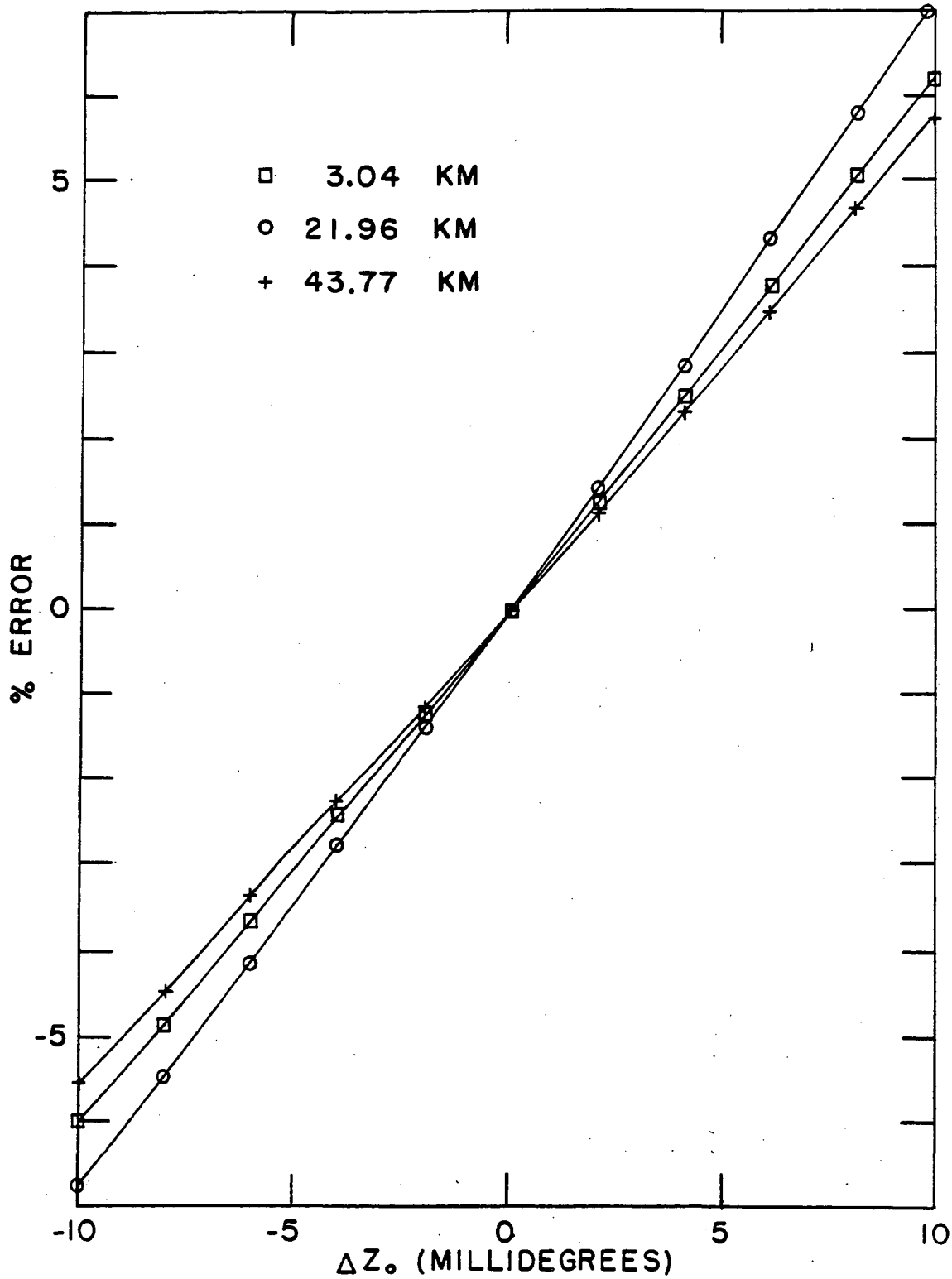

Figure 49: The error in the calculated optical airmass due to error in the apparent zenith angle for tangent heights of 3.04, 21.96, and 43.77 km.

rays at the beginning of this period. Park (14) has shown that for the collection of an interferogram this results in the information about the spectral line strengths and the spectral line half-widths being obtained from rays which traverse different portions of the atmosphere. In addition, because of the finite size of the solar disc viewed by the instrument, rays which reach the instrument at identical apparent zenith angles may have different tangent heights (15). The effects of smearing of the spectral information due to motion of the observer and the finite field of view can be approximated by systematic errors in the apparent zenith angle.

This can be demonstrated by use of Kepler's laws. We have assumed, in order to obtain an estimate of the smearing due to satellite motion, that the orbit of the satellite is circular, coplanar with the sun, a height A above a spherical earth of radius R_e. If the source of radiation is assumed, for now, to be a point source at infinity, the change in apparent zenith angle ΔZ_o of the incoming radiation is equal to the change in polar angle $\Delta\theta$ of the satellite, as shown in Figure 50. Thus ΔZ_o is given by

$$\Delta Z_o = 2\pi\frac{\Delta t}{t_e} , \qquad (31)$$

where Δt is the time necessary for the satellite to move angular distance $\Delta\theta$ and t_e is the period of the satellite

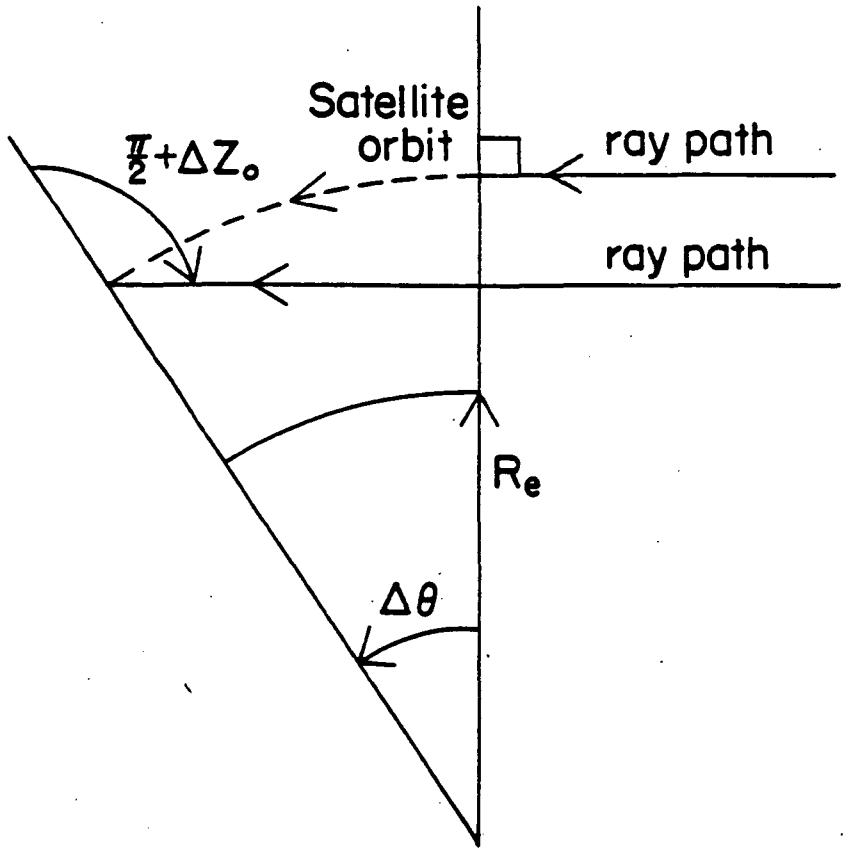

Figure 50: The orbital geometry of a moving satellite observer. The apparent zenith angle of observation changes by ΔZ_o for a change $\Delta\theta$ in the orbital position.

orbit. The period of the orbit is given by Kepler's laws. Therefore the rate of change of the apparent zenith angle is

$$\frac{\Delta Z_o}{\Delta t} = \frac{\sqrt{GM_e}}{(R_e + A_o)^{3/2}} \tag{32}$$

where M_e is the mass of the earth.

The rate of change of the optical airmass encountered by rays reaching the instrument during an occultation was estimated by calculating the optical airmasses for apparent zenith angles determined from Eq. (32) for a constant time spacing $\Delta t' = 0.1$ sec. The optical airmass was computed for the standard values of Table 15. The fractional rate of change of the optical airmass was defined as

$$F = \frac{a_{Z_{o(t)}} - a_{Z_{o(t + \Delta t')}}}{a_{Z_{o(t)}} \Delta t'} \tag{33}$$

where the units of F are $sec.^{-1}$ The values of $F(Z_o)$, shown in Figure 51, were obtained for the U.S. Standard Atmosphere. The rate of change of the airmass depends on the tangent height but is not less than 30%/sec.

The structure of the $F(Z_o)$ curve is due to the temperature variation of the standard atmosphere, shown in Figure 40. The dependence of $F(Z_o)$ on the temperature profile was demonstrated by repeating the computations of Eqs. (32) and (33) using instead a temperature profile which decreased

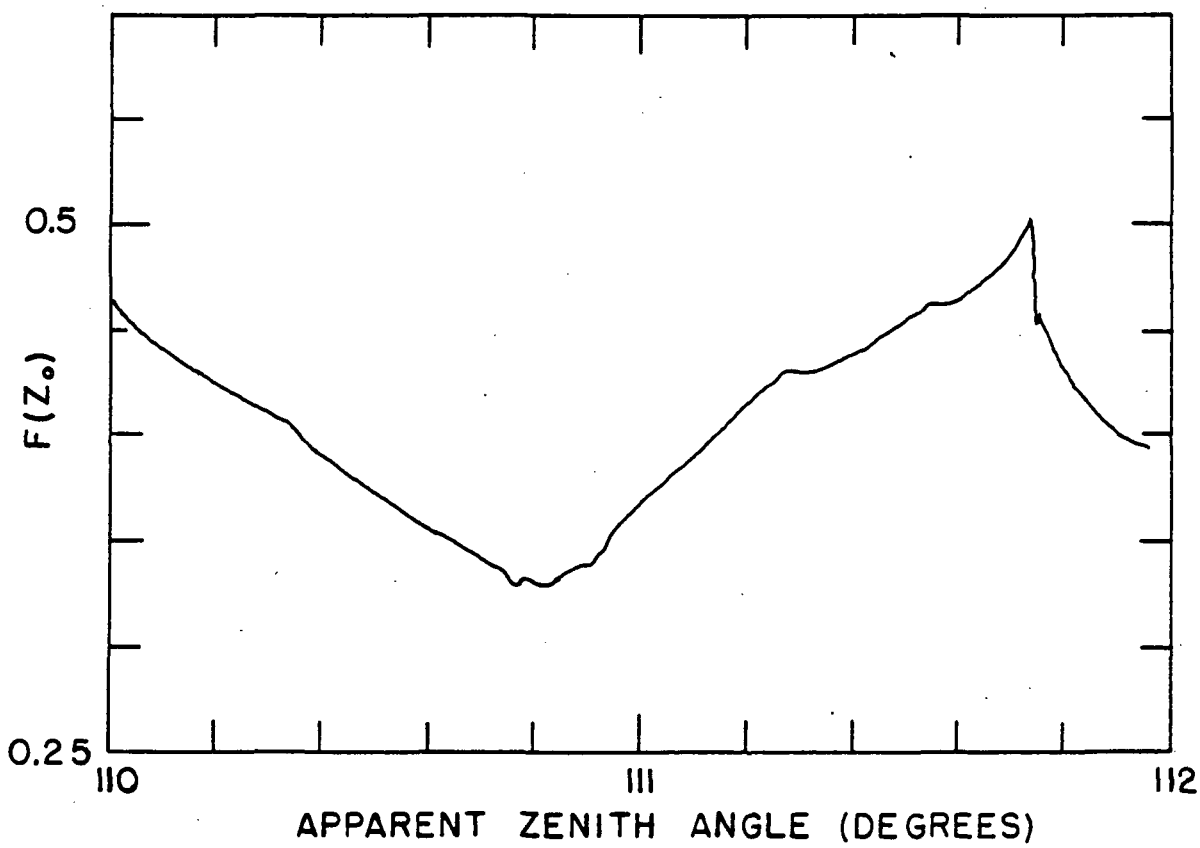

Figure 51: The fractional time rate of change of the optical airmass for a moving satellite observer and the standard atmospheric values as a function of apparent zenith angle. The tangent height range is 80 km to ground level.

linearly with altitude. The values of $F(Z_o)$, shown in Figure 52, were obtained for this temperature profile. The $F(Z_o)$ determination was also made for the case of the U.S. Standard Atmosphere temperature profile but no atmospheric refraction. These values, shown in Figure 53, demonstrate that the shape of the $F(Z_o)$ curve depends only on the atmosperhic temperature profile. This suggests that, in order to estimate this rate of change and therefore the effect of this smearing on the spectral data, the temperature profile must be accurately known.

In addition, for satellite occultation experiments such as ATMOS, the field of view of the instrument is 2 milliradians and thus, from Eq. (30), the variation in the optical airmass traversed by arriving rays can be as great as 70%.

The effects of smearing due to the motion of the observer and the finite field of view are larger than would be expected from errors in the apparent zenith angle alone, and these effects are not easily eliminated from the spectral data. However, the smearing effects on individual lines in a single spectrum are identical (for weak lines). Thus it is possible by comparison of spectral lines resulting from an absorber with a known mixing-ratio profile to spectral lines resulting from an absorber with unknown distribution to eliminate these weighting effects in the mixing-ratio profile determination of the unknown absorber. This method of internal calibration is discussed fully later in this chapter.

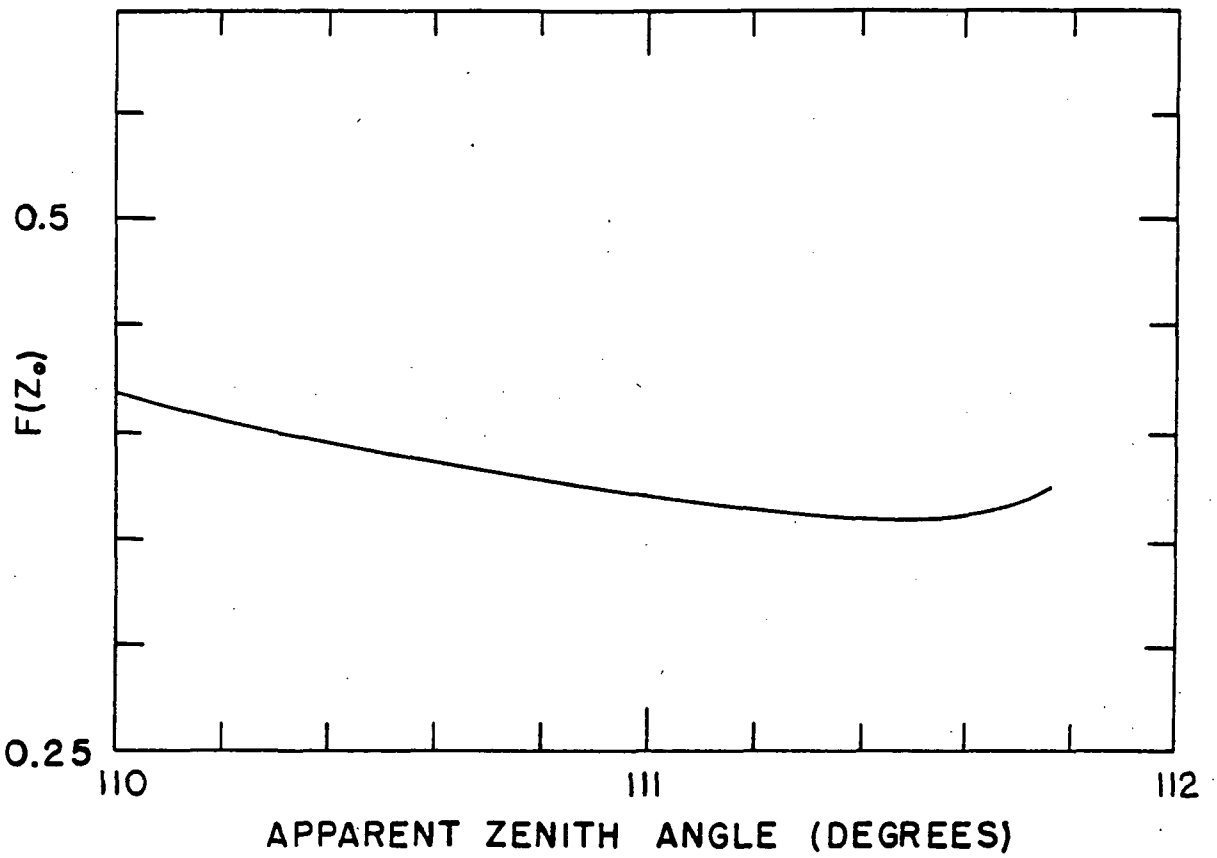

Figure 52: The fractional time rate of change of the optical airmass for a moving satellite observer and a temperature profile which increases linearly with altitude as a function of apparent zenith angle.

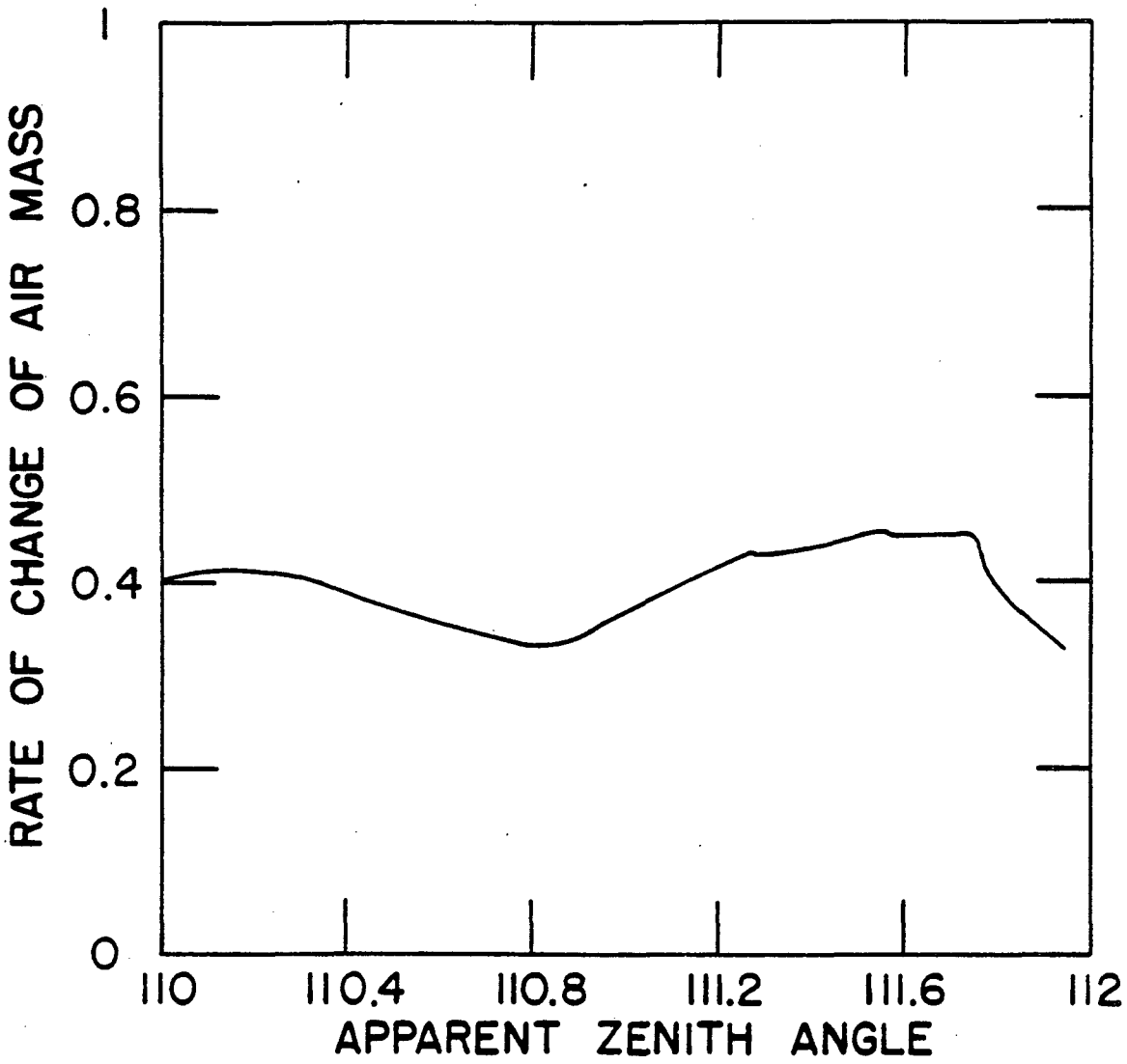

Figure 53: The fractional rate of change of the optical airmass, for a moving satellite observer and assuming no atmospheric refraction, as a function of apparent zenith angle.

3.2.7 Type 3 - latitude

The shape of the earth is a nearly spherical ellipsoid. Since the long atmospheric path lengths for a 500 km observer altitude may result in latitude changes between the observer and the tangent height as large as 10^{o}, it is important to know the magnitude of the errors resulting from changes in latitude along the ray paths.

The change in optical airmass due to changes in the earth's latitude or equivalently the earth's radius can be estimated by starting with Fermat's principle (Eq. (A.1) of Appendix A)

$$n_o r_o \sin Z_o = n_T r_T \tag{34}$$

where

$$r_T = A_T + R_e \ . \tag{35}$$

If refraction is neglected Eq. (34) becomes

$$(A_o + R_e)\sin Z_o = A_T + R_e \ . \tag{36}$$

A change in radius ΔR_e results in a change in tangent height ΔA_T given, from Eq. (36), by

$$\Delta A_T = (\sin Z_o - 1)\Delta R_e \ . \tag{37}$$

Combining Eqs. (12), (17), and (37) yields

$$\frac{\Delta a}{a} = \frac{(1 - \sin Z_o)\Delta R_e}{H_s} \quad . \tag{38}$$

The radius of curvature of the earth is given as a function of latitude by (20)

$$R_e(\phi) = \left\{ \frac{c^4 \cos^2\phi + b^4 \sin^2\phi}{c^2 \cos^2\phi + b^2 \sin^2\phi} \right\}^{\frac{1}{2}} \tag{39}$$

where

$$c = 6378.160 \text{ km} \tag{40}$$

and

$$b = 6356.775 \text{ km} \quad . \tag{41}$$

Thus the fractional error in the airmass can be expressed as a function of latitude by using Eq. (38). The change in optical airmass for a latitude change from 45^o to 55^o is found to be 3.3%. The maximum error in using a latitude of 45^o rather than the true latitude is found to be 10%. Though not large in magnitude for reasonable latitude errors ($\pm 5^o$) higher precision retrievals may be obtainable if the effect of the changing earth's radius is modeled.

The validity of Eq. (38) was tested by varying the earth's latitude with respect to 45^{o}. The error obtained in the optical airmass for the standard value of Table 15 is shown in Figure 54 for rays with four tangent heights. These errors are much larger than those predicted by Eq. (38), although the shapes of the curves agree with that predicted by Eq. (38). Figure 55 shows ΔR_e as a function of latitude, which exhibits the same dependence as the error curves of Figure 54. Similar error curves, but with a much smaller amplitude, shown in Figure 56, were obtained for an observer altitude of 50 km. The large dependence of the amplitude on the observer height suggests that the amplitude of the error curves is incorrect although the functional form is consistent. It is believed that the large amplitude for observers above 50 km is due to an error in the tangent height calculation algorithm used in the slant path calculation (8). This error is not expected to alter any of the other results obtained in this work.

3.2.8 Summary

In this section we have estimated the errors introduced into the determination of the optical airmass traversed by a ray passing through the atmosphere due to improper layer thickness in the calculation, neglect of the effects of refraction, errors in the sea-level pressure, the atmospheric temperature profile, the observer altitude, the apparent

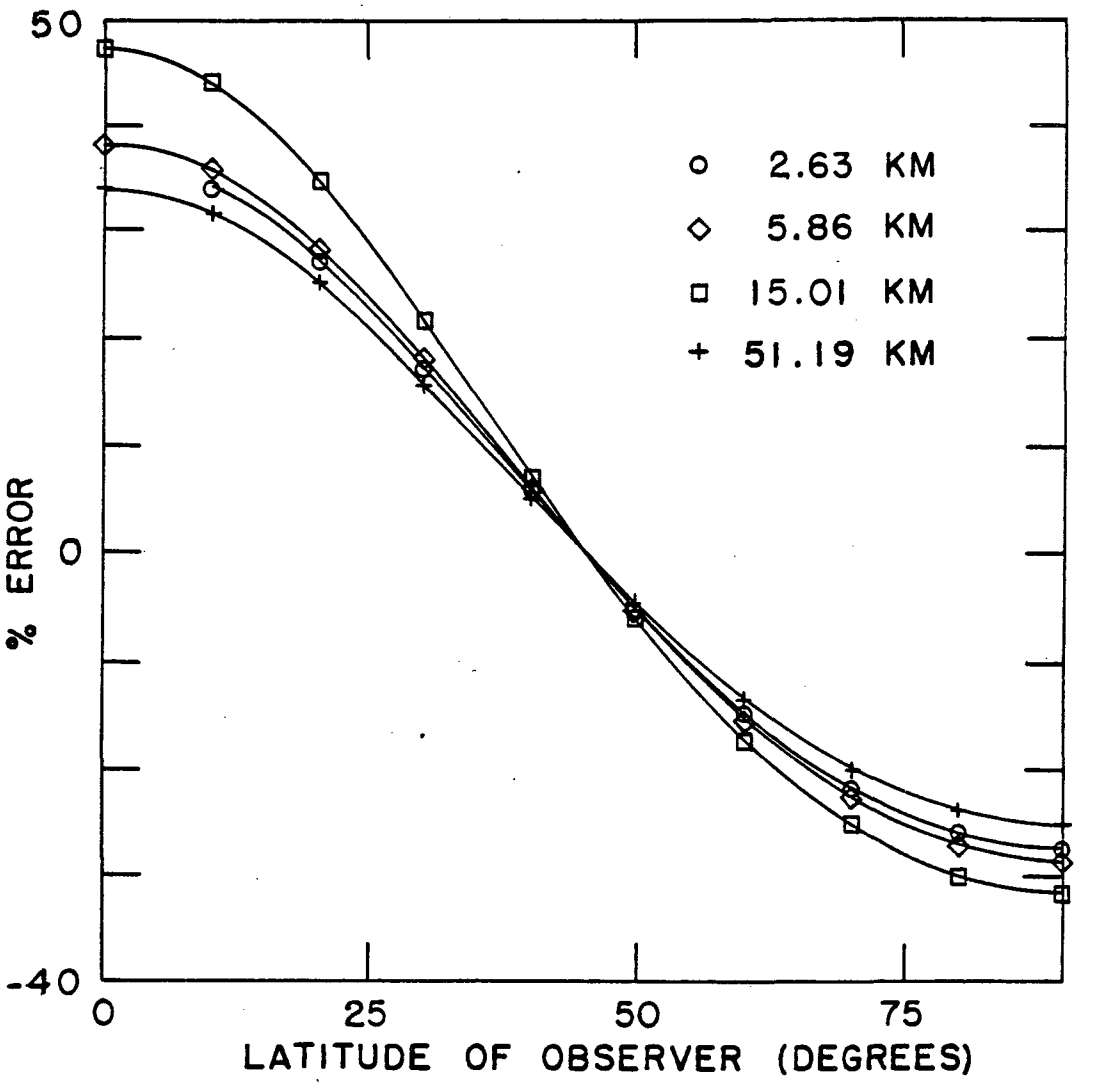

Figure 54: The error in the calculated optical airmass due to error in the latitude with respect to 45° for tangent heights of 2.63, 5.86, 15.01, and 51.19 km and an observer altitude of 500 km.

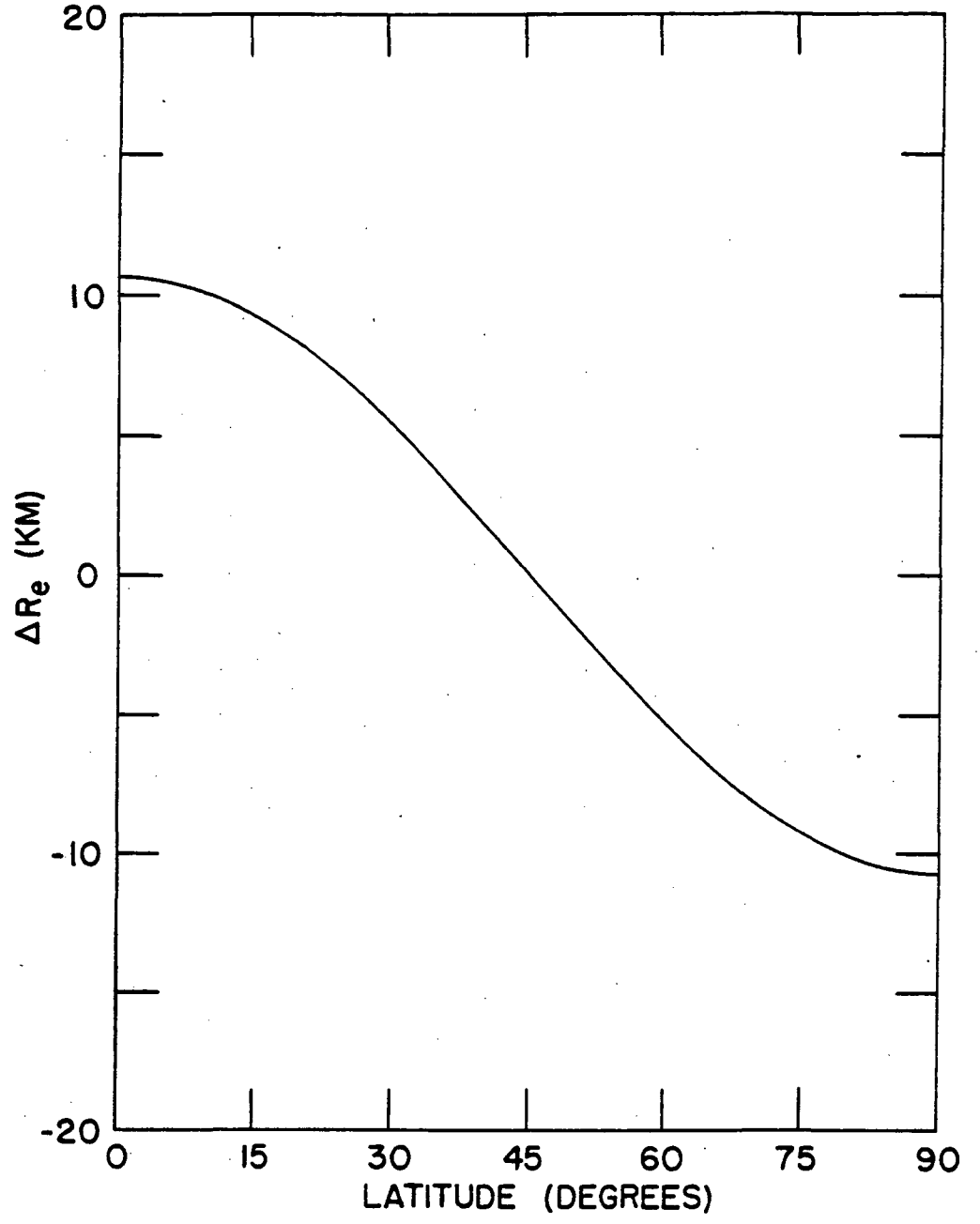

Figure 55: The change in the earth's radius with respect to the value at 45° latitude as a function of latitude.

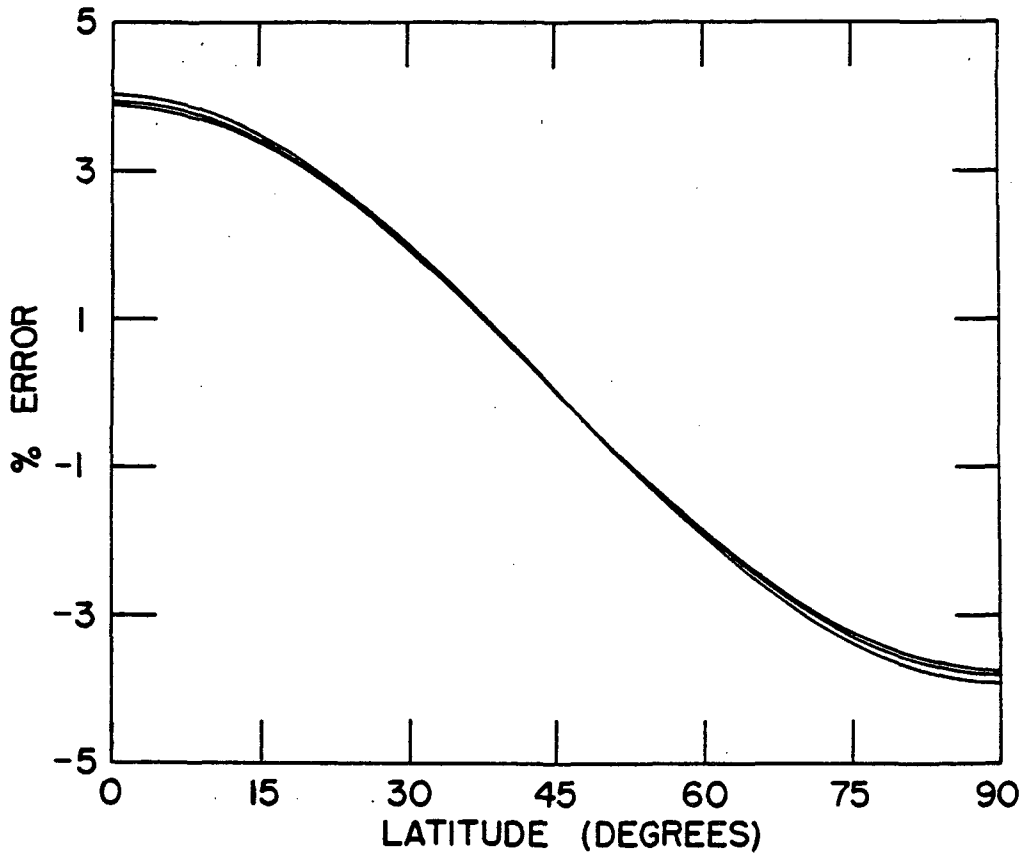

Figure 56: The error in the calculated optical airmass due to error in the latitude with respect to 45^{0} for tangent heights of 25.5, 41.2, and 49.0 km and an observer at 50 km.

zenith angle of arrival of the ray at the observer, and the latitude. By far the largest systematic error in the optical airmass calculation was caused by error in the apparent zenith angle.

A much more interesting problem is that of the effects of these systematic errors on the retrieval of mixing-ratio profiles from absorber amount data. This problem is considered in the next section.

3.3 THE EFFECT ON THE MIXING-RATIO RETRIEVAL

3.3.1 A general formalism of systematic errors

The amount of absorber a_m encountered by radiation traversing the atmosphere is given by

$$a_m = \sum_{j=1}^{N} m_j \rho_j \delta \ell_j \ . \tag{42}$$

It is assumed in the following analyses that the absorber amount can be exactly determined from analysis of experimental data (i.e., equivalent width analysis) and that $\Delta a_m = 0$. This implicitly assumes that the absorber amount data considered here contain no experimental noise. The effects of noise, described in the previous chapter, must be added to the effects due to systematic errors examined in this section in order to determine the total error in the retrieved mixing-ratio profile.

Since $\Delta a_m = 0$, the variation of Eq. (42) due to variable x becomes

$$0 = \sum_{j=1}^{N} (\rho_j \delta \ell_j \frac{\Delta m_j}{\Delta x} \Delta x + m_j \delta \ell_j \frac{\Delta \rho_j}{\Delta x} \Delta x + m_j \rho_j \frac{\Delta \delta \ell_j}{\Delta x} \Delta x) \quad . \tag{43}$$

If Δx represents a change in the air density $\Delta \rho$ and if the effects of refraction are ignored then the $\Delta \delta \ell_j / \Delta x$ terms are identically zero since the ray path is a straight line from source to observer. In this case, since the retrieved mixing-ratio values are assumed to be linearly indepednent, Eq. (43) reduces to

$$\rho_j \Delta m_j + m_j \Delta \rho_j = 0 \tag{44}$$

or

$$\frac{\Delta m_j}{m_j} = -\frac{\Delta \rho_j}{\rho_j} \quad . \tag{45}$$

But from Eq. (6)

$$\frac{\Delta \rho_j}{\rho_j} = \frac{\Delta \rho (o)}{\rho (o)} \quad , \tag{46}$$

so

$$\frac{\Delta m_j}{m_j} = -\frac{\Delta \rho (o)}{\rho (o)} \tag{47}$$

which combined with Eq. (10) yields

$$\frac{\Delta m_j}{m_j} = - \frac{\Delta a}{a} . \qquad (48)$$

Consequently, the error in the retrieved mixing-ratio value at any altitude is given by Eqs. (13), (25), (28), (30), and (38).

The effects of systematic errors in the parameters in these relations on retrieved mixing-ratio profiles have been investigated by analyzing absorber amount data calculated for the standard values of Table 15 by the methods described in the previous chapter assuming various systematic errors in the calculation of the a_{ij} matrix elements of Eq. (2.70). The 125 absorber amounts were calculated for the constant mixing-ratio profile of Figure 11 and an apparent zenith angle spacing of 0.0098903^{o}. In these retrievals no simulated noise was added to these data values. The effects of the systematic errors were investigated by comparing mixing-ratio values for $N_R = 50$ to the true mixing-ratio profile.

3.3.2 Type 1 - refraction

If refraction is ignored in the calculation of the retrieval matrix substantial errors occur in the retrieved mixing-ratio values at low altitudes. The error in the retrieved mixing-ratio values as a function of altitude due to the neglect of refraction is shown in Figure 57. Below

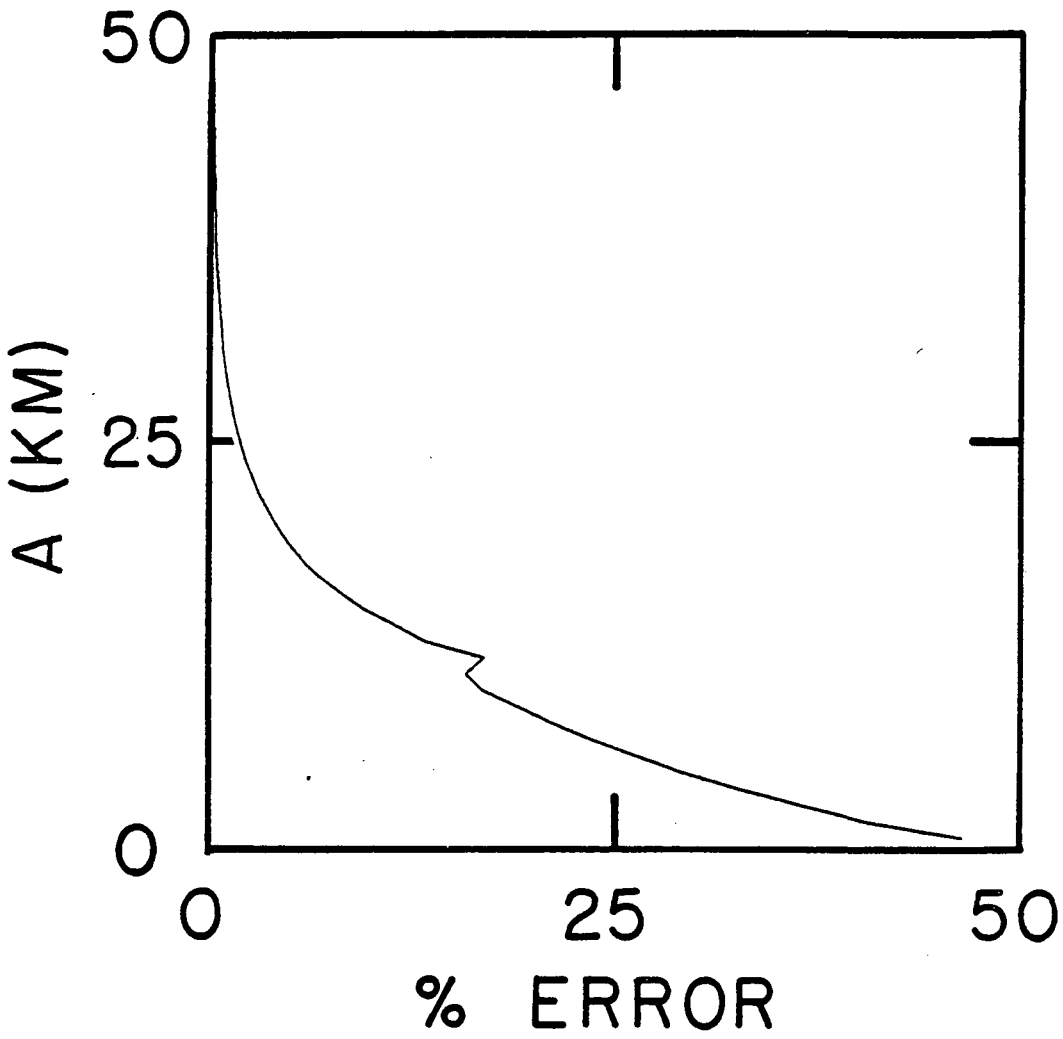

Figure 57: The error in the retrieved constant mixing-ratio profile due to neglect of the effects of refraction.

25 km the error increases rapidly near the earth's surface. Above 25 km the error in the retrieved mixing-ratio values is less than 1%. Thus refraction can be ignored above 25 km but must be properly modeled below 25 km in order to avoid systematic errors in the retrieval. The feature at 10 km, shown in Figure 57, is believed to be due to the shape of the temperature profile at the tropopause and the thickness of the layers used in the calculation.

3.3.3 Type 2 - sea-level pressure

The error in the jth retrieved mixing-ratio value is found by combining Eqs. (13) and (48) yielding

$$\frac{\Delta m_j}{m_j} = -\frac{\Delta P(o)}{P(o)} \quad . \tag{49}$$

Thus the error in the retrieval should be independent of altitude. For an error of 5% in the sea-level pressure the error in the mixing-ratio retrieval should be 5% at all altitudes.

Errors in the retrieved mixing-ratio profile obtained for sea-level pressure errors of ±5% are shown in Figure 58. As expected the error is about ±5% at all altitudes. The departure from this at low altitudes is due to the effects of refraction which have not been included in the derivation of Eq. (49). The feature in the error curves at 10 km is believed to be due to the shape of the temperature profile at the

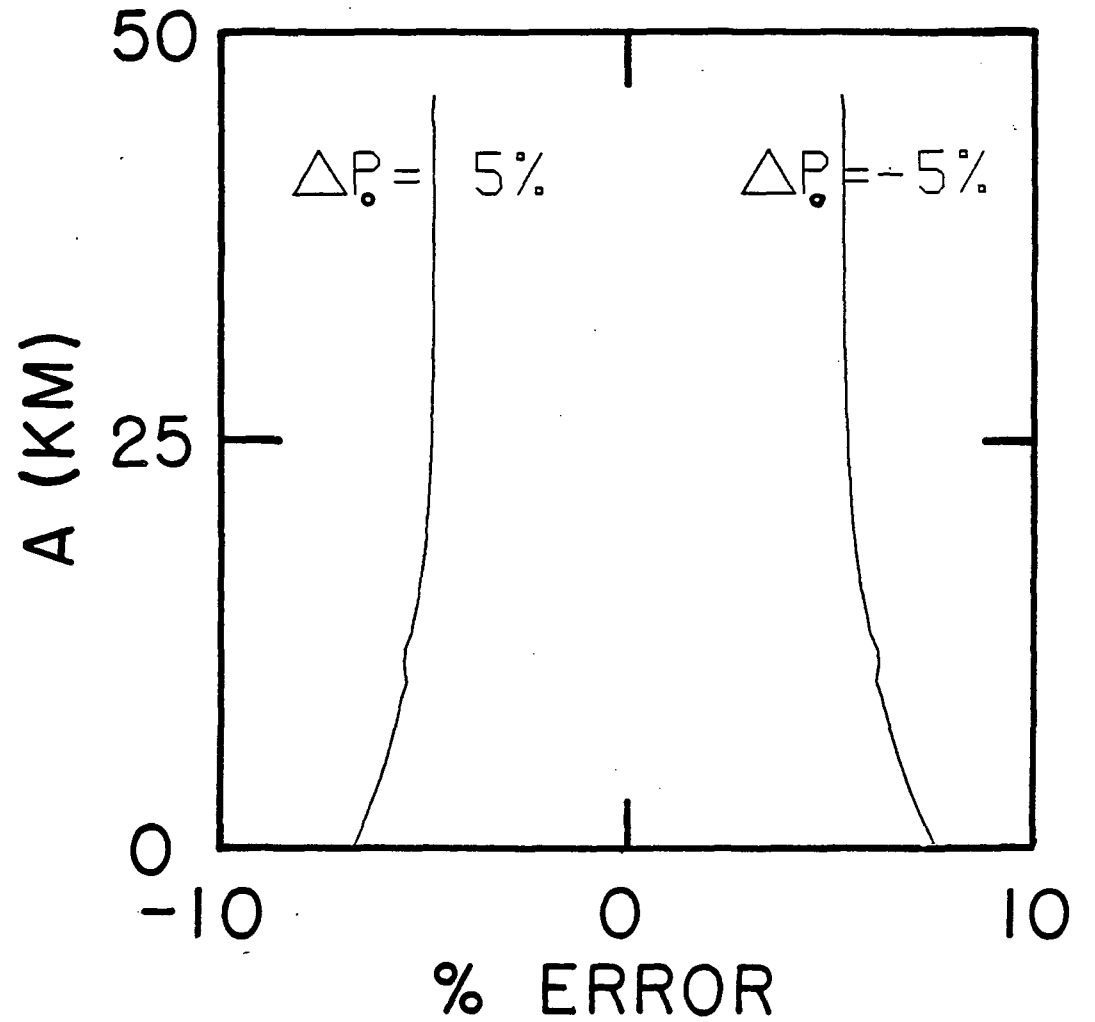

Figure 58: The error in the retrieved constant mixing-ratio profile due to errors in the sea-level pressure of ±5%.

tropopause and the layer thickness used for the calculation.

3.3.4 Type 2 - temperature profile

The error in the jth retrieved mixing-ratio value for an error in an isothermal temperature profile of ΔT at all altitudes is found as a function of altitude by combining Eqs. (25) and (48) giving

$$\frac{\Delta m_j}{m_j} = - \frac{(A - H_s)\Delta T}{H_s T} . \qquad (50)$$

Thus the error in the mixing-ratio value at an altitude equal to the scale height is zero independent of the temperature profile error. At 50 km the error in the retrieval is ±11% for a systematic temperature error of ±5 K at all altitudes. The problem of local temperature variations has not been considered.

The results of retrievals done for systematic temperature errors of ±5 K are shown in Figure 59. As expected the error in the mixing-ratio retrieval is zero near an altitude equal to the scale height and increases in magnitude with altitude above this point. The error at 50 km is larger than that predicted by Eq. (50) because this equation was derived assuming an isothermal atmosphere.

The altitude dependence of the mixing-ratio value error caused by temperature profile errors is unique to this systematic error (of those discussed in this work). Thus the inherent error in the retrieved mixing-ratio profile due to

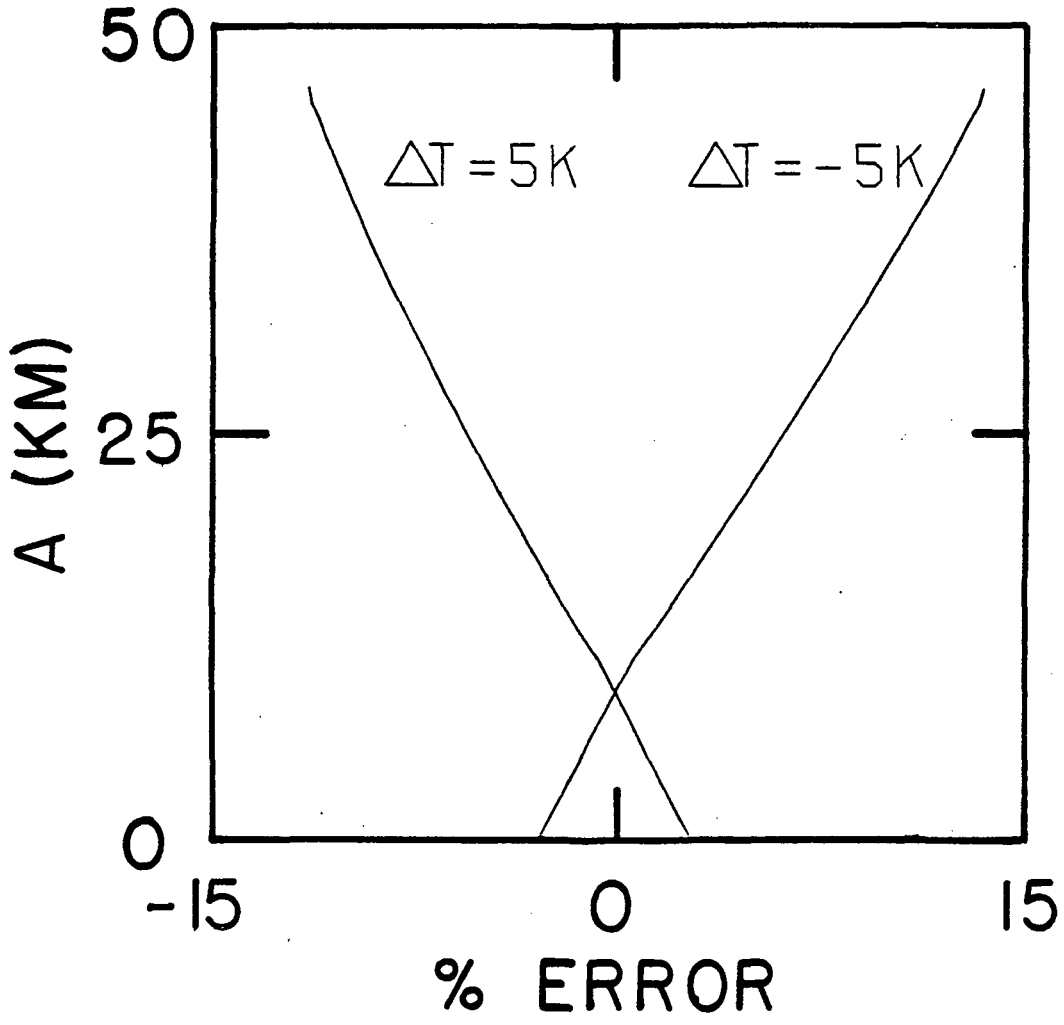

Figure 59: The error in the retrieved constant mixing-ratio profile due to errors in the temperature profile of ±5 K at all altitudes.

temperature errors cannot be reduced by adjusting the other parameter values. Therefore, the temperature profile should be known accurately and, if necessary derived from the same spectral data used for the mixing-ratio profile retrieval (21). Although not discussed in this work, it is planned to describe a method to retrieve temperature profiles later.

3.3.5 Type 3 - observer altitude

The error in the retrieved mixing-ratio value due to error in the observer altitude is found by combining Eqs. (28) and (48) giving

$$\frac{\Delta m_j}{m_j} = \frac{\Delta A_o \sin Z_o}{H_s} \quad . \tag{51}$$

This error, like that obtained for sea-level pressure errors, should be independent of altitude. For an observer altitude error of 1 km the error predicted from Eq. (51) is ~14% at all altitudes.

The mixing-ratio retrieval value errors, shown in Figure 60, were obtained for an error of ±1 km in observer height from analysis of the absorber amounts calculated from the standard values. The mean value of the error is approximately 14% as predicted. However, the features shown in Figure 60 are believed to be due to the temperature variation of the standard profile and the layer thickness used in the calculation.

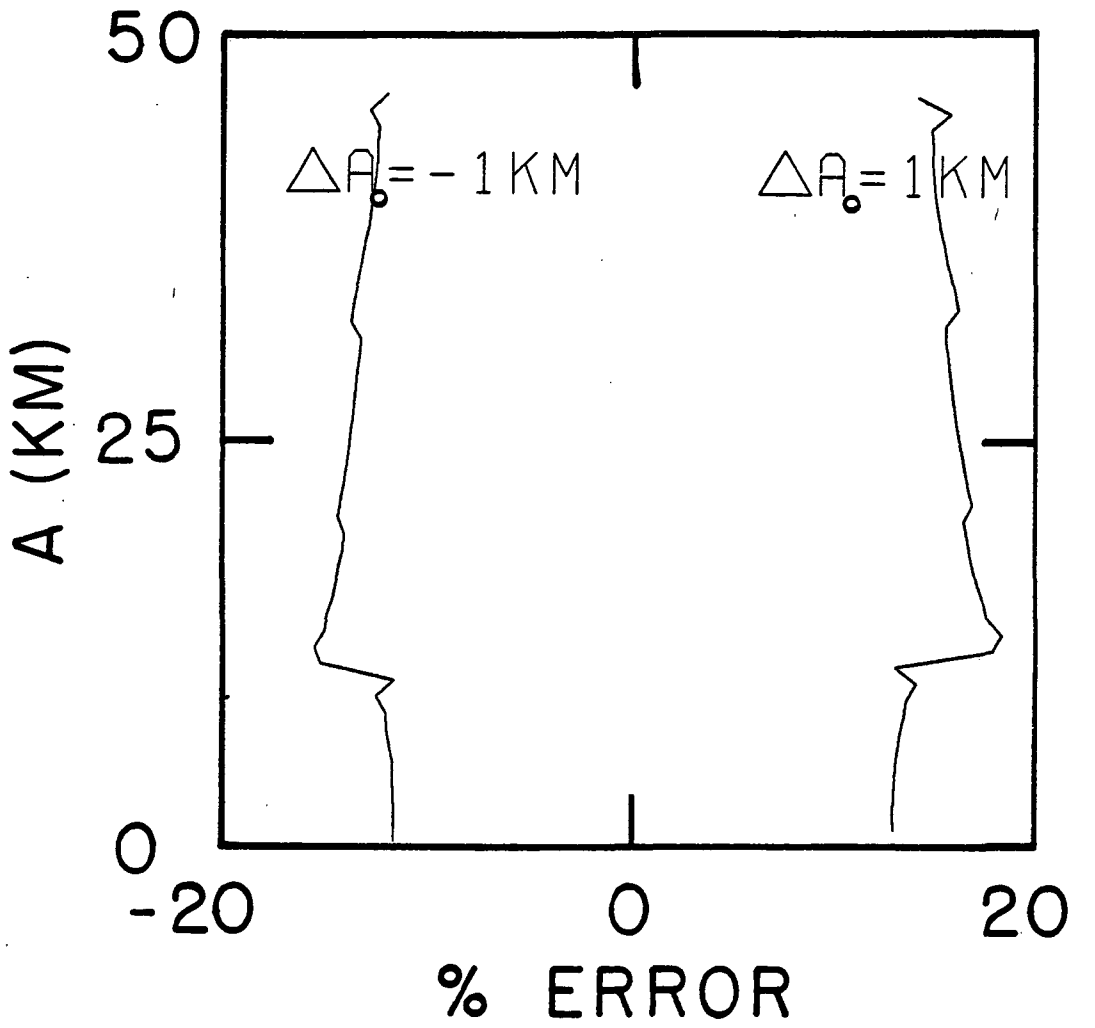

Figure 60: The error in the retrieved constant mixing-ratio profile due to errors in the observer altitude of ±1 km.

3.3.6. Type 3 - apparent zenith angle

Similarly the error, due to errors in the apparent zenith angle, in the jth layer is given by

$$\frac{\Delta m_j}{m_j} = - L \frac{\Delta Z_o}{H_s} . \qquad (52)$$

An apparent zenith angle systematic error of 0.01° results in an error in the retrieved mixing-ratio value of 6% at all altitudes.

The results of retrievals done for apparent zenith angle errors of ±0.01° are shown in Figure 61. As expected the error is nearly constant with altitude and has a mean value of approximately 6%. The structure in the error curves is almost identical to that obtained for the observer altitude errors. The similarity of Figure 60 and 61 suggests that systematic errors in the apparent zenith angle are indistinguishable from systematic errors in the observer altitude.

3.3.7 Type 3 - latitude

The mixing-ratio error due to latitude error is given by

$$\frac{\Delta m_j}{m_j} = - \frac{(1 - \sin Z_o) \Delta R_e(\phi)}{H_s} . \qquad (53)$$

For a latitude error of ±5° with respect to the standard value of 45° the error predicted by Eq. (53) is 1.8%. This error like that found for sea-level pressure, observer altitude, and

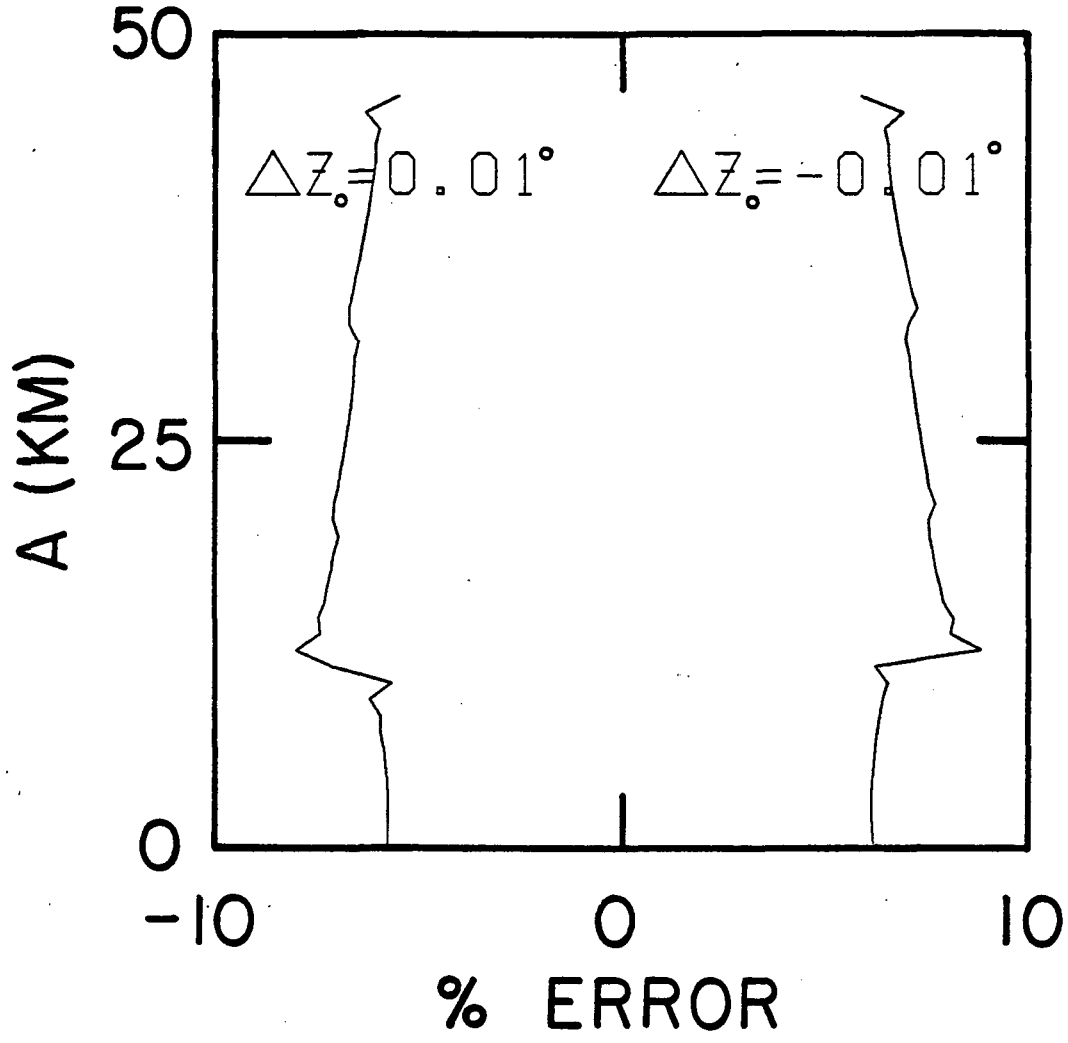

Figure 61: The error in the retrieved constant mixing-ratio profile due to errors in the apparent zenith angle of $\pm 0.01^{o}$.

apparent zenith angle errors should be independent of altitude in the absorbing atmosphere.

The results obtained from the analysis of the standard absorber amount data, shown in Figure 62, gives an error three times larger than that predicted by Eq. (53). This is believed to be due to the algorithmic error in the slant-path calculation mentioned in the previous section. The shape of the error curves, however, are identical to that obtained for the observer altitude and apparent zenith angle errors.

3.3.8 Summary

By analysis of synthetic absorber amount data with no added noise, assuming various systematic errors in the describing parameters, we have determined the error in retrieved mixing-ratio profiles as a function of altitude caused by these systematic errors.

It was found that refraction becomes significant in the retrieved profile below 25 km and its importance increases rapidly with decreasing altitude. In order to retrieve accurate mixing-ratio profiles below 25 km the effects of atmospheric refraction must be modeled properly.

The error in the retrieved mixing-ratio profiles obtained for systematic errors in the temperature profile increased linearly with altitude and was zero at an altitude approximately equal to the scale height. The functional form of this systematic error was different from that obtained for all the others

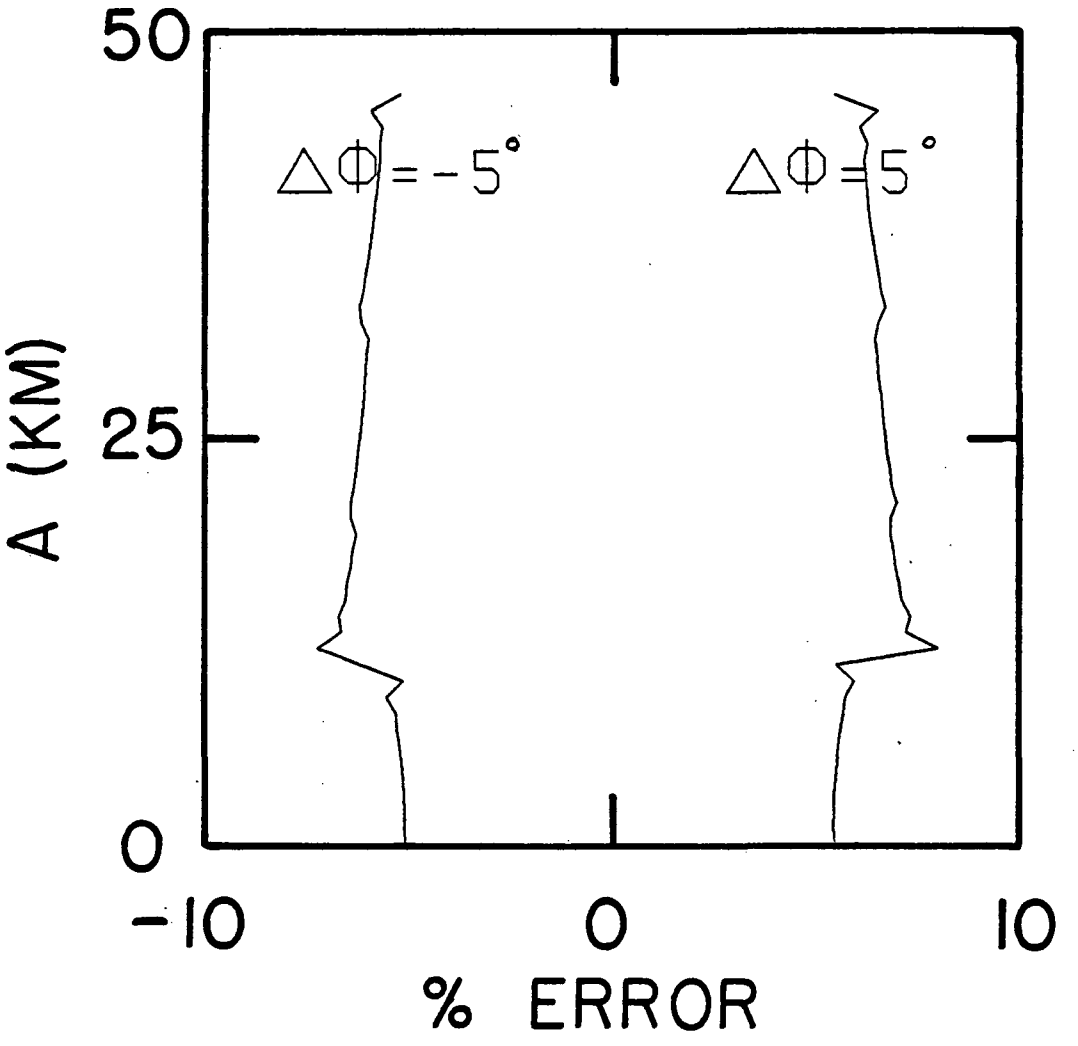

Figure 62: The error in the retrieved constant mixing-ratio profile due to errors in the latitude of ±5°.

suggesting that this error can only be reduced by a more precise determination of the temperature profile from analysis of the same spectral data used to retrieve the mixing-ratio profiles.

The errors due to systematic errors in the sea-level pressure, the apparent zenith angle, the observer altitude, and the latitude are essentially identical and independent of altitude. Consequently, the effects of an error in any of these parameters on the retrieval of a mixing-ratio profile are indistinguishable from the effects of errors in the other parameters. This implies that a systematic error in the observer altitude could be compensated by an appropriate adjustment of the other parameters. The result would be the retrieval of a mixing-ratio profile with no apparent systematic errors (provided that refraction is modeled and the temperature profile is precisely known). A method of internal calibration of spectral data which makes use of this technique will be described later in this chapter.

3.4 ESTIMATE OF TOTAL SYSTEMATIC ERROR

Although individually the contribution of each of the systematic errors discussed in the previous section may be small compared to the uncertainty caused by the presence of experimental noise, in combination these errors can significantly alter the results obtained in a mixing-ratio profile retrieval. For the design of occultation experiments it is necessary to know the accuracy required for the determination of the physical

parameters in order to maintain a desired error in the mixing-ratio profile retrieval. Conversely, it may also be necessary to determine the total error due to possible errors in these physical parameters. Specifically, for the evaluation of experimental results, the total error in the retrieved mixing-ratio values due to the presence of systematic error can be computed.

In this section the experimental design requirements for an error in the retrieved mixing-ratio values of 1% for each of the systematic errors (excluding refraction) discussed in the previous section is investigated. This represents a total systematic error of about 5% in the retrieved mixing-ratio values. In addition, the altitudes below which each of the errors is significant compared to the uncertainty in the mixing-ratio value due to experimental noise is computed. The calculation of this altitude allows the determination of those portions of the retrieved profile significantly affected by the systematic errors.

In order to determine the magnitudes of the systematic errors necessary to give a total error of 5% Eqs. (49)-(53) were solved for each error by substituting in $\Delta m_j/m_j = 0.01$. The parameter errors which result in a mixing-ratio value error of 1% are listed in Table 21. These systematic errors have been listed in order of the accuracy necessary to obtain an error of 1%. For example, an apparent zenith angle error of 0.002^{o} is a change of only 0.002% with respect to the

Table 21: Systematic errors in physical parameters which give a 1% error in the retrieved mixing-ratio profiles.

Physical parameter	Dependence of error in mixing-ratio on height	Systematic error which gives a 1% error in mixing-ratio profile
refraction	important below 25 km	at all altitudes below 25 km if neglected
apparent zenith angle	independent of height	0.002°
satellite height	independent of height	75 m
temperature profile	increases with height	0.1 K at 25 km
sea-level pressure	independent of height	10 mb
latitude	independent of height	2.5°

standard values of Table 15, while a latitude error of 2.5 represents a change in latitude of about 5.6% with respect to the standard value. Thus the error in the apparent zenith angle was judged the more critical, and so on.

The errors in the experimental parameters listed in Table 21 indicate the precision necessary in an experiment to yield a total systematic error of 5% in the retrieved mixing-ratio values. It is not likely, due to smearing caused by the motion of the observer and the finite size of the solar disc viewed by the instrument, that an overall precision as high as this is possible for satellite experiments. The magnitudes assumed in the previous section for the systematic errors are more probable.

The magnitudes of the systematic errors used in the previous section are listed in Table 22. These errors may result in a total error in the retrieved mixing-ratio values of up to 30%. A measure of the significance of these systematic errors is the altitude range over which these errors are larger than the uncertainty in the retrieved mixing-ratio values due to the uncertainty of experimental noise. These altitudes were calculated, and are listed in Table 22, for each of the systematic errors and the conditions: 125 data values with an SNR of 100 and the retrieved number of mixing-ratio values equal to 50 and 10. Thus for a mixing-ratio value spacing of 10 km the systematic errors are individually larger than the uncertainty due to noise below 24 km. In this case more than half

Table 22: The altitude at which the error in the mixing-ratio profile due to each systematic error is less than the uncertainty due to noise for N_O = 125, SNR = 100, and N_R values of 50 and 100.

Physical parameter	Systematic error	Altitude at which systematic error is less than uncertainty due to noise	
		N_R = 50	N_R = 100
apparent zenith angle	0.01°	6.6 km	17 km
satellite height	1 km	12.0 km	23 km
temperature profile	5 K	0.0 km	4 km
sea-level pressure	5%	5.4 km	16 km
latitude	5°	0.0 km	9 km

the altitude range of the retrieval will contain mixing-ratio value errors primarily due to systematic errors. Thus, in order to obtain meaningful profile retrievals it is necessary that these errors be reduced. A method for reducing the effect of these systematic errors is discussed in the next section.

The relations derived in this chapter for the retrieved mixing-ratio value errors due to systematic errors are valid for all observer altitudes. The errors due to observer altitude, sea-level pressure, and temperature profile errors are essentially the same for all observer altitudes. For the case of a balloon observer (i.e., an observer altitude of about 30 km) the error in the retrieved mixing-ratio values caused by an error in the apparent zenith angle (for apparent zenith angles greater than 90°) of 0.01° is about 2%, and the error due to an error in the latitude of 5° is 0.1%. Thus the systematic error due to these parameters is much less for a balloon observer. However, as shown in Table 23, typical errors in the physical parameters give a total error of about 14% in the retrieved mixing-ratio values independent of altitude. This suggests that many of the reported mixing-ratio profiles retrieved from the analysis of data obtained from balloon-borne instruments may have been overly optimistic in their reported uncertainties. Realistic errors in the physical parameters are necessary if the accuracy of retrieved profiles is to be gauged.

Table 23: The error in retrieved mixing-ratio profiles due to typical systematic errors for an observer altitude of 30 km.

Physical parameters	Systematic error	Error in mixing-ratio profile
apparent zenith angle	0.01°	2.00%
satellite height	0.5 km	7.00%
temperature profile	5 K	0.25%
sea-level pressure	5%	5.00%
latitude	1°	0.02%

For the case of a ground-level observer the systematic errors due to the apparent zenith angle, latitude, and observer altitude errors are eliminated. The remaining errors due to errors in the sea-level pressure and the temperature profile (including errors due to "horizontal" variations of the sea-level pressure and the temperature profile) should be small compared to the error in the retrieved mixing-ratio profile caused by noise. Thus it is not expected that these systematic errors will have much affect on the retrieval of mixing-ratio profiles from ground-level observations unless the SNR of the data is large.

3.5 INTERNAL CALIBRATION OF OCCULTATION SPECTRA

3.5.1 Internal calibration method

It was demonstrated in section 3.3 that when the information about the atmospheric paths is obtained from external sources several errors affect the retrieved profiles in nearly identical ways. This occurs in part because the spectral information concerning the atmosphere, carried by a ray with a fixed tangent height originating outside the atmosphere and collected outside the atmosphere, is not influenced by the positions of the source or the detector and hence by the particular sets of parameters which describe these positions. As shown in Figure 63 the ray path through the atmosphere is identical for an apparent zenith angle of 110.807° together with an observer altitude of 500 km to the path of a ray with

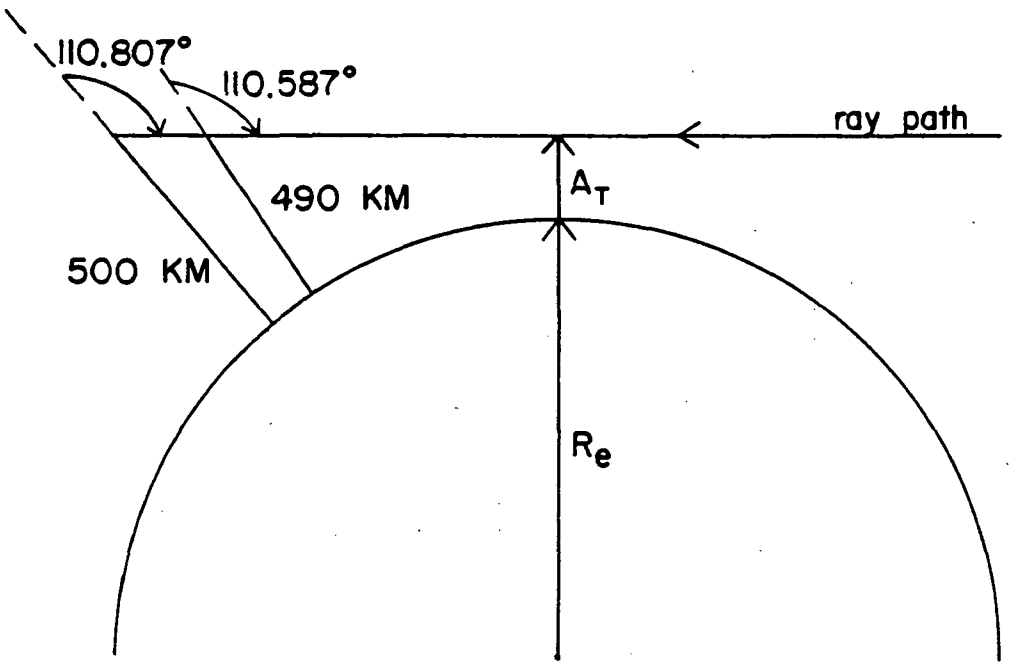

Figure 63: Identical ray paths for two sets of apparent zenith angle - observer altitude pairs.

apparent zenith angle of 110.587° together with an observer atltitude of 490 km. If the tangent height of the observed radiation can be determined the particular values assumed for the observer parameters do not affect the spectral analysis as long as the tangent height corresponds to that obtained from the data. Thus it is possible to choose pairs of values for the apparent zenith angle and the observer altitude such that the ray path is consistent with that obtained from the data. This is the essence of the internal calibration method.

It has also been noted that the quality of the spectra is degraded by the field of view of the instrument, satellite motion (14), atmospheric refraction, and temperature and density profile variations along the atmospheric path (15) and that it is unlikely that all of these effects can be satisfactorily modeled in the analysis.

Internal calibration removes many of these errors but also introduces new ones. In this method information about the atmospheric path is obtained from absorption lines in the spectra. Lines of CO_2 are often measured because its vertical and latitudinal mixing-ratio is nearly constant and the parameters of many CO_2 lines are accurately known. We consider, initially, the information obtained by measuring the equivalent widths of a single CO_2 line, with a temperature-independent line intensity, in a single spectrum. This allows one aspect of the path, such as the total amount of CO_2 (which gives the tangent height of the ray), to be obtained. The additional information

obtained by measuring the equivalent width of several lines in different regions of the curve of growth or by measuring lines whose intensities are temperature dependent is considered later in this section.

If W_o and W_1 are the equivalent widths, in a single spectrum, of weak lines of CO_2 and a trace gas, respectively, and if the corresponding line intensities S_o and S_1 are temperature independent, then from Eq. (2.9) the amount of CO_2 along the path is

$$a_o = W_o/S_o \tag{54}$$

and the amount of the other absorber is

$$a_1 = W_1/S_1 \ . \tag{55}$$

If the CO_2 mixing-ratio m_o is constant with height and along the ray path traversed then the total optical airmass traversed is

$$a = \frac{W_o}{S_o m_o} \tag{56}$$

and the mean mixing-ratio of the absorber along the path is give by

$$m_1 = \frac{a_1}{a} \ . \tag{57}$$

These simple results are obtained because the incremental equivalent widths are additive. In this approach it is assumed that both equivalent widths have been subjected to the same averaging due to the smearing caused by the field of view of the instrument, the satellite motion, and the temperature and density profile variations. If the spectra are obtained by a Fourier Transform Spectrometer information concerning both of the lines W_o and W_1 is collected simultaneously. Provided the lines are both weak, both of these equivalent widths are subjected to the same weighting processes which are then automatically ratioed out of the final results. Thus the values or the total airmass traversed and the mean mixing-ratio of the unknown absorber given by Eqs. (55) and (57) do not contain the implicit errors associated with the uncorrectable smearing effects of the external calibration methods.

The elimination of the smearing effects represents the principle advantage of the internal calibration method. These effects are extremely difficult to characterize analytically, yet by internal calibration of the spectral data this difficulty is eliminated. The problem then reduces to the idealized analysis described in the previous chapter.

The corresponding effective tangent height of the rays producing the spectrum can be found from comparison of the total airmass traversed to the schematic optical airmass plot, shown in Figure 64, which could be obtained from the slant-path calculating program (7,8). The tangent height for an optical

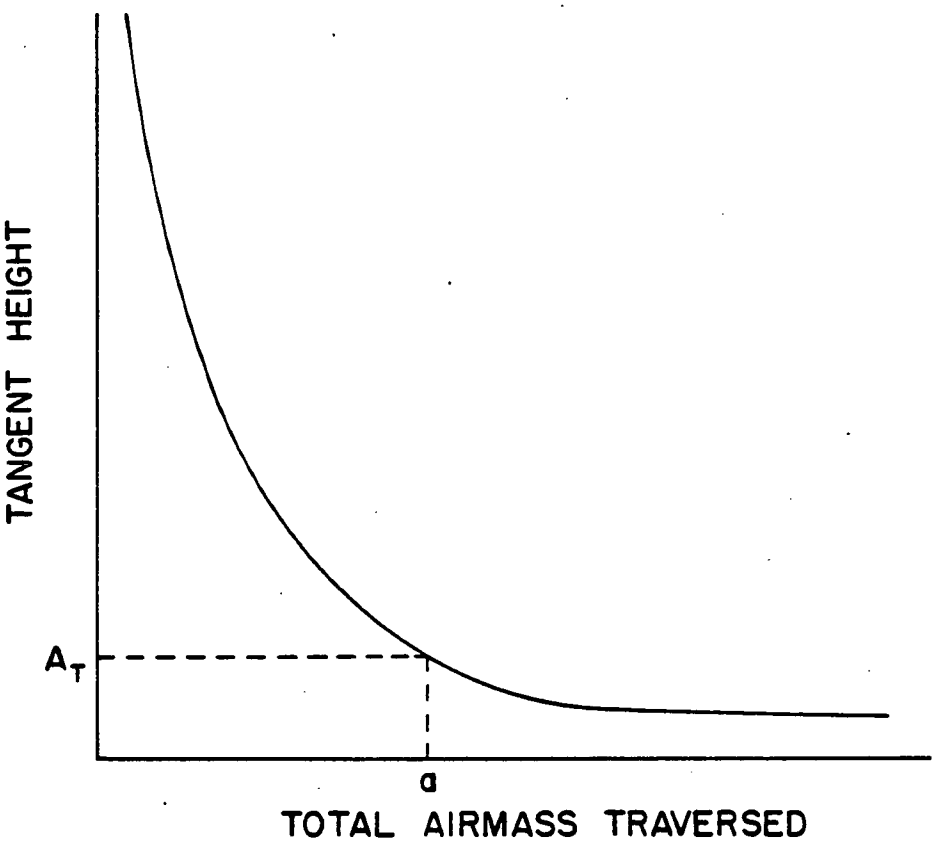

Figure 64: Schematic total optical airmass curve.

airmass a is found from Figure 64 to be A_T.

If we consider N_o spectra obtained for different paths through the atmosphere, the N_o tangent height values could be obtained from Figure 64. A set of effective zenith angles together with an effective observer altitude can be chosen to give the correct tangent heights given from Figure 64. The set of constituent absorber amounts (obtained from equivalent width analysis of a spectral line of the constituent) together with the corresponding effective apparent zenith angles and observer altitude constitute a data set identical to those considered previously in this work. However, the systematic errors due to the apparent zenith angle and the observer altitude errors as well as smearing due to satellite motion, field of view of the instrument, and temperature and density profile variations have been eliminated by the internal calibration method.

In order to calculate the optical airmass curve shown in Figure 64 it is necessary to assume values for the temperature profile and the reference level pressure. If either of these is erroneous, then from Eqs. (13) and (25) the optical airmass curve of Figure 64 will be shifted from its true position. Thus the tangent height for each of the N_o spectra will be improperly determined. However, the retrieved mixing-ratio values will not be in error since the density of the incorrect density profile at this altitude is the same as the correct density at the correct tangent height.

Other systematic errors result if the line intensities of the CO_2 lines, the mixing-ratio value of CO_2 or the measured equivalent widths of the CO_2 lines are incorrect. The optical airmass determined using erroneous values for any of these parameters will also be in error, and consequently, the corresponding tangent height and the retrieved mixing-ratio values. Finally, although systematic errors in the constituent line intensities and the measured constituent equivalent widths do not affect the determination of the tangent heights of the rays, these errors result in errors in the constituent absorber amount and consequently, the retrieved constituent mixing-ratio values.

These systematic errors are summarized in Table 24 together with the errors in the retrieved mixing-ratio values due to typical systematic errors. For the case of a 2% error in each of the spectral line intensities and measured equivalent widths the total error in the retrieved mixing-ratio values will be about 5% at all altitudes. No errors in these retrieved mixing-ratio vaules result from systematic errors in either the reference level pressure or the temperature profile. However, these systematic errors as well as those due to the CO_2 spectral line parameters cause a shift in the altitudes of the retrieved mixing-ratio values due to the error in the tangent heights obtained from Figure 64. For the typical errors listed in Table 24 the total shift in the retrieved mixing-ratio profile should be about 0.4 km.

Table 24: The effects of systematic errors on mixing-ratio profiles retrieved using internal calibration.

Physical parameter	Systematic error	Error in tangent height	Error in mixing-ratio of trace gas
surface pressure	3%	0.20 km	none
temperature profile		depends on altitude	none
CO_2 intensity S_o	2%	0.14 km	2%
CO_2 equivalent width W_o	2%	0.14 km	2%
CO_2 mixing-ratio m_o	2%	0.14 km	2%
trace gas intensity S_1	2%	none	2%
trace gas equivalent width W_1	2%	none	2%

An error of 0.4 km in the tangent height is much less than the expected vertical resolution of trace gas profiles expected to be obtained from typical occultation data. As shown in the second chapter, this resolution is typically several kilometers with uncertainties in the profiles of 10% or greater. Thus the method of internal calibration appears to be adequate for these types of measurements.

The internal calibration method is useful in eliminating the systematic errors due to observer geometry parameter and atmospheric thermal structure parameter errors. This method also eliminates the smearing effects mentioned previously by comparison of constituent equivalent widths to those obtained from a gas with a known constant mixing-ratio profile such as CO_2. The additional systematic errors which result from errors in the spectral line parameters are small enough to imply that internal calibration methods should be used to analyze spectra which contain suitable weak lines.

3.5.2 Relative times of data collection

The rate of change dZ_{oi}/dt of the zenith angles of the incoming rays and the corresponding rate of change dA_T/dt of the tangent height of the rays reaching a satellite are nearly constant in a given occultation. Thus the scatter in the observed values of the optical airmasses obtained from Eq. (56) or the equivalent tangent height A_{Ti} with time allows the consistency of the data to be estimated. Systematic shifts between

the values obtained by internal calibration of the spectra and those calculated from the orbital parameters may be due, for example, to timing errors. Differences in the shapes of the curves at low tangent heights may be caused by improperly corrected refraction effects. However, the data in Figure 59 indicate that small errors in the temperature profile do not cause significant errors, due to refraction, in the mixing-ratio profiles.

Uncertainties in the CO_2 mixing-ratio or departure from local thermodynamic equilibrium may produce differences between the observed and calculated curves for small airmasses. However, good agreement is expected in the shapes of the curves for rays with tangent heights between about 20 and 50 km.

3.5.3 Measurements of several lines

The bands and lines of CO_2 have a wide range of intensities and it is expected that the equivalent widths of a number of lines can be measured in each spectrum. This enables the consistency of the measurements in a given spectrum to be estimated and allows those lines which are too weak to be measured accurately, which lie outside the linear region of growth of the equivalent width, or which are blended with other lines to be rejected. The effective SNR can be improved by measuring a number of lines.

Because of the very large variation in the airmasses traversed by rays with tangent heights from 0 to above 50 km

it is necessary to measure CO_2 lines with a corresponding range of temperature independent intensities in order to maintain high precision. In general, this will require measurements of CO_2 lines, with small lower state energies, in bands with different intensities.

3.5.4 Lines not in the linear region

It has so far been assumed that the equivalent widths of the CO_2 calibration lines can be obtained from

$$W(Z_{oi}) = \sum_j \Delta W_{ij} \quad . \tag{58}$$

If the CO_2 lines are not in the linear region of growth the incremental widths ΔW_{ij} depend on the local atmospheric temperature and density and they are no longer additive. The weighting of such lines over the field of view of the instrument and other smearing effects is different from that for weaker CO_2 lines or weak lines of trace gases.

In these cases one of the principle advantages of the internal calibration method, the ability to assume that the smearing effects are the same for all lines, is lost. It is therefore, important to choose CO_2 calibration lines which are in or close to the linear region of the curve of growth.

3.5.5 Measurements of temperature dependent lines

Because the atmosphere is not isothermal the weighting of the equivalent widths of the lines over the field of view depends on the temperature dependence of the lines in addition to other effects previously considered. Since the strongest lines of most trace gases are not strongly temperature dependent, CO_2 lines with a similar temperature dependence should be chosen for calibration.

3.6 SUMMARY

In this chapter we have investigated the effects of various systematic errors on the determination of the optical airmass traversed by a ray passing through the atmosphere and the mixing-ratio profiles retrieved from analysis of absorber amount data containing no noise. Expressions have been obtained for each of these resulting errors in the optical airmass and the retrieved mixing-ratio values as a function of altitude.

It was found that refraction becomes significant below 25 km and its importance increases rapidly with decreasing altitude. In order to retrieve accurate mixing-ratio profiles below 25 km the effects of atmospheric refraction must be modeled correctly.

The error in the calculated optical airmass and the retrieved mixing-ratio values due to systematic errors in the temperature profile of the entire atmosphere increased linearly with altitude and was zero at an altitude approximately equal

to the scale height.

The errors due to systematic errors in the sea-level pressure, the apparent zenith angle, the observer altitude, and the latitude are essentially identical and independent of altitude. However, the errors, due to systematic errors in the latitude were found to be negligible for reasonable errors in the latitude.

A method was presented by which the systematic errors due to temperature profile, sea-level pressure, apparent zenith angle, and observer altitude errors can be eliminated in the retrieval of mixing-ratio profiles from equivalent width data by comparison of the equivalent width of a spectral line of the trace gas to the equivalent width of a CO_2 line in the same spectrum. If the CO_2 lines used for comparison are weak, this internal calibration method also eliminates the smearing effects due to the field of view of the instrument, satellite motion, and temperature and density profile variations along the ray paths. The systematic errors inherent to the internal calibration method should be less than those resulting from external calibration methods.

In this chapter we have not considered the information contained in the shape of spectral lines. This problem is considered in the next chapter. Also considered in the next chapter is the analysis of ATMOS spectra obtained from a recent ground-level test of the ATMOS instrument. As noted in this chapter the systematic errors caused by errors in the observer

geometry parameters are not significant for the analysis of spectra obtained from ground-level providing the SNR of the data is not large. Thus systematic errors due to errors in these parameters are not considered in the next chapter.

REFERENCES

1) J. M. Russell III and S. R. Drayson, J. Atm. Sci., 29, 376 (1972).

2) J. M. Russell III, J. H. Park, and S. R. Drayson, Appl. Opt., 16, 607 (1977).

3) R. G. Roble and R. B. Norton, J. Geophys. Res., 77, 3524 (1972).

4) J. C. Gille and F. B. House, J. Atm. Sci., 28, 1427 (1971).

5) J. K. G. Watson and P. K. L. Yin, Appl. Opt., 14, 549 (1975).

6) A. Goldman, D. G. Murcray, F. H. Murcray, W. J. Williams, J. N. Brooks, and C. M. Bradford, J. Geophys. Res., 78, 5273 (1973).

7) D. E. Snider, J. Atm. Sci., 32, 2173 (1975).

8) D. E. Snider and A. Goldman, "Refractive Effects in Remote Sensing of the Atmosphere with Infrared Transmission Spectroscopy," BRL Report no. 1970, Ball. Res. Lab., Aberdeen Proving Grounds, Maryland (1975).

9) B. Edlen, Metrologia, 2, 71 (1966)

10) M. Brown, ed., BMDP Statistical Software 1981, Univ. California Press, Berkeley (1981).

11) J. M. Russell III and L. L. Gordley, J. Atm. Sci., 36, 2259 (1979).

12) J. C. Gille, P. L. Bailey, and J. M. Russell III, Phil. Trans. Roy. Soc. Lond. A, 296, 205 (1980).

13) U.S. Standard Atmosphere 1976, NOAA-S/T-76-1562, GPO, Washington, D.C. (1976).

14) J. H. Park, Appl. Opt., 21, 1356 (1982).

15) D. A. Roewe, J. C. Gille, and P. L. Bailey, Appl. Opt., 21, 3775 (1982).

16) H. A. Lorentz, collected papers, Vol. 2, The Hague (1936).

17) Daily Weather Maps Weekly Series, U.S. Department of Commerce, April 7-13, 1980.

18) A. J. Kantor, "Variability of Atmospheric Density in the Middle Atmosphere," AFGL-TR-83-0079, AFGL Hanscom AFB, Massachusetts, 01731(1983).

19) U.S. Standard Atmosphere Supplements 1966, GPO, Washington, D.C. (1966).

20) J. R. Hankey, The American Ephemeris and Nautical Almanac 1974, GPO, Washington, D.C. (1971).

21) C. P. Rinsland, A. Goldman, F. J. Murcray, D. G. Murcray, M. A. H. Smith, R. K. Seals Jr., J. C. Larsen, and P. L. Rinsland, J. Quant. Spect. Rad. Trans., 30, 327 (1983).

Chapter IV

SPECTRAL CURVE-FITTING

4.1 INTRODUCTION

In the second chapter the problem of the retrieval of vertical mixing-ratio profiles from the analysis of absorber amount data was discussed. The information content of such data was estimated by determining the uncertainty and vertical resolution of the absorber mixing-ratio profile as a function of altitude. In the third chapter the effects of systematic errors on this profile were estimated by assuming incorrect values for the required geometric and atmospheric parameters. The data analyzed so far consisted of one piece of information, the total amount of absorber along the path (equivalent width data), for each spectrum collected. In this chapter the retrieval of mixing-ratio profiles by fitting the shape of spectral features is considered.

The problem of spectral curve-fitting is treated in two parts. The first part is the retrieval of a constant mixing-ratio profile from a single spectral line for a ground-level observer. In the weak line approximation this reduces to a linear inversion problem to which the analysis techniques described in the previous two chapters can be applied. The uncertainty as a function of altitude was obtained for

various mixing-ratio value spacings.

In the second part the results of the error analysis in the previous chapters is used to analyze spectral data obtained from a ground-level test of the ATMOS instrument. Non-linear least squares analysis (1) was used to retrieve mixing-ratio profiles for N_2O and CH_4 from these data.

These retrievals demonstrate that as expected there is little height discrimination in a single ground-level occultation spectrum even if the spectral line shapes are modeled.

4.2 THE INFORMATION CONTENT OF SPECTRAL LINE SHAPES

4.2.1 General comments

The data analyzed in the previous chapters were the sums of the absorber amounts in individual layers

$$a_{mij} = m_j \rho_j \delta \ell_{ij} \cdot \qquad (1)$$

Each of the a_{mij} consisted of the desired mixing-ratio weighted by the local air density and path length. The ability to discriminate the vertical distribution of the absorber depended on the variations in the path segment lengths $\delta \ell_{ij}$ and on the angle of arrival of the rays. Since the weighting of the mixing-ratio by the air density is the same for all angles Z_o the density, as such, does not influence the derived vertical resolution directly. It does, however, affect the profile uncertainty. Indeed, the curves in Figures 16, 18, and 19 show

that the mixing-ratio uncertainty increases by a factor of 100 for a 30 km increase in altitude, both above and below the observer, in a manner which is directly proportional to the variation in the air density.

Goldberg (2) has shown that, for rays with $Z_o<90^o$ and no refraction, the path elements

$$\delta\ell = (1 + A/R_e)\,\delta A/(\cos^2 Z_o + 2A/R_e + A^2/R_e^2)^{\frac{1}{2}} \qquad (2)$$

where R_e is the radius of the earth and δA is the layer thickness. As $R_e \to \infty$

$$\delta\ell \simeq \sec Z_o\,\delta A \ . \qquad (3)$$

In this plane-parallel approximation there is no change in the relative lengths of path segments through layers at different altitudes with incoming angle Z_o and hence no height discrimination can be obtained.

For altitudes below 50 km in the earth's atmosphere Eq. (2) can be approximated by

$$\delta\ell \simeq (\cos^2 Z_o + 2A/R_e)^{-\frac{1}{2}}\delta A \ . \qquad (4)$$

Significant differences between Eqs. (3) and (4) occur as $Z_o \to 90^o$ and the minimal resolution above the instrument, illustrated in Figure 21, is due to small deviations from this

behavior. However, at these large angles, other effects such as atmospheric refraction, smearing caused by the portion of the solar disc viewed, and the time required for an observation must also be carefully considered if accurate profiles are to be retrieved.

All the rays reaching an instrument, located above the surface, at angles greater than 90^{o}, pass the earth at some minimum distance D. If refraction is neglected, the path length through a layer a distance A above this minimum is

$$\delta \ell \simeq [(R_e + D)/2(A - D)]^{\frac{1}{2}} \delta A \ , \tag{5}$$

or, with respect to the minmum height,

$$\delta \ell \simeq (R_e'/2A')^{\frac{1}{2}} \delta A \ , \tag{6}$$

where $R_e' = R_e + D$ and $A' = (A - D)$.

The changes in the lengths of the path segments $\delta \ell$, and hence the weighting due to the geometry, are very large near the minimum height which, in turn, varies rapidly with Z_o.

Some typical weighting curves have been described by Farmer (3) and Conrath (4). The weighting curves for the analysis of absorber amount data in the second chapter decreased exponentially with altitude. It is these large variations which allow the high resolution, described by Eq. (2.83), to be obtained below the observer.

Since the geometry associated with occultations observed from the earth and the physical characteristics (especially the density profile) of the atmosphere are nearly constant, then the vertical resolution and uncertainty for a given profile obtained from equivalent width data with a fixed SNR and N_o are completely determined. Any additional improvement must therefore come from the measurement of other spectral properties.

4.2.2 Vertical profiles from line shape analysis

The spectra of many infrared-absorbing gases consist of individual lines whose shapes are pressure and temperature dependent. We have investigated the information contained in a single line observed with infinite resolving power.

For an absorber in the lower part of the atmosphere the line shape can often be described by

$$k(\nu) = \frac{S\alpha(A)}{\pi(\Delta\nu^2 + \alpha^2(A))} , \qquad (7)$$

where S is the intensity, α is the collision-broadened width of the line, and $k(\nu)$ is the absorption coefficient at $\Delta\nu = |\nu - \nu_o|$.

It is assumed, initially, that the intensity and width are temperature independent, that

$$\alpha(A) = \alpha(o) \frac{\rho(A)}{\rho(o)} , \qquad (8)$$

and that the data consist of absorptance values $A(\nu)$ obtained from the observed spectral transmittances $T(\nu)$, where

$$A(\nu) = 1 - T(\nu) . \qquad (9)$$

Provided $A(\nu) << 1$,

$$A(\nu_n) = \sum_j A_j(\nu_n) , \qquad (10)$$

where

$$A_j(\nu_n) = m_j k_j(\nu_n) \rho_j \delta \ell_j . \qquad (11)$$

The spectral absorptances thus depend on the desired mixing-ratios weighted by the local air density, path length, and absorption coefficient. An example of such a spectral line, shown in Figure 65, is due to an absorber with a constant mixing-ratio.

Near line center $k_j(\nu_o) \sim S/\pi\alpha_j$ and thus, from Eqs. (7), (8), and (11) the spectral absorptance is independent of air density. Conversely, for $\Delta\nu >> \alpha$, the spectral absorptance is proportional to the square of the air density. It is these differences which might allow the inference of the height distribution of an absorber from a single spectrum.

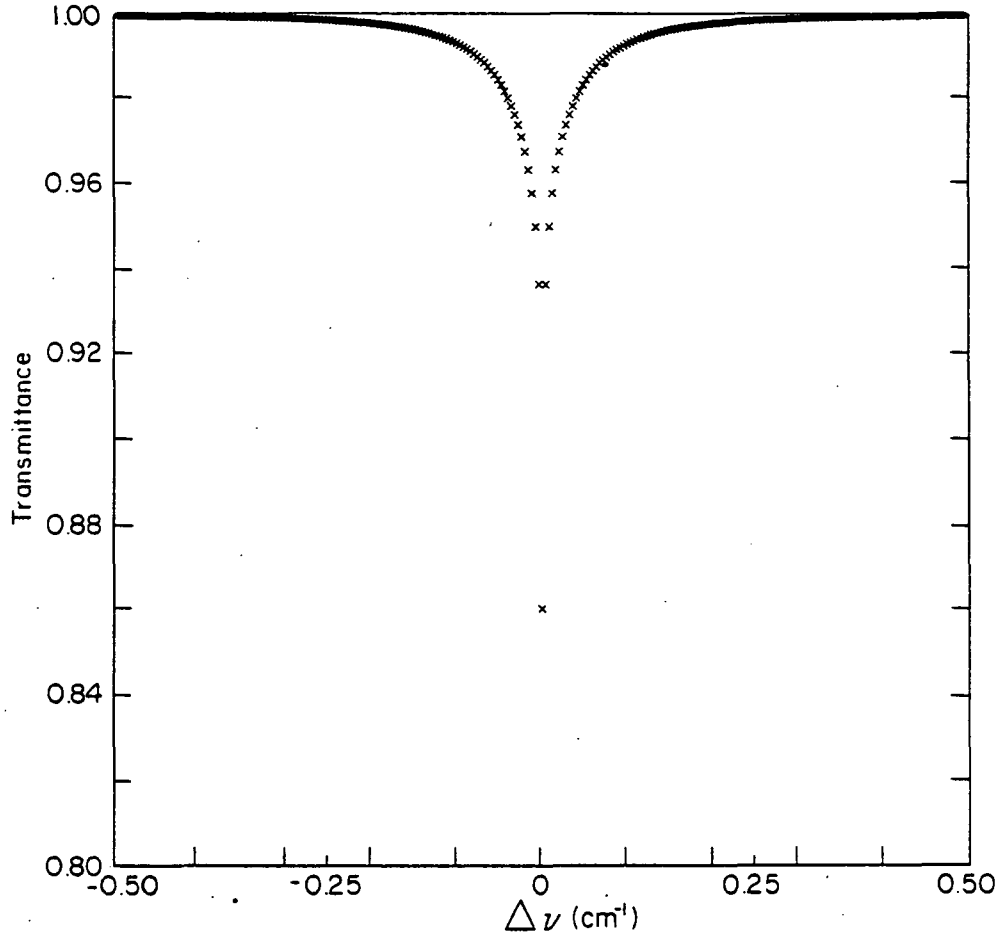

Figure 65: A weak Lorentzian spectral line calculated for line intensity of π, half-width of 0.1 cm^{-1}, spectral value spacing of 0.004 cm^{-1}, a constant mixing-ratio of 1.0, and a ground-level observer.

Local mixing-ratios were retrieved by linear, least squares analysis of 125 equally spaced $A(\nu)$ values, over the range $0<\Delta\nu<5\alpha(0)$, to which normally-distributed noise was added to give a SNR of 100 at $\Delta\nu=\infty$.

Some results for $N_R = 2$, 4, and 5 are shown in Figure 66. The uncertainty increases more slowly with altitude than in Figure 18 but, at ground-level, it is an order of magnitude larger. Thus, even in this idealized situation, essentially no height discrimination is possible above the instrument.

In practice, information is lost because of finite spectral resolution and the inverse exponential, rather than linear, change in absorptance with increasing absorber amount in the path. Also, in the mid-infrared, where many features of trace atmospheric constituents occur, the Lorentz width approaches the Doppler width at heights between 30 and 40 km. Above this height the dependence of the absorption coefficient at $\Delta\nu = 0$ on the air density, decreases to zero and there is little advantage over the measurement of the equivalent width of the feature.

It can similarly be expected that the ability to discriminate the height of the absorber, based on the temperature dependence of the line width, is minimal because of the slow variation of temperature in the lower atmosphere. Line intensities are also temperature dependent and Toth (5) has suggested that the atmospheric temperature profile can be obtained by observing CO_2 absorption lines arising from high energy states

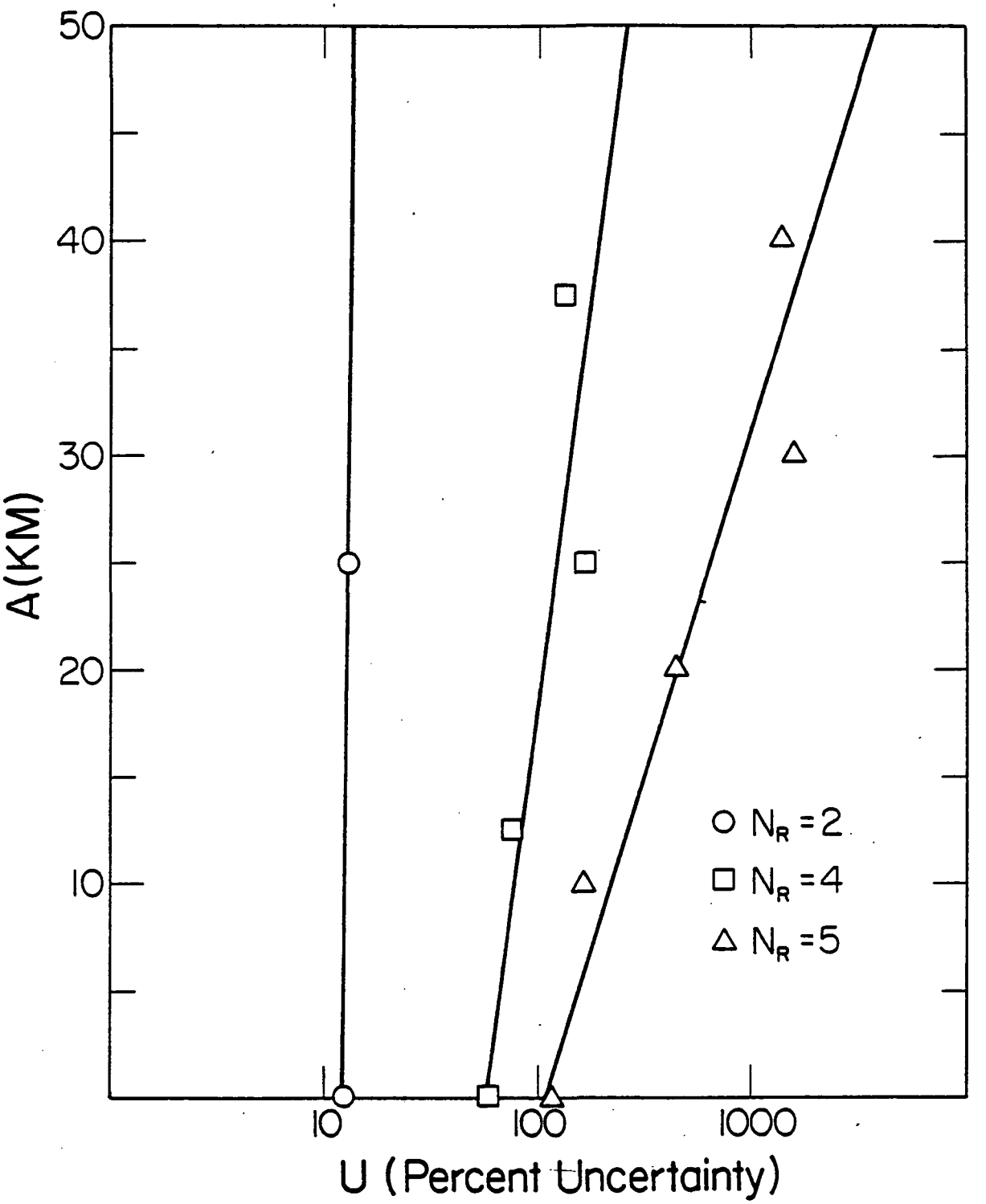

Figure 66: The uncertainty in the mixing-ratio values retrieved from data shown in Figure 65 for value spacings of 25, 12, and 10 km.

in solar spectra. However, only a small fraction of the total number of observable lines of most molecules have a strong temperature dependence. Analyses based on these effects will tend to emphasize the lower, warmer regions of the atmosphere. It is unlikely that these temperature variations can be used to obtain good profiles.

4.3 ANALYSIS OF ATMOS DATA

4.3.1 General comments

In the previous section we have shown that there is little added height discrimination for a ground observer by consideration of the line shape. This means that a mixing-ratio profile retrieved from a single line of a single spectrum obtained at ground-level can only contain a small number of discrete values, if no a priori assumptions about the shape are made. If several lines in the same spectrum are analyzed simultaneously the uncertainty in the retrieved mixing-ratio values should be reduced, but the vertical resolution is not expected to be improved. If, in addition, the spectrum analyzed has finite spectral resolution and if the spectral line parameters are uncertain the actual information content of the spectrum is less. Thus, from a single spectral line observed at ground-level it is expected that not more than one well-determined mixing-ratio value can be obtained. Therefore, unless the SNR is very high, for ground-level observations it is only possible to retrieve the total column amount of the absorber

(or one mean mixing-ratio value) (6). The retrieval of one mixing-ratio value is equivalent to assuming that the profile to be retrieved is constant with altitude. Since the mixing-ratio profiles of N_2O and CH_4 are essentially constant with altitude below 15 km (7), this assumption is appropriate for the retrievals discussed in this section.

In October 1982 in Lexington, Massachusetts, several solar spectra covering the region 600 to 4700 cm^{-1} were taken in a ground-level test of the ATMOS interferometer shown in Figure 2. The path difference of the interferometer was 103.92 cm and the spectral resolution was 0.0096 cm^{-1}. The average signal values as a function of wavenumber, shown in Figure 67, were obtained from 16 spectra in the region 2400 to 2600 cm^{-1}. The wavenumber spacing of these data was 0.0075 cm^{-1} and the observer altitude was 0.5 km above sea-level. The experimental conditions for these spectra are summarized in Table 25.

Since, as noted previously, not more than one mixing-ratio value can be expected from analysis of a ground-level spectrum we have analyzed the spectral data of Figure 67 by assuming the absorber mixing-ratio values to be retrieved were constant with altitude. By this method we have been able to obtain mean mixing-ratio values for N_2O and CH_4 using the spectral curve-fitting technique described below.

Figure 67: ATMOS spectra taken in October 1982 in Lexington, Massachusetts.


TRANSMITTANCE
0.00
0.50
1.00
2400.00
2440.00
2480.00
2520.00
2560.00
2600.
WAVENUMBER

Figure 67

Table 25: Experimental conditions for the recent test of the ATMOS instrument.

Location	Lexington, Massachusetts
Time	October 1982
Altitude	0.5 km above sea-level
Apparent zenith angle	60^{o}
Spectral region covered	600-4700 cm^{-1}
Path difference of instrument	103.92 cm
Spectral resolution	0.0096 cm^{-1}
Spacing of spectral values	0.0075 cm^{-1}

4.3.2 The spectral curve-fitting technique

The observed signal $I(\nu_i)$ obtained at frequency ν_i in an absorption spectrum is usually related to the absorber amount u encountered along the homogeneous path and the absorption coefficient $k(\nu_i)$ of the absorber by Beer's law

$$I(\nu_i) = I_o(\nu_i)\exp[-k(\nu_i)u] \quad , \tag{12}$$

where $I_o(\nu_i)$ is the signal obtained in the absence of the absorber and u is given by m x a where m is the mixing-ratio in the homogeneous path and a the optical airmass.

In the lower portion of the atmosphere the line shape can be assumed to be Lorentzian and given by

$$k_\ell(\nu_i) = \frac{S_\ell}{\pi} \frac{\alpha_\ell}{(\nu_i - \nu_{o\ell})^2 + \alpha_\ell^2} \tag{13}$$

for the ℓth spectral line. The dependence of the half-width α on the temperature and pressure is often written as

$$\alpha_\ell = \alpha_{o\ell}\left(\frac{T_o}{T}\right)^{\frac{1}{2}} \frac{P_o}{P} \tag{14}$$

and the line intensity S_ℓ as

$$S_\ell = S_{o\ell}\left(\frac{T_o}{T}\right)^{\beta} \exp[-E_\ell(T_o - T)/0.6946T\ T_o] \tag{15}$$

where $\beta = 1$ for N_2O and CH_4 (8). The reference temperature and pressure T_o and P_o for the AFGL line listing, used in this analysis, were 296 K and 1 atm respectively (9).

In order to analyze the data in Figure 67 the path of the observed radiation was partitioned into three regions in which the atmosphere was approximated by a homogeneous layer. This was accomplished by dividing the ray path into three portions such that the optical airmass encountered in each of the portions was identical to the others. The regions thus selected were 0.5 - 3.5 km, 3.5 - 8.5 km, and 8.5 - 40 km. The absorption coefficient was obtained assuming that the temperature in the ith region was given by the mass weighted average

$$T_i = \frac{\sum_{j=N_{oi}}^{N_i} a_j T_j}{a_i'} \tag{16}$$

where N_{oi} is the lower boundary of the ith region and N_i the upper boundary, and the pressure was given by

$$P_i = \frac{\sum_{j=N_{oi}}^{N_i} a_j P_j}{a_i'} . \tag{17}$$

The optical airmass a_i' in the ith region is

$$a_i' = \sum_{j=N_{oi}}^{N_i} a_j \tag{18}$$

where a_j is the airmass in the jth layer.

It is convenient to define a coefficient $K(\nu_i)$ by the relation

$$K(\nu_i) = \sum_{j=1}^{3} k_j(\nu_i) a_j' \quad . \tag{19}$$

Thus the signal for an absorber with constant mixing-ratio m is given by

$$I(\nu_i) = I_o(\nu_i) \exp[-m(\sum_{j=1}^{3} k_j(\nu_i) a_j')] \quad . \tag{20}$$

In general the absorption coefficient k_j is the sum of the contributions of all the lines in the spectrum. In practice an individual line will only affect the spectrum over some wavenumber range about the line center ν_o. Beyond this range the contribution of the line will be below the level of the experimental noise. In the calculations for this analysis we have assumed a range of 10 cm^{-1} for all the lines in the spectrum.

The spectrum analyzed, shown in Figure 67, contained two strong N_2O bands and some weak CH_4 lines. We have attempted to retrieve both the N_2O and the CH_4 mixing-ratio value assuming the mixing-ratio profiles to be constant with altitude. It was found that the spectral data were shifted by a constant amount over the entire spectral region. This shift was corrected prior to the retrieval of the mixing-ratio values.

Due to the strong wings of nearby CO_2 and N_2 bands the background in the observed spectrum is not constant. If small wavenumber regions (say 10 cm^{-1}) are considered the background I_o can be approximated by

$$I_o(\nu_i) = a_o + a_1(\nu_i - \nu_A) \tag{21}$$

where ν_A refers to the first wavenumber value in the 10 cm^{-1} region. Thus the signal at ν_i can be modeled by

$$I(\nu_i) = (a_o + a_1(\nu_i - \nu_A))\exp[-m_{N_2O}K_{N_2O} + m_{CH_4}K_{CH_4})] \tag{22}$$

if infinite spectral resolution is assumed. Lin et al (10) have shown that small frequency shifts in the spectrum can be modeled by including in the exponential the term

$$\Delta(\nu_i) = \frac{K(\nu_{i+1}) - K(\nu_{i-1})}{\nu_{i+1} - \nu_{i-1}} . \tag{23}$$

Thus Eq. (22) becomes

$$I(\nu_i) = (a_o + a_1(\nu_i - \nu_A))\exp[-(m_{N_2O}K_{N_2O} + m_{CH_4}K_{CH_4} + \alpha_o(\Delta_{N_2O}m_{N_2O} + \Delta_{CH_4}m_{CH_4}))] \tag{24}$$

where α_o is the magnitude of the frequency shift. The retrieved magnitude of α_o was always less than the wavenumber spacing of the data.

At each wavenumber value the coefficients K_{N_2O}, K_{CH_4}, Δ_{N_2O}, and Δ_{CH_4} were computed using the AFGL line listings (9) and assuming that the atmospheric temperature profile was given by the U.S. Standard Atmosphere (11) and the sea-level pressure was 1 atm. The parameters a_o, a_1, α_o, m_{N_2O}, and m_{CH_4} were obtained by fitting Eq. (24) to the spectral data shown in Figure 67 using non-linear least squares analysis techniques (1).

The effects of the instrument, which are usually modeled by the convolution of Eq. (24) with an instrument function, were not included since the spectral resolution of the data shown in Figure 67 (the spectral resolution is given in Table 25) was much less than the half-widths of N_2O or CH_4 at atmospheric pressure (9).

4.3.3 Some results from the analysis of ATMOS data

For convenience the ATMOS data were divided into eight 10 cm^{-1} regions as shown in Figure 68. In each region the parameters in Eq. (24) which give the smallest RSS were obtained by the non-linear least squares analysis technique (1).

The residuals obtained for the retrievals performed on the eight spectral regions are shown in Figures 69-76. The largest features appearing in these residual plots are due to

Figure 68: The eight spectral regions of the ATMOS data analyzed.

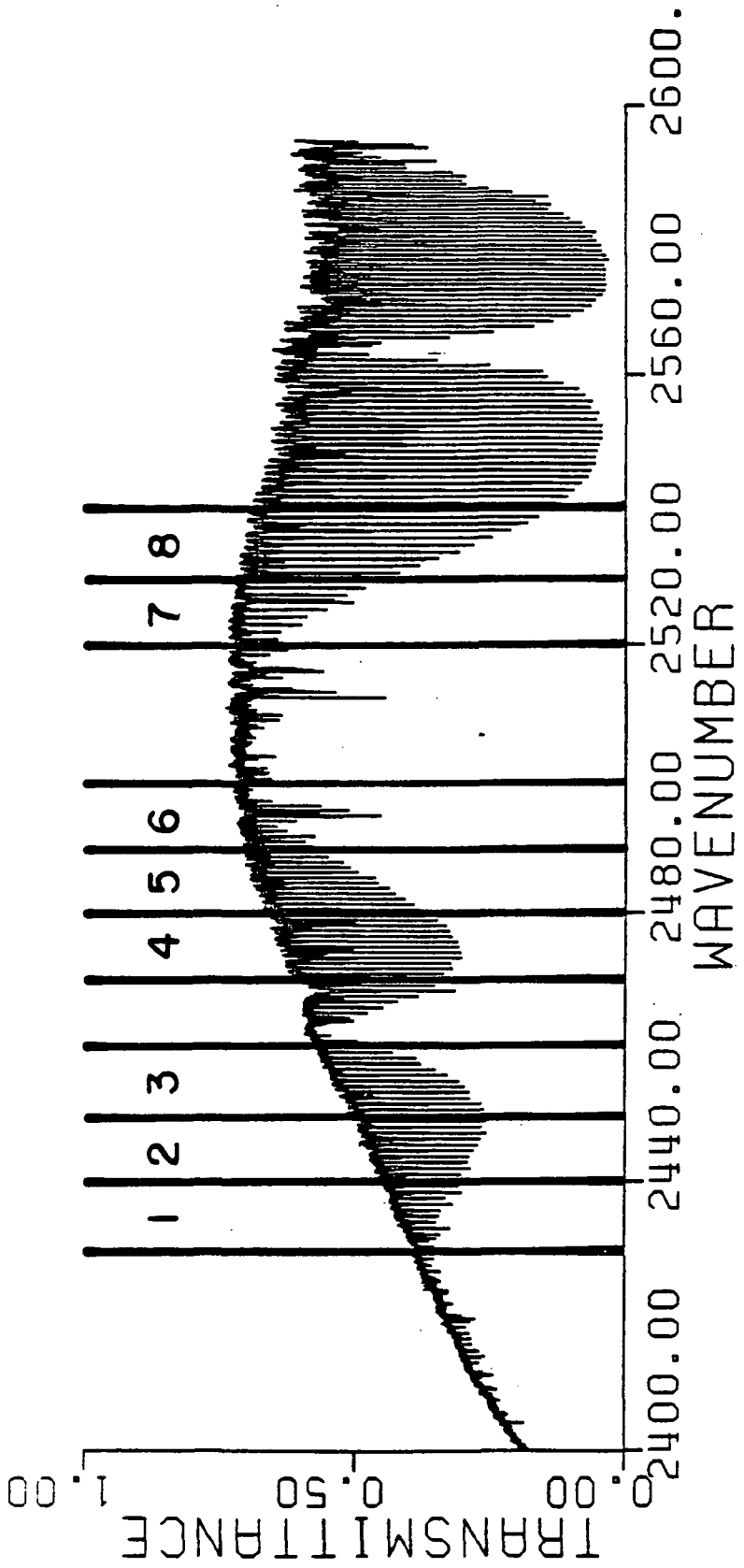
TRANSMITTANCE
0.00
0.50
1.00
2400.00
2440.00
2480.00
2520.00
2560.00
2600.
WAVENUMBER
1
2
3
4
5
6
7
8

Figure 68

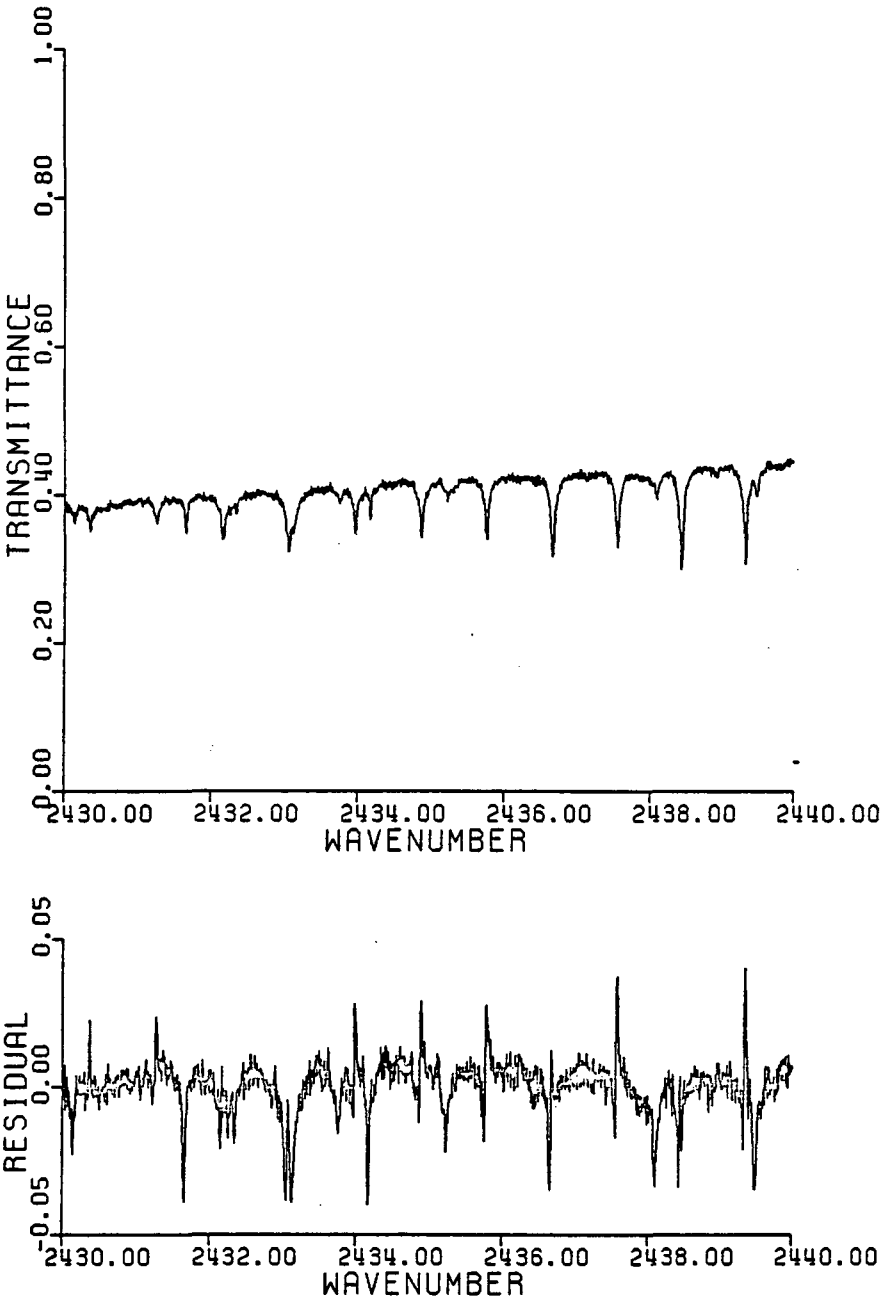

Figure 69: The ATMOS spectra and the residuals obtained by spectral curve-fitting in the region 2430-2440 cm^{-1}.

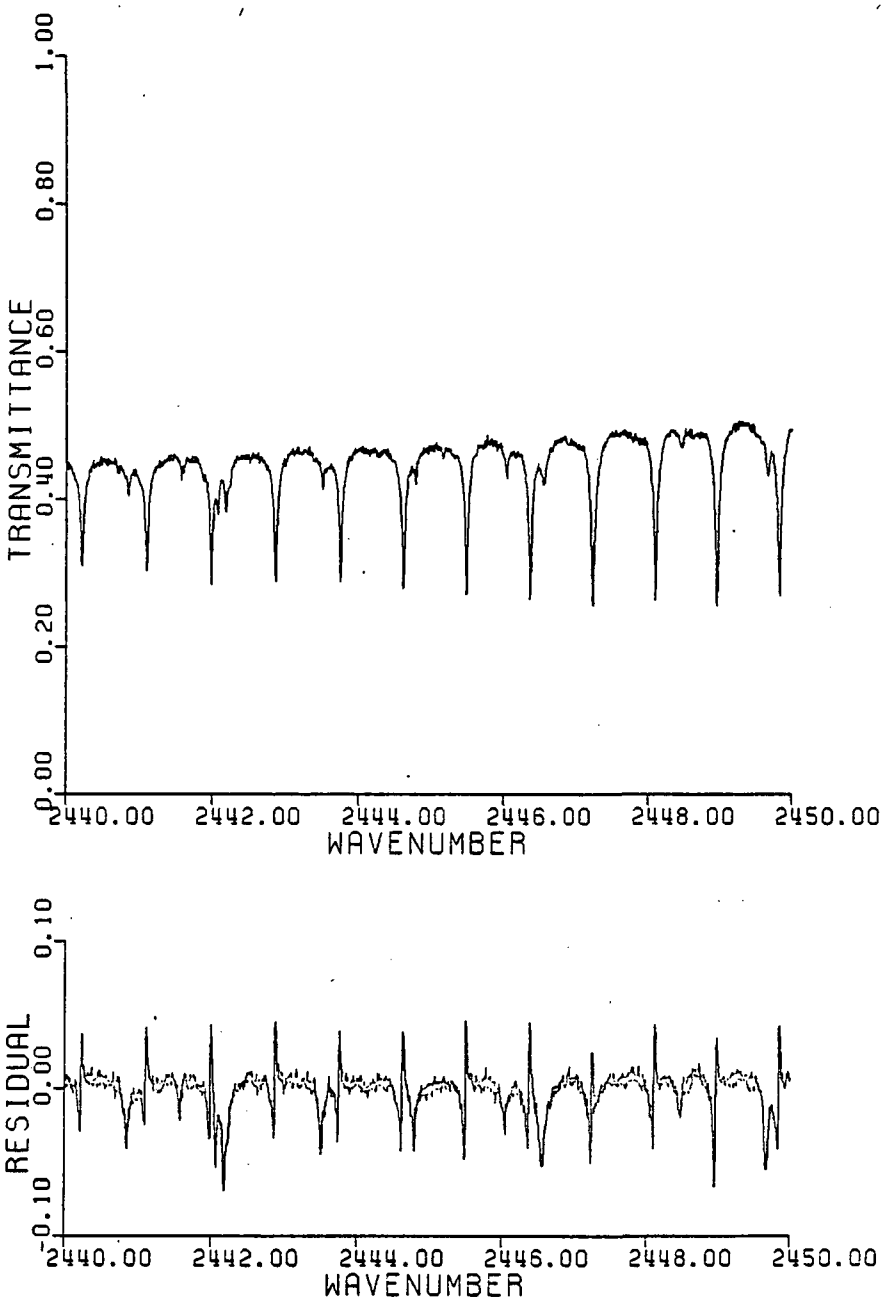

Figure 70: The ATMOS spectra and the residuals obtained by spectral curve-fitting inthe region 2440-2450 cm^{-1}.

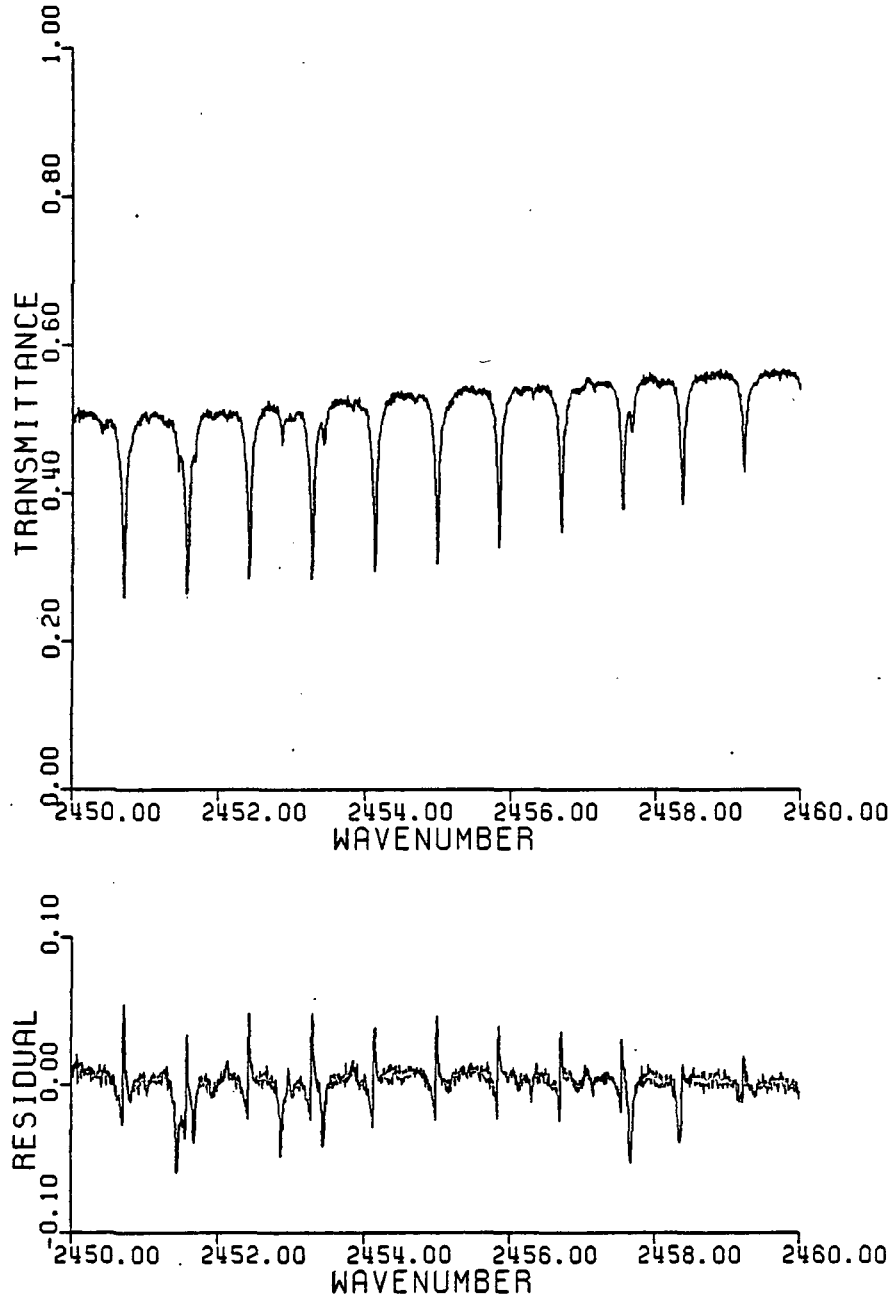

Figure 71: The ATMOS spectra and the residuals obtained by spectral curve-fitting in the region 2450-2460 cm^{-1}.

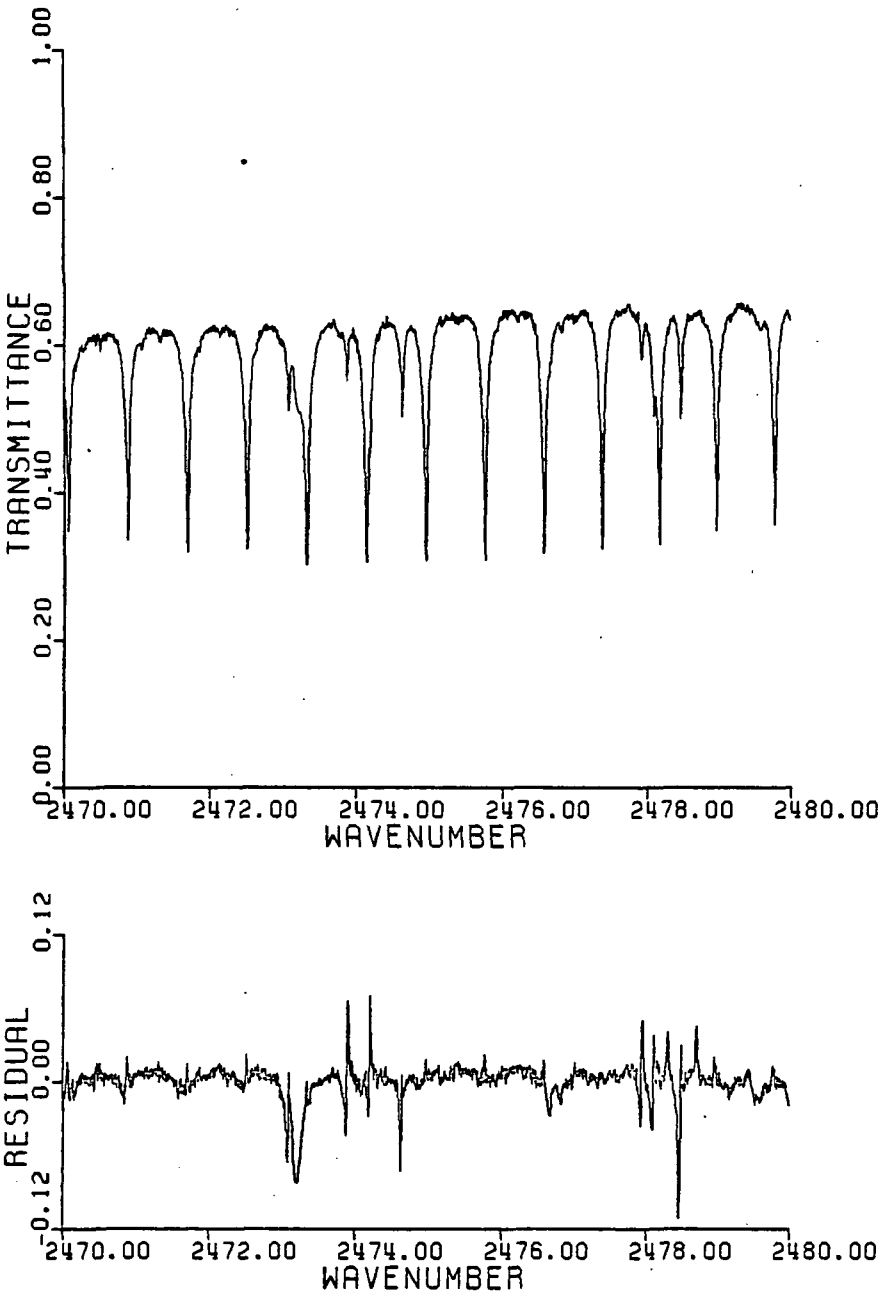

Figure 72: The ATMOS spectra and the residuals obtained by spectral curve-fitting in the region 2470-2480 cm^{-1}.

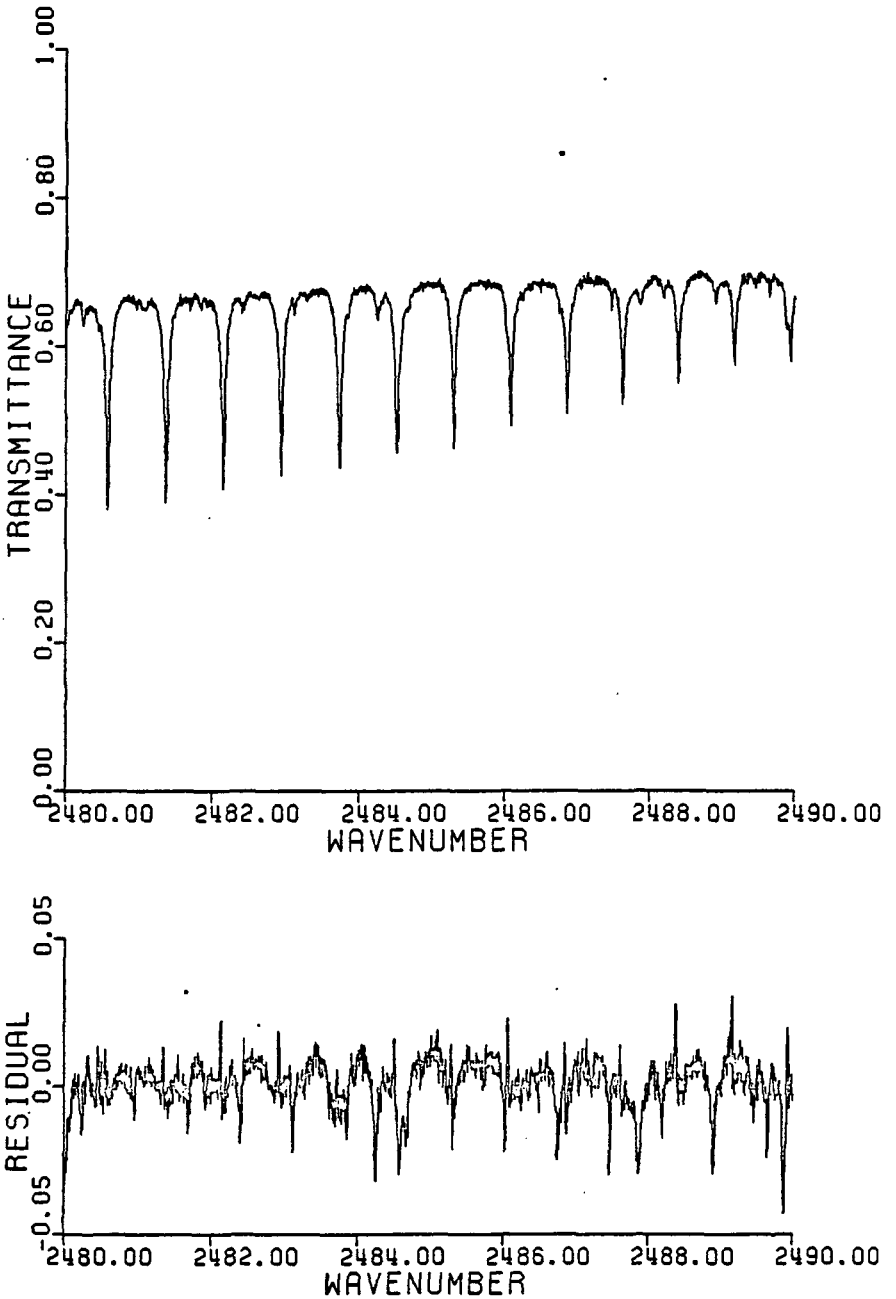

Figure 73: The ATMOS spectra and the residuals obtained by spectral curve-fitting in the region 2480-2490 cm^{-1}.

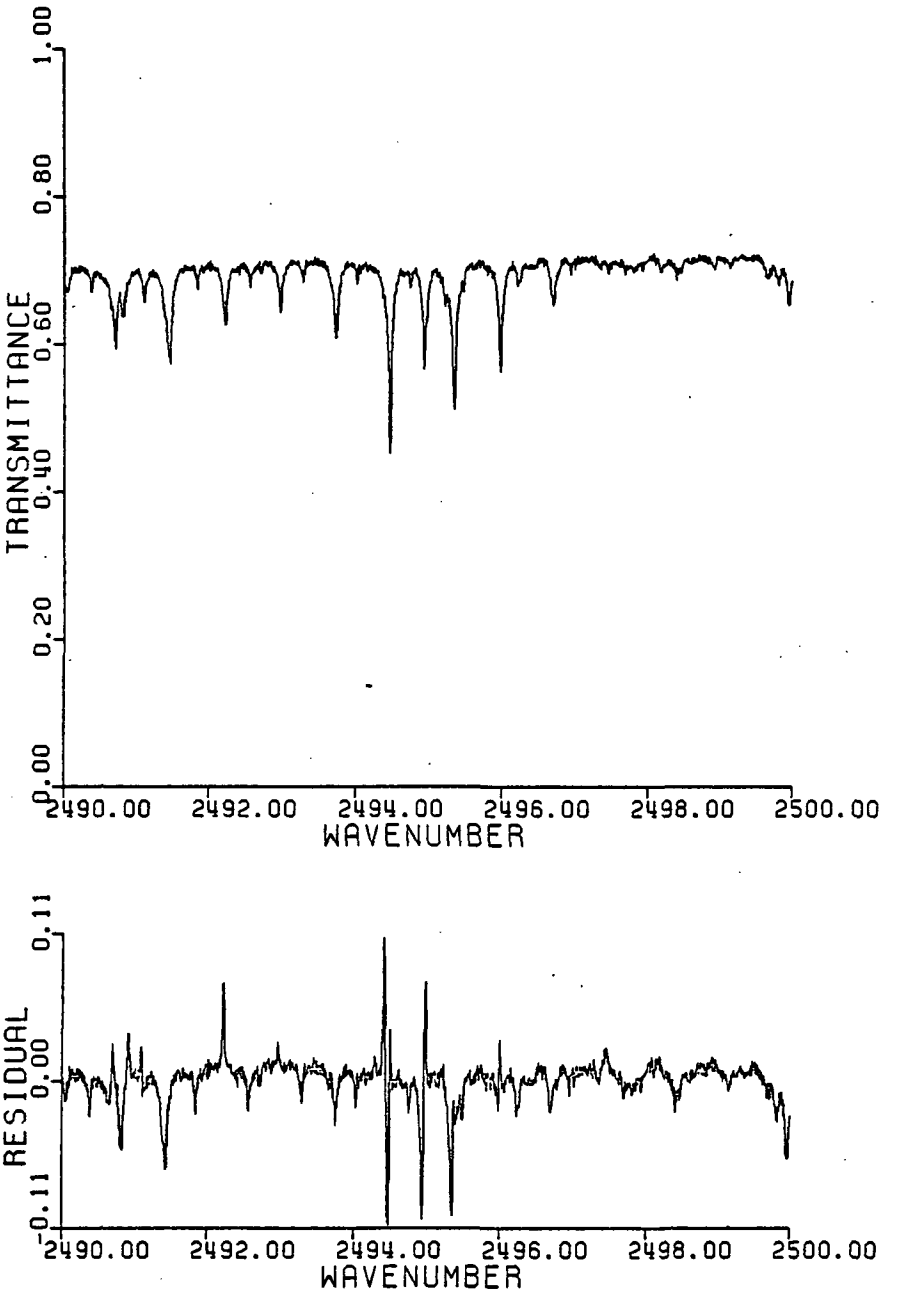

Figure 74: The ATMOS spectra and the residuals obtained by spectral curve-fitting in the region 2490-2500 cm^{-1}.

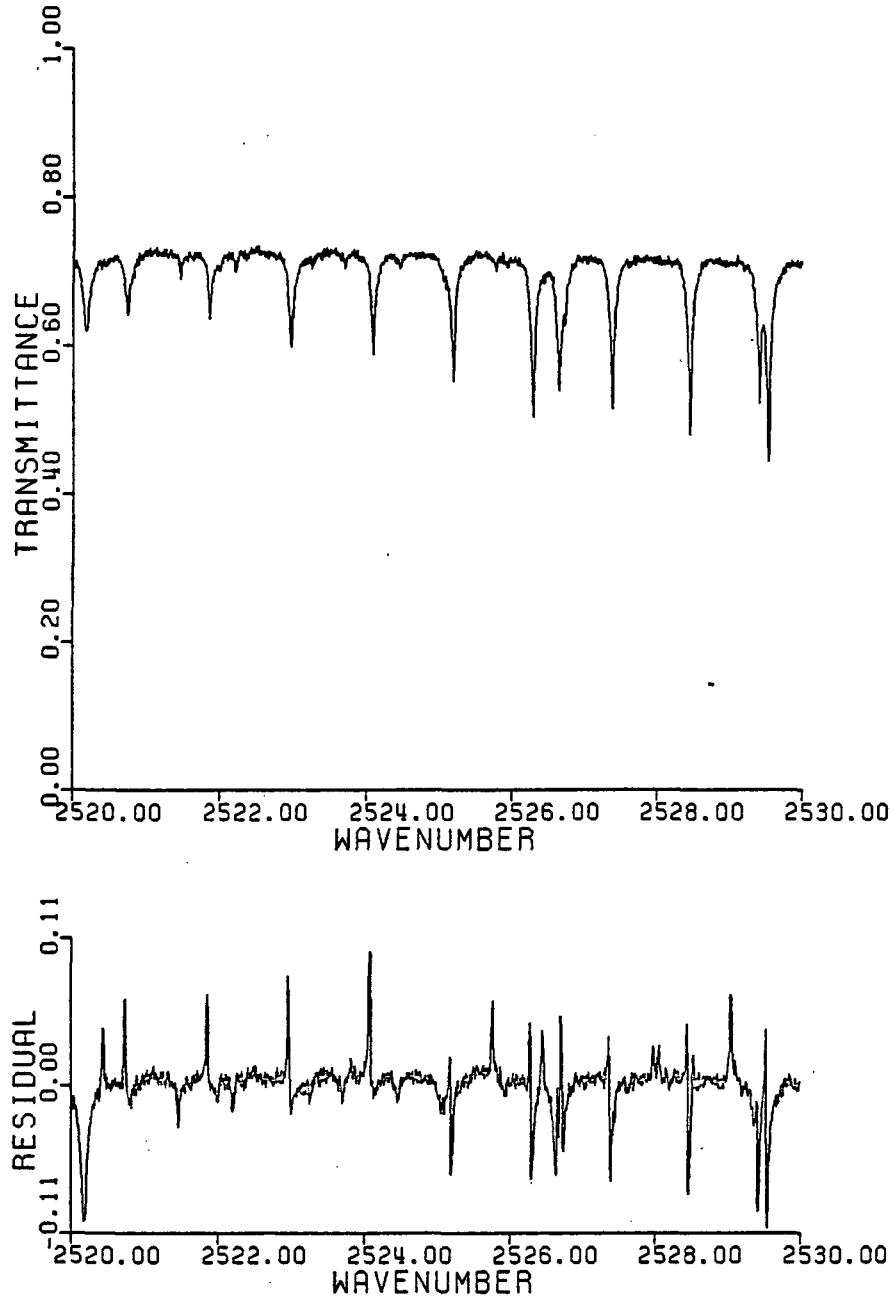

Figure 75: The ATMOS spectra and the residuals obtained by spectral curve-fitting in the region 2520-2530 cm^{-1}.

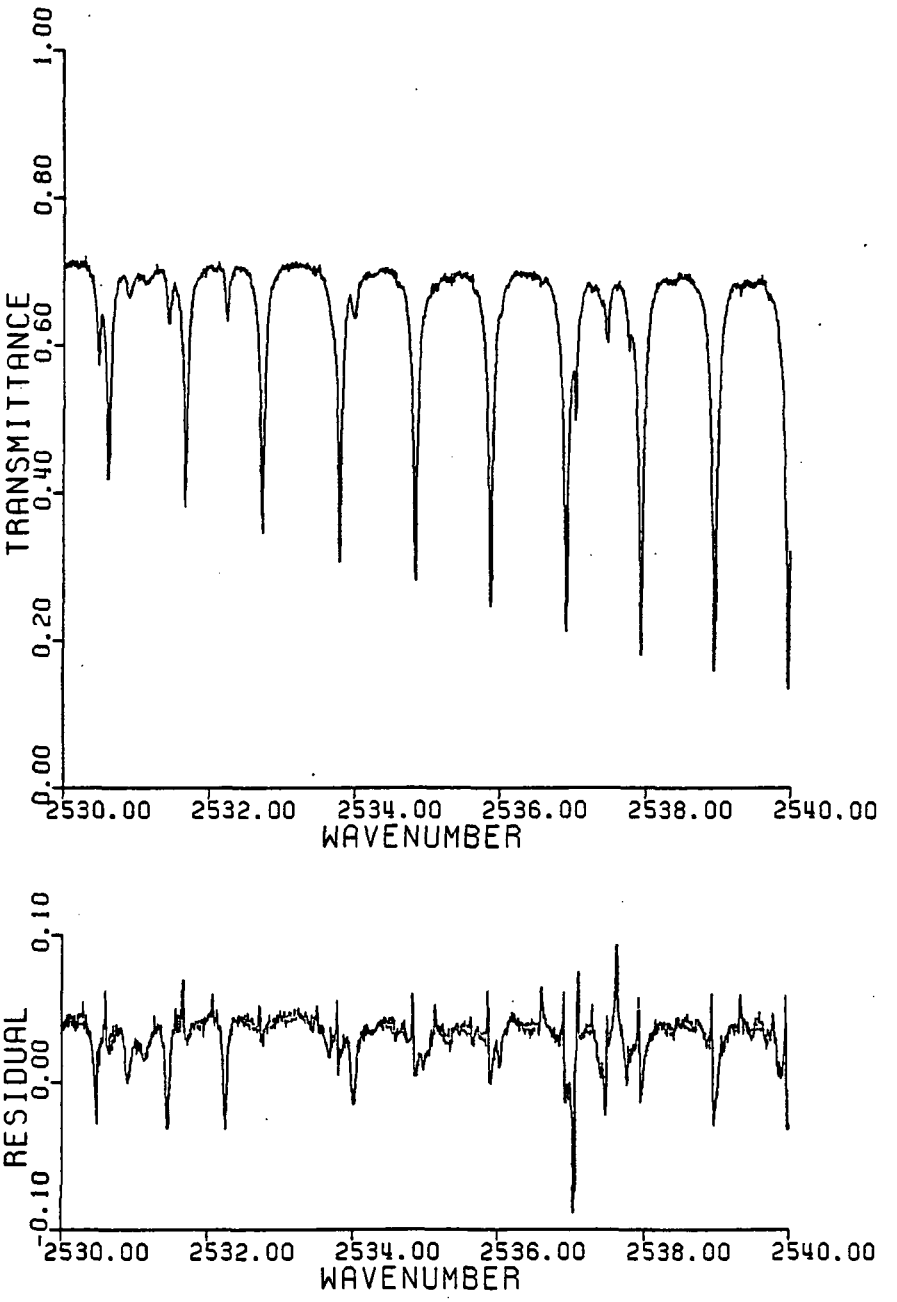

Figure 76: The ATMOS spectra and the residuals obtained by spectral curve-fitting in the region 2530-2540 cm^{-1}.

methane and water vapor lines not included in the AFGL listing and methane line intensities and positions with erroneous values. Another source of the features in these plots may be due to non-linearity of the instrument which causes the observed signal to increase non-linearly for increasing incident radiation on the instrument. This effect was found to be more noticeable in the stronger lines in the spectrum (12).

Several retrievals, not shown, were performed on the portion of the spectrum above 2440 cm^{-1} but the poor fit obtained in this region was attributed to the instrument non-linearity.

The mixing-ratio values obtained for N_2O and CH_4 in the eight regions are listed in Table 26. Due to the poor values given by the AFGL listing for the methane line parameters, the mixing-ratio values obtained for CH_4 vary widely over the regions studied and the uncertainties of these values were large. However, consistent values were found for the N_2O mixing-ratio values. The one exception was for region 7 (2520-2530 cm^{-1}).

Listed in Table 27 are some values for the mixing-ratio value of N_2O obtained by other investigators. The retrieved mixing-ratio values listed in Table 25 were found to be in agreement with those found by other investigators, thus demonstrating that the non-linear, least squares technique is capable of extracting information about the absorber from the spectrum.

Table 26: Mixing-ratio values retrieved by spectral curve-fitting of the ATMOS spectra.

Region #	$\Delta\nu$ (cm^{-1})	$m_{N_2O} \times 10^{-6}$	$m_{CH_4} \times 10^{-6}$	RSS
1	2430-2440	0.257 ± 0.052		0.091
2	2440-2450	0.252 ± 0.026		0.172
3	2450-2460	0.271 ± 0.026		0.109
4	2470-2480	0.266 ± 0.026	1.30 ± 0.65	0.272
5	2480-2490	0.254 ± 0.026	0.45 ± 0.91	0.086
6	2490-2500	0.286 ± 0.13	1.40 ± 0.52	0.326
7	2520-2530	0.187 ± 0.039	1.22 ± 0.65	0.411
8	2530-2540	0.247 ± 0.026	0.73 ± 0.39	0.285

Table 27: Comparison of retrieved N_2O mixing-ratio value to some values reported by other investigators.

Retrieved mixing-ratio of N_2O	Experimental method
262 ppb	average of retrieved values in this work (excluding region 7)
264 ppb	value at 14.6 km from analysis of absorption spectra from balloon-borne instrument (13)
308 ppb	air samples - aircraft (14)
286 ppb	air samples - ground-level (15)
255 ± 6 ppb	air samples - aircraft (16)
260 ppb	infrared absorption spectra from balloon-borne instrument (17)
270 ppb	ground-level infrared absorption spectral curve-fitting (18)
310 ppb	ground-level infrared absorption spectral curve-fitting (19)
300 ± 10 ppb	ground-level infrared absorption spectral curve-fitting (20)

Table 28: The effects of systematic errors on the mixing-ratio values retrieved from the ATMOS spectra for wavenumber region 2480-2490 cm^{-1}.

Physical parameter	Systematic error	Error in N_2O mixing-ratio	Error in CH_4 mixing-ratio	RSS
surface pressure	5%	-2.0%	-6.5%	0.083
temperature profile	5 K at all altitudes	2.0%	2.2%	0.088
line intensities	1% for all lines	-1.2%	-4.4%	0.086
line half-widths	5% for all lines	2.8%	-2.2%	0.083

The effects of systematic errors on the retrieved mixing-ratio values were examined by analyzing the data in Figure 68 assuming that the atmospheric temperatures were higher at all altitudes by 5 K, that the sea-level pressure was 5% larger, that the line intensities given from the AFGL listings are in error by 1%, and the line half-widths in error by 5%. Each error was considered independently. The mixing-ratio values obtained for N_2O and CH_4 together with the RSS retrieved for these systematic errors are listed in Table 28 for the spectral region 2480-2490 cm^{-1}. Comparison of the uncertainties listed in Table 26 with those due to the systematic errors shows that the effects of these errors are less than the uncertainty due to the experimental noise. Thus it is expected that for spectra obtained at ground-level systematic errors should not be significant provided that the SNR<200.

These results show that in order to improve the retrieved mixing-ratio values from spectral data better spectral line parameters are needed in order to calculate the absorption coefficients. The residuals could also be reduced by including instrumental effects such as finite resolution and non-linearity in the retrieval calculation. The results of Table 28 show that small uncertainties in the temperature and pressure values have little effect on the retrieved mixing-ratio values in this particular analysis.

4.4 SUMMARY

In this chapter we have investigated the information content of the shapes of spectral features. It was found that, for a ground-level observer, the height discrimination possible was not much better than that obtainable from the analysis of equivalent width data and the uncertainty at ground-level was actually larger than that obtained from equivalent width analysis (for a layer spacing of 25 km and an SNR of 100 the uncertainty in the retrieved mixing-ratio at ground-level was 12%). This uncertainty is due in part to incorrect AFGL parameters (9). Thus very limited vertical resolution is expected and only one mean mixing-ratio is expected from the curve-fitting of ground-level spectral data with an SNR of 100.

Spectral data obtained from a recent ground-level test of the ATMOS instrument were analyzed by non-linear least squares techniques in order to retrieve the mixing-ratio values of N_2O and CH_4. The N_2O mixing-ratio value of 262 ppb obtained by this analysis was found to be essentially in agreement with mixing-ratio values reported by other investigators.

For ground-level observations, systematic errors in the parameters describing the structure of the atmosphere or the spectral line parameters were found to have only a small effect on the retrieved mixing-ratio values (not more than a 3% error in the retrieved mixing-ratio value for a 5% error in sea-level pressure, 5 K error in the temperature profile, 1% error in the line intensities, or 5% error in the line half-widths). The

uncertainty in the retrieved mixing-ratio value due to experimental noise was much larger (~10%) than that caused by the systematic errors, in agreement with the results of the previous chapters.

The accuracy of the retrieved mixing-ratio values could be improved if instrumental effects such as non-linearity and the finite resolution of the instrument were included in the mathematical model. Improvement in these values (especially that obtained for CH_4) could also be obtained if the spectral line parameters are more accurately determined and if the apparent zenith angle of observation is more accurately known.

The analysis of ATMOS spectra obtained from ground-level is not a complete test of its possible performance in space. The data analyzed in this work were obtained from an early test of the ATMOS instrument which was conducted to determine any possible modifications needed in the experimental design. However, our analyses show that the ATMOS data are analyzable since the results in general confirm prediction. The spectral data collected by ATMOS in space are expected to be of much higher quality. Thus due to a more favorable observer geometry and higher quality data it is expected that accurate, high-resolution mixing-ratio profiles are retrievable from the analysis of ATMOS data.

REFERENCES

1) M. Brown, ed., BMDP Statistical Software 1981, Univ. California Press, Berkeley (1981).

2) L. Goldberg, Astrophys. J., 113, 567 (1951).

3) C. B. Farmer, Can. J. Chem., 52, 1544 (1974).

4) B. J. Conrath in Inversion Methods in Atmospheric Remote Sounding, A. Deepak, ed., pp. 155-193, Academic Press, New York (1977).

5) R. A. Toth, Appl. Opt., 16, 2661 (1977).

6) R. Zander, G. M. Stokes, and J. W. Brault, Geophys. Res. Lett., 10, 521 (1983).

7) The Stratosphere 1981: Theory and Measurement, WMO Global Ozone Research and Monitoring Project, Report no. 11, 1982.

8) G. Herzberg, Molecular Spectra and Molecular Structure II. Infrared and Raman Spectra of Polyatomic Molecules, Van Nostrand, New York, 505 (1945).

9) R. A. McClatchey, W. S. Benedict, S. A. Clough, D. E. Burch, R. F. Calfee, K. Fox, L. S. Rothman, and J. S. Garing, Environ. Res. Paper, No. 434, AFCRL-TR-73-0096 (1976).

10) C. L. Lin, E. Niple, J. H. Shaw, and J. G. Calvert, Appl. Spect., 33, 487 (1979).

11) U.S. Standard Atmospheric 1976, NOAA-S/T-76-1562, GPO, Washington, D.C. (1976).

12) R. Norton, Personal communication.

13) C. P. Rinsland, A. Goldman, F. J. Murcray, D. G. Murcray, M. A. H. Smith, R. K. Seals Jr., J. C. Larsen, and P. L. Rinsland, Appl. Opt., 21, 4351 (1982).

14) J. S. Levine and E. F. Shaw Jr., Nature, 303, 312 (1983).

15) R. F. Weiss, J. Geophys. Res., 86, 7185 (1981).

16) P. W. Krey, R. J. Lagomarsino, and M. Schonberg, Geophys. Res. Lett., 4, 271 (1977).

17) J. Hahn and C. Junge, Z. Naturforsch., 329, 190 (1977).

18) Y. S. Chang, J. H. Shaw,.J. G. Calvert, and W. M. Uselman, J. Quant. Spect. Rad. Trans., 19, 599 (1978).

19) Y. S. Chang, J. H. Shaw, J. G. Calvert, and W. M. Uselman, J. Quant. Spect. Rad. Trans., 18, 589 (1977).

20) Y. S. Chang, J. H. Shaw, J. G. Calvert, and W. M. Uselman, J. Quant. Spect. Rad. Trans., 19, 599 (1978).

Chapter V

CONCLUSIONS

5.1 INTRODUCTION

In this work we investigated the retrieval of constituent mixing-ratio profiles from solar absorption spectra by considering primarily the information contained in a single weak spectral line. This information consists of the total absorber amount, which can be obtained by measurement of the equivalent width of the line, and the shape of the spectral line. We investigated the retrieval of mixing-ratio profiles from equivalent width analysis of spectral lines and curve-fitting.

The methods used in this work to retrieve mixing-ratio profiles from spectral data required no a priori assumptions about the shape of the profile to be retrieved. These methods also retrieved all the mixing-ratio values simultaneously, and thus no errors were introduced into the solution by the analytical method. Our investigations have determined, for a given set of experimental conditions, the limit to the quality of the retrieved mixing-ratio profiles.

5.2 EQUIVALENT WIDTH DATA

From the analyses of sets of 125 synthetic total absorber amounts, corresponding to 125 different paths through

the atmosphere and observer altitudes of 500, 30, and 0 km, calculated using the slant path program of Snider and Goldman (1) and a constant mixing-ratio profile, we retrieved up to 100 discrete constituent mixing-ratio values between 0 and 50 km altitude by the linear least squares technique. The program used for the retrieval (P9R (2)) obtained both the discrete mixing-ratio values and their standard deviations. The retrieved standard deviations were used to determine the uncertainty in the mixing-ratio values due to simulated random noise as a function of altitude.

The uncertainty in the retrieved mixing-ratio values was found to increase exponentially with altitude (see Figures 16, 18, and 19), to be inversely proportional to the SNR (see Tables 4, 8, and 10) and $N_O^{\frac{1}{2}}$ (see Tables 5, 9, and 11), to be proportional to the number of retrieved mixing-ratio values N_R (see Figures 16, 18, and 19), to be independent of the observer altitude (Figure 19), and was 45 times larger for soundings in the atmosphere above the observer than below (Figure 18). These general relations were true independent of the mixing-ratio profile examined (section 2.7).

The vertical resolution of the retrieved mixing-ratio profiles for an uncertainty constant with altitude degraded exponentially with altitude (Eqs. (2.83) and (2.84)), was inversely proportional to the SNR and $N_O^{\frac{1}{2}}$, was proportional to the number of retrieved mixing-ratio values, was independent

of the observer altitude, and was 45 times worse above the observer than below. These vertical resolution relations can be used to determine the spacing of the mixing-ratio values which gives an uncertainty in the retrieved values constant with altitude (section 2.6.2).

The uncertainty expressions obtained in this work suggest that many investigators may have underestimated the errors in their reported retrievals from solar spectra. By the methods outlined in this work it is now possible to estimate the uncertainty in a mixing-ratio profile retrieval based entirely on the experimental conditions and not on any a priori assumptions about the errors.

5.3 SYSTEMATIC ERRORS

We have also investigated the effects of systematic errors in the sea-level pressure, the temperature profile, the observer altitude, the apparent zenith angle of arrival of the radiation, and the latitude of observation on the retrieval of mixing-ratio profiles from absorber amount data.
A synthetic data set with no added noise and a constant mixing-ratio profile was analyzed assuming errors in each of these quantities. The systematic error as a function of altitude was obtained by comparison of the retrieved values to the true profile. The errors obtained agree with those predicted from variation of the absorber amount equation.

The mixing-ratio error due to temperature profile error was found to increase linearly with altitude and was zero at an altitude approximately equal to the scale height (Figure 59). The mixing-ratio errors due to errors in the sea-level pressure, the observer altitude, the apparent zenith angle, and the latitude were found to be essentially independent of altitude (Figures 58, 60-62) suggesting that the effects of these systematic errors on the mixing-ratio profile are indistinguishable.

Other errors due to neglect of refraction, motion of the observing instrument and the field of view of the instrument were also investigated. The error due to neglect of refraction was found to increase rapidly with decreasing altitude below 25 km (Figure 57). The smearing due to motion of the observer causes the optical airmass traversed to change by up to 30%/sec (Figure 51) and the smearing due to the field of view of the instrument implies that the observed radiation will have traversed an optical airmass uncertain by up to 70% (for a 2 milliradian field of view). These effects must be properly modeled in order to retrieve meaningful mixing-ratio profiles.

An internal calibration method was presented by which these smearing effects and the other systematic errors can be eliminated. The mean optical airmass traversed by the radiation (as well as the tangent height of the radiation) can be determined by measuring the equivalent width of a weak

spectral line due to a gas with known constant mixing-ratio such as CO_2 in the spectrum containing the constituent spectral line to be measured. Effective values can be determined for the apparent zenith angle and the observer altitude from this optical airmass which eliminate the systematic errors. In addition, since both the CO_2 line and the constituent line are subjected to the same weighting over the path due to the smearing effects, these effects are eliminated. This allows many of the effects due to systematic errors and smearing to be removed from the retrieved mixing-ratio profiles of trace gases.

5.4 SPECTRAL CURVE-FITTING

The additional information contained in the shape of the spectral line was examined by using a non-linear least squares technique (2) to fit the spectral line shape. An ideal line was considered with no degradation due to finite resolution or smearing effects. It was found that for a Lorentz-shaped line the uncertainties in the retrieved mixing-ratio profile increased more slowly with altitude than that obtained from analysis of equivalent widths (Figures 18 and 66) but was much larger at 0 km for an SNR of 100. Thus the vertical resolution will not be much better if the spectral shape is analyzed than that if it is obtained from the analysis of equivalent widths.

A curve-fitting technique was used to analyze spectra near 2500 cm^{-1} obtained from a recent ground-level test of the ATMOS instrument to obtain mean mixing-ratio values for N_2O and CH_4. The retrieved CH_4 mixing-ratio value was not accurate due to poor line parameter values for CH_4 in the region studied given by the AFGL line listings (3). The mixing-ratio value obtained for N_2O was in agreement with those reported by other investigators (Table 27) but uncertainties in the apparent zenith angle and possible uncorrected non-linearities in the data preclude obtaining definitive absolute values for the N_2O mixing-ratio.

5.5 FINAL COMMENTS

The uncertainty and the vertical resolution of mixing-ratio profiles retrieved from spectral analysis depend on the number of observations, the tangent height spacing of these observations, the SNR, and the method of analysis. For an SNR of about 100 the vertical resolution of mixing-ratio profiles obtained from equivalent width analysis of a single spectral line from ATMOS spectra will not be better than 5 km due to spectral smearing. Thus the spacing of the retrieval values should not be less than 2.5 km. The uncertainties in the retrieved values will increase exponentially with altitude for a constant value spacing, however, these uncertainties can be reduced by increasing the mixing-ratio value spacing or by analyzing a number of spectral

lines in each spectrum.

Finally CO_2 lines in each spectrum can be used to internally calibrate the ATMOS data to eliminate the effects of the systematic errors and the spectral smearing. The resultant uncertainty in the values retrieved from equivalent width analysis of a single spectral line is not expected to be less than 10% due to uncertainties in the spectral line parameters (line intensities and half-widths) necessary for the internal calibration. However, this uncertainty can be reduced by using more accurate spectral parameters.

Other analytical techniques such as the simultaneous spectral curve-fitting of several spectra together with more accurate spectral line parameters may allow mixing-ratio profiles of trace gases with high vertical resolution and small uncertainties to be retrieved from analysis of ATMOS spectra. The ATMOS experiment will allow a large vertical range of coverage, the simultaneous retrieval of the mixing-ratio profiles of many trace gases, and the continuous monitoring of the temporal variations of these profiles. This information is essential for an understanding of the atmosphere.

REFERENCES

1) D. E. Snider and A. Goldman, "Refractive Evvects in Remote Sensing of the Atmosphere with Infrared Transmission Spectroscopy," BRL Report no. 1970, Ball. Res. Lab., Aberdeen Proving Grounds, Maryland (1975).

2) M. Brown, ed., BMDP Statistical Software 1981, Univ. California Press, Berkeley (1981).

3) R. A. McClatchey, W. S. Benedict, S. A. Clough, D. E. Burch, R. F. Calfee, K. Fox, L. S. Rothman, and J. S. Garing, Environ. Res. Paper, No. 434, AFCRL-TR-73-0096 (1976).

Appendix A

THE THEORY OF SLANT PATH CALCULATIONS

A.1 INTRODUCTION

To analyze spectral data obtained from radiation passing through the atmosphere it is necessary to know the influence of the atmosphere on the path traversed by the radiation and the amount of absorber encountered by the radiation. The variation of the air density and the refractive index of air with altitude make it difficult to do these calculations accurately. If the atmosphere is divided into concentric layers, as shown in Figures 3 and 77, the total path through the atmosphere is the sum of the paths through each layer.

The following derivation for the path traversed and the optical airmass encountered in each layer is based on the analysis of Treve (1,2). These relations have been used in the program described by Snider (3) and Snider and Goldman (4). A version of this program, modified to allow observer altitudes up to 500 km was used to perform all the ray path calculations in this work.

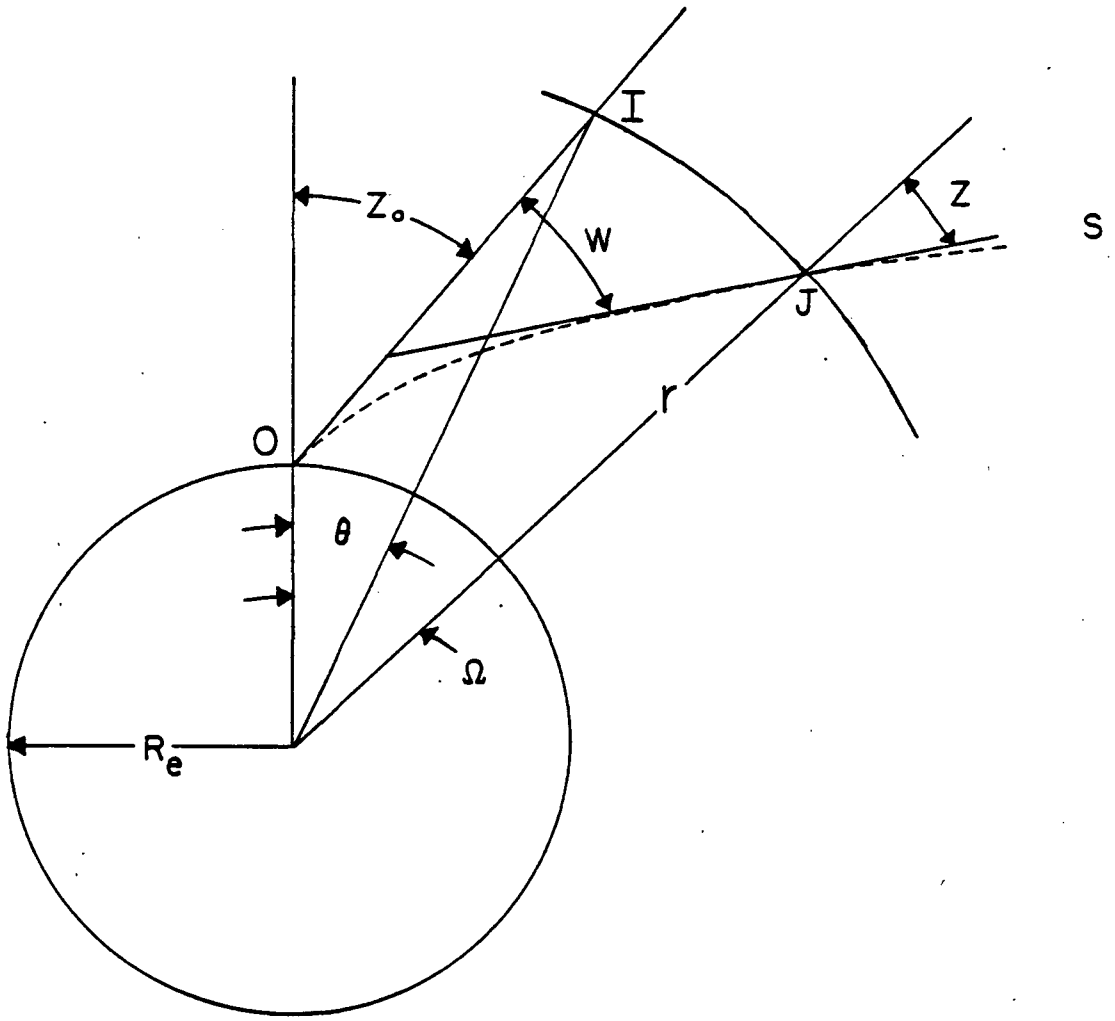

Figure 77: The slant path of radiation through the refracting atmosphere.

A.2 ASSUMPTIONS USED IN THE DERIVATION

The method described by Treve makes several assumptions about the physical properties of the atmosphere and the shape of the earth. The effects of turbulence in the atmosphere have not been considered. The assumptions used were:

1) The local surface of the earth is spherical, although the earth's radius is latitude dependent.
2) The index of refraction of the atmosphere depends only on the altitude.

From assumption 1) the radial vectors joining the earth's center and the points along the ray path (shown in Figure 77) will be normal to the local earth's surface. Based on assumption 2) the path will lie in the plane defined by O, J. and the center of the earth (see Figure 77). The ray tracing problem reduces to a two-dimensional calculation in this plane. These assumptions also imply that Fermat's principle yields

$$nr\sin z = \text{constant} \tag{1}$$

where z is the local zenith angle of the ray, r the radius vector, and n the index of refraction.

3) The index of refraction is given by the Lorenz-Lorentz formula (5).

4) The atmosphere contains no water vapor.

5) The composition of the atmosphere is constant with position so that the number of dispersive molecules per unit volume is proportional to the density. Thus the Lorenz-Lorentz formula is

$$\frac{1}{\rho_m}\frac{n^2-1}{n^2+2} = \text{constant} \tag{2}$$

where ρ_m is the mass density of air.

6) The atmosphere is in hydrostatic equilibrium. Consequently the pressure P is given in terms of the altitude A by the differential equation

$$dP = -g\rho_m dA \tag{3}$$

where the acceleration due to gravity g is altitude dependent.

7) The atmosphere is a perfect gas obeying

$$\rho_m = \frac{PM}{R^*T} \, . \tag{4}$$

8) The pressure is given by

$$P = k\rho_m^{\Gamma} \, . \tag{5}$$

By use of the other assumptions Γ is found to depend on the atmospheric temperature gradient which varies with height. Although Eq. (5) is used by Treve (1,2) and Snider and Goldman (4) it is not necessary for the derivation of the relations used for the slant path calculation, as will be shown. It is used here to be consistent with the formalism developed by Treve and Snider and Goldman.

9) The variation of the index of refractions with wavelength of dry air at T = 288 K and P - 1 atm is given by Edlen's formula (6)

$$(n-1)\times 10^8 = 6432.8 + 2949810.(146-1/\lambda^2)^{-1} + 25540(41-1/\lambda^2)^{-1} \qquad (6)$$

where the wavelength λ is in μm.

10) The ith layer is characterized by the values A_i and A_{i+1} of the altitude at the bottom and top of the layer, the temperature T_i at the bottom of the layer and $(dT/dA)_i$ within the layer.

A.3 THE GEOPOTENTIAL ALTITUDE

It is convenient for calculations describing the earth's atmosphere to use the geopotential height equivalent for the geometric altitude A. The potential energy per unit mass at altitude A is given by

$$\mu = \int_0^A g(A)dA \ . \qquad (7)$$

The geopotential meter m′ is defined as the work done in lifting a unit mass one geometric meter through a region in which the acceleration due to gravity is identically $g_o = 9.80665$ m/s. Thus the geopotential height is given by

$$H = \frac{\mu}{g_o'} \tag{8}$$

where g_o' has magnitude g_o and units m^2/s^2m'. Combining Eqs. (7) and (8) gives

$$H = \frac{1}{g_o'}\int_o^A g(A)dA \ . \tag{9}$$

The acceleration due to gravity at altitude A is obtained using Newton's law of gravitation

$$g = g_o \left(\frac{R_e}{R_e+A}\right)^2 \ . \tag{10}$$

The geopotential equivalent of geometric altitude A is found by evaluation of the integral

$$H = \frac{1}{g_o'}\int_o^A g_o \left(\frac{R_e}{R_e+A}\right)^2 dA \ . \tag{11}$$

Integration of Eq. (11) yields

$$H = \frac{g_o}{g_o'}\left(\frac{R_e A}{R_e+A}\right) \ . \tag{12}$$

The term g_o/g_o' (= 1 m'/m) is the conversion factor from geometric to geopotential meters. If $\gamma = g_o/g_o'$ Eq. (12) becomes

$$H = \gamma \left(\frac{R_e A}{R_e + A} \right) \quad . \tag{13}$$

In terms of the radial position r (= $R_e + A$) the geopotential height is

$$H = \gamma R_e^2 \left(\frac{1}{R_e} - \frac{1}{r} \right) . \tag{14}$$

Using Eq. (13) the geopotential height of any geometric altitude can be calculated. The zero of geopotential is at sea level at all latitudes.

A.4 THE RAY GEOMETRY

The path of radiation leaving the source at astronomical zenith angle Z_S and arriving at the observer at apparent zenith angle Z_o is shown in Figure 77.* By similar triangles the angular refraction W is

$$W = Z + \Omega - Z_o \tag{15}$$

where Z is the zenith angle at intermediate point J.

*Note that any point along the path can be considered the source or the observer, so that Figure 77 and the formalism developed here are also true in each individual layer.

If the ray is traced towards the source from point J a distance ds, as in Figure 78, the radius r is increased by dr and the polar angle by $d\Omega$. Thus

$$\tan Z = \frac{r d\Omega}{dr} \tag{16}$$

and

$$\cos Z = \frac{dr}{ds} \quad . \tag{17}$$

In terms of the zenith angle Z

$$d\Omega = \tan Z \frac{dr}{r} \tag{18}$$

and

$$ds = \frac{dr}{\cos Z} \quad . \tag{19}$$

Application of the law of sines on the triangle shown in Figure 79 gives

$$\frac{r_o}{\sin(Z_o-\theta)} = \frac{r}{\sin(180^o-Z_o)} \tag{20}$$

where θ is the polar angle of the apparent location of point J. Equation (20) simplifies to

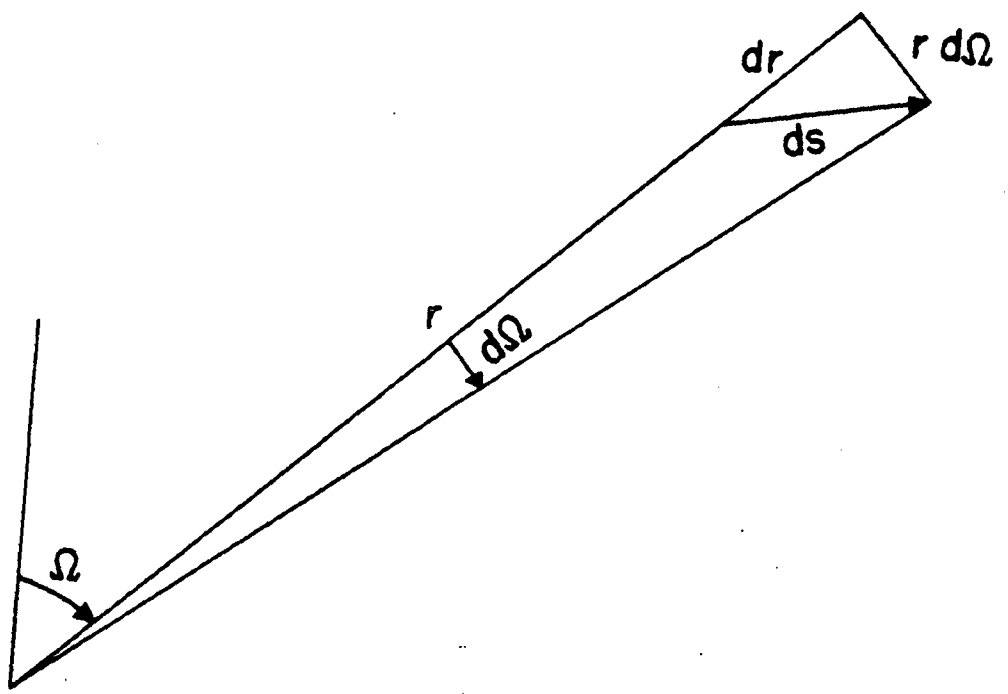

Figure 78: The incremental slant path.

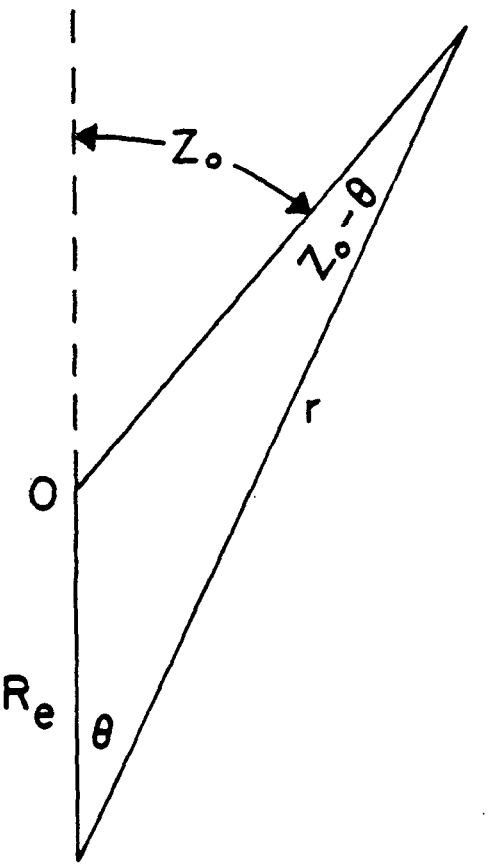

Figure 79: The apparent zenith angle - apparent polar angle slant path triangle.

$$r\sin(Z_o - \theta) = r_o \sin Z_o \ . \tag{21}$$

A.5 THE ATMOSPHERIC PARAMETERS

The hydrostatic equation can be expressed in terms of the geopotential height using the differential form of Eq. (9)

$$gdA = g_o' dH \ . \tag{22}$$

Combining Eqs. (22) and (3) gives

$$dP = -g_o' \rho_m dH \ . \tag{23}$$

The differential of Eq. (5) is

$$dP = k\Gamma \rho_m^{\Gamma-1} d\rho_m \ . \tag{24}$$

The ideal gas law together with Eq. (5) gives

$$dT = \frac{Mk(\Gamma - 1)\rho^{\Gamma-2} d\rho_m}{R^*} \tag{25}$$

Substitution of Eqs. (22) and (23) into Eq. (25) yields

$$dT = -\frac{g_o' M}{R^*} \frac{(\Gamma - 1)}{\Gamma} dH \ . \tag{26}$$

Integration of Eq. (26) gives the temperature as

$$T = T_o + L_o(H-H_o) \tag{27}$$

where

$$L_o = \frac{\Delta T}{\Delta H} = - \frac{g_o' M}{R^*} \frac{(\Gamma - 1)}{\Gamma} . \tag{28}$$

The exponent Γ of Eq. (5) is given in terms of the temperature gradient by

$$\Gamma = \frac{g_o M/R^*}{L_o + g_o' M/R^*} . \tag{29}$$

Thus Γ varies with altitude and for the U.S. Standard Atmosphere 1976 (7) has values in the range $-1.4<\Gamma<1.4$. The expression given in Eq. (5), which has the form of the adiabatic equation, does not correctly describe the earth's atmosphere since the atmospheric motion is generally not adiabatic (8). As will be shown, assumption 8) is not necessary. Alternate derivations performed without using this assumption yielded identical relations for the pressure at altitude A. This derivation is described in the next section. The formalism using Γ is given below.

Rearranging the terms in Eq. (24) gives

$$d\rho_m = \frac{dP}{k \Gamma \rho_m^{\Gamma - 1}} \tag{30}$$

Combining with Eq. (23), Eq. (30) becomes

$$\frac{d\rho_m}{\rho_m} = - \frac{g_o' dH}{k\Gamma \rho_m^{\Gamma-1}} \tag{31}$$

which with the ideal gas law reduces to

$$\frac{d\rho_m}{\rho_m} = - \frac{1}{\Gamma} \frac{g_o' M}{R^*} \frac{dH}{T} . \tag{32}$$

But T(H) has been found in Eq. (27). Let $\alpha = 1/(\Gamma - 1)$ and $\beta = g_o' M/R^* T_o$. Equation (31) becomes

$$\frac{d\rho m}{\rho_m} = - \frac{\beta}{\Gamma} \frac{dH}{1 + \frac{L_o}{T_o} (H-H_o)} . \tag{33}$$

If $\Gamma \neq 1$ Eq. (33) integrates to give

$$\ln \frac{\rho_m}{\rho_{mo}} = - \frac{\beta}{\Gamma} \frac{T_o}{L_o} \ln[1 + \frac{L}{T_o} (H-H_o)] \tag{34}$$

or

$$\frac{\rho_m}{\rho_{mo}} = [1 + \frac{L_o}{To} (H-H_o)]^{\alpha} \tag{35}$$

If $\Gamma = 1$ then $L = 0$. So Eq. (33) gives upon integration

$$\rho_m = \rho_{mo} \exp[- \beta (H-H_o)] . \tag{36}$$

With Eq. (28) and the definition of β, Eqs. (35) and (36) can be written in the form

$$P = \begin{cases} P_o \left[\dfrac{T_o}{T_o + L_o(H-H_o)} \right]^{\frac{g_o' M}{R^* L_o}} & L_o \neq 0 \\ P_o \exp\left[- \dfrac{g_o' M}{R^* T_o} (H-H_o) \right] & L_o = 0 \end{cases} . \tag{37}$$

A.6 ALTERNATE DERIVATION OF P(H)

The hydrostatic equation, Eq. (23), when combined with ideal gas law gives

$$\frac{dP}{P} = - \frac{g_o' M}{R^* T} dH . \tag{38}$$

The earth's atmosphere up to an altitude of 86 km can be divided into segments in which the temperature gradient is constant. Thus the temperature is given by Eq. (27). Substitution of T(H) into Eq. (38)gives

$$\frac{dP}{P} = - \frac{M g_o'}{R^*} \frac{dH}{T_o + L_o(H-H_o)} . \tag{39}$$

If $L_o = 0$

$$P = P_o \exp \left[- \frac{g_o' M}{R^* T_o} (H-H_o) \right] . \tag{40}$$

If $L_o \neq 0$ then

$$P = P_o \left[\frac{T_o}{T_o + L_o(H-H_o)} \right]^{\frac{g_o' M}{R^* L_o}} . \tag{41}$$

These equations are identical to Eq. (37). Therefore it is not necessary to assume the gas motion is adiabatic (assumption 8)), since the same relations are found by assuming that the temperature gradient is constant in discrete regions of the atmosphere.

A.7 THE POLAR ANGLE Ω

The polar angle Ω of point J can be found in terms of the apparent polar angle θ of point J from (see Eq. (16))

$$d\Omega = \tan Z \frac{dr}{r} \tag{42}$$

where dr/r is given by the differential of Eq. (21)

$$dr\sin(Z_o - \theta) - r\cos(Z_o - \theta)d\theta = 0 \ . \tag{43}$$

Therefore

$$\frac{dr}{r} = \cot(Z_o - \theta)d\theta \ . \tag{44}$$

Fermat's principle can be expressed as

$$nr\sin Z = n_o r_o \sin Z_o \ . \tag{45}$$

If this equation is combined with Eq. (21)

$$\sin Z = \frac{n_o}{n} \sin(Z_o - \theta) \quad . \tag{46}$$

Thus

$$\tan Z = \frac{\frac{n_o}{n} \sin(Z_o - \theta)}{\sqrt{1 - \frac{n_o^2}{n} \sin^2(Z_o - \theta)}} \quad . \tag{47}$$

Let

$$u = 1 - \left(\frac{n}{n_o}\right)^2 \quad . \tag{48}$$

Equation (48) combined with Eq. (47) gives

$$\tan Z = \frac{\cos (Z_o - \theta)}{\sqrt{\cos^2(Z_o - \theta) - u}} \tan (Z_o - \theta) \tag{49}$$

or

$$\tan Z = \left(1 - \frac{u}{\cos^2(Z_o - \theta)}\right)^{-1} \tan (Z_o - \theta) \quad . \tag{50}$$

Combining Eqs. (42), (44), and (50) yields

$$d\Omega = \left(1 - \frac{u}{\cos^2(Z_o - \theta)}\right)^{-\frac{1}{2}} d\theta \quad . \tag{51}$$

The apparent polar angle at the source θ_s is given from Eq. (21) by

$$\theta_s = Z_o - \sin^{-1}\left(\frac{R_e + A_o}{R_e + A_s} \sin Z_o \right) \tag{52}$$

where A_o is the observer height and A_s the source height. Integration of Eq. (51) gives

$$\Omega = \int_o^{\theta_s} \left(1 - \frac{u}{\cos^2(Z_o - \theta)}\right)^{-\frac{1}{2}} d\theta \ . \tag{53}$$

A.8 THE REFRACTIVE ANGLE W

The angular refraction W is given in differential form from Eq. (15) by

$$dW = dZ + d\Omega \tag{54}$$

where $d\Omega$ is defined by Eq. (16). The differential of Eq. (45) gives

$$n\sin Z\, dr + r\sin Z\, dn + nr\cos Z\, dz = 0 \ . \tag{55}$$

Solving for dr

$$dr = \frac{-\sin Z\, r dn - nr\cos Z\, dz}{n\sin Z} \tag{56}$$

or

$$\frac{dr}{r} = -\frac{dn}{n} - \cot Z \, dz \quad . \tag{57}$$

Thus

$$d\Omega = -\tan Z \frac{dn}{n} - dZ \tag{58}$$

and

$$dW = -\tan Z \frac{dn}{n} \quad . \tag{59}$$

The differential of Eq. (48) gives

$$du = -\frac{2ndn}{n_o^2} \quad . \tag{60}$$

Equations (48) and (60) yield

$$\frac{dn}{n} = -\frac{1}{2} \frac{du}{1-u} \quad . \tag{61}$$

Combining Eqs. (16), (59), and (61)

$$dW = \frac{1}{2} r \frac{d\Omega}{dr} \frac{1}{1-u} du \tag{62}$$

or

$$dW = \frac{1}{2} \frac{r}{1-u} \frac{d\Omega}{d\theta} \frac{du}{dr} d\theta \quad . \tag{63}$$

With Eqs. (20) and (51), Eq. (63) becomes

$$dW = \frac{1}{2} \frac{r_o \sin Z_o}{(1-u)\sin(Z_o - \theta)} \left(1 - \frac{u}{\cos^2(Z_o - \theta)}\right)^{-\frac{1}{2}} \frac{du}{dr} d\theta \qquad (64)$$

where u and du/dr are functions of θ.

A.9 DETERMINATION OF $u(\theta)$ AND $du(\theta)/dr$

The quantity $u(\theta)$ and consequently $du(\theta)/dr$ can be obtained using the Lorenz-Lorentz formula

$$\frac{1}{\rho_m} \frac{n^2 - 1}{n^2 + 2} = \frac{1}{\rho_{mo}} \frac{n_o^2 - 1}{n_o^2 + 2} \qquad (65)$$

and introducing the terms

$$\omega = 1 - \frac{\rho_m}{\rho_{mo}} \qquad (66)$$

and

$$\varepsilon_o = n_o - 1 \ . \qquad (67)$$

Rearranging Eq. (65) with Eq. (48) gives

$$\frac{(1-u) - \frac{1}{n_o^2}}{(1-u) - \frac{2}{n_o^2}} = \frac{\rho_m}{\rho_{mo}} \frac{n_o^2 - 1}{n_o^2 + 2} \qquad (68)$$

Solving Eq. (68) for u

$$u = 1 + \frac{\frac{1}{n_o^2} + \frac{2}{n_o^2}\frac{\rho_m}{\rho_{mo}}\frac{n_o^2 - 1}{n_o^2 + 2}}{\frac{\rho_m}{\rho_{mo}}\frac{n_o^2 - 1}{n_o^2 + 2} - 1} \quad . \tag{69}$$

Combining the terms in Eq. (69) and multiplying by $(n_o^2 + 2)/(n_o^2 + 2)$ gives

$$u = \frac{\frac{\rho_m}{\rho_{mo}}(n_o^2 - 1) - (n_o^2 + 2) + \frac{n_o^2 + 2}{n_o^2}\frac{2}{n_o^2}\frac{\rho_m}{\rho_{mo}}(n_o^2 - 1)}{\frac{\rho_m}{\rho_{mo}}(n_o^2 - 1) - (n_o^2 + 2)} \quad . \tag{70}$$

Collecting terms in ρ_m/ρ_{mo}

$$u = \frac{\frac{1}{n_o^2}\left[\frac{\rho_m}{\rho_{mo}}(n_o^2 + 2)(n_o^2 - 1) - (n_o^2 + 2)(n_o^2 - 1)\right]}{\frac{\rho_m}{\rho_{mo}}(n_o^2 - 1) - (n_o^2 + 2)} \quad . \tag{71}$$

In terms of ω Eq. (71) is

$$u = \frac{-\frac{1}{n_o^2}\omega(n_o^2 + 2)(n_o^2 - 1)}{\omega(I - n_o^2) - 3} \tag{72}$$

or

$$u = \frac{\frac{\omega}{n_o^2}(n_o - 1)(n_o^2 + 2)(n_o + 1)}{3(1 + \frac{1}{3}\omega(n_o^2 - 1))} \quad . \tag{73}$$

Substituting ε_o from Eq. (67) into Eq. (73)

$$u = \frac{\frac{2\varepsilon_o\omega}{n_o^2}(1 + \frac{\varepsilon_o}{2})(3 + 2\varepsilon_o + \varepsilon_o^2)}{3\ 1 + \frac{2}{3}\omega\varepsilon_o(1 + \varepsilon_o/2)} \tag{74}$$

or

$$u = \frac{2\varepsilon_o\ (1 + \varepsilon_o/2)\,(1 + \frac{2}{3}\ \varepsilon_o(1 + \varepsilon_o/2))/(1 + \varepsilon_o)^2}{1 + \frac{2}{3}\omega\varepsilon_o(1 + \varepsilon_o/2)} \quad . \tag{75}$$

If

$$C_1 = (1 + \varepsilon_o)\,(1 + \frac{2}{3}\ \varepsilon_o(1 + \frac{\varepsilon_o}{2}))/(1 + \varepsilon_o)^2 \tag{76}$$

and

$$C_2 = \frac{2}{3}\ \varepsilon_o(1 + \frac{\varepsilon_o}{2}) \tag{77}$$

then

$$u = 2\varepsilon_o\omega\frac{C_1}{1 + C_2\omega} \quad . \tag{78}$$

The term ε_o (the value of $n_o - 1$ at the observer) can be calculated using the Lorenz-Lorentz formula and the values of n and ρ_m at sea-level. Thus ε_o does not depend on A or θ.

The quantity $du(\theta)/dr$ is found from the derivative of Eq. (78)

$$\frac{du}{dr} = \frac{2C_1C_2\varepsilon_o}{(1 + C_2\omega)^2}\ \frac{d\omega}{dr} \quad . \tag{79}$$

But $\frac{d\omega}{dr} = -\ \frac{d}{dr}\left(\frac{\rho_m}{\rho_{mo}}\right)$, so

$$\frac{du}{dr} = - \frac{2C_1C_2\varepsilon_o}{(1 + C_2\omega)^2} \frac{d}{dr} \frac{\rho_m}{\rho_{mo}} \quad . \tag{80}$$

A.10 THE OPTICAL AIRMASS

The optical airmass in element ds of the ray path is

$$da = \rho_m ds \tag{81}$$

in Kg/m^2. Combining Eqs. (18), (19), and (81) gives

$$da = \frac{\rho_m r d\Omega}{\sin Z} \quad . \tag{82}$$

Combining Eq. (82) with Eqs. (45) and (21) yields the result

$$da = r_o \sin Z_o \rho_m \frac{(1-u)^{\frac{1}{2}}}{\sin^2(Z_o - \theta)} \frac{d\Omega}{d\theta} d\theta \quad . \tag{83}$$

But ρ_m can be expressed as a function of θ. The term $\rho_m(\theta)$ must be determined before Eq. (83) can be evaluated.

A.11 DETERMINATION OF $\rho_m(\theta)$ AND $\frac{d}{dr}(\rho_m/\rho_{mo})$

The density equations (Eqs. (35) and (36)) can be simplified by defining

$$h = \frac{H - H_o}{\gamma R_e - H_o} \quad . \tag{84}$$

From Eq. (14) h is given by

$$h = 1 - \frac{r_o}{r} \tag{85}$$

and using Eq. (21)

$$h = 1 - \frac{\sin(Z_o - \theta)}{\sin Z_o} \quad . \tag{86}$$

Substituting in the variable h, Eqs. (35) and (36) reduce to

$$\frac{\rho_m}{\rho_{mo}} = \begin{cases} (1 - C_3 h)^{\alpha} & \Gamma \neq 1 \\ e^{-C_4 h} & \Gamma = 1 \end{cases} \tag{87}$$

where

$$C_3 = \frac{\Gamma - 1}{\Gamma} \beta (R_e - H_o) \tag{88}$$

and

$$C_4 = \beta (R_e - H_o) . \tag{89}$$

The derivative $\frac{d}{dr} \frac{\rho_m}{\rho_{mo}}$ is obtained from Eq. (32)

$$\frac{d}{dr} \frac{\rho_m}{\rho_{mo}} = - \frac{\rho_m}{\rho_{mo}} \frac{1}{\Gamma} \frac{g_o' M}{R^*} \frac{1}{T} \frac{dH}{dr} . \tag{90}$$

Equations (84) and (85) give

$$\frac{H - H_o}{\gamma R_e - H_o} = 1 - \frac{r_o}{r} \quad . \tag{91}$$

Therefore

$$\frac{dH}{dr} = \frac{r_o}{r^2}(\gamma R_e - H_o) \tag{92}$$

or, using Eq. (21)

$$\frac{dH}{dr} = \frac{(\gamma R_e - H_o)}{r_o} \frac{\sin^2(Z_o - \theta)}{\sin Z_o} \quad . \tag{93}$$

Thus Eq. (90) becomes

$$\frac{d}{dr}\frac{\rho_m}{\rho_{mo}} = -\frac{\rho_m}{\rho_{mo}} \frac{\beta}{\Gamma} \frac{T_o}{T} \frac{(R - H_o)}{r_o} \frac{\sin^2(Z_o - \theta)}{\sin Z_o} \quad . \tag{94}$$

A.12 THE FINAL INTEGRAL FORMS

The function $u(\theta)$ can be determined by Eqs. (78), (66), (87), and (86) and $du(\theta)/dr$ by Eqs. (80), (66), (87), (86), and (94). Thus the differential expressions for $d\Omega$, dW and da can now be integrated. The polar angle between the source and observer is given by

$$\Omega = \int_o^{\theta_s} \left[1 - \frac{u(\theta)}{\cos^2(Z_o - \theta)}\right]^{-\frac{1}{2}} d_\theta \quad . \tag{95}$$

where θ_s is determined from Eq. (20). The total angular refraction is given by

$$W = \frac{\frac{\beta}{\Gamma}\varepsilon_o C_1 C_2 (R_e - H_o)}{\sin Z_o} \int_o^{\theta_s} \left[1 - \frac{u}{\cos^2(Z_o - \theta)}\right]^{-\frac{1}{2}} \frac{T_o}{T}$$

$$\frac{(1-\omega)\sin(Z_o - \theta)}{(1-u)(1+C_2\omega)^2}\, d\theta \ . \tag{96}$$

And the optical airmass encountered in the ray path by

$$a = \frac{\rho_{mo} R_e^{\,2} \sin Z_o}{(R_e - H_o)} \int_o^{\theta_s} \frac{(1-\omega)}{\sin^2(Z_o - \theta)} \left[(1-u)\right.$$

$$\left.\left\{1 - \frac{u}{\cos^2(Z_o - \theta)}\right\}^{-1}\right]^{\frac{1}{2}} d\theta \ . \tag{97}$$

The expression given in Eq. (97) gives the optical airmass in terms of the mass per unit area. The number of air molecules per unit area encountered along the ray is found by replacing the mass density ρ_m by the number density ρ_v which is given by

$$\rho_v = \frac{\rho_m N_A}{M} \tag{98}$$

where N_A is Avagadro's number. The variable ω in Eq. (97) will not change for this substitution since ω is given in terms of a density ratio.

The number of air molecules per unit area in a vertical column is given by

$$a_v = \int_{R_e}^{R_{TOP}} \rho_v(r)dr \ . \tag{99}$$

where R_{TOP} is the earth-centered radius of the top of the atmosphere. In terms of the geopotential height this expression can be written as

$$a_v = \int_{o}^{H_{TOP}} \rho_v(H)\frac{dH}{\gamma} \ . \tag{100}$$

If a_v is defined as one airmass, then the number of air molecules encountered along the ray path can be expressed in terms of airmasses by taking the ratio a/a_v (thus the term optical airmass).

Equations (95)-(97) were found by Treve to be well-behaved for altitudes less than 90 km. If the atmosphere is divided into a number of concentric layers, successive use of Eqs. (95)-(97) in each layer allows the total path of the radiation to be traced from observer to source. In each layer Z_S becomes the angle of entry of the ray into the layer and Z_O the angle of exit. The optical airmasses calculated in this work were obtained using Eq. (97).

The theory presented in this appendix has been used to determine the temperature profile of the stratosphere (9) and the mixing-ratio profiles of NO, NO_2, HNO_3, O_3, H_2O, and

NO_2 (10-15) from the analysis of infrared solar absorption spectra. This formalism has been found to be useful in accurately approximating the paths traversed by solar radiation.

REFERENCES

1) Y. M. Treve, "New Values of the Optical Air Mass and the Refraction and Comparison with Previous Tables," Technical Report ESD-TDR-64-103, Mitre Corp. (1964).

2) Y. M. Treve, "A New Method for the Calculation of the Atmospheric Refraction and Optical Airmass," (unpublished).

3) D. E. Snider, J. Atm. Sci., 32, 2178 (1975).

4) D. E. Snider and A. Goldman, "Refractive Effects in Remote Sensing of the Atmosphere with Infrared Transmission Spectroscopy," BRL Report no. 1970, Ball. Res. Lab., Aberdeen Proving Grounds, Maryland (1975).

5) H. A. Lorentz, collected papers, Vol. 2, The Hague (1936).

6) B. Edlen, Metrologia, 2, 71 (1966).

7) U.S. Standard Atmosphere 1976, NOAA-S/T-76-1562, GPO, Washington, D.C. (1976).

8) R. G. Fleagle and J. A. Bosinger, An Introduction to Atmospheric Physics, p. 41, Academic Press, New York (1963).

9) C. P. Rinsland, A. Goldman, F. J. Murcray, D. G. Murcray, M. A. H. Smith, R. K. Seals Jr., J. C. Larsen, and P. L. Rinsland, J. Quant. Spect. Rad. Trans., 30, 327 (1983).

10) A. Goldman, F. G. Fernald, W. J. Williams, and D. G. Murcray, Geophys. Res. Lett., 5, 257 (1978).

11) E. Niple, W. G. Mankin, A. Goldman, D. G. Murcray, and F. J. Murcray, Geophys. Res. Lett., 7, 489 (1980).

12) A. Goldman, D. G. Murcray, F. J. Murcray, and E. Niple, Appl. Opt., 19, 3721 (1980).

13) R. D. Blatherwick, A. Goldman, D. G. Murcray, F. J. Murcray, G. R. Cook, and J. W. Van Allen, Geophys. Res. Lett., 7, 471 (1980).

14) M. T. Coffey, W. G. Mankin, and A. Goldman, J. Geophys. Res., 86, 7331 (1981).

15) A. Goldman, F. G. Fernald, F. J. Murcray, F. H. Murcray, and D. G. Murcray, J. Quant. Spect. Rad. Trans., 29, 189 (1982).

Appendix B

Listed below are some of the symbols (and their definitions) used in this work. In general, subscripts 0, S, and T denote the value of the parameter at the observer, source, and tangent height respectively. The subscripts i, j, k, and ℓ denote the value of the parameter in the ith, jth, kth, or ℓth layer. Exceptions to these rules are noted below.

Symbol	Definition
A	The altitude above sea-level in geometric meters.
A_ν	The spectral absorptance at frequency ν.
a	The total optical airmass encountered along a ray path.
a_m	The total amount of an absorber encountered along a ray path.
a_v	The total airmass in a vertical column in the atmosphere.
E_ℓ	The transition energy corresponding to the ℓth spectral line.
$F(Z_o)$	The fractional time rate of change of the optical airmass as a function of the apparent zenith angle.
G	Newton's gravitational constant 6.67×10^{-11} nt - m^2/Kg^2.
$g(A)$	The acceleration due to gravity as a function of altitude.

Symbol	Definition
g_o	The acceleration due to gravity at sea-level $9.80665\ m/s^2$.
g_o'	$9.80665\ m^2/s^2m'$.
H	The altitude above sea-level in geopotential meters.
H_s	The pressure scale height in geometric meters.
$K(\nu)$	The effective spectral absorption coefficient for a layered inhomogeneous atmosphere as a function of frequency.
k_ν	The spectral absorption coefficient at frequency ν.
L_i	The temperature gradient of the ith atmospheric layer.
$\delta\ell_i$	The path length of a ray through the ith layer of the atmosphere.
M	The mean molecular weight of air 28.966 gm/mole.
M_e	The mass of the earth 5.98×10^{24} Kg.
m(A)	The mixing-ratio of an atmospheric constituent as a function of altitude.
N	The number of layers in the layered atmosphere.
N_A	Avagadro's number 6.02×10^{23} molecules/mole.
N_R	The number of retrieved mixing-ratio values.
N_o	The number of values in the retrieval data set.
n_i	The index of refraction of air in the ith layer.
n_o	The index of refraction at sea-level.

Symbol	Definition
$P(A)$	Pressure of the atmosphere as a function of altitude.
$P(o)$	The pressure at sea-level. Also used for sea-level pressure is P_o.
$R_e(\phi)$	The radius of the earth as a function of latitude.
R_o	The vertical resolution of the retrieved mixing-ratio profile at ground-level.
Res	The vertical resolution of the retrieved mixing-ratio profile. Subscript A denotes the region above the observer and B the region below.
R^*	The universal gas constant 8.314 joule/mole K.
r	The radial distance with respect to the earth's center of a point in the atmosphere.
S_ℓ	The spectral line intensity of the ℓth spectral line.
ds	Element of path through the atmosphere.
$T(A)$	Temperature of the atmosphere as a function of altitude.
T_ν	The spectral trasmittance at frequency ν.
t	Time.
t_e	The period of circular satellite orbit.
$U(A)$	The uncertainty of retrieved mixing-ratio values as a function of altitude.
u	$1 - (n/n_o)^2$.
W	The refractive angle of a ray path bent through the atmosphere.
$W(a_m)$	The equivalent width of a spectral line corresponding to a ray path through absorber amount a_m.

Symbol	Definition
Z	The astronomical zenith angle of a ray through the atmosphere.
Z_o	The apparent zenith angle of arrival at the observer of a ray through the atmosphere.
α_ℓ	The half-width of the ℓth spectral line.
α_o	The retrieved frequency shift obtained from spectral curve-fitting.
$\Delta(\nu_i)$	The frequency shift coefficient of α_o at frequency ν_i.
ε	Random experimental noise.
θ	Apparent polar angle of a point along the path of a ray through the atmosphere.
λ	The wavelength in μm of the observed radiation.
$\mu(A)$	The gravitational potential energy per unit mass at altitude A.
ν	Frequency in cm^{-1}.
ν_A	The lowest frequency value of the spectral data analyzed.
$\nu_{o\ell}$	Line center of the ℓth spectral line.
ρ_v	Volume density of the atmosphere.
ρ_m	Mass density of the atmosphere.
$\sigma(A)$	The standard deviation of the retrieved mixing-ratio values.
γ	The conversion factor from geometric to geopotential meters.
ϕ	Earth's latitude.
Ω	Astronomical polar angle of a point along the path of a ray through the atmosphere.
ω	$1 - (\rho/\rho_o)$.